University of California
Santa Barbara

Flow-concentration coupling in entangled polymeric liquids

A dissertation submitted in partial satisfaction
of the requirements for the degree

Doctor of Philosophy
in
Chemical Engineering

by

Michael Chester Burroughs

Committee in charge:

Professor Matthew E. Helgeson, Co-Chair
Professor L. Gary Leal, Co-Chair
Professor Glenn H. Fredrickson
Professor Christopher M. Bates
Professor Omar A. Saleh

September 2021

The Dissertation of Michael Chester Burroughs is approved.

Professor Glenn H. Fredrickson

Professor Christopher M. Bates

Professor Omar A. Saleh

Professor L. Gary Leal, Committee Co-Chair

Professor Matthew E. Helgeson, Committee Co-Chair

August 2021

Flow-concentration coupling in entangled polymeric liquids

by

Michael Chester Burroughs

To my parents, Chet and Jean Burroughs, for being the best role-models, parents, and friends that I could ever imagine.

Acknowledgements

I owe a tremendous amount of gratitude to the many individuals who have helped shape my professional identity and this thesis research over the last 6 years. I credit my accomplishments to the many supportive personal relationships and mentorship that I have been fortunate to receive. I sincerely cherish each and every one of the relationships that I have developed during my time at UCSB, and I hope that we will remain in contact and/or cross paths in the coming years.

First and foremost, I would like to thank my thesis advisors, Matt Helgeson and Gary Leal, for their patience, support, and unwavering belief in my ability as a scientist. I cannot begin to adequately describe how influential Matt and Gary have been to my development through their generosity of time, reassurance when I was nearing despair, and connections to the greater complex fluids community. I like to think that in addition to the skills and scientific expertise that I have developed under Matt and Gary's tutelage, I have also gained two friends. Matt, I am continually impressed by your ability to write and rephrase concepts in an easily digestible way. I hope that some of this skill has rubbed off on me over the course of my Ph.D. Gary, thank you for the level of scrutiny you have applied to everything that I have done. I am fortunate to have worked for someone so deeply invested in the quality of science. I am also appreciative of the perspective you have provided me, which I guess comes from $>$ 50 years of academic experience and decades as editor of a scientific journal! I value, and have undoubtedly benefitted from, your ability to perceive how work will be viewed by the greater fluids and soft matter community.

I would also like to thank the members of my thesis committee: Glenn Fredrickson, Chris Bates, and Omar Saleh. Each of you have helped to shape my research directions and excitement for scientific research in your own way. Glenn, I appreciate your

candid feedback during my annual committee meetings and suggestions for what is the most worthwhile/impactful area to focus my efforts. Chris, thank you for your constant enthusiasm and creativity; in fact, you provided a very uplifting suggestion for experiments when I was nearing wits' end! Omar, thank you for never shying away from asking questions to expose my ability to convey research topics to a more broad scientific audience.

I am grateful for the many people in the UCSB ChE front office staff that ensure smooth operation of this wonderful department. In particular, I want to thank Mike Best, Erica Diaz, Nicole Becker, Rachel Irving, Grace Fox-Tappin, Michelle Fitzgerald, George Crespo, and Ashley Olivo for always being able to promptly address my questions and requests. I would also like to thank the staff that I did no directly interface with, but undoubtedly aided me with their "behind the scenes" work.

My time at UCSB was greatly enhanced by the relationships I made with peers in the Helgeson and Leal research groups. Thank you to the group postdocs (Nino, Bas, Chandi, Josh B., and Tamás) and senior grad students (Juntae, Peng, Gwen, Alexandra, Tuan, Joe, and Nikolai) for your scientific mentorship. I want to particularly thank my fellow classmate and labmate, Patrick, for the *many* afternoon scientific discussions spent over coffee, his contagious excitement for science, and general positivity. I also owe thank you's to the younger graduate students in the group (Jiamin, Tanvi, Serena, Josh S., Scott, and Chelsea) for listening to and providing feedback on many hours of my research talks and the fun times in lab and our (several) group offices over the years. I hope that I have been able to positively influence you all as the postdocs and senior graduate students have for me.

To the incoming UCSB ChE Ph.D. class of Fall 2015: what a ride! Thank you for becoming my first friends out on the West Coast, providing support through our first-year classes, exploring the many restaurants around Santa Barbara, and banding together to

put on the 12^{th} annual Clorox-Amgen Graduate Student Symposium. It is a real pity that the COVID-19 pandemic prevented us from properly saying our goodbyes as each Ph.D. defense passed, but I look forward to reuniting at some point in the future. In the meantime, I will enjoy seeing where everyone's careers take them.

My successes in grad school would not be possible without the support that I received from the people who mean the most to me. I want to thank my parents, the first engineers I ever knew, for providing enriching experiences throughout my upbringing, fostering a family with an unconditional love for one another, and believing in and supporting my interests and pursuits. Thank you to my sister, Mary, and brother-in-law, Raleigh, for equipping me with the perspective of what is required for a Ph.D. in chemical engineering. Thanks to my younger brother, Matt, for providing comedic relief during stressful times through many FaceTime calls. I have enjoyed watching you grow as a Ph.D. student (now candidate!) and hearing about the beginnings of your research project. Lastly, thank you to my youngest brother, Mason, for continually reminding me of what it looks like to be passionate about science. I applaud you for having the courage to be the lone Burroughs sibling to pursue an academic discipline outside of chemical engineering!

Most importantly, I want to thank my girlfriend Patrice. My time at UCSB has been marked by some of my greatest personal and professional struggles, but having a supportive partner to lean on through the, at times, overwhelmingly stressful periods has undoubtedly helped me achieve this milestone. Out of all the people referenced in this tribute, you have provided the most support and seen, up close, the unbelievable highs and lows of my Ph.D. journey. Thank you for your patience with me as I completed this thesis research, your unwavering support, instilling self-confidence through constant reassurance, listening to countless hours of me practice upcoming talks, and for making sure that I don't lose sight of the important things in life.

Curriculum Vitæ

Michael Chester Burroughs

Education

2021	Ph.D. in Chemical Engineering (Expected), University of California, Santa Barbara
2015	B.S. in Chemical Engineering, North Carolina State University

Publications

M. C. Burroughs, A. M. Shetty, L. G. Leal, M. E. Helgeson, "Flow kinematics of bidisperse polymer blends in the melt and in solution" (*in prep*).

M. C. Burroughs, M. E. Helgeson, L. G. Leal, "Signatures of flow-concentration coupling in Large Amplitude Oscillatory Shear" (*in prep*).

M. C. Burroughs, Y. Zhang, A. M. Shetty, C. M. Bates, M. E. Helgeson, and L. G. Leal, "Nonhomogeneous flow in entangled polymer solutions is sensitive to the degree of flow-concentration coupling as revealed by simultaneous measurements of velocity and concentration profiles" (*in prep*).

M. C. Burroughs, Y. Zhang, A. M. Shetty, C. M. Bates, M. E. Helgeson, L. G. Leal, "Flow-induced nonuniformity and shear banding in entangled polymer solutions" *Physical Review Letters* 2021, 126, 207801. DOI: doi:10.1103/PhysRevLett.126.207801

R. D. Corder, P. Adhikari, **M. C. Burroughs**, O. J. Rojas, S. A. Khan, "Cellulose Nanocrystals for Gelation and Percolation-induced Reinforcement of a Photocurable Poly (vinyl alcohol) Derivative", *Soft Matter*, 2020, 16, 8602-8611. DOI: 10.1039/D0SM01376E

M. C. Burroughs, A. M. Shetty, L. G. Leal, M. E. Helgeson, "Coupled non-homogeneous flows and flow-enhanced concentration fluctuations during startup shear of entangled polymer solutions", *Physical Review Fluids*, 2020, 5, 043301. DOI: 10.1103/PhysRevFluids.5.043301

P. Cheng, **M. C. Burroughs**, L. G. Leal, M. E. Helgeson, "Distinguishing shear thinning from shear banding in flows with a stress gradient", *Rheologica Acta*, 2017, 56, 1007-1032. DOI: 10.1007/s00397-017-1051-y

M. C. Burroughs*, S. M. Bhaway*, P. Tangvijitsakul, K. A. Cavicchi, M. D. Soucek, B. D. Vogt, "Cooperative Assembly of Metal Nitrate and Citric Acid with Block Copolymers: Role of Carbonate Conversion Temperature on the Mesostructure of Ordered Porous Oxides", *Journal of Physical Chemistry C*, 2015, 22, 12138-12148. DOI: 10.1021/acs.jpcc.5b02177 (* indicates co-first author)

N. A. Burns, **M. C. Burroughs**, H. Gracz, C. Q. Pritchard, A. H. Brozena, J. Willoughby, S. A. Khan, "Cyclodextrin facilitated electrospun chitosan nanofibers", *RSC Advances*, 2015, 5, 7131-7137. DOI: 10.1039/c4ra09662b

Conference Presentations

M. C. Burroughs, L. G. Leal, M. E. Helgeson, "Shear banding instabilities caused by flow-concentration coupling in viscoelastic polymer solutions" *Virtual Workshop on Viscoelastic Flow Instabilities and Elastic Turbulence*. Princeton Center for Theoretical Science. January 7, 2020. *Invited talk

M. C. Burroughs, A. M. Shetty, L. G. Leal, M. E. Helgeson, "Coupled shear banding and flow-induced demixing in entangled polymer solutions" *18th International Congress on Rheology*. Rio de Janeiro, Brazil. December 14, 2020.

M. C. Burroughs, M. E. Helgeson, L. G. Leal, "Non-homogeneous flows in entangled polymer solutions driven by flow-concentration coupling" *91st Annual Meeting of the Society of Rheology*. Raleigh, NC. October 22, 2019.

M. C. Burroughs, M. E. Helgeson, L. G. Leal, "Understanding flow-concentration coupling in entangled polymer solutions" *12th Annual Amgen-Clorox Graduate Student Symposium*. UC Santa Barbara, Santa Barbara, CA. October 4, 2019.

M. C. Burroughs, M. E. Helgeson, L. G. Leal, "Non-homogeneous flows and flow-enhanced concentration fluctuations during startup shear of entangled polymer solutions" *SoCal Fluids XIII*. UC Santa Barbara, Santa Barbara, CA. April 20, 2019.

M. C. Burroughs, M. E. Helgeson, L. G. Leal, "Nonhomogeneous flows during startup shear of highly entangled polystyrene solutions" *90th Annual Meeting of the Society of Rheology*. Houston, TX. October 15, 2018.

Abstract

Flow-concentration coupling in entangled polymeric liquids

by

Michael Chester Burroughs

Flow-based polymer processing is ubiquitous in the formation of soft materials for applications ranging from healthcare to packaging. Polymer processing strategies have historically been determined empirically, where the maximum flow rate is often established by the onset of visual distortions from uniform flow. Such an approach prohibits predictive flow calculations for arbitrary flow environments and polymeric formulations. Theoretical advances over the past several decades have enabled molecularly informed rheological modeling of entangled polymer liquids; however, most models assume that the fluid composition remains uniform during flow. Several exceptions to this assumption are known for polymer solutions such as shear-enhanced concentration fluctuations and polymer migration across curved streamlines, but these effects are typically not accounted for in models due to the belief that these compositional heterogeneities either occur on a small scale, with an insignificant effect on the bulk flow behavior, or on diffusive timescales, which are much longer than typical processing flows. This belief has been challenged by a recently developed two-fluid theory for entangled polymers, which, under certain conditions, predicts that uniform flow is unstable due to a shear-induced demixing instability that results in shear banding (*i.e.*, two or more regions of distinct shear rates across the fluid under a shear flow); however, there is a lack of experimental measurements to directly compare with this theory.

To fill this gap, this dissertation experimentally explores the coupling of shear-induced compositional changes to bulk flow behavior in entangled polymer liquids. To do this,

a combination of novel rheo-optical techniques are developed and used to quantify both fluid velocity and concentration fields. Qualitatively different results are observed depending on the number of entanglements and osmotic susceptibility of the polymer solutions. For entangled polystyrene in dioctyl phthalate, spatial variations of shear-enhanced concentration fluctuations in startup shear are coupled to changes in the bulk flow. In particular, the presence of mesoscopic concentration heterogeneities coincides with a local effective viscosity increase of the fluid. Conversely, entangled polybutadiene in dioctyl phthalate exhibits macroscopic heterogeneities in concentration that coincide with shear banded velocity profiles, consistent with a two-fluid model that couples the flow to polymer concentration. The effect of polydispersity on the flow behavior of entangled polymer liquids was investigated by using chemically homologous, bidisperse polymer blends. Interestingly, differences in the flow behavior were observed for blends of equivalent numbers of entanglements, but different blend compositions. Lastly, the two-fluid model for entangled polymer solutions is used to investigate nonuniform flows that arise from shear-induced demixing in complex flow protocols (*i.e.*, large amplitude oscillatory shear (LAOS)).

The results of this dissertation underscore the possibility for non-local concentration changes in flows of entangled polymeric liquids, and reveal a wide range of flow phenomena that result when it is operative. More generally, the concept of flow-concentration coupling is likely applicable to many other complex fluids and should be accounted for in future models to accurately describe their rheology.

Contents

Curriculum Vitae **viii**

Abstract **x**

List of Figures **xv**

List of Tables **xxii**

1 Introduction **1**
1.1 Motivation 1
1.2 Project introduction 2
1.3 Objectives 8
1.4 Outline of dissertation 9

Bibliography **11**

2 Rheological and optical methods for complex fluids **15**
2.1 Abstract 15
2.2 Materials and preparation 16
2.3 Rheological characterization 17
2.4 Rheo-optical methods 20
2.5 Fluorescent-tagging of polybutadiene 24
2.6 Summary and outlook 25

Bibliography **27**

3 A two-fluid model for entangled polymer solutions **29**
3.1 Introduction 29
3.2 The two-fluid formalism for solutions 30
3.3 The stress tensor for entangled polymeric liquids 31
3.4 Predictions of the two-fluid Rolie-Poly model 34
3.5 Summary 38

Bibliography **40**

4 Local flow-concentration coupling in entangled polystyrene solutions **41**
4.1 Abstract . . . 41
4.2 Introduction . . . 42
4.3 Materials and methods . . . 46
4.4 Results and discussion . . . 49
4.5 Conclusions . . . 71

Bibliography **73**

5 Non-local flow-concentration coupling in entangled polybutadiene solutions **79**
5.1 Abstract . . . 79
5.2 Introduction . . . 80
5.3 Materials and Methods . . . 82
5.4 Results and Discussion . . . 85
5.5 Conclusions . . . 91

Bibliography **94**

6 Sensitivity of flow-concentration coupling to fluid properties **99**
6.1 Abstract . . . 99
6.2 Introduction . . . 100
6.3 Materials and methods . . . 106
6.4 Results and discussion . . . 108
6.5 Conclusions . . . 137

Bibliography **141**

7 A two-fluid model for entangled bidisperse polymer blends **145**
7.1 Introduction . . . 145
7.2 Categorizing the rheology of bidisperse blends . . . 146
7.3 The two-fluid formalism for bidisperse blends . . . 148
7.4 Describing bidisperse polymer blends in terms of the Rolie-Double-Poly model . . . 150
7.5 Stability predictions . . . 153
7.6 Transient flow calculations using the two-fluid RDP model . . . 153
7.7 Summary . . . 155

Bibliography **157**

8 A study of the flow kinematics and composition of entangled bidisperse polymer blends **159**
8.1 Abstract . . . 159
8.2 Introduction . . . 160
8.3 Materials and experimental methods . . . 163
8.4 Results and discussion . . . 166
8.5 Conclusions . . . 178

Bibliography **181**

9 A numerical study of the two-fluid Rolie-Poly model in Large Amplitude Oscillatory Shear **185**
9.1 Abstract . . . 185
9.2 Introduction . . . 186
9.3 Methods . . . 190
9.4 Results and discussion . . . 192
9.5 Conclusions . . . 203

Bibliography **205**

10 Conclusions **208**
10.1 Summary . . . 208
10.2 Conclusions . . . 209
10.3 Future directions . . . 212

Bibliography **215**

List of Figures

1.1 (a) Space-filling polymer chain with characteristic size, R_g (radius of gyration) and (b) sensitivity of polymer chain packing to increasing polymer volume fraction. 3

1.2 Time-dependent relaxation modulus for increasing time following a step strain. τ_e corresponds to the relaxation time of an entanglement segment, whereas τ_d represents the longest relaxation time (chain reptation). . . . 4

1.3 Microscopic entangled network is coarse grained into a confining tube made up of the topological constraints on an individual chain. 5

1.4 Representative shear rate dependence of the viscosity of an entangled polymeric liquid. 6

1.5 Cartoon representation of uniform and shear banded flows (left). Non-monotonic flow curve illustrating the constitutive instability explanation for why shear banded flows occur (right). 7

1.6 (a) Illustration of shear-enhanced thermal fluctuations in polymer solutions (black dots represent solvent molecules) (b) representative small angle scattering and microscopy images showing qualitative changes upon increasing shear rate. Reprinted (adapted) with permission from *Macromolecules* 1997, 30, 23, 7232-7236. Copyright 1997 American Chemical Society. 8

2.1 Experimental approach used in this dissertation research for characterizing entangled polymer liquids. 16

2.2 Rheo-Particle Tracking Velocimetry (rheo-PTV) setup. Glass tracer particles are illuminated in the flow-gradient plane using a laser sheet. Reflections from the glass tracer particles are imaged with an objective and camera mounted beneath the transparent flow cell. Displacements of particles between adjacent image pairs acquired at a particular frame rate are converted to velocities. 22

2.3 Rheo-microscopy optical setup. The transparent flow cell is located between cross polarizers that are oriented 90° to one another. Light transmission and optical heterogeneity is detected with a CCD camera mounted below the flow cell. 23
2.4 Rheo-fluorescence optical setup. A fluid with trace amounts of fluorophore is illuminated with excitation filtered light. The resulting fluorescence intensity is measured with an objective and CCD camera after the light is further filtered through an emission wavelength bandpass filter. 25
2.5 (a) Fluorescent-tagging reaction of polybutadiene and the fluorophore, coumarin, and (b) gel permeation chromatography (GPC) traces that confirm the fluorophore is bound to the polymer. 26

3.1 Cartoon illustration detailing the conceptual idea of a two-fluid model. Flow ($\boldsymbol{u}$) fields of polymer ($\boldsymbol{u}_p$) and solvent ($\boldsymbol{u}_s$) are coupled by friction (ζ) and conservation of mass (ϕ) is ensured through species continuity. . 30
3.2 Stability diagram as determined from a linear stability analysis on the two-fluid model equations. The boundaries of instability in entanglement density versus Wi space depend on the particular value of E. Adapted from Peterson *et al.* (2016) [3]. 35
3.3 Two-fluid model predictions of the steady state (a) concentration and (b) velocity profile at varying degrees of flow-concentration coupling (E) for $Z = 66$ and $Wi = 6$. 36
3.4 Two-fluid model predictions for transient evolution of the (a) concentration and (b) velocity profile for $Z = 66$, $E = 0.20$, and $Wi = 4$ in Taylor-Couette flow with curvature $q = \frac{R_i - R_o}{R_i} = 0.029$. The line colors in (b) correspond to the same t/τ_d as in (a). 38

4.1 (a) Linear viscoelastic frequency sweeps for three entangled PS/DOP solutions. Measurements were conducted at a strain = 1%, and (b) verification of Cox-Merz rule for shear rates employed in this study. 51
4.2 Rolie-Poly model flow curve predictions (lines) and measured steady state shear stresses (symbols) for (a) 5 wt% PS(8.42M)/DOP, (b) 10 wt% PS(8.42M)/DOP, and (c) 16 wt% PS(3.84M)/DOP. 53
4.3 (a) Wi dependence of the peak strain (γ_{max}, strain at which the shear stress exhibits an overshoot) following startup shear where the solid and dashed lines indicate power law slopes of 0.45 and 0.28, respectively, and (b) the ratio of the maximum shear stress to the shear stress at steady state ($\sigma_{overshoot}/(\sigma_{steady\ state})$ for varying Wi. 56
4.4 Velocity profiles for 10 wt% PS(8.42M)/DOP ($Z = 36$) at varying applied Wi for times between $t/\tau_d \approx 7$ and 11 after startup of shear flow. 59

4.5 Transient response of PS/DOP solution with $Z = 16$ to step shear of $Wi_{app} = 5.05$ (a) shear stress and (b) velocity profile data. The symbols overlaid on the shear stress response correspond to the time at which the velocity profiles in (b) were measured. Black dashed lines denote the homogeneous Rolie-Poly model prediction for the transient shear stress in (a) and the steady velocity in (b). 60
4.6 Transient response of PS/DOP solution with $Z = 36$ to a step shear of $Wi_{app} = 5.29$ (a) measured shear stress response and (b) determined velocity profiles for discrete points in time following the startup of flow. Symbols overlaying the measured shear stress in (a) coincide with the point in time of each velocity profile in (b). 62
4.7 Transient response of PS/DOP solution with $Z = 30$ to a step shear of $Wi_{app} = 5.14$ (a) the measured shear stress and (b) the determined velocity profiles at discrete points in time following the startup of flow. 63
4.8 Rheo-microscopy images showing the development and decay of flow-enhanced concentration fluctuations in 16 wt% PS(3.84M)/DOP at $Wi_{app} = 11.1$. (a) prior to the shear stress overshoot (b-c) shortly after the shear stress overshoot (c) at long times following the shear stress overshoot when the stress has reached a constant value. 65
4.9 Transient development of velocity profiles of 16 wt% PS(3.84M)/DOP at $Wi_{app} = 11.1$ overlaid on corresponding images collected in rheo-microscopy with a bandpass filter applied showing shear-enhanced concentration fluctuations at (a) $t/\tau_d = 0.04$, (b) $t/\tau_d = 1.9$, and (c) $t/\tau_d = 24.62$. 68
4.10 Normalized transient viscosity as measured by the rheometer compared to spatially-resolved apparent viscosities adjacent to the inner and outer cylinders of the Taylor-Couette geometry for 10 wt% PS(8.42M)/DOP at $Wi_{app} = 5.29$. The open symbols represent the local transient viscosities normalized by the steady state viscosities at the locally measured shear rates $\eta(\dot{\gamma}_{inner})^{SS}$ and $\eta(\dot{\gamma}_{outer})^{SS}$. The solid black line represents the measured transient viscosity at the nominal imposed shear rate normalized by the steady state viscosity. 70

5.1 (a) Cartoon of PBD tagged with coumarin fluorophore (PBDC) and the resulting fluorescence across a concentration series of PBDC (vials), (b) rheofluorescence setup with 350 nm incident light and emission wavelengths filtered to 415 nm, (c) representative data for quiescent fluorescence versus fluorescence measured under shear. 83
5.2 Steady state velocity profile of 10 wt% PBd(1M)-DOP with $Z = 38$ at $Wi_{app} = 5$ with model fits for varying E. The position (r/H) is determined by normalizing the radial distance from the moving wall (r) by the fluid thickness (H). 86

5.3 (a,b) Steady state velocity profiles for varying Wi_{app} at $T = 50$ ℃. Symbols correspond to experimentally measured values from rheo-PTV and solid lines are two-fluid model predictions for $E = 0.11$. (c) Interface widths of the flow profiles calculated using the method detailed in Cheng et al. [51]. 88
5.4 Transient evolution of the concentration profile as measured from rheo-fluorescence under an applied shear flow of (a) $Wi_{app} = 2.7$ and (b) $Wi_{app} = 5$. Error bars represent the standard error associated with the fluorescence pixel intensities within each bin. 89
5.5 Steady state concentration profiles at varying Wi_{app}. Symbols reflect experimentally measured concentration estimates from rheo-fluorescence and solid lines correspond to model predictions for $E = 0.11$. Error bars represent the standard error associated with the fluorescence pixel intensities within each bin. 92

6.1 Small amplitude oscillatory shear frequency sweeps showing the linear viscoelasticity of the entangled PBD-DOP solutions for (a) $Z = 38$ and (b) $Z = 66$ at varying temperatures. Inset plots show the estimated longest relaxation time at each temperature as determined from the crossover frequency of G' and G''. 110
6.2 Time-averaged steady state velocity profiles for PBD-DOP solution with $Z = 38$. (a,b) $T = 16$ ℃ (c,d) $T = 21$ ℃ (e,f) $T = 50$ ℃. 112
6.3 Time-averaged steady state velocity profiles for PBD-DOP solution with $Z = 66$. (a,b) $T = 16$ ℃ (c,d) $T = 21$ ℃ (e,f) $T = 50$ ℃. 115
6.4 Two-fluid R-P model fits to experimentally measured velocity profiles (a) $Z = 38$, $Wi_{app} = 6.4$ (b) $Z = 66$, $Wi_{app} = 4.7$ (c) evaluation of model fit to experimental data depending on the value of E used in the model calculation. 117
6.5 (a) Two-fluid R-P model fits to experimentally measured velocity profiles at varying Wi_{app} using a single value of E ($E = 0.18$) and (b) value of E that yields the best fit to measured velocity profiles across range of Wi_{app} at each T. 119
6.6 Concentration profiles determined from rheo-fluorescence in PBD-DOP solution with $Z = 38$. Solid lines represent the resulting model fits determined from fitting to the measured velocity profiles with no further adjustable parameters. 121
6.7 Concentration profiles determined from rheo-fluorescence for PBD-DOP solution with $Z = 66$. Solid lines represent the resulting model fits determined from fitting to the measured velocity profiles with no further adjustable parameters. 123
6.8 Wall slip in the $Z = 38$ PBD-DOP solution for varying Wi_{app} at the (a) inner wall and (b) outer wall. 125

6.9 Wall slip in the $Z = 66$ PBD-DOP solution for varying Wi_{app} at the (a) inner wall and (b) outer wall. 126
6.10 rLOESS determined (a) interface location and (b) interface width for varying Wi_{app} and T in the $Z = 38$ PBD-DOP solution. 128
6.11 rLOESS determined (a) interface location and (b) interface width for varying Wi_{app} and T in the $Z = 66$ PBD-DOP solution. 130
6.12 (a) Transient shear stress development under shear of $Wi_{app} = 3.2$ at $T = 21$ ℃ for the $Z = 38$ PBD-DOP solution. The black line corresponds to measured shear stress whereas symbols correspond to the times at which the velocity profiles were measured in (b) and (c). 131
6.13 (a) Transient shear stress for $Wi_{app} = 3.2$ at $T = 16$ ℃ in the $Z = 38$ PBD-DOP solution. The black line corresponds to the measured shear stress and the symbols correspond to the times at which the velocity profiles in (b) and (c) were measured. 132
6.14 (a) Transient shear stress for $Wi_{app} = 5$ at $T = 50$ ℃ for the $Z = 38$ PBD-DOP solution. The black line corresponds to the measured shear stress whereas the symbols represent the times at which the velocity profiles in (b) and (c) were measured. 134
6.15 Transient response of PBD-DOP solution with $Z = 66$ at $T = 16$ ℃ and $Wi_{app} = 9.8$. (a) the evolution of the measured shear stress following the startup of shear. The symbols correspond to the times at which each velocity profile was measured in (b) and (c). (b) The transient velocity profiles measured from $t/\tau_d = 0.07$ to 13 and (c) from $t/\tau_d = 50.0$ to 86. . 136
6.16 Transient response of PBD-DOP solution with $Z = 66$ at $T = 50$ ℃ and $Wi_{app} = 4.7$. (a) the evolution of the measured shear stress following the startup of shear. The symbols correspond to the times at which each velocity profile was measured in (b) and (c). (b) The transient velocity profiles measured from $t/\tau_d = 0.05$ to 15 and (c) from $t/\tau_d = 23$ to 90.1. . 138
6.17 Transient response of PBD-DOP solution with $Z = 66$ at $T = 50$ ℃ and $Wi_{app} = 12$. (a) the evolution of the measured shear stress following the startup of shear. The symbols correspond to the times at which each velocity profile was measured in (b) and (c). (b) The transient velocity profiles measured from $t/\tau_d = 0.05$ to 0.21 and (c) from $t/\tau_d = 28$ to 180. 139

7.1 Cartoon illustration of the Viovy diagram which characterizes regions of different rheological behavior depending on Gr and Z_L. 149
7.2 Predicted stability depending on the dispersity ($I_P = \bar{Z}(\frac{\phi_L}{Z_L} + \frac{\phi_S}{Z_S})$) of the blend and applied Wi for a bidisperse blend with $\phi_L = 0.5$. The unstable region extends to lower Wi and a larger dispersity range as Z_L increases. Reprinted with permission from Peterson, Fredrickson, and Leal, *Journal of Rheology*, **64**, 1391, (2020). Copyright 2020, The Society of Rheology. . 154

7.3 Transient evolution of shear-induced demixing of a Region III bidisperse blend with $Z_L = 100$ and $Z_S = 30$ deformed under a constant shear stress ($\sigma_{xy} = 0.16$) at (a) short times following the onset of concentration heterogeneity growth, (b) moderate times, and (c) steady state. Reprinted with permission from Peterson, Fredrickson, and Leal, *Journal of Rheology*, **64**, 1391, (2020). Copyright 2020, The Society of Rheology. 156

8.1 (a) Classic Viovy diagram for characterizing bidisperse blends according to the Graessley number and effective long chain entanglements (cartoon illustration of Region III blend and Region III blend "in solution". 165
8.2 Small amplitude oscillatory shear rheology of (a) Region III and Region IV bidisperse blends and (b) Region III blend in solution. The strain amplitude was set to 1% for all measurements. 168
8.3 Predictions of the Wi sensitivity of eigenvalues according to a linear stability analysis using a two-fluid model for bidisperse blends. 170
8.4 Flow kinematics of the Region III blend in solution at varying Wi_{app}. . . 172
8.5 Concentration profiles of the Region III blend in solution measured by rheo-fluorescence under shear at specified Wi_{app}. 173
8.6 Flow kinematics of the Region III blend at varying Wi_{app}. 175
8.7 Concentration profiles of the Region III blend measured by rheo-fluorescence under shear at specified Wi_{app}. 176
8.8 Flow kinematics of the Region IV blend at varying Wi_{app}. 177
8.9 Concentration profiles of the Region IV blend measured by rheo-fluorescence under shear at specified Wi_{app}. 179

9.1 Representative elastic (left) and viscous (right) Lissajous-Bowditch curves, illustrating how the measured shear stress can be plotted parametrically against either the imposed strain (left) or shear rate (right). 188
9.2 Pipkin diagram of (a) elastic and (b) viscous Lissajous-Bowditch curves at particular Wi and De. All data were computed using the two-fluid Rolie-Poly model with $Z = 40$ and $E = 0$ (the flow and concentration remain uniform). 194
9.3 Stability boundaries for the two-fluid Rolie-Poly model with $Z = 40$ in steady shear and LAOS flows as determined from numerical simulation. The demixing instability was initiated by ($\partial\bar{\phi}_0 = 1 \times 10^{-5}$) perturbations to the initial concentration profile. 196
9.4 Steady time-varying velocity profiles (top) and corresponding concentration profiles (bottom). $Wi = 8$, $De = 0.1$, $Z = 40$, and $E = 0.20$. 198
9.5 Velocity (top) and concentration (bottom) profiles when the wall imposed shear rate is at a maximum for varying degrees of flow-concentration coupling. $Wi = 8$, $De = 0.1$, and $Z = 40$. 199
9.6 Sensitivity of elastic (left) and viscous (right) Lissajous-Bowditch plots to the degree of flow-concentration coupling (E). $Wi = 8, De = 0.05, Z = 40$. 201

9.7 Spatially resolved Lissajous-Bowditch curves illustrating the difference in local material strain and strain rates. $Wi = 8$, $De = 0.1$, $Z = 40$, and $E = 0.20$. Legend is the same for top two plots. 203

List of Tables

4.1 Viscoelastic solution properties determined from rheological measurements. The Rouse time was calculated from the measured τ_d (s) and the relation $\tau_d/\tau_R = 3Z$. 50

8.1 Compositional, rheological, and molecular details of each entangled polymer blend in this study. 166

Chapter 1

Introduction

1.1 Motivation

Polymeric materials are ubiquitous in products encountered on a daily basis, spanning numerous industries such as automotive [1], personal care [2], healthcare [3], and packaging [4]. In many applications, polymers are entangled and processed as either solutions (polymer dissolved in a small molecule solvent) or melts (pure polymer – no solvent). The entanglements polymer chains form with one another are known to give rise to peculiar rheological properties that complicate materials processing. In order to transform the polymer feedstock into useful plastic materials, some form of processing and transport must occur.

The optimal processing conditions for polymer solutions and melts are often determined empirically, where the maximum flow rate is determined from the onset of observed flow complications and anomalous flow. This empirical approach to characterizing polymeric material flow behavior is problematic for numerous reasons. First, is that the maximum flow rate identified in this way is often painfully slow, which, in turn, limits the speed at which polymeric materials can be manufactured. Additionally, this ap-

proach to determining processing conditions for polymeric materials is not rooted in any molecularly based theory, and therefore prevents physically based design rules from being established. Alternatively, an accurate molecular theory that describes the underlying physics of entangled polymeric liquids would permit a fundamental understanding of the physics and flow behavior of entangled polymeric materials, and potentially identify strategies for processing flows that avoid or bypass empirically determined flow limitations.

Models of entangled polymers often presume that the fluid composition remains uniform during processing; however, there are several known exceptions to this assumption. This dissertation research investigates the extent to which this conjecture is valid and directly compares the predictions of two-fluid models accounting for concentration heterogeneities in polymer solutions and melts with experimental measurements.

1.2 Project introduction

Polymers are long chain macromolecules formed by many repeat units (monomers) covalently bound to one another. These molecules adopt a "random walk" configuration in space. This random walk results in space-filling spheres of individual molecules in solution or the melt, with a characteristic size of R_g where $R_g = \frac{bN^{1/2}}{\sqrt{6}}$ and b is the Kuhn length and N is the number of Kuhn monomers, as shown in Figure 1.1. In the dilute limit ($\phi < \phi^*$), polymer molecules in solution are non-interacting with one another. Above a critical overlap concentration (ϕ^*), the polymer chains begin to interact and interpenetrate each other. Above the entanglement concentration ($\phi_e = 4\phi^*$) [5], the polymer chains are entangled and form a "transient network" that relaxes on a time scale characteristic of diffusive motion of the polymer chains. The architecture and size of polymer molecules give rise to many interesting and sometimes desirable properties such as

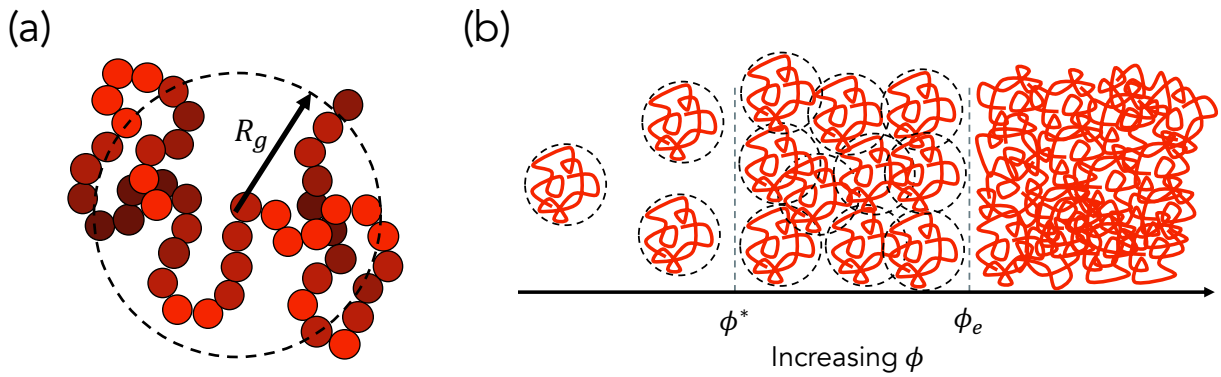

Figure 1.1: (a) Space-filling polymer chain with characteristic size, R_g (radius of gyration) and (b) sensitivity of polymer chain packing to increasing polymer volume fraction.

viscoelasticity, where the fluid exhibits both viscous (liquid-like) and elastic (solid-like) properties depending on the magnitude and rate of deformation. The transient network of entangled polymer chains results in a plateau modulus (G_N^0) over intermediate time scales, where $G_N^0 = \nu k_B T$ with ν representing the number density of entanglement strands, k_B the Boltzmann constant, and T the temperature (Figure 1.2). For times greater than the diffusive time scale for polymer chain relaxation (τ_d), the transient entanglement network is able to relax and the polymeric fluid behaves as a viscous liquid. de Gennes was the first to envision the dynamics of these entangled polymer chains as reptation past fixed obstacles [6]. Reptation dynamics were successfully incorporated into a constitutive model for entangled polymers by Doi and Edwards [7]. The conceptual picture that emerged is that individual polymer chains are restricted within a "confining tube", a coarse-grained view of the molecular entanglement network (Figure 1.3), where the tube walls are comprised of entanglements from neighboring chains. While this early constitutive model only accounted for stress relaxation by curvilinear diffusion along the confining tube [7], a process known as reptation, decades of improvements to this tube-based model have resulted in the addition of other stress relaxation mechanisms known to be present in entangled polymeric liquids. These mechanisms include

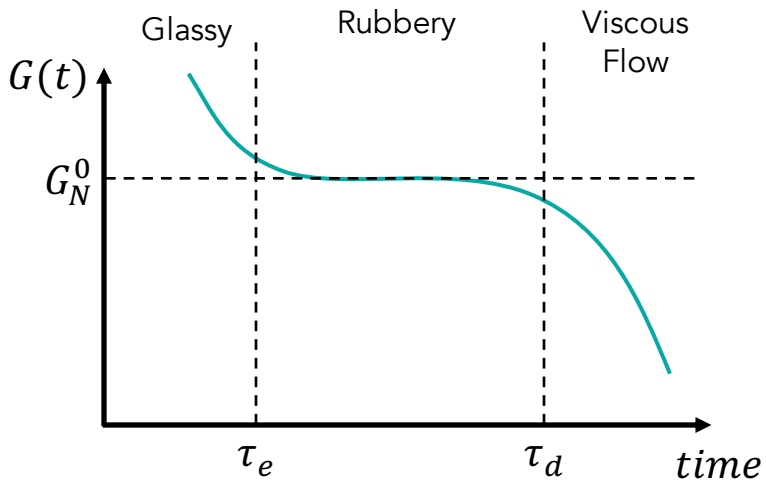

Figure 1.2: Time-dependent relaxation modulus for increasing time following a step strain. τ_e corresponds to the relaxation time of an entanglement segment, whereas τ_d represents the longest relaxation time (chain reptation).

constraint release [8, 9], due to the reptative motion of the confining chains, convective constraint release [9], which accounts for a reduction in the number of entanglements under fast flows, contour length fluctuations [8, 10], due to the motion of chain ends, and chain retraction [11], resulting from the relaxation of stretch. To date, the most sophisticated tube-based constitutive theory for entangled polymers is the GLaMM model [12], which accounts for the full spectrum of relaxation modes by these mechanisms but is often far too computationally expensive for predictive flow calculations. Alternatively, a single-mode simplication of the GLaMM model, the so-called Rolie-Poly model [13], was developed for quick numerical calculations. The Rolie-Poly model retains the underlying physics of the GLaMM model and yields similarly accurate results in comparison to experimental data.

A constitutive relationship for entangled polymeric liquids enables predictive calculations for how the material will respond in different flows. Importantly, these models account for the known non-Newtonian behavior of entangled polymers. Namely, the viscosity varies with applied shear rate (unlike the case for Newtonian fluids such as water

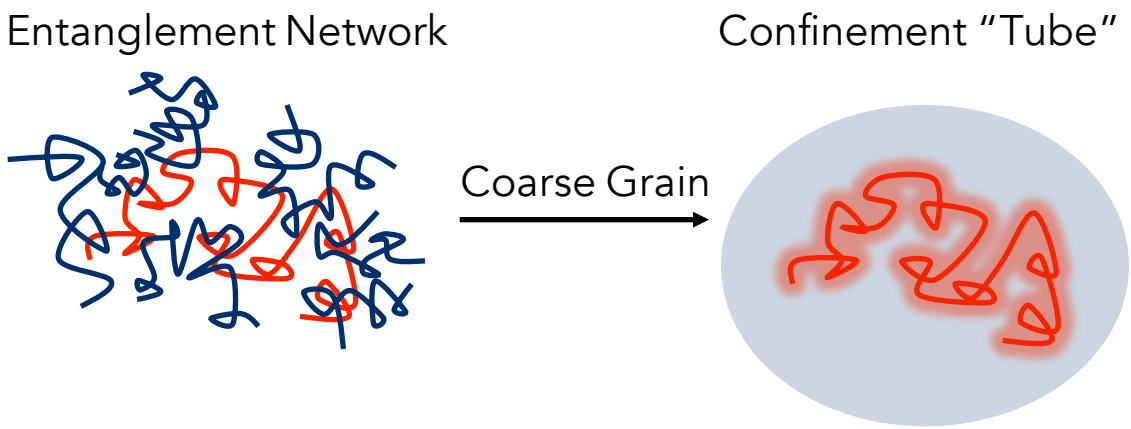

Figure 1.3: Microscopic entangled network is coarse grained into a confining tube made up of the topological constraints on an individual chain.

and honey). Instead, it is well-known that entangled polymer solutions and melts exhibit shear-thinning behavior above a critical applied shear rate ($\dot{\gamma}_{crit} = 1/\tau_d$) (Figure 1.4), where the viscosity decreases with a characteristic dependence on shear rate. Alternatively, some fluids, such as concentrated cornstarch, exhibit shear-thickening behavior where the fluid viscosity increases with the applied shear rate.

Normal stress differences that are present in shear flows of viscoelastic fluids result in complex flows that stray from the typically assumed 1D linear flow profile. Normal stress differences across curved streamlines generate "hoop stresses" which result in fluid flow towards the axis of rotation, commonly known as "rod-climbing" or the "Weissenberg effect". Additionally, the presence of normal stress differences can result in viscoelastic instability and turbulent flow patterns, in the absence of inertia [14]. A fluid can undergo a shear banding flow instability when there is a nonmonotonic relationship between shear stress (σ_{xy}) and shear rate ($\dot{\gamma}$).

Uniform simple shear flow is unstable if the shear stress decreases as shear rate increases (*i.e.*, $\frac{d\sigma_{xy}}{d\dot{\gamma}} < 0$). This means that if a fluid with nonmonotonic constitutive behavior is subjected to a shear rate within the unstable region, the fluid will spontaneously separate into a shear banded flow profile, where the two local shear rates correspond to

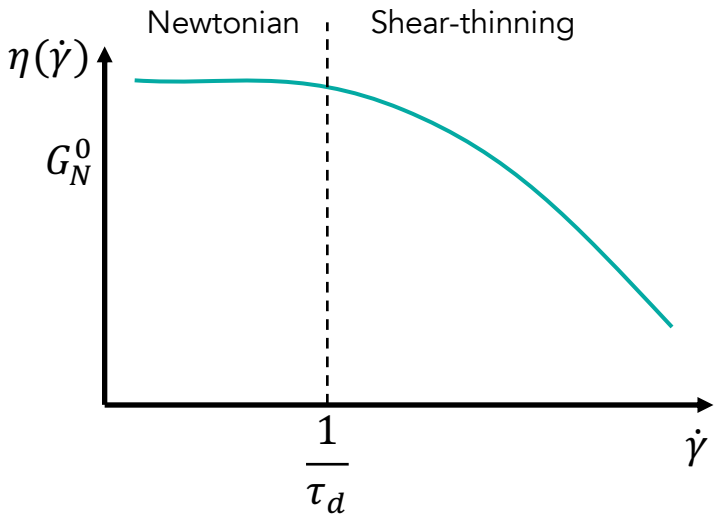

Figure 1.4: Representative shear rate dependence of the viscosity of an entangled polymeric liquid.

stable shear rates at the same applied shear stress as the unstable applied shear rate (Figure 1.5). This type of shear banded flow behavior has been observed in numerous fluids, such as wormlike micelles [15–20], soft colloidal glasses [21, 22], and telechelic polymers [23], and is commonly explained by a nonmonotonic constitutive relationship, but whether it occurs in entangled polymeric liquids has been a topic of considerable controversy in recent years [24–27].

One of the main reasons shear banding is not believed to occur in entangled polymeric liquids is due the agreement between tube-based constitutive models and experimental rheological data which exhibit monotonic constitutive behavior. There have been reports that identify the connection between apparent shear banding and flow complications such as wall slip and edge fracture, and in some cases, it was suggested that any experiments of entangled polymer solutions exhibiting shear banded flows suffer from such flow complications compromising the interpretation of the data [24, 27, 28].

Both experiments that confirm [29, 30] and deny [24, 26] the existence of shear banding in entangled polymer solutions lack a comparison to established theory for entangled

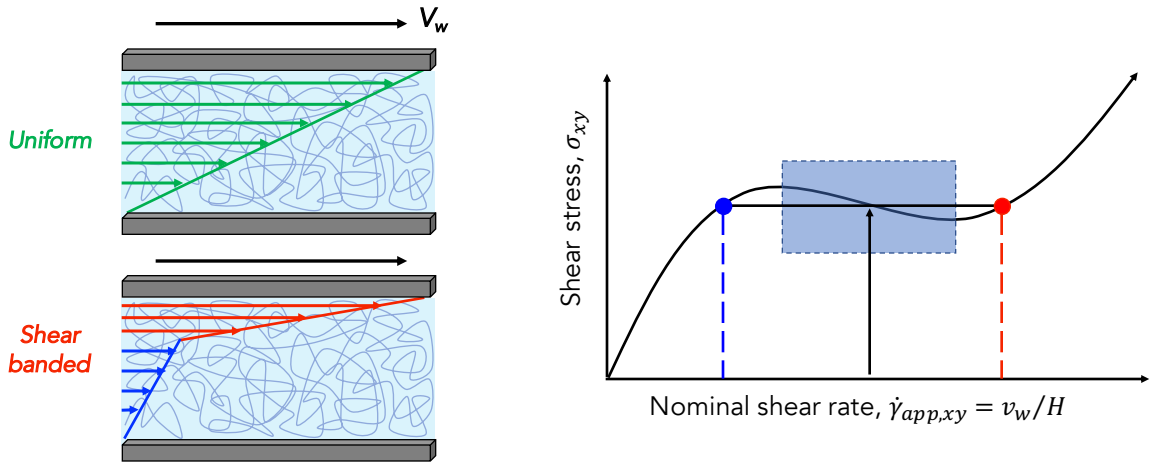

Figure 1.5: Cartoon representation of uniform and shear banded flows (left). Non-monotonic flow curve illustrating the constitutive instability explanation for why shear banded flows occur (right).

polymeric liquids. Further, these experimental studies assume that the fluid composition remains homogeneous in shear, at least to the extent that heterogeneities in composition do not affect the flow kinematics. This assumption is not strictly true, as there are several known exceptions to this assumption on a mesoscale such as shear-enhanced crystallization [31] and shear-enhanced concentration fluctuations (SECF) [32–34], as well as bulk changes resulting from radial migration of polymers across curved streamlines in dilute solutions [35, 36]. In particular, numerous reports have shown that flow enhances thermal fluctuations in polymer concentration and leads to mesoscopic fluid heterogeneities (Figure 1.6). These fluctuations arise due to a balance of elastic, osmotic, and drag forces on the polymer. It is unclear, however, the extent to which SECF influence the macroscopic flow kinematics.

Recently, a two-fluid model that accounts for a coupling of flow to concentration with a monotonic constitutive relationship for entangled polymers has shown that heterogeneities in fluid composition are linearly unstable for certain conditions [37–39]. Details on the model formulation and specific predictions of the model are included in Chapter

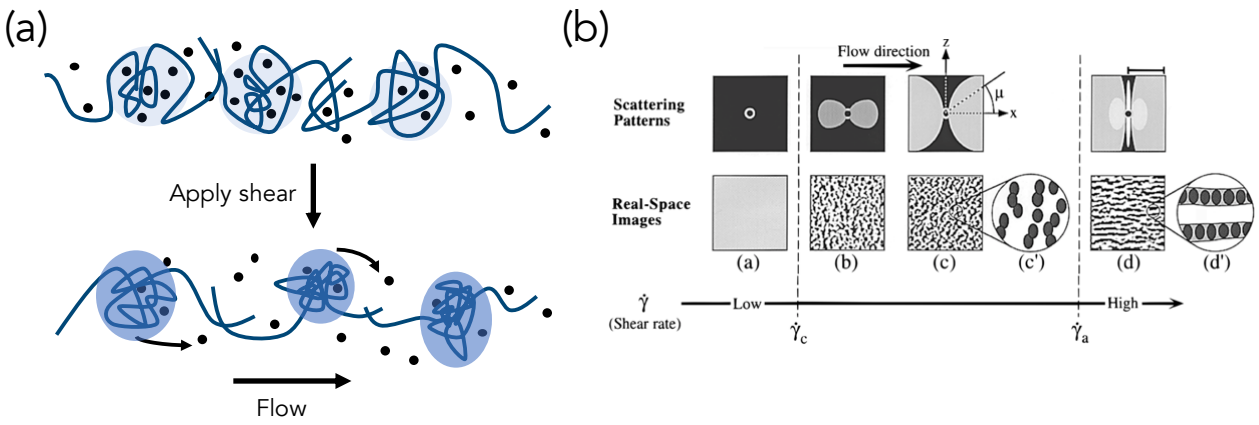

Figure 1.6: (a) Illustration of shear-enhanced thermal fluctuations in polymer solutions (black dots represent solvent molecules) (b) representative small angle scattering and microscopy images showing qualitative changes upon increasing shear rate. Reprinted (adapted) with permission from *Macromolecules* 1997, 30, 23, 7232-7236. Copyright 1997 American Chemical Society.

3. The significance of these model predictions are profound from both the fundamental polymer physics perspective and the rheological modeling of complex fluid flow more broadly. Specifically, this two-fluid model shows that: (1) shear banded flows can arise from a mechanism aside from a conventional constitutive instability, and (2) the wide assumption of compositional homogeneity could drastically misrepresent the actual rheological behavior of entangled polymeric fluids. Thus, it is imperative that an experimental investigation of flow-concentration coupling be conducted to verify the predictions of this two-fluid model as well as understand the prevalence of flow-concentration coupling in entangled polymer systems.

1.3 Objectives

This dissertation research seeks to accomplish several aims, including:

1. Develop reliable methods to measure and interpret the flow behavior of entangled polymeric liquids. Namely, the flow kinematics, rheology, and concentration het-

erogeneities

2. Study the effect of shear-enhanced concentration fluctuations on macroscopic flow of entangled polymer solutions

3. Quantify the extent of flow-induced, macroscopic concentration heterogeneity in entangled polymer solutions and investigate the dependence of fluid properties

4. Investigate effects of molecular weight dispersity on flow stability in bidisperse polymer blends

5. Study the effects of concentration heterogeneities and nonuniform flows in time-varying shear flows

1.4 Outline of dissertation

This dissertation is organized in the following way: Chapter 1 provides an overview of entangled polymer rheology and motivation for the necessity of studying flow-concentration coupling. Chapter 2 details the rheological, rheo-optical, and synthetic experimental methods and materials used in this dissertation research. Chapter 3 introduces the two-fluid model that accounts for flow-induced concentration heterogeneities and serves as the theoretical basis for the studies of entangled polymer solutions. This Chapter presents the model equations as well as the relevant stability and flow predictions. Chapter 4 presents the results of an experimental study investigating the connection between shear-enhanced concentration fluctuations and the macroscopic flow kinematics in polystyrene in dioctyl phthalate solutions – the classic system to study such flow-enhanced microscale concentration heterogeneities. This Chapter is based off of the work included in the publication [Burroughs *et al. Phys. Rev. Fluids* (2020) [40]]. Chapter 5 introduces a rheo-fluorescence method for quantifying changes to the bulk concentration in a polymeric

fluid and shows experimental confirmation of the theoretical prediction of coupling flow to concentration. This Chapter is based off of the work detailed in the publication [Burroughs *et al. Phys. Rev. Lett.* (2021) [41]]. Chapter 6 follows up on the work of Chapter 5 to further study the strength of flow-concentration coupling in model polybutadiene in dioctyl phthalate solutions. This Chapter is based off of the material included in a soon to be submitted manuscript. Chapter 7 introduces a model that accounts for polymer blends with a bidisperse molecular weight distribution. The blend model, originally published in [Peterson *et al. J. Rheol.*(2020) [42]], is generalizable to true polydispersity, but we only consider the special case of bidispersity in this dissertation research. Chapter 8 consists of an experimental study of the flow kinematics of bidisperse blends and the influence of a third (diluting component). These results are part of a manuscript that is currently in preparation. Chapter 9 consists of a numerical study of time-varying nonlinear shear flow of entangled polymer solutions. Shortcomings of common analysis techniques are discussed as it pertains to nonhomogeneous flow and an initial attempt to reconcile these issues is presented. These results are part of a manuscript that is currently in preparation. Finally, Chapter 10 concludes this dissertation with a summary of the conclusions and a discussion of future work.

Bibliography

[1] J. M. Garcés, D. J. Moll, J. Bicerano, R. Fibiger, and D. G. McLeod, "Polymeric nanocomposites for automotive applications," *Advanced Materials*, vol. 12, no. 23, pp. 1835–1839, 2000.

[2] D. N. Breslauer, "Recombinant Protein Polymers: A Coming Wave of Personal Care Ingredients," *ACS Biomaterials Science and Engineering*, vol. 6, no. 11, pp. 5980–5986, 2020.

[3] R. Duncan, H. Ringsdorf, and R. Satchi-Fainaro, "Polymer therapeutics - Polymers as drugs, drug and protein conjugates and gene delivery systems: Past, present and future opportunities," *Journal of Drug Targeting*, vol. 14, no. 6, pp. 337–341, 2006.

[4] R. Muthuraj, M. Misra, and A. K. Mohanty, "Biodegradable compatibilized polymer blends for packaging applications: A literature review," *Journal of Applied Polymer Science*, vol. 135, no. 24, p. 45726, 2018.

[5] M. Rubinstein and R. H. Colby, *Polymer Physics*. Oxford: Oxford University Press, 2003.

[6] P. G. de Gennes, "Reptation of a Polymer Chain in the Presence of Fixed Obstacles," *The Journal of Chemical Physics*, vol. 55, no. 2, p. 572, 1971.

[7] M. Doi and S. F. Edwards, "Dynamics of Concentrated Polymer Systems: Part III - The Constitutive Equation," *Journal of the Chemical Society, Faraday Transactions 2: Molecular and Chemical Physics*, vol. 74, pp. 1818–1832, 1978.

[8] A. E. Likhtman and T. C. B. McLeish, "Quantitative theory for linear dynamics of linear entangled polymers," *Macromolecules*, vol. 35, no. 16, pp. 6332–6343, 2002.

[9] S. T. Milner, T. C. B. McLeish, and A. E. Likhtman, "Microscopic theory of convective constraint release," *Journal of Rheology*, vol. 45, no. 2, pp. 539–563, 2001.

[10] S. Milner and T. McLeish, "Reptation and contour-length fluctuations in melts of linear polymers," *Physical Review Letters*, vol. 81, no. 3, pp. 725–728, 1998.

[11] D. W. Mead, R. G. Larson, and M. Doi, "A Molecular Theory for Fast Flows of Entangled Polymers," *Macromolecules*, vol. 31, no. 22, pp. 7895–7914, 1998.

[12] R. S. Graham, A. E. Likhtman, T. C. B. McLeish, and S. T. Milner, "Microscopic theory of linear, entangled polymer chains under rapid deformation including chain stretch and convective constraint release," *Journal of Rheology*, vol. 47, no. 5, p. 1171, 2003.

[13] A. E. Likhtman and R. S. Graham, "Simple constitutive equation for linear polymer melts derived from molecular theory: Rolie-Poly equation," *Journal of Non-Newtonian Fluid Mechanics*, vol. 114, no. 1, pp. 1–12, 2003.

[14] A. Groisman and V. Steinberg, "Elastic turbulence in a polymer solution flow," *Nature*, vol. 405, pp. 53–55, 2000.

[15] J.-B. Salmon, A. Colin, S. Manneville, and F. Molino, "Velocity profiles in shear-banding wormlike micelles.," *Physical review letters*, vol. 90, no. June, p. 228303, 2003.

[16] M. R. López-González, W. M. Holmes, P. T. Callaghan, and P. J. Photinos, "Shear banding fluctuations and nematic order in wormlike micelles," *Physical Review Letters*, vol. 93, no. 26, p. 268302, 2004.

[17] M. W. Liberatore, F. Nettesheim, N. J. Wagner, and L. Porcar, "Spatially resolved small-angle neutron scattering in the 1-2 plane: A study of shear-induced phase-separating wormlike micelles," *Physical Review E - Statistical, Nonlinear, and Soft Matter Physics*, vol. 73, no. 2, p. 020504, 2006.

[18] M. R. Lopez-Gonzalez, W. M. Holmes, and P. T. Callaghan, "Rheo-NMR phenomena of wormlike micelles," *Soft Matter*, vol. 2, no. 10, pp. 855–869, 2006.

[19] M. E. Helgeson, P. A. Vasquez, E. W. Kaler, and N. J. Wagner, "Rheology and spatially resolved structure of cetyltrimethylammonium bromide wormlike micelles through the shear banding transition," *Journal of Rheology*, vol. 53, no. 2009, p. 727, 2009.

[20] K. W. Feindel and P. T. Callaghan, "Anomalous shear banding: Multidimensional dynamics under fluctuating slip conditions," *Rheologica Acta*, vol. 49, no. 10, pp. 1003–1013, 2010.

[21] S. A. Rogers, D. Vlassopoulos, and P. T. Callaghan, "Aging, yielding, and shear banding in soft colloidal glasses," *Physical Review Letters*, vol. 100, no. 12, p. 128304, 2008.

[22] R. Besseling, L. Isa, P. Ballesta, G. Petekidis, M. E. Cates, and W. C. Poon, "Shear banding and flow-concentration coupling in colloidal glasses," *Physical Review Letters*, vol. 105, no. 26, p. 268301, 2010.

[23] J. F. Berret and Y. Séréro, "Evidence of shear-induced fluid fracture in telechelic polymer networks," *Physical Review Letters*, vol. 87, no. 4, p. 048303, 2001.

[24] Y. Li, M. Hu, G. B. McKenna, C. J. Dimitriou, G. H. McKinley, R. M. Mick, D. C. Venerus, and L. A. Archer, "Flow field visualization of entangled polybutadiene solutions under nonlinear viscoelastic flow conditions," *Journal of Rheology*, vol. 57, no. 5, pp. 1411–1428, 2013.

[25] S.-Q. Wang, G. Liu, S. Cheng, P. E. Boukany, Y. Wang, X. Li, Y. Li, M. Hu, G. B. McKenna, C. J. Dimitriou, G. H. McKinley, R. M. Mick, D. C. Venerus, and L. a. Archer, "Letter to the Editor: Sufficiently entangled polymers do show shear strain localization at high enough Weissenberg numbers"," *Journal of Rheology*, vol. 58, no. 4, pp. 1059–1069, 2014.

[26] Y. Li and G. B. McKenna, "Startup shear of a highly entangled polystyrene solution deep into the nonlinear viscoelastic regime," *Rheologica Acta*, vol. 54, no. 9-10, pp. 771–777, 2015.

[27] Y. Li, M. Hu, G. B. McKenna, C. J. Dimitriou, G. H. McKinley, R. M. Mick, D. C. Venerus, and L. A. Archer, "Response to: Sufficiently entangled polymers do show shear strain localization at high enough Weissenberg numbers"," *Journal of Rheology*, vol. 58, no. 4, pp. 1071–1082, 2014.

[28] E. J. Hemingway and S. M. Fielding, "Edge-Induced Shear Banding in Entangled Polymeric Fluids," *Physical Review Letters*, vol. 120, no. 13, p. 138002, 2018.

[29] S. Ravindranath, S.-Q. Wang, M. Olechnowicz, and R. P. Quirk, "Banding in simple steady shear of entangled polymer solutions," *Macromolecules*, vol. 41, no. 7, pp. 2663–2670, 2008.

[30] P. E. Boukany, S.-Q. Wang, S. Ravindranath, and L. J. Lee, "Shear banding in entangled polymers in the micron scale gap: a confocal-rheoscopic study," *Soft Matter*, vol. 11, pp. 8058–8068, 2015.

[31] G. Kumaraswamy, A. M. Issaian, and J. A. Kornfield, "Shear-enhanced crystallization in isotactic polypropylene. 1. Correspondence between in situ rheo-optics and ex situ structure determination," *Macromolecules*, vol. 32, no. 22, pp. 7537–7547, 1999.

[32] E. Helfand and G. H. Fredrickson, "Large Fluctuations in Polymer Solution under Shear," *Physical Review Letters*, vol. 62, no. 21, pp. 2468–2471, 1989.

[33] X. L. Wu, D. J. Pine, and P. K. Dixon, "Enhanced concentration fluctuations in polymer solutions under shear flow," *Physical Review Letters*, vol. 66, no. 18, pp. 2408–2411, 1991.

[34] R. G. Larson, "Flow-induced mixing, demixing, and phase transitions in polymeric fluids," *Rheologica Acta*, vol. 31, no. 6, pp. 497–520, 1992.

[35] K. A. Dill and B. H. Zimm, "A rhelogical separator for very large DNA molecules," *Nucleic Acids Research*, vol. 7, no. 3, pp. 735–749, 1979.

[36] M. J. MacDonald and S. J. Muller, "Experimental study of shear-induced migration of polymers in dilute solutions," *Journal of Rheology*, vol. 40, no. 2, p. 259, 1996.

[37] M. Cromer, M. C. Villet, G. H. Fredrickson, and L. G. Leal, "Shear banding in polymer solutions," *Physics of Fluids*, vol. 25, no. 5, p. 051703, 2013.

[38] M. Cromer, G. H. Fredrickson, and L. G. Leal, "A study of shear banding in polymer solutions," *Physics of Fluids*, vol. 26, no. 6, p. 063101, 2014.

[39] J. D. Peterson, M. Cromer, G. H. Fredrickson, and L. G. Leal, "Shear banding predictions for the two-fluid Rolie-Poly model," *Journal of Rheology*, vol. 60, no. 5, pp. 927–951, 2016.

[40] M. C. Burroughs, A. M. Shetty, L. G. Leal, and M. E. Helgeson, "Coupled nonhomogeneous flows and flow-enhanced concentration fluctuations during startup shear of entangled polymer solutions," *Physical Review Fluids*, vol. 5, no. 4, p. 043301, 2020.

[41] M. C. Burroughs, Y. Zhang, A. M. Shetty, C. M. Bates, L. G. Leal, and M. E. Helgeson, "Flow-Induced Concentration Nonuniformity and Shear Banding in Entangled Polymer Solutions," *Physical Review Letters*, vol. 126, no. 20, p. 207801, 2021.

[42] J. D. Peterson, G. H. Fredrickson, and L. G. Leal, "Shear Induced Demixing in Bidisperse and Polydisperse Polymer Blends: Predictions From a Multi-Fluid Model," *Journal of Rheology*, vol. 64, no. 6, p. 1391, 2020.

Chapter 2

Rheological and optical methods for complex fluids

2.1 Abstract

The bulk rheology of different complex fluids is intimately tied to their underlying microstructure. As discussed in Chapter 1, it is the topological entanglements which are formed in concentrated, high molecular weight polymeric liquids that give rise to their unique rheology. Rheological stress measurements alone are often insufficient to fully characterize the dynamics of complex fluids (such as entangled polymeric liquids), and thus, a multifaceted experimental approach to the characterization of entangled polymeric liquids is adopted in this dissertation research (Figure 2.1). This Chapter details the fundamentals pertinent to each experimental measurement type. Additional procedural details for each technique are included, as necessary, in subsequent chapters.

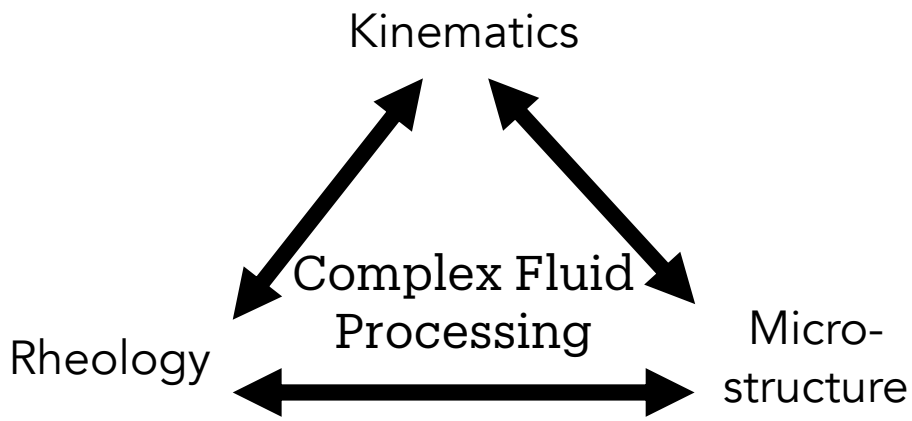

Figure 2.1: Experimental approach used in this dissertation research for characterizing entangled polymer liquids.

2.2 Materials and preparation

Polystyrene (PS, $M_w = 3.84 \times 10^6$ and 8.42×10^6 g/mol with $Đ = 1.04$ and 1.17, respectively) was purchased from Tosoh Biosciences, LLC. Polybutadiene (PBD, $M_w = 18.4 \times 10^3$, 4.30×10^5, 8.17×10^5, and 9.6×10^5 g/mol with $Đ = 1.02$, 1.03, 1.05, and 1.08, respectively) were purchased from Polymer Standards Services. Polybutadiene (PBD, $M_w = 1.69 \times 10^5$ g/mol with $Đ = 1.07$) was purchased from Polymer Source, Inc. Butadiene oligomer (CAS No. 9003-17-2) was purchased from Sigma-Aldrich. Dioctyl phthalate (CAS No. 117-81-7, ≥99.5%) was purchased from Sigma-Aldrich. 2,2-Dimethoxy-phenylacetophenone (DMPA, ACROS Organics, CAS No. 24650-42-8, 99%) was purchased from Fisher Scientific. 7-mercapto-4-methylcoumarin (CAS No. 137215-27-1, ≥97.0%) was purchased from Sigma-Aldrich. Anhydrous tetrahydrofuran (THF, CAS No. 109-99-9, ≥99.9%, inhibitor-free) was purchased from Sigma-Aldrich. All chemicals were used as received without further purification. 10 μm diameter glass tracer particles were donated by TSI, Inc.

High molecular weight polystyrene and polybutadiene melts were used to prepare entangled polymeric liquids of varying numbers of entanglements and composition. These

samples were prepared by adding polymer solids and solvent (either dioctyl phthalate or low molecular weight polymer) to a 50 mL glass vial. The number of entanglements per chain (Z) was determined from

$$Z = \frac{M_w}{M_e}\phi^{\alpha} \tag{2.1}$$

where M_w is the weight-averaged molecular weight, M_e is the entanglement molecular weight (which depends on the constituent polymer chemistry), ϕ is the polymer concentration, and α is the dilution exponent. $\alpha = 1.0$ is used for determining Z in bidisperse blends, and $\alpha = 1.2$ is used for determining Z in polymer solutions where the solvent is not an oligomeric analogue of the polymer. Approximately 30 mL of toluene was added to the sample mixture to serve as a cosolvent and aid in dissolution. The samples were stirred at a low rate with a magnetic stir bar in an oil bath at $T = 50$ ℃ until mixture was homogeneous (typically several days to a week). Once homogeneous, the samples were uncapped in a fume hood under continued heating and stirring to allow for toluene evaporation. After a couple of days, the resulting fluid became too viscous to stir via magnetic stir bar, so the sample vials were transferred to a vacuum oven to remove residual toluene.

2.3 Rheological characterization

All rheological measurements were performed on either a MCR 300 (Paar Physica), MCR 702 (Anton Paar), or AR-G2 (TA Instruments) stress-controlled rheometer. As will be discussed, the MCR 300 and MCR 702 were fitted with custom optical elements to enable simultaneous particle tracking velocimetry and fluorescence measurements, respectively.

2.3.1 Linear viscoelasticity

In the linear viscoelastic regime, a fluid is subjected to a strain of sufficiently small amplitude such that the response is linear (*i.e.*, $\sigma(t) = G\gamma(t)$). Small amplitude oscillatory shear (SAOS) protocols are often used to measure the linear viscoelastic response of entangled polymer liquids across a range of applied frequencies. In a SAOS experiment, a shear strain (γ) of the form

$$\gamma = \gamma_0 \sin(\omega t) \tag{2.2}$$

is imposed on the fluid with a corresponding strain rate ($\dot{\gamma}$) of the form

$$\dot{\gamma} = \gamma_0 \omega \cos(\omega t) \tag{2.3}$$

where γ_0 is the strain amplitude, ω is the oscillation frequency, and t is time. In the linear regime, the resulting shear stress measured by the rheometer is some phase-shift of the imposed deformation

$$\sigma(t) = \gamma_0[G'(\omega)\sin(\omega t) + G''(\omega)\cos(\omega t)] = \sigma_0 \sin(\omega t + \delta) \tag{2.4}$$

where $G'(\omega)$ is the elastic (storage) modulus and $G''(\omega)$ is the viscous (loss) modulus, which can be defined in terms of a phase angle (δ) as

$$G' = \frac{\sigma_0}{\gamma_0}\cos(\delta) \tag{2.5}$$

and

$$G'' = \frac{\sigma_0}{\gamma_0}\sin(\delta) \tag{2.6}$$

respectively.

2.3.2 Nonlinear shear flows

A shear deformation is considered nonlinear if it results in non-Newtonian flow behavior (*i.e.*, the shear viscosity (η) varies with applied $\dot{\gamma}$). In an oscillatory flow, the nonlinear regime is marked by sufficiently high strain amplitude such that the measured $\sigma(t)$ is no longer described by a simple sinusoidal phase shift (δ).

Steady shear flow

One common rheometric flow protocol is steady shear flow, in which the fluid is subjected to a drag flow between two surfaces by rotating one of the surfaces at a fixed rate (imposing a steady shear rate on the material). The strength of the applied shear flow is characterized by the dimensionless parameter known as the Weissenberg number

$$Wi = \tau_d \dot{\gamma} \tag{2.7}$$

where τ_d is the longest relaxation time of the fluid. Thus, when the applied shear rate exceeds the relaxation time of the fluid (*i.e.*, $Wi > 1$), the flow is defined as nonlinear.

The flow is considered to have reached steady-state when the measured shear stress is time invariant. When steady shear measurements are performed over a wide range of shear rates, a so-called flow curve, information pertaining to the material's constitutive behavior can be inferred. As mentioned in Chapter 1, certain flow complications, namely shear banding, can arise due to a constitutive instability where the shear stress is multi-valued over a range of shear rates as indicated by a shear stress plateau in the measured flow curve.

Central to the interpretation of rheological measurements and data is the assumption that the flow kinematics remain uniform under an applied shear rate. As discussed in Chapter 1, the shear banding flow instability is a violation of this uniform flow as-

sumption. Characterization of a fluid's flow field is thus imperative to properly analyze rheological data.

Startup shear flow

The transient flow behavior of complex fluids can be investigated with startup shear rheological experiments. In these measurements, a fluid is typically subjected to an instantaneous ramp up to a specified shear rate and held at this shear rate for a specified amount of time. The stresses in the fluid evolve transiently in response to the imposed flow and, in time, reach a steady-state value. Again, implicit to the interpretation of these data is the assumption that the flow remains uniform.

Large amplitude oscillatory shear

An emerging rheological flow protocol is that of Large Amplitude Oscillatory Shear (LAOS). In this type of experiment, a time-varying nonlinear oscillatory shear strain is imposed on the material. As evident from the name, the amplitude of this oscillatory shear strain is "large", and the stress response of the fluid is no longer a simple sinusoidal phase shift ($0^\circ \leq \delta \leq 90^\circ$). More complex data interpretation methods are required to understand the information collected during LAOS experiments. Some of these methods are discussed in detail within Chapter 9.

2.4 Rheo-optical methods

Additional characterization methods are necessary to complement standard rheological measurements of complex fluids. In particular, combined rheological and optical techniques provide information relating to fluid kinematics and microstructure.

2.4.1 Kinematics (particle tracking velocimetry)

One method to directly measure the flow field of complex fluids is by using a technique known as particle tracking velocimetry. In this technique, small ($\approx 10\,\mu$m in diameter) glass particles are suspended in solution and illuminated in the flow-gradient plane by a laser sheet. Reflections from the glass tracer particles allow for visualization of the fluid's flow field. The displacements are tracked from frame to frame in a recorded video. The local velocities are then calculated from the corresponding displacements and the image frame rate.

The image processing algorithm for identifying and tracking particles was based on the technique developed by Crocker and Greer [1]. We utilize a custom optical setup integrated with a Paar Physica MCR 300 rheometer to perform these PTV measurements simultaneously with rheological experiments (Figure 2.2). This setup has been described in detail in several publications [2–4]. Briefly, the flow geometry consists of a Taylor-Couette flow cell with a transparent quartz outer cup and an anodized aluminum inner cylinder. Temperature control was supplied by passing water through an annulus within the transparent cup. The target temperature was confirmed by measuring the temperature of the fluid using a thermocouple at several locations. The inner cylinder height is 15.7 mm. The inner cylinder radius (R_i) is 17 mm and the cup radius (R_o) is 17.5 mm. This results in a flow domain that is 500 μm thick and a curvature of $q = (R_o - R_i)/R_i = 0.029$. To circumvent flow complications arising from edge effects [5–10], a stainless steel lid with compatible dimensions to the Taylor-Couette flow cell was machined to sit on top of the fluid and serve as a solid upper boundary.

The typical protocol for loading was to add the sample to the transparent cup with a spatula at an elevated temperature to accelerate equilibration. Once the loaded sample conformed to the transparent cup and was free of bubbles introduced from loading, the

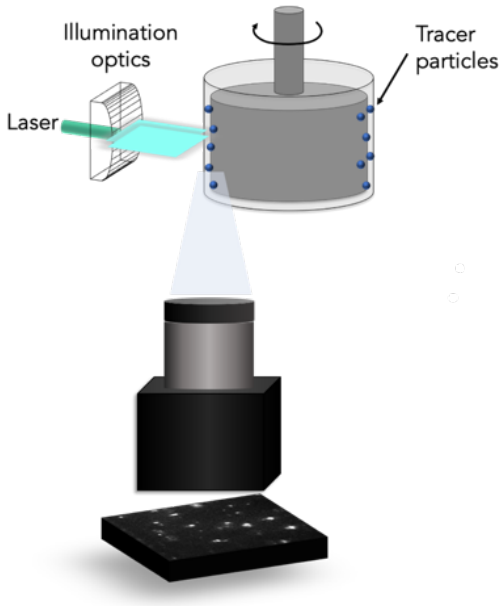

Figure 2.2: Rheo-Particle Tracking Velocimetry (rheo-PTV) setup. Glass tracer particles are illuminated in the flow-gradient plane using a laser sheet. Reflections from the glass tracer particles are imaged with an objective and camera mounted beneath the transparent flow cell. Displacements of particles between adjacent image pairs acquired at a particular frame rate are converted to velocities.

anodized aluminum bob was slowly lowered into the fluid to avoid excessive normal force. Once the bob was fully submerged in the fluid, a minimum of 1 hour was allowed for equilibration. Prior to any measurements, preshear at a very low shear rate was applied to the fluid to erase any residual stresses due to sample loading effects.

2.4.2 Morphology and composition

Additional details of complex fluids under flow can be obtained using rheo-microscopy and scattering techniques. Micrographs and 2D scattering patterns enable microscopic heterogeneities and orientation of the fluid to be quantified. These measurements were performed on a MCR 702 rheometer using an identical flow geometry as specified for the rheo-PTV measurements.

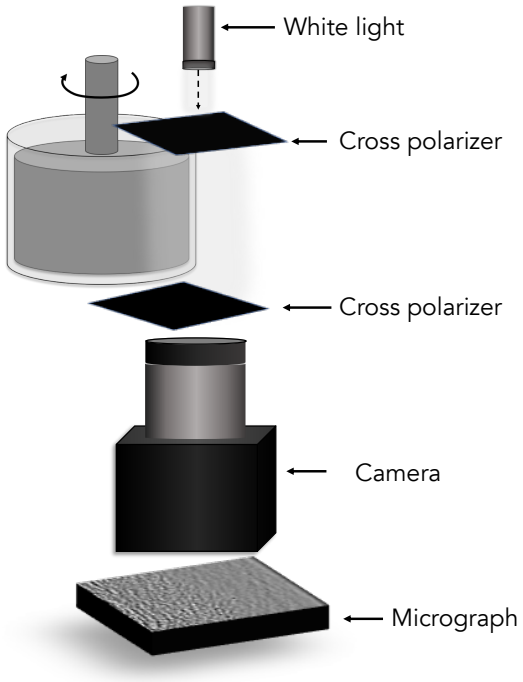

Figure 2.3: Rheo-microscopy optical setup. The transparent flow cell is located between cross polarizers that are oriented 90° to one another. Light transmission and optical heterogeneity is detected with a CCD camera mounted below the flow cell.

Rheo-microscopy

In rheo-microscopy measurements, details of fluid compositional heterogeneity can be detected optically due to refractive index differences between solute and solvent (*i.e.*, polymer and solvent) [11]. As discussed in Chapter 1, compositional heterogeneities are well-documented for entangled polymer solutions, arising in the form of shear-enhanced concentration fluctuations. Additionally, the use of cross polarizers, as shown in Figure 2.3, enable information to be collected about microstructural orientation of the fluid. No light will transmit through the cross polarizers for an isotropically-oriented fluid (uniform refractive index), but transmission will occur as the fluid is oriented along the polarization axis. Thus, these measurements allow for the detection of both fluid orientation and compositional heterogeneity.

Rheo-fluorescence

Fluorescence microscopy is a widely utilized technique for visualizing isolated components in colloidal and biological mixtures. Typically, a fluorescent dye that preferentially binds to a specific component is added to visualize particular assemblies or domains. We have developed a fluorescence technique to estimate changes to polymer composition in flow.

A fluorophore is a molecule that is excited by light of a specific wavelength. The fluorophore correspondingly emits this absorbed energy at a higher wavelength (lower energy). The measured fluorescence intensity (I) depends on the path length (k), irradiation intensity (P_0), and concentration of fluorophores (ϕ) according to

$$I = kP_0\phi \tag{2.8}$$

The dependence of the fluorescence intensity on concentration allows us to relate spatial changes of the fluorescence intensity to spatial changes of the fluorophore (polymer) concentration according to

$$\frac{\phi(r,t,\dot{\gamma})}{\phi_0} \approx \frac{I(r,t,\dot{\gamma}) - I_{bg}}{I_0 - I_{bg}}. \tag{2.9}$$

2.5 Fluorescent-tagging of polybutadiene

Polybutadienes of varying molecular weight were fluorescently tagged with the fluorophore coumarin (Figure 2.5). In a typical reaction, approximately 0.1 g of PBD was added to a round bottom flask along with 140 mL of anhydrous THF. The solution was

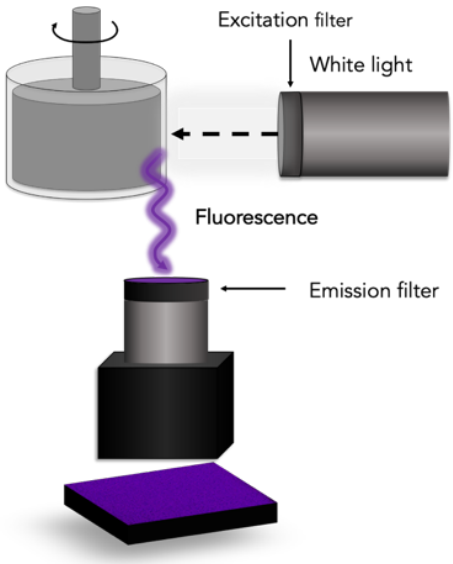

Figure 2.4: Rheo-fluorescence optical setup. A fluid with trace amounts of fluorophore is illuminated with excitation filtered light. The resulting fluorescence intensity is measured with an objective and CCD camera after the light is further filtered through an emission wavelength bandpass filter.

mixed with a magnetic stir bar on a stir plate until fully dissolved. Next the reaction initiator, DMPA, and the fluorophore, 7-mercapto-4-methylcoumarin, were added to the mixture in a 1:10 molar ratio of initiator to fluorophore. The molar ratio of fluorophore to polymer was approximately 1:72. The round bottom flask was then purged with nitrogen gas for at least 30 minutes prior to reaction. The reactions were performed under 365 nm UV light at room temperature for 5 – 15 minutes depending on the polybutadiene molecular weight. PBDC samples were purified by rotovaping off THF and precipitating in acetone three times. Typical yield was approximately 80%.

2.6 Summary and outlook

The methods detailed in this chapter enable a robust characterization of the nonlinear flow behavior of entangled polymeric liquids. While this dissertation research is inter-

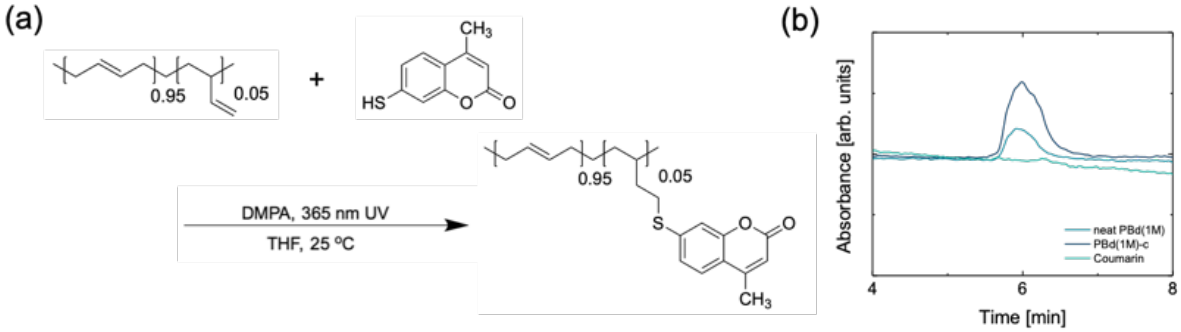

Figure 2.5: (a) Fluorescent-tagging reaction of polybutadiene and the fluorophore, coumarin, and (b) gel permeation chromatography (GPC) traces that confirm the fluorophore is bound to the polymer.

ested in entangled polymeric liquids, the characterization methods may be implemented for different classes of complex fluids and soft materials. The results presented in subsequent chapters highlight the necessity for such a multifaceted experimental approach. Whenever possible, standard rheological stress measurements should be supplemented with kinematic and morphological characterization.

Bibliography

[1] J. Crocker and D. Grier, "Methods of Digital Video Microscopy for Colloidal Studies," *Journal of Colloid and Interface Science*, vol. 179, no. 1, pp. 298–310, 1996.

[2] Y. T. Hu and A. Lips, "Kinetics and mechanism of shear banding in an entangled micellar solution," *Journal of Rheology*, vol. 49, no. 5, pp. 1001–1027, 2005.

[3] P. Cheng, M. C. Burroughs, L. G. Leal, and M. E. Helgeson, "Distinguishing shear banding from shear thinning in flows with a shear stress gradient," *Rheologica Acta*, vol. 56, no. 12, pp. 1007–1032, 2017.

[4] M. C. Burroughs, A. M. Shetty, L. G. Leal, and M. E. Helgeson, "Coupled nonhomogeneous flows and flow-enhanced concentration fluctuations during startup shear of entangled polymer solutions," *Physical Review Fluids*, vol. 5, no. 4, p. 043301, 2020.

[5] C. Sui and G. B. McKenna, "Instability of entangled polymers in cone and plate rheometry," *Rheologica Acta*, vol. 46, no. 6, pp. 877–888, 2007.

[6] Y. Li and G. B. McKenna, "Startup shear of a highly entangled polystyrene solution deep into the nonlinear viscoelastic regime," *Rheologica Acta*, vol. 54, no. 9-10, pp. 771–777, 2015.

[7] Y. W. Inn, K. F. Wissbrun, and M. M. Denn, "Effect of Edge Fracture on Constant Torque Rheometry of Entangled Polymer Solutions," *Macromolecules*, vol. 38, no. 22, pp. 9385–9388, 2005.

[8] E. J. Hemingway, H. Kusumaatmaja, and S. M. Fielding, "Edge Fracture in Complex Fluids," *Physical Review Letters*, vol. 119, p. 028006, 2017.

[9] E. J. Hemingway and S. M. Fielding, "Edge-Induced Shear Banding in Entangled Polymeric Fluids," *Physical Review Letters*, vol. 120, no. 13, p. 138002, 2018.

[10] E. J. Hemingway and S. M. Fielding, "Edge fracture of entangled polymeric fluids: onset criterion and possible mitigation strategy," *Journal of Rheology*, vol. 63, no. 5, p. 735, 2019.

[11] G. G. Fuller, *Optical Rheometry of Complex Fluids*. New York: Oxford University Press, Inc., 1995.

Chapter 3

A two-fluid model for entangled polymer solutions[1]

3.1 Introduction

The purpose of this Chapter is to introduce the model formulation and equations for describing the rheology of entangled polymer solutions. The Chapter begins with an introduction to the two-fluid formalism and constitutive equation for entangled polymer liquids. Following the discussion of model formulation, predictions for shear-induced demixing in entangled polymer solutions are presented with an interest in comparison to experimental measurements. Importantly, *homogeneous* rheological models solve the Navier-Stokes equations for a given constitutive relationship but assume uniform composition in the fluid. The results in this Chapter show that the two-fluid formalism, connecting fluid stress and concentration, reveals a shear-induced demixing instability that leads to profound changes to the flow.

[1]The contents of this Chapter are based on the model developed and refined in Cromer *et al.* (2013 and 2014) [1, 2] and Peterson *et al.* (2016) [3].

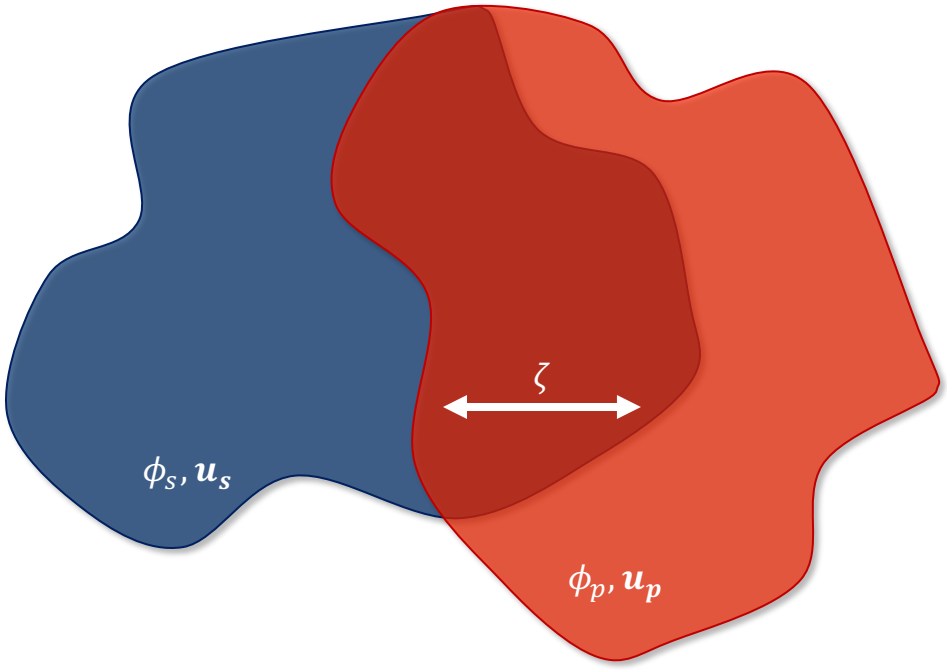

Figure 3.1: Cartoon illustration detailing the conceptual idea of a two-fluid model. Flow ($\boldsymbol{u}$) fields of polymer ($\boldsymbol{u}_p$) and solvent ($\boldsymbol{u}_s$) are coupled by friction (ζ) and conservation of mass (ϕ) is ensured through species continuity.

3.2 The two-fluid formalism for solutions

Complex fluids are mixtures of two or more different components. Often times the fluid consists of a Newtonian solvent with an additional component that renders the fluid non-Newtonian. Thus, it is strategic to describe the rheology of a complex fluid by coupling the governing equations of the solvent and additive. de Gennes was the first to present a model of polymer solutions as two continua (polymer and solvent) coupled by friction and global incompressibility [4] (Figure 3.1). In this "two-fluid" formalism, the total velocity vector ($\boldsymbol{u}$) is written as the volume-weighted sum of each component

$$\boldsymbol{u} = \phi \boldsymbol{u}_p + (1 - \phi)\boldsymbol{u}_s \tag{3.1}$$

where $\boldsymbol{u}_p$ and $\boldsymbol{u}_s$ are the polymer and solvent velocities, respectively. Neglecting inertia, a momentum balance for each component can be written as

$$0 = \nabla \cdot \boldsymbol{\Pi} + \phi(-\nabla p + \eta_p \nabla^2 \boldsymbol{u}) - \zeta(\boldsymbol{u}_p - \boldsymbol{u}_s) \tag{3.2}$$

for the polymer species and

$$0 = (1-\phi)(-\nabla p + \eta_s \nabla^2 \boldsymbol{u}) + \zeta(\boldsymbol{u}_p - \boldsymbol{u}_s) \tag{3.3}$$

for the solvent species, where the subscripts p and s indicate polymer and solvent specific properties, respectively, η is the viscosity, p is the isotropic pressure, ζ is the frictional coupling between polymer and solvent, and $\boldsymbol{\Pi}$ is the total stress tensor. The equations can be combined to yield

$$0 = -\nabla p + \varpi \nabla^2 \boldsymbol{u}_s + \nabla \cdot \boldsymbol{\Pi} \tag{3.4}$$

where ϖ is the ratio of the solvent viscosity (η_s) to the polymer viscosity (η_p).

3.3 The stress tensor for entangled polymeric liquids

Up to now, the two-fluid model derivation has been devoid of any constitutive model-specific terms, and, aside from subscripts, it is not specific to polymers; however, in this work, we are interested in the dynamics of entangled polymeric liquids, which have been accurately described by tube-based models. The main conceptual basis for tube-based constitutive models is that the many topological constraints (entanglements) acting on a single chain are coarse grained to a single chain within a "confining tube". The total

stress tensor is defined as

$$\boldsymbol{\Pi} = (\boldsymbol{Q} - \boldsymbol{I}) - \boldsymbol{I}\pi^{el} - \boldsymbol{\pi}. \tag{3.5}$$

The first term on the right-hand side represents the stress contribution of the polymer, where the configuration tensor $\boldsymbol{Q}$=$\langle \mathbf{RR} \rangle / R_0^2$ relates the second moment of the end-to-end vector to the equilibrium value. π^{el} is the isotropic elastic stress defined as

$$\pi^{el} = \frac{1}{2}(\alpha - 1)(\mathrm{Tr}(\boldsymbol{Q}) - 3 - \ln(\det(\boldsymbol{Q}))) \tag{3.6}$$

where α is the concentration scaling exponent of the shear modulus ($\alpha = 2.25$), and $\boldsymbol{\pi}$ is the osmotic stress described by

$$\boldsymbol{\pi} = \frac{1}{E}(\frac{1}{2}\bar{\phi}^2\boldsymbol{I} - (\frac{\bar{\xi}_0}{\bar{H}})^2\bar{\phi}^{-\frac{3}{2}}[(\bar{\phi}\nabla^2\bar{\phi} - \frac{1}{4}|\nabla\bar{\phi}|^2)\boldsymbol{I} - \nabla\bar{\phi}\nabla\bar{\phi}]) \tag{3.7}$$

where $(\bar{\xi}_0)$ is the dimensionless solution correlation length, $\bar{H}$ is the dimensionless gap width, and E is the elastic to osmotic ratio, which describes the degree of flow-concentration coupling and is defined as

$$E = \frac{G(\phi)}{\chi^{-1}\phi^2}. \tag{3.8}$$

where $G(\phi)$ is the shear modulus and χ^{-1} is the osmotic susceptibility. Using the momentum balances, it can be shown that a difference in the species velocities is driven by a divergence in stress as

$$\boldsymbol{u}_p - \boldsymbol{u}_s = \bar{\phi}^{-\frac{3}{2}}\frac{E}{\bar{H}^2}\nabla \cdot \boldsymbol{\Pi}. \tag{3.9}$$

Additionally, for no flow-concentration coupling (*i.e.*, $E = 0$), the right-hand side of the equation is equal to zero, meaning that there is no difference between species velocities. Conversely, there will be differences in the species velocities when a divergence in stress

occurs for any non-zero value of E. The concentration evolution is described by

$$\frac{\partial \bar{\phi}}{\partial t} = -\nabla \cdot (\boldsymbol{u}_p \bar{\phi}) \tag{3.10}$$

where $\bar{\phi}$ is the polymer concentration normalized by the initial, uniform polymer concentration.

3.3.1 The Rolie-Poly constitutive equation

The Rolie-Poly constitutive equation [5], a single-mode approximation of the GLaMM model [6], describes the relaxation dynamics of entangled polymeric liquids

$$\frac{\partial \boldsymbol{Q}}{\partial t} + \boldsymbol{u}_p \cdot \nabla \boldsymbol{Q} - (\nabla \boldsymbol{u}_p)^T \cdot \boldsymbol{Q} - \boldsymbol{Q} \cdot \nabla \boldsymbol{u}_p = -\bar{\phi}^{-\frac{3}{2}} (\boldsymbol{Q} - \boldsymbol{I}) + 2\frac{\tau_d}{\tau_R}(1-\lambda^{-1})(\boldsymbol{Q} + \lambda^{-1}(\boldsymbol{Q} - \boldsymbol{I})) \tag{3.11}$$

where τ_d is the timescale for reptation out of the original confining tube, τ_R is the timescale for Rouse relaxation that describes the unhindered wriggling motion of a polymer chain along its primitive path, and $\lambda = \sqrt{Tr(\boldsymbol{Q})/3}$ represents the degree of chain stretch. Time (t) is dimensionless and scaled by τ_d and the velocity ($\boldsymbol{u}_p$) is scaled by Wi, where Wi is defined as the product of the applied shear rate ($\dot{\gamma}$) and the gap width (H). The left-hand side of the equation is the upper-convected time derivative of the configuration tensor (*i.e.*, the confining tube). The right-hand side of the equation represents the different mechanisms for stress relaxation. The first term on the right-hand side accounts for stress relaxation by reptation. This mode of stress relaxation is described by a single exponential time relaxation towards equilibrium ($\boldsymbol{Q}$=$\boldsymbol{I}$). The second term on the right-hand side describes stress relaxation by both convective constraint release (CCR) and chain retraction (from stretch). Convective constraint release accounts for the removal of entanglements as neighboring chains are convected above the rate of reptation. Finally,

chain retraction describes the relaxation from a stretched state, when the shear rate exceeds the rate of Rouse relaxation.

3.4 Predictions of the two-fluid Rolie-Poly model

Several quantities must be specified to perform numerical simulations of the two-fluid Rolie-Poly model. In particular, the number of entanglements (Z), the nominal Weissenberg number (Wi), the degree of flow-concentration coupling (E), viscosity ratio of solvent to polymer (ϖ), the flow geometry curvature (q), and the ratio of the solution correlation length to the fluid gap thickness (ξ/H) can all be independently measured or estimated from polymer scaling theory.

3.4.1 Stability predictions

A linear stability analysis on the two-fluid model equations results in the following criterion for instability

$$\frac{\partial Q^0_{xy}}{\partial \dot{\gamma}^0} + \varpi < \alpha E Q^0_{xy}[1 + (\bar{k}\frac{\bar{\xi}_0}{\bar{H}})^2 - \alpha E \Pi^{0,(n)}_{yy}]^{-1}(-\frac{\partial \Pi^{0,(n)}_{yy}}{\partial \dot{\gamma}^0}). \tag{3.12}$$

Using this instability criterion , regions where shear-induced demixing occur are predicted depending on the entanglement density and the applied Weissenberg number (Wi), as shown in Figure 3.2. As seen from the right-hand side, large normal stresses (in excess of shear stresses) promote instability, driving polymer migration across streamlines. In the absence of flow-concentration coupling (*i.e.*, $E = 0$), the stability criterion reduces to $\frac{\partial Q^0_{xy}}{\partial \dot{\gamma}^0} + \varpi < 0$, which is the common criterion for constitutive instability.

Two regions of instability are observed, one at moderate Wi and a second at high Wi (Figure 3.2). The mechanism driving instability of compositional changes to the

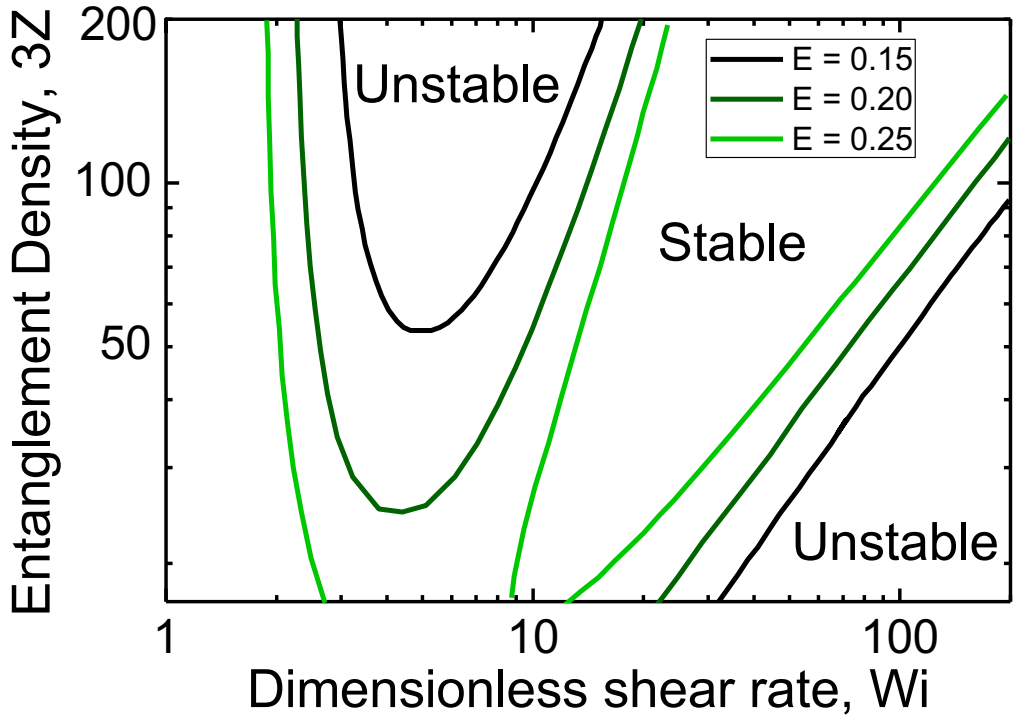

Figure 3.2: Stability diagram as determined from a linear stability analysis on the two-fluid model equations. The boundaries of instability in entanglement density versus Wi space depend on the particular value of E. Adapted from Peterson *et al.* (2016) [3].

fluid depends on the location of instability. In the unstable region at moderate Wi, fluctuations in composition via the Helfand-Fredrickson mechanism are unstable and result in macroscopic shear-induced demixing, where local concentration fluctuations coarsen in time under an applied flow reminiscent of quiescent fluid-fluid phase separation. At high Weissenberg number, the instability results from contributions resulting from the isotropic elastic stress terms, which are large due to chain stretching.

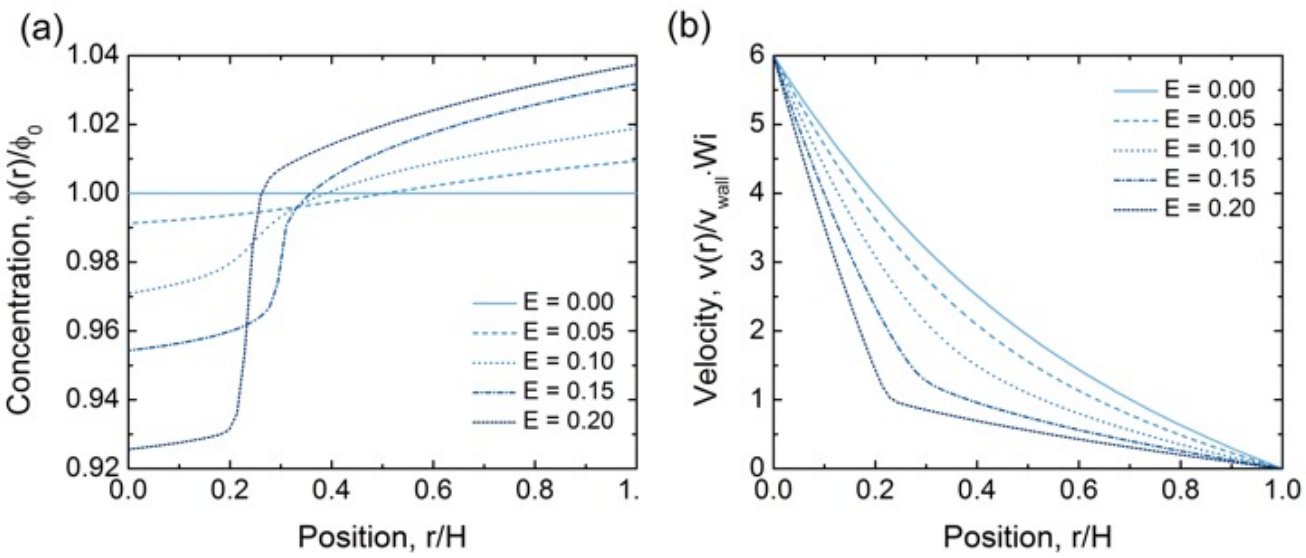

Figure 3.3: Two-fluid model predictions of the steady state (a) concentration and (b) velocity profile at varying degrees of flow-concentration coupling (E) for $Z = 66$ and $Wi = 6$.

3.4.2 Predictions of concentration profile sensitivity to E with corresponding velocity profiles

The magnitude of nonuniform flow is dependent upon the degree of flow-concentration coupling. Figure 3.3 illustrates the sensitivity of the two-fluid model predictions to particular values of the flow-concentration coupling parameter, E. The magnitude of concentration heterogeneity increases and the interface, separating regions of high and low concentration in the fluid, becomes sharper with increasing E (Figure 3.3(a)). The changes in fluid composition also impact the resultant flow profiles (Figure 3.3(b)). As E is increased, the flow profiles become more convincingly shear banded resulting from the sharp interface width separating the bands of different concentration (Figure 3.3(a)).

3.4.3 Transient predictions of the concentration profile evolution with corresponding velocity profiles

As discussed earlier, at moderate Wi fluctuations in concentration via the Helfand-Fredrickson mechanism for SECF [7] are linearly unstable for certain fluid parameters, and undergo a coarsening process reminiscent of Oswaldt ripening to form macroscopic gradients in polymer concentration. The transient development of concentration profile coarsening is shown in Figure 3.4(a). At early times following the startup of shear flow, there is a depletion of polymer concentration at the moving wall ($r/H = 0.0$) and an enrichment of polymer concentration at the stationary wall ($r/H = 1.0$) (Figure 3.4(a)). At longer times, large heterogeneities are observed within the bulk of the fluid (centered around $r/H = 0.3$), which coarsen to larger length scales and result in a steady-state concentration profile that consists of a low concentration band adjacent to the moving wall and a high concentration band in the region adjacent to the stationary wall. The variation of concentration within the high concentration band is the result of the inherent shear stress gradient in a Taylor-Couette flow cell that drives polymer migration across curved streamlines (*i.e.*, $\sigma_{r\theta} \sim 1/r^2$). The time evolution of the concentration profile under flow results in noticeable changes to the flow profile (Figure 3.4(b)).

The predicted flow profile is linear when the concentration profile is uniform at short times following shear startup. The flow profile exhibits curvature at moderate times resulting from the depletion and enrichment of polymer at the boundaries and the combination of shear thinning rheological behavior in a Taylor-Couette flow with an intrinsic shear stress gradient. As a result of concentration heterogeneities in the bulk, "stair steps" of varying local shear rates are observed in the flow profiles at long times prior to a steady-state shear banded flow profile with a high shear band that coincides with the low concentration band and a low shear band that coincides with the high concentration

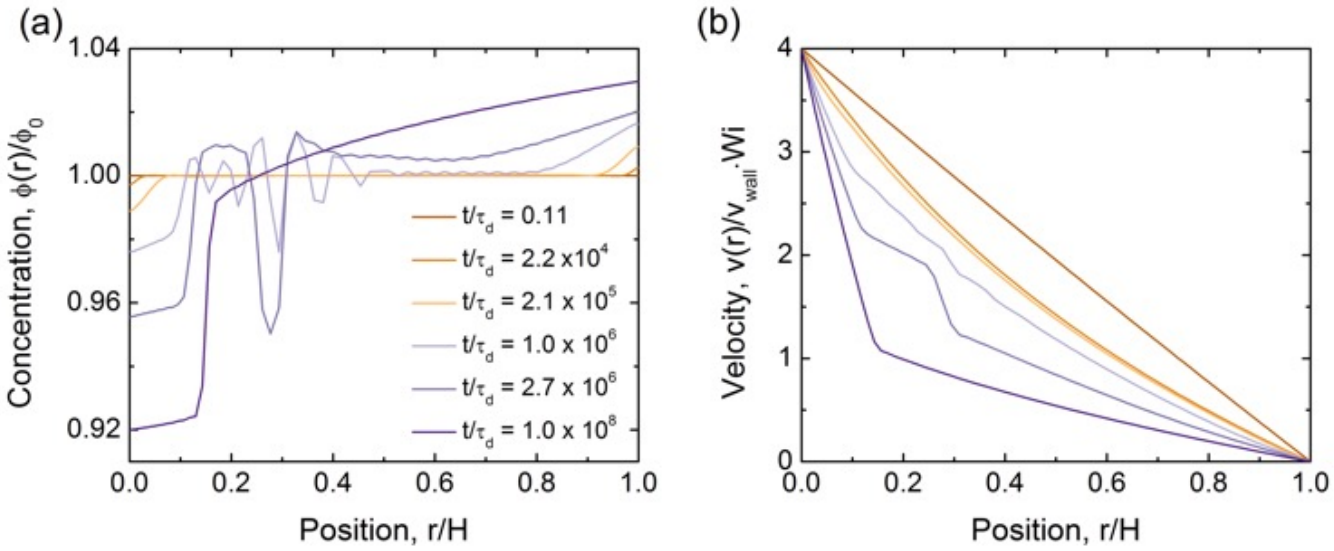

Figure 3.4: Two-fluid model predictions for transient evolution of the (a) concentration and (b) velocity profile for $Z = 66$, $E = 0.20$, and $Wi = 4$ in Taylor-Couette flow with curvature $q = \frac{R_i - R_o}{R_i} = 0.029$. The line colors in (b) correspond to the same t/τ_d as in (a).

band.

3.5 Summary

In this Chapter, we have summarized the details of a two-fluid Rolie-Poly model for describing the rheology of entangled polymer solutions. The model exhibits a shear-induced demixing instability at moderate and high Wi depending on the molecular details of the fluid, such as the number of entanglements, viscosity ratio of solvent to polymer, osmotic susceptibility, and polymer volume fraction. Importantly, this instability suggests that nonuniform concentration profiles develop under shearing of entangled polymer solutions and suggests these changes to the concentration profile result in profound changes to the bulk flow behavior. We experimentally explore the extent to which these concentration heterogeneities in entangled polymer solutions alter the measure flow profiles in Chapters

4, 5, and 6.

Bibliography

[1] M. Cromer, M. C. Villet, G. H. Fredrickson, and L. G. Leal, "Shear banding in polymer solutions," *Physics of Fluids*, vol. 25, no. 5, p. 051703, 2013.

[2] M. Cromer, G. H. Fredrickson, and L. G. Leal, "A study of shear banding in polymer solutions," *Physics of Fluids*, vol. 26, no. 6, p. 063101, 2014.

[3] J. D. Peterson, M. Cromer, G. H. Fredrickson, and L. G. Leal, "Shear banding predictions for the two-fluid Rolie-Poly model," *Journal of Rheology*, vol. 60, no. 5, pp. 927–951, 2016.

[4] P. G. De Gennes, "Dynamics of Entangled Polymer Solutions. I. The Rouse Model," *Macromolecules*, vol. 9, no. 4, pp. 587–593, 1976.

[5] A. E. Likhtman and R. S. Graham, "Simple constitutive equation for linear polymer melts derived from molecular theory: Rolie-Poly equation," *Journal of Non-Newtonian Fluid Mechanics*, vol. 114, no. 1, pp. 1–12, 2003.

[6] R. S. Graham, A. E. Likhtman, T. C. B. McLeish, and S. T. Milner, "Microscopic theory of linear, entangled polymer chains under rapid deformation including chain stretch and convective constraint release," *Journal of Rheology*, vol. 47, no. 5, p. 1171, 2003.

[7] E. Helfand and G. H. Fredrickson, "Large Fluctuations in Polymer Solution under Shear," *Physical Review Letters*, vol. 62, no. 21, pp. 2468–2471, 1989.

Chapter 4

Local flow-concentration coupling in entangled polystyrene solutions[1]

4.1 Abstract

The flow behavior of entangled polymer solutions in simple shear flow is often assumed to be uniform, both in terms of the velocity gradient and polymer concentration. However, there is growing evidence of non-uniform "banded" transient or steady state flows of entangled polymer solutions. The present work considers a distinct phenomenon, whereby transient banding is concomitant with the presence of local shear-enhanced concentration fluctuations. Experimental observations are made using combined rheological measurements with simultaneous particle tracking velocimetry (rheo-PTV) and microscopy (rheo-microscopy) during startup shear in Taylor-Couette flow of entangled polymer solutions of polystyrene (PS) in a marginal solvent, dioctyl phthalate (DOP), at various entanglement numbers (Z). At high Z, the flow develops transient, non-

[1]The contents of this Chapter are reprinted with permission from Burroughs, Shetty, Leal, and Helgeson, *Physical Review Fluids*, **5**, 043301, 2020. Copyright 2020 by the American Physical Society.

homogeneous "banded" velocity profiles over a wide range of imposed shear rates that are inverted from those expected for Taylor-Couette flow, which then relax to a nearly uniform shear rate at steady state. Rheo-microscopy reveals that these transient banded states are accompanied by strong shear-enhanced concentration fluctuations localized to the region of lowest local shear rate. We hypothesize that such finite-amplitude concentration fluctuations lead to increased dissipation that contributes a higher local "effective" fluid viscosity that, in turn, could produce the observed flow non-uniformity. In spite of the non-uniformity of the flow and the concentration fluctuations, the measured apparent rheology of the fluids is in qualitative agreement with both prior experimental studies and model predictions based on a Rolie-Poly model under the assumption that the fluid remains homogeneous, suggesting that this behavior is only observable through spatially-resolved measurements of fluid flow and concentration.

4.2 Introduction

A long-standing goal of polymer physics is to develop a microscopically based constitutive theory to model how the microstructure of entangled polymers under flow results in the measured macroscopic stresses. To date, tube-based models, derived from the Doi-Edwards constitutive equation [1] constructed from the reptation idea of de Gennes [2], have been the most successful in achieving this goal. In part, this success is due to the identification and inclusion of a number of relaxation mechanisms in addition to reptation (contour length fluctuations (CLF), thermal constraint release (TCR), convective constraint release (CCR), and relaxation of chain stretch) [3–7]. Although comparison of these models with linear viscoelastic data has shown remarkable agreement, accurate prediction of nonlinear rheological properties has proven to be more challenging. One possible issue could be the description of chain dynamics in the nonlinear regime, which

has received intense theoretical investigation [3, 5, 6, 8, 9]. Another possible issue is the assumption, made in nearly all studies, that the fluids (and viscoelastic flows they give rise to) remain homogeneous. In the case of polymer solutions, this means that the polymer concentration remains uniform mesoscopically and across macroscopic length scales.

Contrary to this assumption, some polymer-solvent combinations exhibit shear-enhanced concentration fluctuations as indicated by strong fluctuations in measurable optical properties [10–16]. In particular, solutions of polystyrene (PS) in dioctyl phthalate (DOP) have been examined extensively for understanding the occurrence of shear-enhanced concentration fluctuations due to the temperature-dependent solvent quality and large refractive index contrast between PS and DOP [10–13, 15–26]. Although fluid velocities have not typically been measured, it has generally been assumed that these concentration fluctuations are not accompanied by any measurable change in the macroscopic flow. Another possibility, presumably at higher shear rates is that the same physics responsible for concentration fluctuations, may lead to shear-induced demixing on a macroscopic scale, and thus to "banding" of the macroscopic concentration profiles as predicted in recent work [27–32]. When this shear-induced "banding" of the polymer concentration profile occurs, it is clear that there must be corresponding changes in the macroscale flow. For planar shear flow, the velocity profile is predicted to have a banded shape in the absence of a constitutive instability. To date, however, the simultaneous occurrence of banded concentration and velocity profiles has yet to be demonstrated experimentally [29].

Recently, there have been some reported velocimetry experiments that are inferred to represent shear banding [4, 33–39], either as a transient during startup of shear, or as steady state profiles, in both cone-and-plate and Couette devices. Unlike other fluids, it is currently believed that banding in polymers is not due to constitutive instability [4]. However, most of these studies lacked the spatial resolution to differentiate shear banding

from other effects. One possibility in Couette flow is that shear-thinning can enhance the intrinsic curvature of the velocity profiles so that they can mistakenly be identified as shear banding [40]. It has also been suggested that these non-homogeneous flows may be a consequence of edge fracture and/or slip [41–44]. This may well be true in some or even many cases, but is also noteworthy that none of the prior studies have included any measurements of the concentration profiles.

When flow inhomogeneity is observed in commonly used rotational rheometric flows, it usually exists with the high shear rate region nearest the moving boundary where the shear stress is largest [45]. Specifically, in Taylor-Couette devices, there is a dimensionless curvature of the geometry (q) that depends on the ratio of the gap width ($R_o - R_i$) to inner cylinder radius, (R_i), ($q = (R_o - R_i)/R_i$), which is accompanied by a similar gradient in shear stress. Correspondingly, in a polymer solution, the high shear rate region is usually observed near the rotating inner cylinder. However, in rare cases, reversed profiles have been reported for cone-and-plate flow [4, 35, 46], with the high shear rate region near the stationary boundary. Surprisingly, when the transient shear stress is measured during startup in the latter cases, it agrees qualitatively with expectations for an entangled polymer solution, with a transient overshoot in the measured shear stress exhibiting all of the expected behavior (such as the dependence on the time to the maximum shear stress having the usual dependence on shear rate). One observation common to all systems in startup of shear flow is that the onset of non-homogeneous velocity profiles occurs shortly after the shear stress maximum.

To date, as noted earlier, the role of shear-enhanced concentration fluctuations in entangled polymer solutions has been neglected in experimental studies of non-homogenous flows. Specifically, in experimental studies of shear-enhanced concentration fluctuations, the velocity profiles were not measured. Nevertheless, it has been shown, both theoretically [14, 47–49] and experimentally [11–13, 16, 17, 21, 23, 24, 50, 51], that shear flow can

amplify and orient concentration fluctuations in entangled polymer solutions. Polymer solutions near an equilibrium phase boundary are particularly susceptible to such fluctuations due to the approach toward vanishing osmotic compressibility near the critical point.

Experimentally, concentration heterogeneities can be detected using in situ microscopy and light scattering [52], and possess a characteristic length ($l_c = \sqrt{D\tau_d}$), which depends on the longest relaxation time (τ_d) and the cooperative diffusivity (D), that corresponds to the length scale at which the rates of stress relaxation and polymer diffusion are equal [48]. In high molecular weight, semi-dilute entangled polymers, l_c can be large relative to the polymer radius of gyration. Even though it is generally believed that these finite-amplitude concentration fluctuations occur at a local scale, it is foreseeable that sufficiently long-range concentration fluctuations (or gradients thereof) may alter the flow uniformity of entangled polymer solutions. However, this possibility has not received detailed study [53].

In the present work, we report combined rheometry and velocimetry measurements on the flow of entangled polystyrene (PS) in dioctyl phthalate (DOP) solutions in a Taylor-Couette device modified to eliminate edge fracture over an extended shear rate range. The goal is to better understand the possible coupling between shear-enhanced concentration fluctuations and the potential for non-homogeneous flows of entangled polymer solutions. These measurements confirm that non-homogeneous flow can occur as a transient in highly entangled polymer solutions, where the velocity profile develops two regions of different shear rate shortly after the startup of shear flow. Unexpectedly, however, the PS/DOP system at high concentrations (large Z) shows banded profiles that have the inverse configuration to that usually expected for Taylor-Couette flow, with the high shear rate region nearest the stationary outer cylinder. To our knowledge, such an inverted profile cannot be predicted with any existing constitutive model for homogeneous polymer

solutions. Corresponding in situ rheo-microscopy measurements reveal that pronounced flow-enhanced concentration fluctuations transiently appear, evolve, and subside as the flow evolves toward steady state. Furthermore, the region of strong flow-enhanced concentration heterogeneities is observed to coincide with the low shear rate portion of the velocity profiles adjacent to the moving cylinder (where the shear stress is largest). We suspect that increased dissipation, and correspondingly an increased effective viscosity, of the fluid due to finite-amplitude concentration fluctuations may provide a possible explanation for this previously unreported behavior.

4.3 Materials and methods

Polystyrene (PS) with reported molecular weights of 3.84×10^6 and 8.42×10^6 g/mol and polydispersity indices of 1.04 and 1.17, respectively, was purchased from Tosoh Biosciences, LLC. Dioctyl phthalate (DOP) (CAS #: 117-81-7, $\geq$ 99.5%) was purchased from Sigma-Aldrich. Glass tracer particles with a diameter of $\approx 10\ \mu$m were donated by TSI Incorporated. All materials were used as supplied without further purification. Highly entangled PS/DOP solutions were prepared by adding DOP to desired amounts of PS and tracer particles. The labeling convention adopted for the PS/DOP solutions was based on the concentration and molecular weight of PS (*i.e.*, 10 wt% PS(8.42M)/DOP corresponds to a solutions that is 10 wt% PS with a molecular weight of 8.42×10^6 g/mol). The number of entanglements (Z) per chain was estimated by

$$Z = \frac{M_w}{M_e}\phi^{\alpha} \tag{4.1}$$

where M_w is the weight-average molecular weight, M_e is the entanglement molecular weight in the melt (13,500 g/mol for PS), and the dilution exponent α was assumed to

be 1.2 to directly compare with previous work on shear banding in polymer solutions where this same exponent was used [37, 41, 42, 46]. For 10 g samples, $\sim$ 50 mL toluene was added as a co-solvent to aid in dissolution. The samples were mixed for several days on a stir plate at a temperature of 50 ℃. Once the polymer was completely dissolved, the toluene was evaporated in a fume hood until the samples became too viscous to mix with a stir bar. The remaining toluene was removed by placing the samples in a vacuum oven (≈ -350 mm Hg) until the residual toluene fell below 0.1 wt% of the total sample as determined gravimetrically. The final concentration of tracer particles was 300-500 ppm.

All linear viscoelasticity and particle tracking measurements were conducted on an Anton Paar MCR-300 stress-controlled rheometer described previously [54]. The rheometer was equipped with a Taylor-Couette flow cell comprised of a transparent quartz cup, where the temperature was controlled by flowing water from a water bath through an annulus in the quartz. The quartz cup is 22 mm deep and the inner cylinder (bob), with an anodized aluminum surface, was 16 mm tall. The bob has a diameter of 34 mm and the inner diameter of the cup was 35 mm, yielding a gap size of 0.5 mm and a curvature $q = 0.029$. The diameter of the bob was selected to minimize the effect of curvature on the experiments.

The transparent quartz cup allowed for particle tracking velocimetry (PTV) measurements to be conducted simultaneously with rheological experiments as described in detail elsewhere [54]. Briefly, plano-convex and concave lenses were used to transform the light from a laser head into a 2D sheet. The laser sheet illuminated tracer particles from the side of the flow cell in the velocity-velocity gradient plane within the geometry gap. A camera positioned underneath the Taylor-Couette flow cell captured images at a fixed frame rate depending on the applied shear rate. The tracer particles were identified, and their displacements between subsequent image pairs calculated, using an

image processing algorithm [55]. In all PTV measurements, the illuminated plane was roughly 3 mm above the bottom edge of the Taylor-Couette bob. We observe no changes in the measured velocity profiles upon varying position of the illuminated plane from 1 mm from the bottom edge of the bob to its midplane. This result, as well as visual observation, confirms the absence of curvature-induced elastic instability as predicted by Larson *et al.* [56] to occur in Taylor-Couette flows at a sufficiently large Weissenberg number. This absence of elastic instability in our experiments is in agreement with the instability criterion proposed by Larson *et al.* [56]; for the curvature of $q = 0.029$, this criterion predicts that the critical Weissenberg number for the Taylor-Couette flow cell is approximately 35, which is much higher than the applied Wi used in this study.

The degree of shear-enhanced concentration fluctuations was controlled by varying the temperature of the PS/DOP solutions. PS/DOP has a well-characterized theta temperature of 22 ℃. We employed a higher temperature of 50 ℃ for PTV measurements with the higher concentration PS solutions as a means to control the magnitude of turbidity, which was too strong for particle tracking measurements when these samples were sheared near the theta temperature.

Bright field rheo-microscopy measurements were performed on an Anton Paar MCR-702 stress-controlled rheometer. The rheometer was fitted with a transparent quartz cup of similar dimensions as used in the rheo-PTV measurements as well as the same anodized aluminum bob. A white LED light source was positioned above the Taylor-Couette cell to illuminate the fluid. A 10× / NA = 0.28 objective (Mitutoyo, Japan) with a CCD camera (1.4 Megapixel Mini Enclosed Color Camera, Model #: Lm165C, Lumenera) was mounted underneath the flow cell to image the fluid in transmission mode. The focal depth of the objective was 3.5 μm. Crossed polarizers were placed above and below the flow cell at 90° relative polarization in order to minimize noise in the microscopy images. A digital Fourier bandpass filter for structures between 0.49 and 1.95 μm^{-1} was applied

to each captured image. This range was believed to capture the length scale of actual shear-induced structures in the fluid based upon the optical heterogeneities observed in the raw microscopy images.

To minimize the effect of edge fracture, a stainless-steel lid was machined and placed on top of the fluid The sample is loaded into the quartz cup in excess so that it comes in contact with the lid after the bob is fully submerged, yielding geometrically symmetric boundary conditions on the top and bottom of the Taylor-Couette flow cell. We expect that any secondary flow resulting from the boundaries will only be significant over distances comparable to the gap width (500 μm). The results of this paper are found to be invariant to the vertical location of the PTV measurement as measured at several positions from near the bottom edge of the bob to the midplane. In addition, the results reported are the same over observable time scales with and without the stainless-steel lid; therefore, we conclude that the presence of a lid on top of the fluid only serves to extend the lifetime of a reliable rheological measurement.

Samples were loaded into the quartz cup by spatula at an elevated temperature to reduce the time needed for the polymer solutions to equilibrate. Once the air bubbles introduced by loading were eliminated, the bob was slowly lowered into the sample to avoid excessive normal forces.

4.4 Results and discussion

4.4.1 Linear rheological characterization of polystyrene solutions

Three solutions of entangled polystyrene (PS) in dioctyl phthalate (DOP) were prepared, with entanglement numbers (Z) ranging from 16 to 36. The linear viscoelastic response of each PS/DOP solution is shown in Figure 4.1(a). For each solution, the

frequency of the crossover of the storage modulus (G') and the loss modulus (G'') is separated from the local minimum in G'' (which appears at higher frequency) by approximately three decades, indicating significant entanglement. The relaxation time for reptation (τ_d) is the inverse of the frequency at which G' and G'' crossover, determined by linear interpolation. The plateau modulus (G_N^0) is defined as the value of G' at the frequency where G'' exhibits a local minimum.

Complex viscosities (η^*) were extracted from linear viscoelastic frequency sweeps. Shear viscosities (η) were determined by averaging the measured viscosity at long times following a rapid ramp of the inner cylinder from rest to the target wall velocity necessary to achieve a specified shear rate (assuming homogeneous shear flow). The Cox-Merz rule is satisfied for each solution, demonstrated by a simultaneous plot of $\eta^*(\omega)$ and $\eta(\dot{\gamma})$, Figure 4.1(b). Table 4.1 summarizes the rheological properties for each solution. All three solutions show evidence of a zero-shear viscosity given by the plateau in viscosity at low shear rates and shear thinning above an approximate shear rate given by τ_d^{-1}. The degree of shear thinning, characterized by a dependence of $\dot{\gamma}^n$ of $-0.89 \leq n \leq -0.81$, agrees with previous reports on entangled polymer solutions [7, 9].

Table 4.1: Viscoelastic solution properties determined from rheological measurements. The Rouse time was calculated from the measured τ_d (s) and the relation $\tau_d/\tau_R = 3Z$.

Solution	Entanglements per chain, Z	Reptation time, τ_d (s)	Plateau modulus, G_N^0 (Pa)	Zero-shear viscosity, η_0 (Pa s)	Recoverable compliance, J_e^0 (Pa^{-1}	Rouse time, τ_R (s)
5 wt% PS(8.42M)-DOP	16	60.9	126	4.29×10^3	9.78×10^{-3}	1.27
10 wt% PS(8.42M)-DOP	36	55.5	701	2.66×10^4	1.78×10^{-3}	0.51
16 wt% PS(3.84M)-DOP	30	51.4	3.29×10^3	7.77×10^4	4.41×10^{-4}	0.57

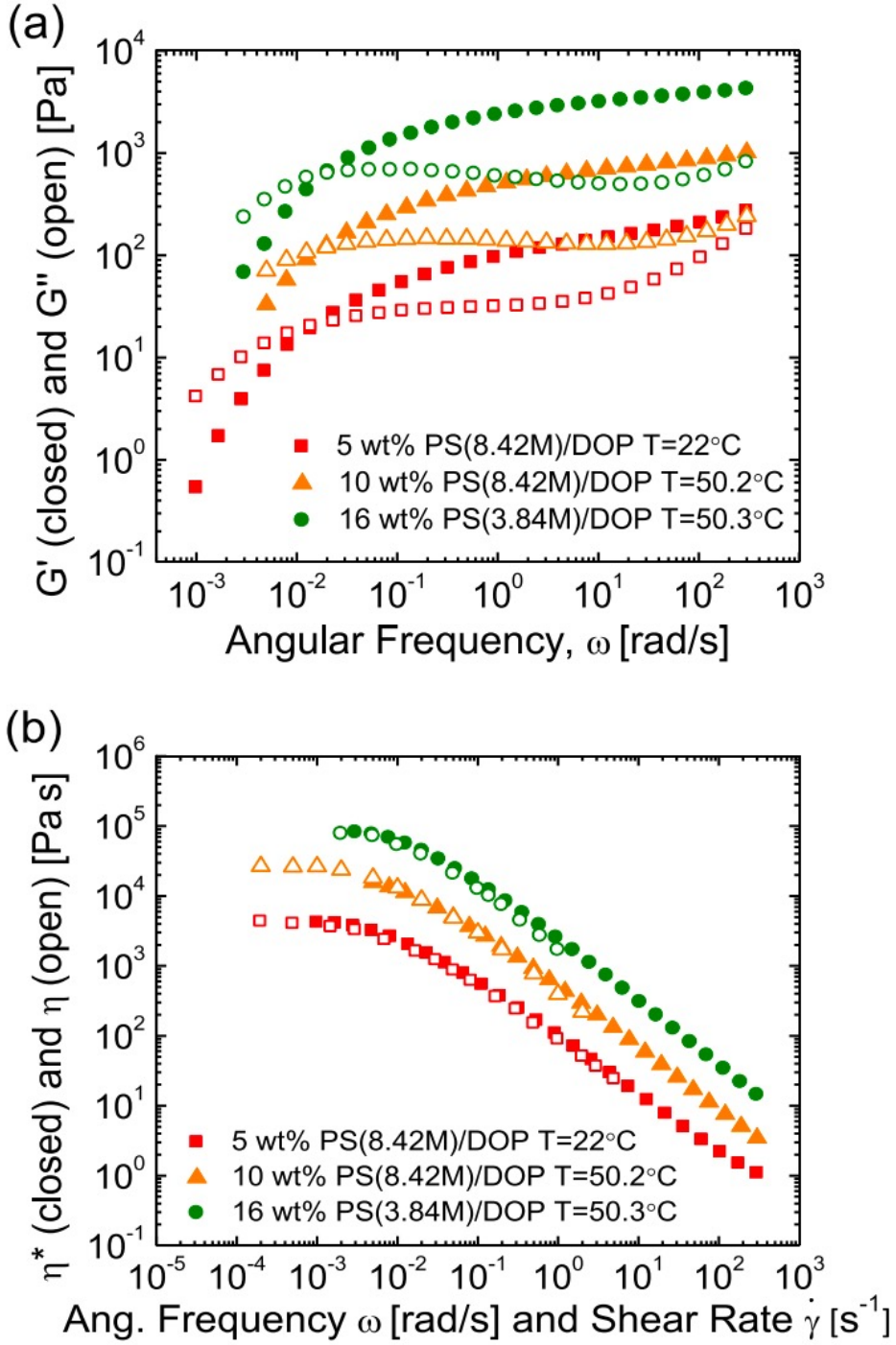

Figure 4.1: (a) Linear viscoelastic frequency sweeps for three entangled PS/DOP solutions. Measurements were conducted at a strain = 1%, and (b) verification of Cox-Merz rule for shear rates employed in this study.

4.4.2 Comparison of steady state experimental data to the homogeneous Rolie-Poly model

To confirm that the measured rheology of the fluids in this study does not behave unusually across the range of conditions investigated, the variations in measured steady state shear stresses for the three different entangled solutions with varying imposed nominal Wi_{app} where

$$Wi_{app} = \tau_d \, \dot{\gamma} \tag{4.2}$$

were compared to predictions from the homogeneous Rolie-Poly (R-P) constitutive model (Figure 4.2). For comparison, the shear stress ($\sigma_{r\theta}$) was determined from the measured torque of the rheometer and the recoverable compliance (J_e^0) was calculated from the zero-frequency extrapolation of the linear viscoelastic data in Figure 4.1(a), given by

$$\lim_{\omega \to 0} \frac{G'(\omega)}{G'(\omega)^2 + G''(\omega)^2}. \tag{4.3}$$

The shear rate used to determine Wi was based on the nominal imposed shear rate (Wi_{app}), which assumes a linear velocity profile. In the linear flow regime ($Wi < 1$), Newtonian behavior is predicted and observed for all three entangled solutions, as reflected in a linear slope of $\sigma_{r\theta} \, J_e^0$ versus Wi. For nonlinear flows ($Wi > 1$), all solutions exhibit a weaker dependence of $\sigma_{r\theta} \, J_e^0$ versus Wi. The broader transition from Newtonian behavior to a weak plateau in $\sigma_{r\theta} \, J_e^0$ relative to the (R-P) model predictions could result from the polydispersity of the polystyrene used in experiments, leading to a distribution of relaxation times that is neglected by the single-mode R-P model.

Otherwise, for steady state flows, the homogeneous R-P model appears to accurately describe both the linear and nonlinear shear rheology of the three entangled solutions. Both the model and measured shear stress values are strictly increasing (monotonic) for

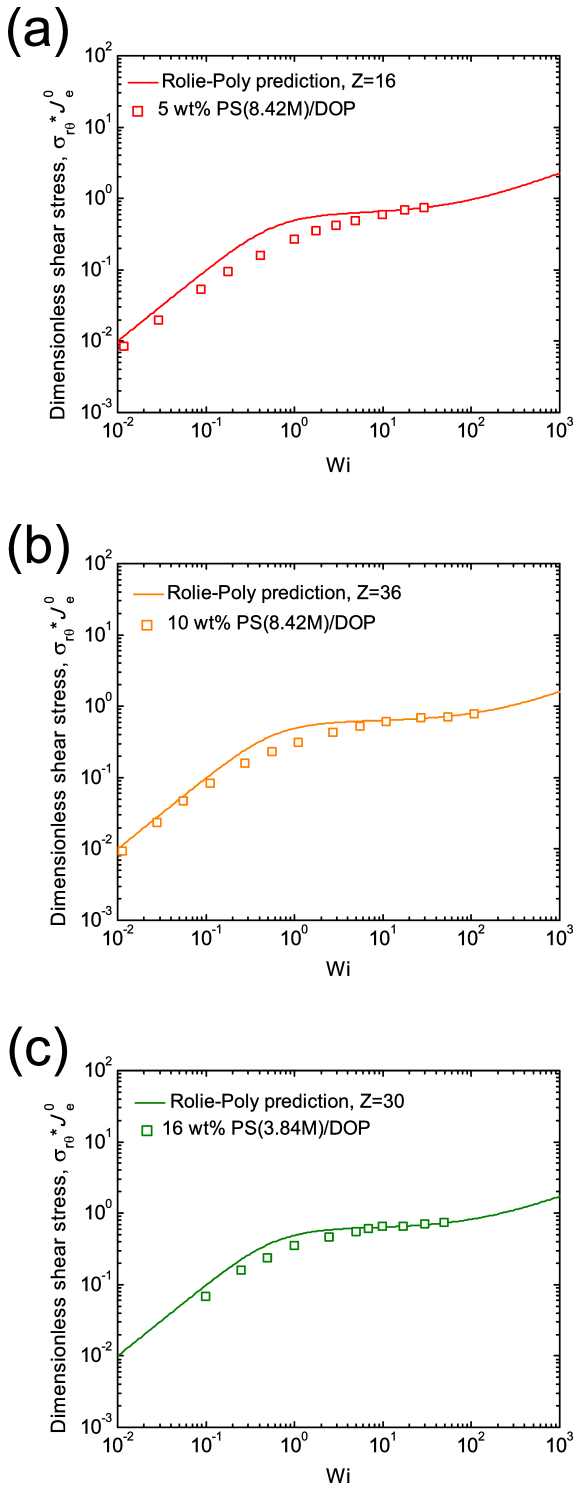

Figure 4.2: Rolie-Poly model flow curve predictions (lines) and measured steady state shear stresses (symbols) for (a) 5 wt% PS(8.42M)/DOP, (b) 10 wt% PS(8.42M)/DOP, and (c) 16 wt% PS(3.84M)/DOP.

all applied Wi, which precludes the possibility of flow instability arising from a nonmonotonic flow curve.

4.4.3 Comparison of transient experimental data to previous work

The transient shear stress results were found to agree with previously reported startup shear experiments on entangled PS/DOP solutions, albeit with fewer entanglements per chain ($Z \approx 13$) [57]. Figure 4.3 illustrates the influence of applied Wi on the transient stress response for the three entangled PS/DOP solutions, as well as previously reported results for an entangled PS/DOP solution [57]. More specifically, the strain at which the shear stress overshoot occurs following the startup of flow increases above $Wi \approx 10$ in all solutions (Figure 4.3(a)). For $Wi \leq 10$ the strain at the shear stress overshoot is around 2, in agreement with past reports.

The ratio of the shear stress at the overshoot to the steady state value for varying Wi also agrees quantitatively with literature values for $Z = 16$ (Figure 4.3(b)). However, the solutions with $Z = 30$ and 36 have lower values of the ratio $\sigma_{overshoot}/\sigma_{steady\,state}$ for high Wi compared to the solutions with lower Z. The difference between the high Wi values of $\sigma_{overshoot}/\sigma_{steady\,state}$ in PS/DOP solutions with high and low entanglements could be due to more chain stretching in the less entangled solutions relative to the highly entangled solutions (*i.e.*, longer Rouse relaxation times). In summary, aside from a quantitative difference in the ration $\sigma_{overshoot}/\sigma_{steady\,state}$ with Wi for the solutions with higher levels of entanglement, the measured rheology of the PS/DOP solutions agrees qualitatively and quantitatively with what has been reported in the literature previously, and there is no evidence that can be discerned from the shear stress data (or the homogeneous R-P model predictions) that potentially suggests a departure from homogeneous flow of the entangled polymer solutions in the startup of shear flow.

4.4.4 Observation of non-homogeneous flow in highly entangled solution

To investigate the kinematic response of entangled polymer solutions subjected to startup of steady shear flow, rheo-PTV measurements were conducted to obtain the velocity profile and shear stress at numerous nominal imposed Wi to be quantified simultaneously. In a Taylor-Couette geometry, curvature or "bowing" in the measured velocity profiles is expected, resulting from the inherent shear stress gradient for flow between concentric cylinders ($\sigma_{r\theta} \sim 1/r^2$), with the highest shear rate at the inner (moving) cylinder and lowest at the outer (stationary) cylinder. For shear thinning fluids, this curvature in the measured velocity profile is more pronounced than for a Newtonian fluid, due to the nonlinear dependence of shear stress on shear rate.

There is a strong departure from this expected flow behavior in highly entangled PS/DOP solutions. A representative example is the measured velocity profiles in the range $t/\tau_d = 7 - 11$ following the startup of shear flow in 10 wt% PS(8.42M)/DOP ($Z = 36$), which are inversely "bowed" for a wide range of Wi_{app} (Figure 4.4). Such nonhomogeneous flow profiles are surprising since steady shearing for $10\tau_d$ is commonly believed to be sufficient time to achieve steady state flow, as determined by the measured shear stress. Non-zero velocities at $r/H = 1$ are also observed and are presumably due to wall slip at the stationary quartz boundary. Attempts to eliminate wall slip by applying a plastic film to the quartz boundary were found to complicate the measurements as the fluid would inevitably delaminate the film from the quartz surface, yielding a non-uniform gap length around the Taylor-Couette flow cell. The presence of wall slip could certainly amplify the magnitude of the observed inversely bowed velocity profiles, but transient changes in the velocity profiles are observed even after the slip velocity has reached a steady state. For $Wi_{app} \geq 5.55$, the velocity profiles appear to have two distinct regions

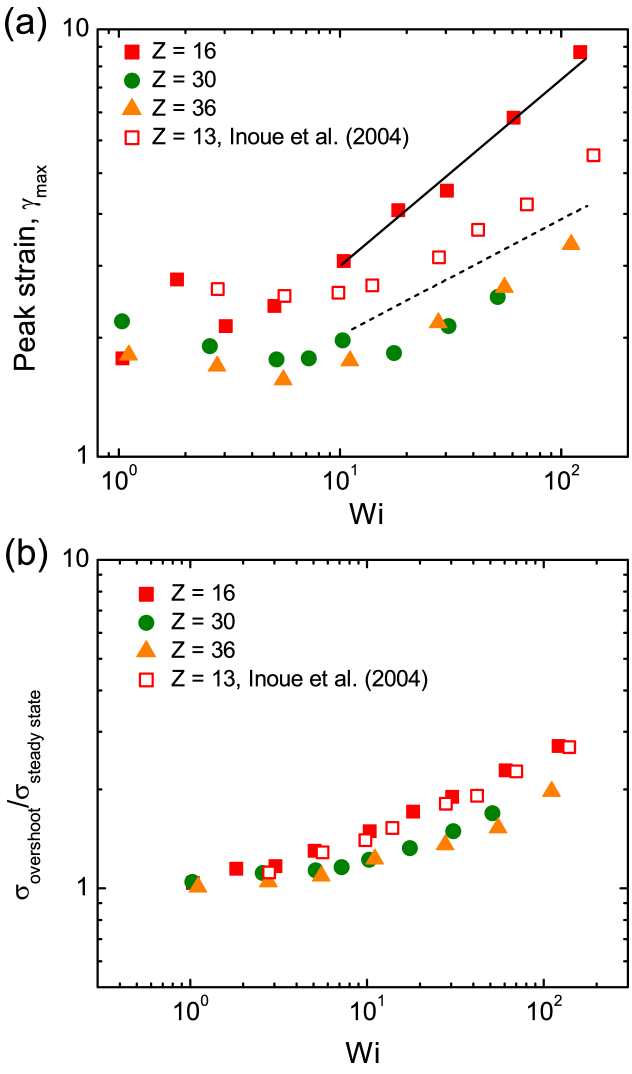

Figure 4.3: (a) Wi dependence of the peak strain (γ_{max}, strain at which the shear stress exhibits an overshoot) following startup shear where the solid and dashed lines indicate power law slopes of 0.45 and 0.28, respectively, and (b) the ratio of the maximum shear stress to the shear stress at steady state ($\sigma_{overshoot}/(\sigma_{steady\ state})$ for varying Wi.

of differing shear rate, where the high shear rate region is adjacent to the stationary boundary and the low shear rate region is next to the moving boundary. This disagrees with the expectation for nonhomogeneous flows that the highest shear rate occurs in the region of highest shear stress (*i.e.*, the moving boundary). To investigate the flow kinematics of entangled polymer solutions further, we studied the transient development of the inversely bowed velocity profiles and consider a phenomenon that could potentially explain the observation of nonhomogeneous flow.

4.4.5 Transient development of flows during startup of steady shear

Moderately entangled solutions ($Z = 16$)

For $Wi_{app} > 1$, an overshoot in the transient shear stress occurs in entangled PS/DOP solutions (Figure 4.5(a)). The initial shear stress response in startup of steady shear flow is governed by the elasticity of the fluid. As seen for a moderately entangled ($Z = 16$) solution of 5 wt% PS(8.42M)/DOP in Figure 4.5(b), the velocity profile remains linear prior to the overshoot in the shear stress at $t/\tau_d = 0.45$. After the overshoot, the shear stress decreases slowly toward its steady state value, and the velocity profile develops curvature that can be explained by the geometrically imposed stress gradient of the Taylor-Couette geometry. Such a curved velocity profile is stable for the remainder of the experiment, showing no changes for a period spanning $100\tau_d$. For $Z = 16$, the measured rheology and flow kinematics thus match expectations from the homogenous R-P model (Figure 4.5(b), dotted line). Thus, when the solution is only moderately entangled ($Z = 16$) the development of both the shear stress and velocity profiles correspond to expectations for a homogeneous fluid in a homogenous flow. Specifically, the inverted velocity profiles apparent for the more highly entangled solutions (Figure 4.4) are not observed when

$Z = 16$.

Highly entangled solutions ($Z = 30$ and 36)

For $Z = 36$ (Figure 4.6(a)), the qualitative response of the measured shear stress following startup of continuous shear flow is similar to that in Figure 4.5(a), where a shear stress overshoot occurs shortly after shearing commences, followed by a slow decrease to the steady state shear stress. One noticeable difference in the measured shear stress in Figure 4.6(a) is the small second overshoot at long times ($t/\tau_d \approx 30 - 40$). This second overshoot in the shear stress has been observed in investigations of shear-enhanced concentration fluctuations in entangled polymer solutions and was attributed to the onset of shear-induced demixing [57–60]. The time at which the second overshoot occurs is sensitive to the temperature, polymer molecular weight, polymer concentration, and applied shear rate [59, 60].

Despite the agreement in the apparent rheological behavior between the experiments and homogeneous Rolie-Poly model predictions (Figure 4.2(c)), the measured transient velocity profiles of the highly entangled solutions show a qualitative departure from the R-P model predictions as well as the expectations for a homogeneous fluid. In Figure 4.6(b), the velocity profile is initially linear without any curvature following the startup of shear. After the shear stress overshoot, the inversely-bowed velocity profile develops and reaches a maximum severity (as measured by the difference in shear rate between the two regions) when $t/\tau_d \approx 1.40$, approximately when the shear stress reaches a local minimum. At longer times, the velocity profile begins to relax to the expected, nearly linear form. This relaxation process occurs through a decrease in the difference in shear rate between the two regions, while at the same time the interface between the two regions moves toward the inner moving cylinder and the measured shear stress increases. At very long times following the startup of shear flow, the velocity profile reaches a steady shape

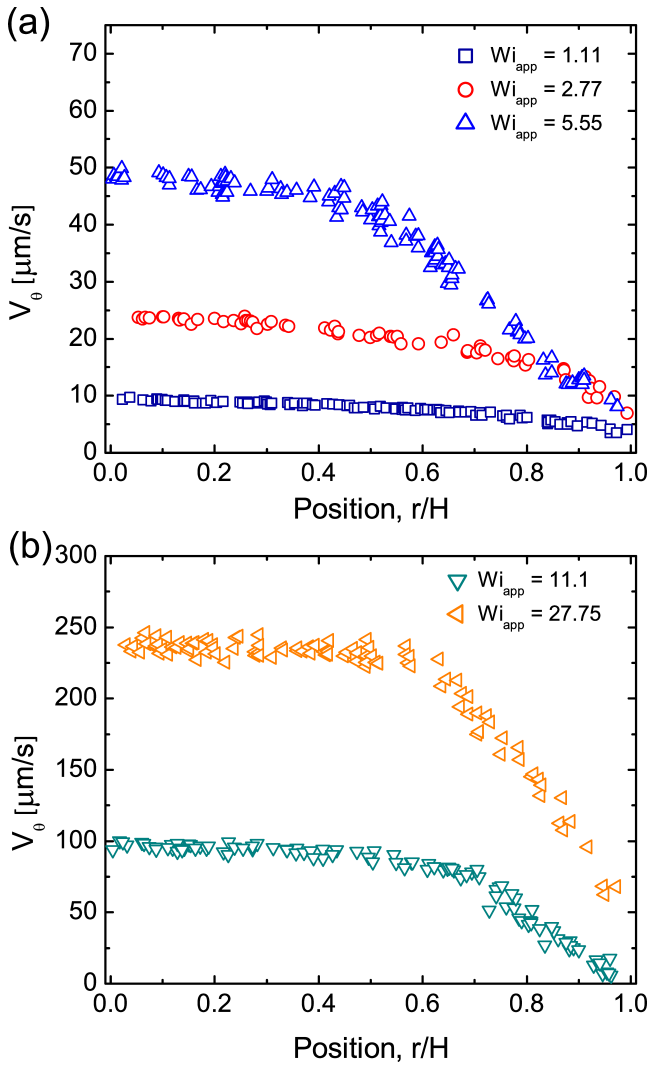

Figure 4.4: Velocity profiles for 10 wt% PS(8.42M)/DOP ($Z = 36$) at varying applied Wi for times between $t/\tau_d \approx 7$ and 11 after startup of shear flow.

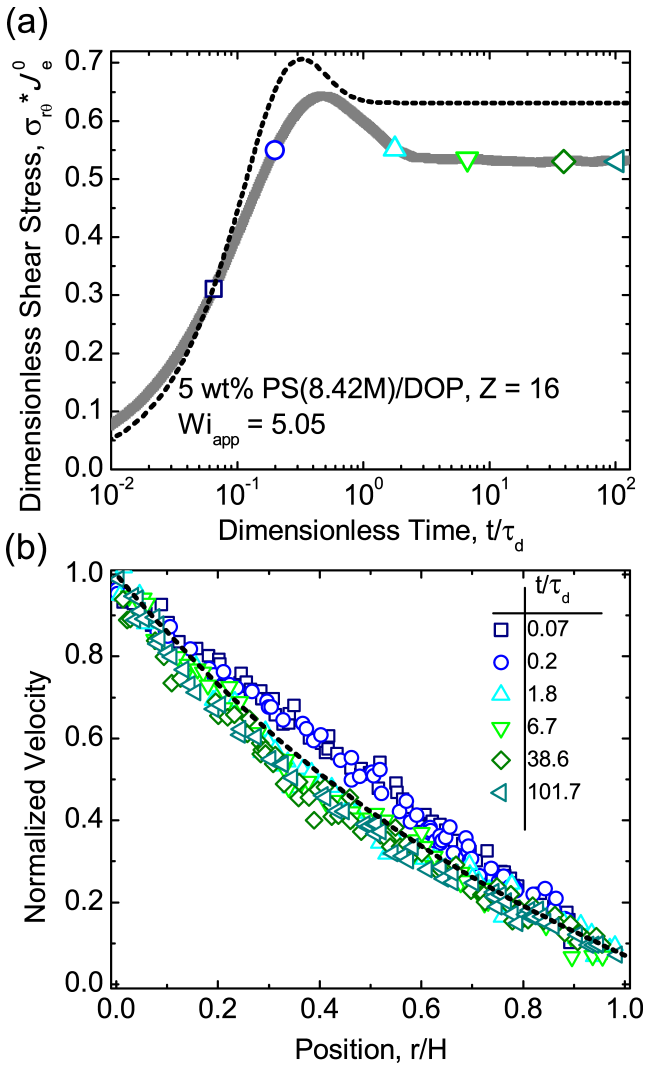

Figure 4.5: Transient response of PS/DOP solution with $Z = 16$ to step shear of $Wi_{app} = 5.05$ (a) shear stress and (b) velocity profile data. The symbols overlaid on the shear stress response correspond to the time at which the velocity profiles in (b) were measured. Black dashed lines denote the homogeneous Rolie-Poly model prediction for the transient shear stress in (a) and the steady velocity in (b).

where the highest shear rate is next to the moving boundary as expected, and at this point the velocity profile matches what is predicted using the homogeneous R-P model after accounting for the appreciable wall slip at both the inner and outer boundaries.

The measured shear stress and velocity profiles for the solution with $Z = 30$ (16 wt% PS(3.84M)/DOP) are qualitatively similar to that for $Z = 36$ (10 wt% PS(8.42M)/DOP) despite the sample having higher concentration, lower polymer molecular weight, and slightly lower degree of entanglement (Figure 4.7). This suggests that the inversely-bowed profiles observed transiently in Figure 4.4 and Figure 4.6(b) are not an artifact of the specific sample or polymer used. The velocity profiles in Figure 4.7(b) depart from the expected linear form shortly after the initiation of shear flow. Even in the fluid with $Z = 30$, there is a large difference between the measured shear rate adjacent to the moving and stationary boundaries. Again, at long times the high shear region adjacent to the stationary boundary is no longer present, and the fluid's velocity profile appears nearly linear with some wall slip.

4.4.6 Development of localized flow-enhanced concentration heterogeneities in startup shear

A possible explanation for the low shear rate region adjacent to the moving wall is localized shear-enhanced concentration fluctuations. Based on typical values of the diffusivity (D) and reptation time (τ_d) for entangled polymer solutions, the length scale for concentration heterogeneities is estimated to be $O(\mu\text{m})$ due to the competition between diffusion and stress relaxation ($\sqrt{D\,\tau_d} = l_c$). These micron-scale heterogeneities could increase dissipation, and therefore act to increase the effective viscosity of the fluid. More specifically, because the shear-induced enhancement of concentration heterogeneities is sensitive to the local shear stress, a stress gradient (such as encountered

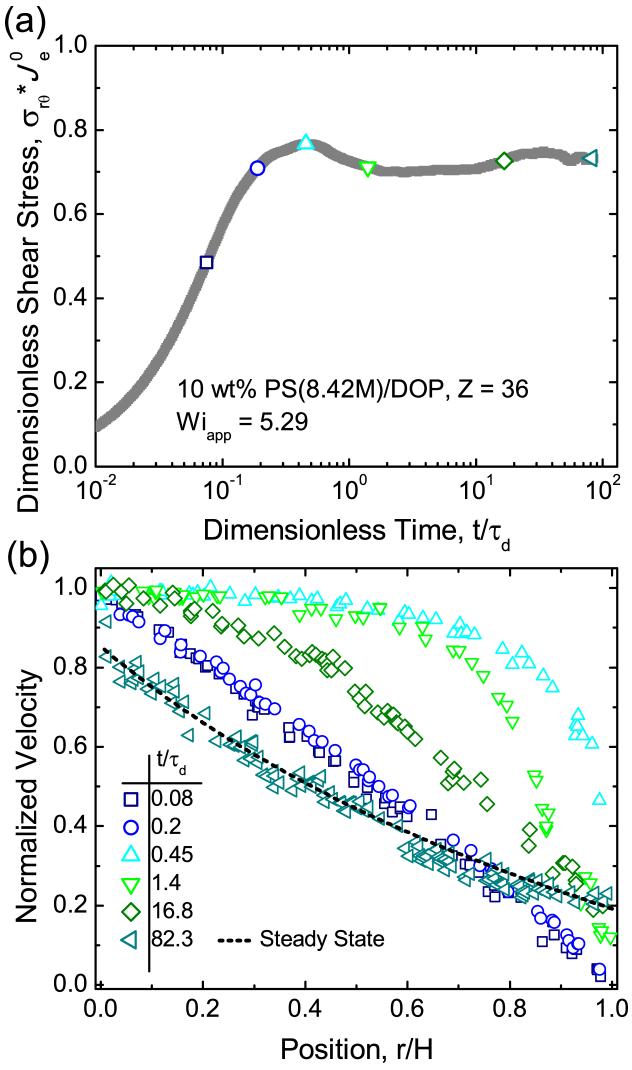

Figure 4.6: Transient response of PS/DOP solution with $Z = 36$ to a step shear of $Wi_{app} = 5.29$ (a) measured shear stress response and (b) determined velocity profiles for discrete points in time following the startup of flow. Symbols overlaying the measured shear stress in (a) coincide with the point in time of each velocity profile in (b).

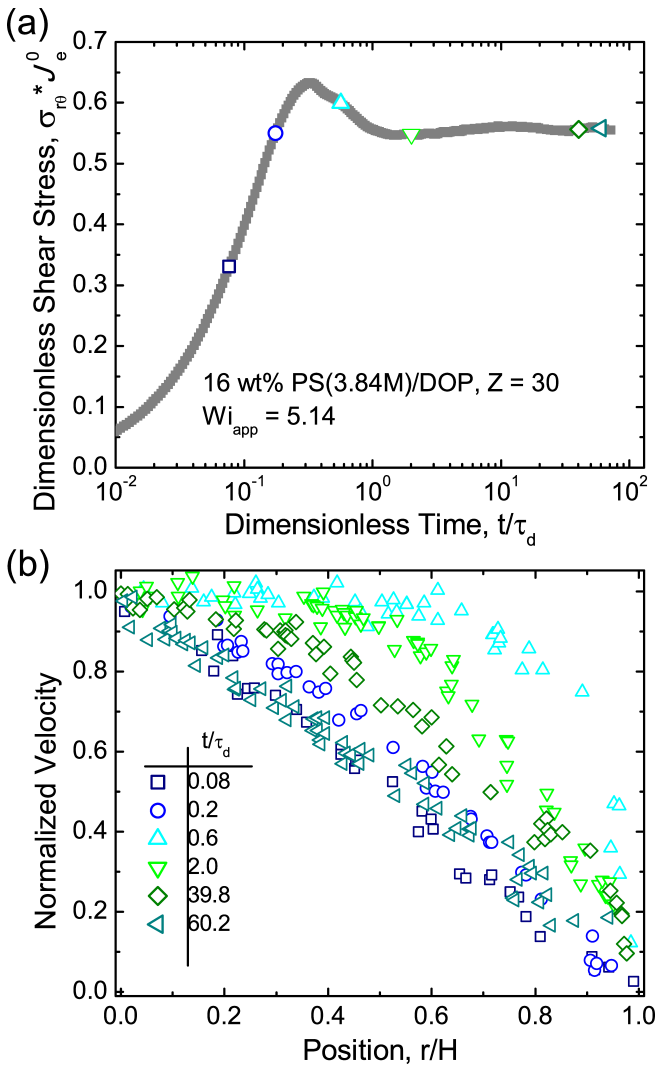

Figure 4.7: Transient response of PS/DOP solution with $Z = 30$ to a step shear of $Wi_{app} = 5.14$ (a) the measured shear stress and (b) the determined velocity profiles at discrete points in time following the startup of flow.

in the Taylor-Couette geometry) could consequently produce spatial variations in the concentration fluctuations and therefore the local effective fluid viscosity. For example, if shear-enhanced concentration fluctuations were largest in the region of highest local stress (the inner rotating cylinder), this could increase the effective viscosity by such an amount as to produce the observed low shear rate region near the moving cylinder in our experiments.

To further investigate the presence of such flow-enhanced concentration fluctuations in startup shear flow, and their relationship to the observed nonhomogeneous flow, *in situ* rheo-microscopy measurements were performed on the PS/DOP solutions. The $Z = 30$ PS/DOP fluid exhibits fluctuations in concentration shortly after initiation of shear (Figure 4.8). The fluid is initially optically isotropic (Figure 4.8(a), dark between cross polarizers), then becomes oriented along the flow direction (Figure 4.8(b-c), bright), and finally becomes dark again at long times (Figure 4.8(d), steady flow). Applying a digital Fourier bandpass filter emphasizes the presence of heterogeneities in the fluid indicated by optical turbidity by removing long wavelength illumination gradients while preserving the local structure of the birefringent texture. These heterogeneities first appear at the moving cylinder (Figure 4.8(b)), and then propagate into the bulk (Figure 4.8(c)). At long times (Figure 4.8(d)) the heterogeneities appear to subside. To further highlight the emergence and disappearance of strong flow-enhanced concentration fluctuations, we average the image intensity along the vertical (flow) direction (Figure 4.8, bottom row). As apparent in Figure 4.8(c), there is a periodicity to the contour profile. Based on the periodicity in the contour profile, it is estimated that the fluctuations are $8.5 - 9.5\mu$m, slightly larger than results of lower molecular weight PS/DOP solutions [12, 13, 24, 52]. We note that there is no discernible change of turbidity in the rheo-PTV images upon shearing the $Z = 16$ fluid at $T = 22$ ℃, where the inversely-bowed velocity profiles are not observed, but we do observe changes in turbidity in the rheo-PTV images upon

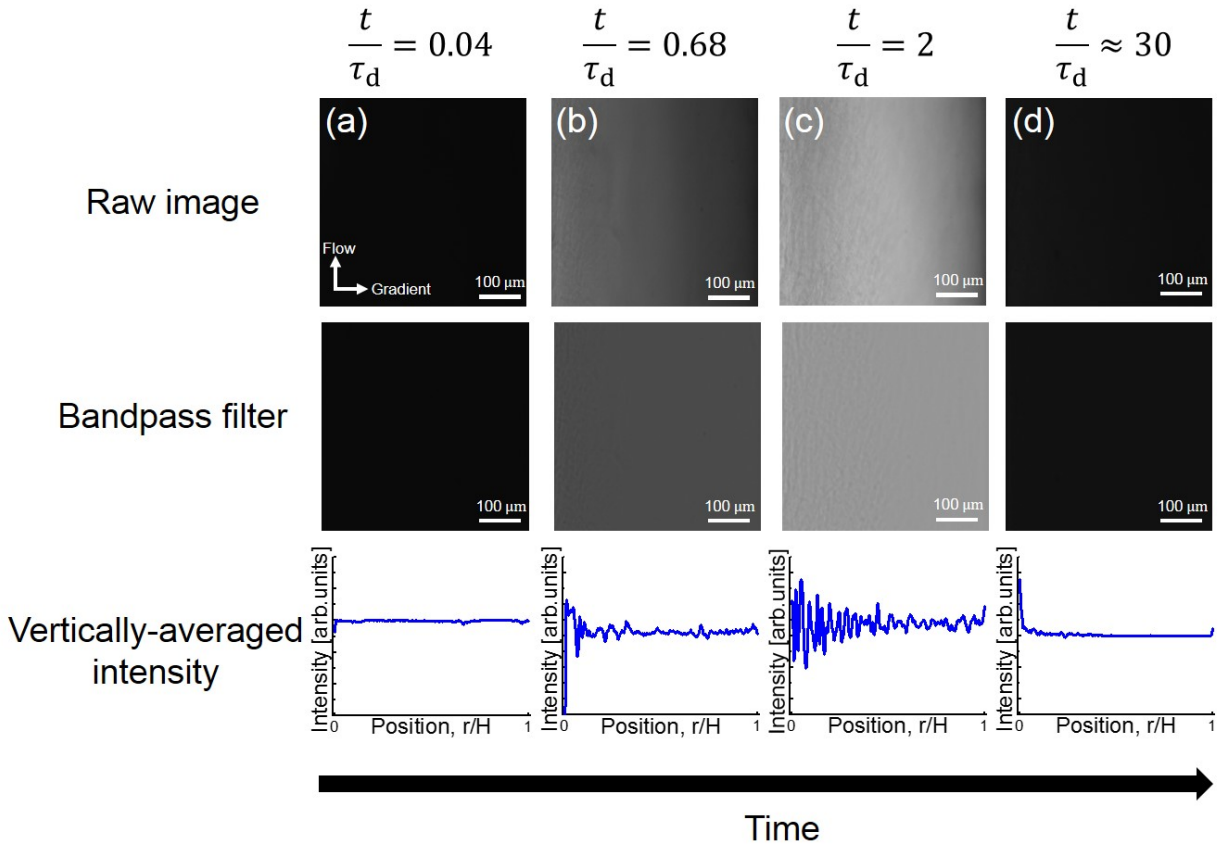

Figure 4.8: Rheo-microscopy images showing the development and decay of flow-enhanced concentration fluctuations in 16 wt% PS(3.84M)/DOP at $Wi_{app} = 11.1$. (a) prior to the shear stress overshoot (b-c) shortly after the shear stress overshoot (c) at long times following the shear stress overshoot when the stress has reached a constant value.

shearing the $Z = 30$ and 36 fluids at $T = 50$ ℃. These preliminary results suggest that inversely-bowed velocity profiles do not occur in the absence of shear-enhanced turbidity.

Interestingly, we find a strong correlation between the observed regions of concentration heterogeneity and the local shear rate in these regions when nonhomogeneous velocity profiles develop (Figure 4.9). Prior to the overshoot in shear stress, the velocity profile remains uniform and there are no apparent heterogeneities in the rheo-microscopy images (Figure 4.9(a)). Following the overshoot in the shear stress, the fluid develops noticeable optical heterogeneities that are spatially non-uniform (Figure 4.9(b)). The location of the heterogeneities, adjacent to the moving cylinder, coincides with the location and width of the low shear rate region as measured from rheo-PTV (Figure 4.9(b)). Finally, at long times, the presence of heterogeneities in the rheo-microscopy images subsides, and the velocity profile returns to a homogeneous shear rate. To rationalize this behavior, we suggest that flow-enhanced concentration heterogeneities increase the local "effective" fluid viscosity. In Taylor-Couette flow, the shear stress is highest at the inner moving cylinder and lowest at the stationary outer cylinder. By increasing the local fluid viscosity, the apparent shear rate must therefore decrease to maintain stress continuity across the fluid. These results suggest that the mechanism by which non-homogeneous flow arises in the highly entangled PS/DOP solutions is closely related to, if not caused by, the appearance of local concentration fluctuations in the region of highest shear stress near the inner moving wall. An obvious question, given the large changes in the velocity profiles, is whether the required changes in the apparent viscosity are "reasonable". The velocity gradient in the low shear rate region decreases by as much as a factor of 13 relative to the nominal imposed shear rate ($\dot{\gamma}_{app}$), which might superficially suggest that concentration fluctuations correspond to an increase of the apparent viscosity of a similar magnitude. Although we do not have a theoretical means at this stage to estimate how much change the additional dissipation could generate, a factor of 13 would seem to be

"unreasonable". However, it is important to recognize that the change in the velocity gradient in the low shear rate region is significantly amplified by strong shear thinning in the high shear rate region.

One way to see this is to calculate the local apparent viscosities in the high and low shear rate regions (Figure 4.10). The local viscosity of the low shear rate region adjacent to the inner cylinder ($\eta^+_{inner}(t)$) is given by

$$\eta^+_{inner}(t) = \frac{\sigma_{inner}(t)}{\dot{\gamma}_{inner}(t)} \tag{4.4}$$

Here $\dot{\gamma}_{inner}(t)$ is the measured shear rate in the region adjacent to the inner cylinder as quantified from a linear regression of the velocity profile data over which an approximately constant velocity gradient is observed. $\sigma_{inner}(t)$ represents a spatially-averaged shear stress over the width of the low shear rate region, calculated by means of the known shear stress gradient in Taylor-Couette flow, given by

$$\sigma(r,t) = \sigma_{wall}(t)\frac{R_i^2}{(r/H + R_i)^2} \tag{4.5}$$

where $\sigma_{wall}(t)$ is the shear stress measured by the rheometer. Similarly, the local apparent viscosity of the outer region is calculated by

$$\eta^+_{outer}(t) = \frac{\sigma_{outer}(t)}{\dot{\gamma}_{outer}(t)}. \tag{4.6}$$

Here $\dot{\gamma}_{outer}$ is the measured shear rate adjacent to the outer cylinder as computed from a linear regression of the velocity profile in the high shear region over which an approximately constant velocity gradient is observed. $\sigma_{outer}(t)$ represents a spatially-averaged shear stress over the width of the high shear rate region, calculated following the same procedure as for $\sigma_{inner}(t)$. The results for η^+_{outer} and η^+_{inner} are plotted in Figure 4.10,

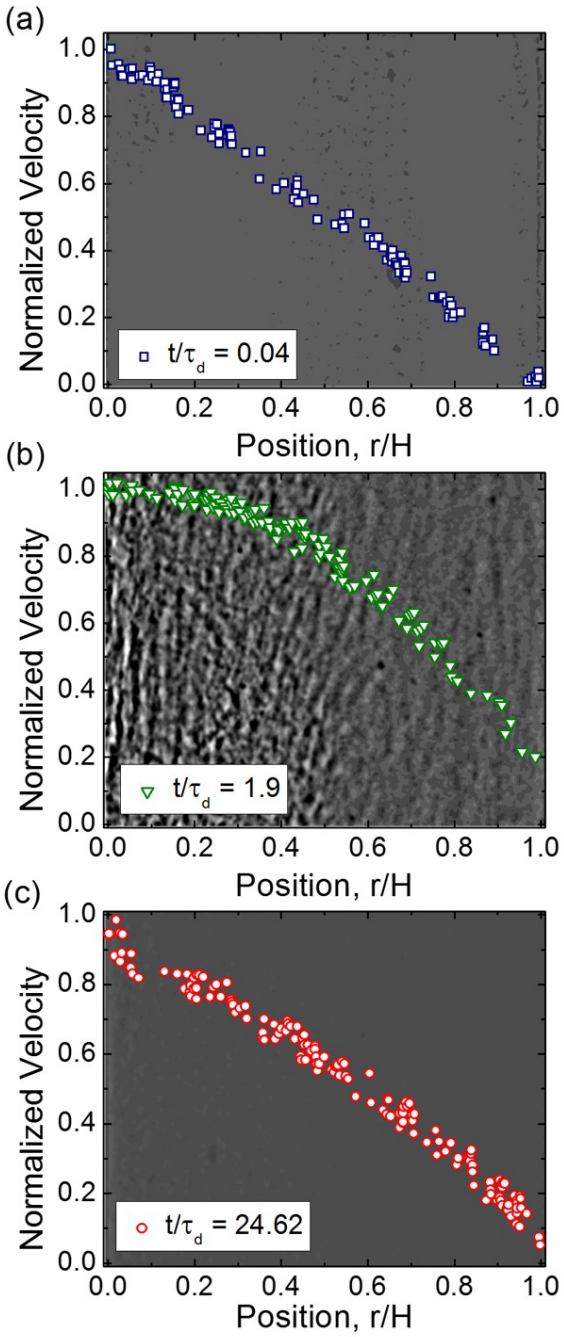

Figure 4.9: Transient development of velocity profiles of 16 wt% PS(3.84M)/DOP at $Wi_{app} = 11.1$ overlaid on corresponding images collected in rheo-microscopy with a bandpass filter applied showing shear-enhanced concentration fluctuations at (a) $t/\tau_d = 0.04$, (b) $t/\tau_d = 1.9$, and (c) $t/\tau_d = 24.62$.

normalized by the measured steady state viscosity at the corresponding local shear rate, $\eta(\dot{\gamma}_{inner})^{SS}$ and $\eta(\dot{\gamma}_{outer})^{SS}$, respectively. These ratios, $\eta^{+}_{outer}/\eta(\dot{\gamma}_{outer})^{SS}$ and $\eta^{+}_{inner}/\eta(\dot{\gamma}_{inner})^{SS}$, quantify the deviation in the locally observed viscosity relative to the steady state due to the transient viscoelasticity of the fluid. This deviation includes any possible effects due to concentration fluctuations and concomitant non-homogeneous flow. We compare this quantity in Figure 4.10 to the apparent transient viscosity determined from the measured wall shear stress, $\sigma_{wall}(t)$, and $\dot{\gamma}_{app}$,

$$\eta^{+}_{app}(t) = \frac{\sigma_{wall}(t)}{\dot{\gamma}_{app}} \tag{4.7}$$

normalized by its steady state value, $\eta(\dot{\gamma}_{app})^{SS}$. This latter ratio, $\eta^{+}_{app}/\eta(\dot{\gamma}_{app})^{SS}$, represents the deviation of the apparent transient viscosity from its steady state value in the absence of any information about the velocity profile due to apparent viscoelastic effects. Given these definitions, it is then clear that any deviation of the locally observed viscosity ratios, $\eta^{+}_{inner}/\eta(\dot{\gamma}_{inner})^{SS}$ and $\eta^{+}_{outer}/\eta(\dot{\gamma}_{outer})^{SS}$, from the apparent viscosity ratio $\eta^{+}_{app}/\eta(\dot{\gamma}_{app})^{SS}$ are due solely to the effects of the nonhomogenous velocity profile, which we have hypothesized as being due to the effects of concentration fluctuations (Figure 4.10). The value of $\eta^{+}_{outer}/\eta(\dot{\gamma}_{outer})^{SS}$ (open blue circles), in which the amplitude of transient concentration fluctuations remains small throughout the measurement, is consistent at all times with the measured steady state viscosity at the local shear rate in a homogeneous fluid (i.e., $\eta^{+}_{outer}/\eta(\dot{\gamma}_{outer})^{SS} \approx 1$). On the other hand, $\eta^{+}_{inner}/\eta(\dot{\gamma}_{inner})^{SS}$ (open red squares), in which the amplitude of shear-ehanced concentration fluctuations is large, is found to exceed the steady state viscosity by about a factor of 3. While a 3-fold enhancement of viscosity due to fluctuations in concentration still seems somewhat large, it is important to note that there are currently no theories capable of predicting how large of a change in viscosity that shear-enhanced concentration fluctuations could produce.

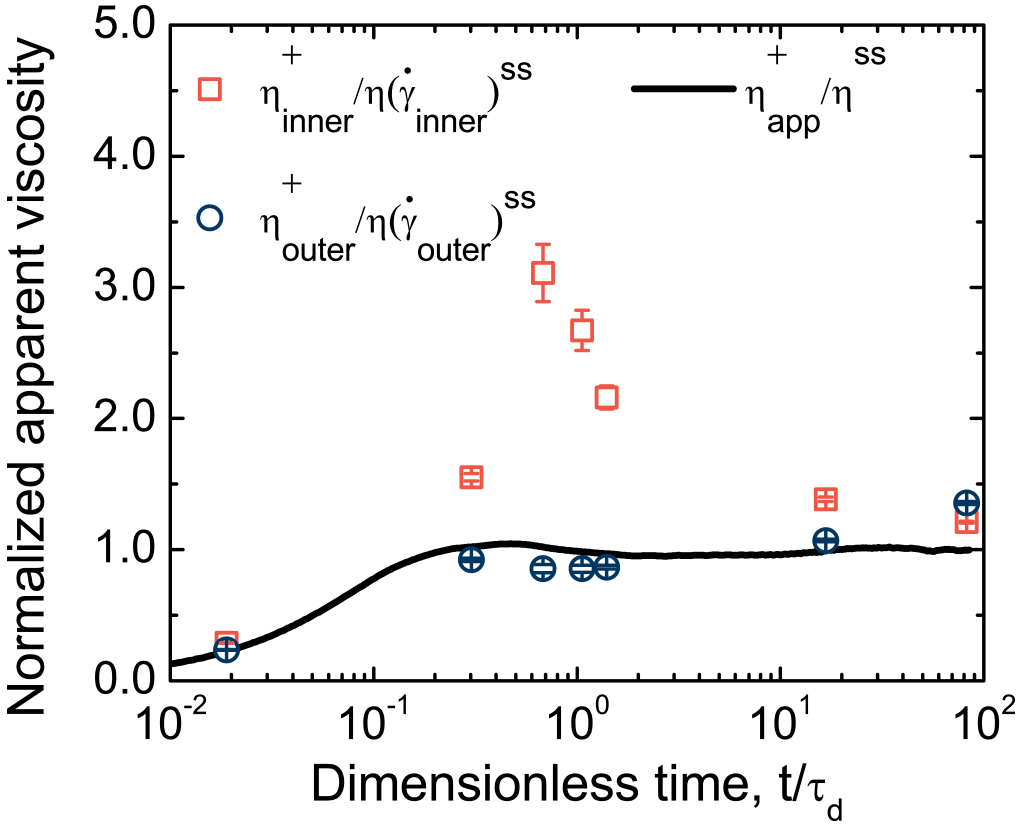

Figure 4.10: Normalized transient viscosity as measured by the rheometer compared to spatially-resolved apparent viscosities adjacent to the inner and outer cylinders of the Taylor-Couette geometry for 10 wt% PS(8.42M)/DOP at $Wi_{app} = 5.29$. The open symbols represent the local transient viscosities normalized by the steady state viscosities at the locally measured shear rates $\eta(\dot{\gamma}_{inner})^{SS}$ and $\eta(\dot{\gamma}_{outer})^{SS}$. The solid black line represents the measured transient viscosity at the nominal imposed shear rate normalized by the steady state viscosity.

As already stated, the fact that only a factor of 3 change in the apparent viscosity is required to account to the observed changes in the velocity gradient in the low shear rate region is a consequence of the very significant reduction of the viscosity in the high shear rate region due to the effects of shear thinning.

4.5 Conclusions

Rheo-PTV measurements of highly entangled polystyrene solutions reveal departures from uniform flow during startup shear that cannot be explained by the expected rheology of a homogeneous polymeric fluid. Despite these departures from the anticipated behavior, the transient and steady state shear stresses of all solutions investigated agree with Rolie-Poly model predictions and previously reported experiments. *In situ* rheo-microscopy measurements confirm the presence of shear-enhanced concentration fluctuations in the highly entangled fluids. Specifically, a spatial gradient in the magnitude of the concentration fluctuations is found to coincide with an inverse gradient in the local shear rate. To our knowledge, this is the first experimental observation of non-homogeneous flows in entangled polymers involving coupling of banded flows to local concentration fluctuations. Because the fluids we study are representative of a large body of near-critical polymer solutions, these new findings call for deeper examination of the generality of this behavior to other material systems involving polymer solutions, and also potentially other fluids exhibiting coupling of thermal fluctuations and flow [61–66].

A possible explanation of this phenomenon is that the presence of concentration heterogeneities increases the local effective viscosity of the fluid through extra dissipation. Based on this proposed mechanism, we expect that the transient non-homogeneous flows reported here should also occur in other situations where flow produces sufficiently strong spatial variations in the amplitude of concentration fluctuations. Recently developed rheological models involving the coupling of entangled polymer dynamics with non-local concentration fluctuations are a logical starting point for developing a full theoretical description of the phenomena we report [28, 29]. However, due to the necessity for numerically resolving 3D spatiotemporally evolving concentration fields, we leave such investigations to future studies.

This work provides further support that nonhomogeneous flow can occur in startup shear of entangled polymer solutions even when potential experimental artifacts known to nonlinear rheology are accounted for and highlights the importance of considering fluid non-uniformities when interpreting the nonhomogeneous flow of polymeric fluids. It also calls for deeper fundamental studies into the influence of enhanced local concentration fluctuations on the rheology of polymer solutions, and the coupling of these effects to the underlying flow. Finally, we note that the findings of this work could have more general consequences involving the effects of flow-enhanced thermal fluctuations on other transport properties, as well as other fields that could be coupled with enhanced fluctuations.

Bibliography

[1] M. Doi and S. F. Edwards, "Dynamics of Concentrated Polymer Systems: Part III - The Constitutive Equation," *Journal of the Chemical Society, Faraday Transactions 2: Molecular and Chemical Physics*, vol. 74, pp. 1818–1832, 1978.

[2] P. G. de Gennes, "Reptation of a Polymer Chain in the Presence of Fixed Obstacles," *The Journal of Chemical Physics*, vol. 55, no. 2, p. 572, 1971.

[3] D. W. Mead, R. G. Larson, and M. Doi, "A Molecular Theory for Fast Flows of Entangled Polymers," *Macromolecules*, vol. 31, no. 22, pp. 7895–7914, 1998.

[4] Y. T. Hu, L. Wilen, A. Philips, and A. Lips, "Is the constitutive relation for entangled polymers monotonic?," *Journal of Rheology*, vol. 51, no. 2, pp. 275–295, 2007.

[5] S. T. Milner, T. C. B. McLeish, and A. E. Likhtman, "Microscopic theory of convective constraint release," *Journal of Rheology*, vol. 45, no. 2, pp. 539–563, 2001.

[6] R. S. Graham, A. E. Likhtman, T. C. B. McLeish, and S. T. Milner, "Microscopic theory of linear, entangled polymer chains under rapid deformation including chain stretch and convective constraint release," *Journal of Rheology*, vol. 47, no. 5, p. 1171, 2003.

[7] E. Menezes and W. W. Graessley, "Nonlinear Rheological Behavior of Polymer Systems for Several Shear-Flow Histories," *Journal of Polymer Science, Part B: Polymer Physics*, vol. 20, pp. 1817–1833, 1982.

[8] A. E. Likhtman and R. S. Graham, "Simple constitutive equation for linear polymer melts derived from molecular theory: Rolie-Poly equation," *Journal of Non-Newtonian Fluid Mechanics*, vol. 114, no. 1, pp. 1–12, 2003.

[9] S. Costanzo, Q. Huang, G. Ianniruberto, G. Marrucci, O. Hassager, and D. Vlassopoulos, "Shear and Extensional Rheology of Polystyrene Melts and Solutions with the Same Number of Entanglements," *Macromolecules*, vol. 49, no. 10, pp. 3925–3935, 2016.

[10] C. Rangel-Nafaile, A. B. Metzner, and K. F. Wissbrun, "Analysis of Stress-Induced Phase Separations in Polymer Solutions," *Macromolecules*, vol. 17, pp. 1187–1195, 1984.

[11] T. Kume, T. Hashimoto, T. Takahashi, and G. G. Fuller, "Rheo-optical studies of shear-induced structures in semidilute polystyrene solutions," *Macromolecules*, vol. 30, no. 23, pp. 7232–7236, 1997.

[12] X. L. Wu, D. J. Pine, and P. K. Dixon, "Enhanced concentration fluctuations in polymer solutions under shear flow," *Physical Review Letters*, vol. 66, no. 18, pp. 2408–2411, 1991.

[13] P. K. Dixon, D. J. Pine, and X. L. Wu, "Mode selection in the dynamics of sheared polymer solutions," *Physical Review Letters*, vol. 68, no. 14, pp. 2239–2242, 1992.

[14] E. Helfand and G. H. Fredrickson, "Large Fluctuations in Polymer Solution under Shear," *Physical Review Letters*, vol. 62, no. 21, pp. 2468–2471, 1989.

[15] J. W. van Egmond, D. E. Werner, and G. G. Fuller, "Time-dependent small-angle light scattering of shear-induced concentration fluctuations in polymer solutions," *The Journal of Chemical Physics*, vol. 96, no. 10, p. 7742, 1992.

[16] T. Hashimoto and K. Fujioka, "Shear-Enhanced Concentration Fluctuations in Polymer Solutions as Observed by Flow Light Scattering," *Journal of the Physical Society of Japan*, vol. 60, no. 2, pp. 356–359, 1991.

[17] S. Saito, T. Hashimoto, I. Morfin, P. Lindner, and F. Boué, "Structures in a semidilute polymer solution induced under steady shear flow as studied by small-angle light and neutron scattering," *Macromolecules*, vol. 35, no. 2, pp. 445–459, 2002.

[18] M. K. Endoh, S. Saito, and T. Hashimoto, "Shear-induced structures in semidilute polystyrene solution: Effect of solvent quality," *Macromolecules*, vol. 35, no. 20, pp. 7692–7699, 2002.

[19] S. Saito, T. Hashimoto, I. Morfin, P. Lindner, F. Boué, and D. J. Pine, "Phase separation in a polymer solution induced by steady and large amplitude oscillatory shear flow," *Macromolecules*, vol. 36, no. 10, pp. 3745–3748, 2003.

[20] L. Hilliou and D. Vlassopoulos, "Time-Periodic Structures and Instabilities in Shear-Thickening," *Industrial & Engineering Chemistry Research*, vol. 41, no. 25, pp. 6246–6255, 2002.

[21] M. K. Endoh, M. Takenaka, T. Inoue, H. Watanabe, and T. Hashimoto, "Shear small-angle light scattering studies of shear-induced concentration fluctuations and steady state viscoelastic properties," *Journal of Chemical Physics*, vol. 128, no. 16, 2008.

[22] P. Moldenaers, H. Yanase, J. Mewis, G. G. Fuller, C.-S. Lee, and J. Magda, "Flow-induced concentration fluctuations in polymer solutions: Structure/property relationships," *Rheologica Acta*, vol. 32, no. 1, pp. 1–8, 1993.

[23] T. Kume, T. Hattori, and T. Hashimoto, "Time Evolution of Shear-Induced Structures in Semidilute Polystyrene Solutions," *Macromolecules*, vol. 30, no. 3, pp. 427–434, 1997.

[24] K. Migler, C. H. Liu, and D. J. Pine, "Structure evolution of a polymer solution at high shear rates," *Macromolecules*, vol. 29, no. 5, pp. 1422–1432, 1996.

[25] H. Yanase, P. Moldenaers, J. Mewis, V. Abetz, J. van Egmond, and G. G. Fuller, "Structure and dynamics of a polymer solution subject to flow-induced phase separation," *Rheologica Acta*, vol. 30, no. 1, pp. 89–97, 1991.

[26] S. Saito, K. Matsuzaka, and T. Hashimoto, "Structures of a semidilute polymer solution under oscillatory shear flow," *Macromolecules*, vol. 32, no. 15, pp. 4879–4888, 1999.

[27] M. Cromer, M. C. Villet, G. H. Fredrickson, and L. G. Leal, "Shear banding in polymer solutions," *Physics of Fluids*, vol. 25, no. 5, p. 051703, 2013.

[28] M. Cromer, G. H. Fredrickson, and L. G. Leal, "A study of shear banding in polymer solutions," *Physics of Fluids*, vol. 26, no. 6, p. 063101, 2014.

[29] J. D. Peterson, M. Cromer, G. H. Fredrickson, and L. G. Leal, "Shear banding predictions for the two-fluid Rolie-Poly model," *Journal of Rheology*, vol. 60, no. 5, pp. 927–951, 2016.

[30] S. M. Fielding and P. D. Olmsted, "Kinetics of the shear banding instability in startup flows.," *Physical Review E*, vol. 68, no. 3, p. 036313, 2003.

[31] S. M. Fielding and P. D. Olmsted, "Early stage kinetics in a unified model of shear-induced demixing and mechanical shear banding instabilities.," *Physical review letters*, vol. 90, no. 22, p. 224501, 2003.

[32] S. M. Fielding and P. D. Olmsted, "Flow phase diagrams for concentration-coupled shear banding," *European Physical Journal E*, vol. 11, no. 1, pp. 65–83, 2003.

[33] S. Ravindranath, S.-Q. Wang, M. Olechnowicz, and R. P. Quirk, "Banding in simple steady shear of entangled polymer solutions," *Macromolecules*, vol. 41, no. 7, pp. 2663–2670, 2008.

[34] P. E. Boukany, S.-Q. Wang, S. Ravindranath, and L. J. Lee, "Shear banding in entangled polymers in the micron scale gap: a confocal-rheoscopic study," *Soft Matter*, vol. 11, pp. 8058–8068, 2015.

[35] S. Cheng and S.-Q. Wang, "Is shear banding a metastable property of well-entangled polymer solutions?," *Journal of Rheology*, vol. 56, no. 6, pp. 1413–1428, 2012.

[36] S. Jaradat, M. Harvey, and T. A. Waigh, "Shear-banding in polyacrylamide solutions revealed via optical coherence tomography velocimetry," *Soft Matter*, vol. 8, no. 46, pp. 11677–11686, 2012.

[37] Y. T. Hu, "Steady-state shear banding in entangled polymers?," *Journal of Rheology*, vol. 54, no. 6, pp. 1307–1323, 2010.

[38] S. Shin, K. D. Dorfman, and X. Cheng, "Shear-banding and superdiffusivity in entangled polymer solutions," *Physical Review E*, vol. 96, no. 6, pp. 1–9, 2017.

[39] S. Shin, K. D. Dorfman, and X. Cheng, "Effect of edge disturbance on shear banding in polymeric solutions," *Journal of Rheology*, vol. 62, no. 6, pp. 1339–1345, 2018.

[40] P. Cheng, M. C. Burroughs, L. G. Leal, and M. E. Helgeson, "Distinguishing shear banding from shear thinning in flows with a shear stress gradient," *Rheologica Acta*, vol. 56, no. 12, pp. 1007–1032, 2017.

[41] Y. Li, M. Hu, G. B. McKenna, C. J. Dimitriou, G. H. McKinley, R. M. Mick, D. C. Venerus, and L. A. Archer, "Flow field visualization of entangled polybutadiene solutions under nonlinear viscoelastic flow conditions," *Journal of Rheology*, vol. 57, no. 5, pp. 1411–1428, 2013.

[42] Y. Li and G. B. McKenna, "Startup shear of a highly entangled polystyrene solution deep into the nonlinear viscoelastic regime," *Rheologica Acta*, vol. 54, no. 9-10, pp. 771–777, 2015.

[43] C. Sui and G. B. McKenna, "Instability of entangled polymers in cone and plate rheometry," *Rheologica Acta*, vol. 46, no. 6, pp. 877–888, 2007.

[44] Y. W. Inn, K. F. Wissbrun, and M. M. Denn, "Effect of Edge Fracture on Constant Torque Rheometry of Entangled Polymer Solutions," *Macromolecules*, vol. 38, no. 22, pp. 9385–9388, 2005.

[45] J. M. Adams and P. D. Olmsted, "Nonmonotonic Models are Not Necessary to Obtain Shear Banding Phenomena in Entangled Polymer Solutions," *Physical Review Letters*, vol. 102, no. 6, p. 067801, 2009.

[46] S. Ravindranath and S.-Q. Wang, "Steady state measurements in stress plateau region of entangled polymer solutions: Controlled-rate and controlled-stress modes," *Journal of Rheology*, vol. 52, no. 2008, p. 957, 2008.

[47] S. T. Milner, "Dynamical theory of concentration fluctuations in polymer solutions under shear," *Physical Review E*, vol. 48, no. 5, pp. 3674–3691, 1993.

[48] H. Ji and E. Helfand, "Concentration fluctuations in sheared polymer solutions," *Macromolecules*, pp. 3869–3880, 1995.

[49] A. Onuki, "Dynamic equations of polymers with deformations in semidilute regions," *Journal of the Physical Society of Japan*, pp. 3423–3426, 1990.

[50] H. Murase, T. Kume, T. Hashimoto, and Y. Ohta, "Shear-induced structures in semidilute solution of ultrahigh molecular weight polyethylene at temperature close to equilibrium dissolution temperature," *Macromolecules*, vol. 38, no. 15, pp. 6656–6665, 2005.

[51] M. K. Endoh, M. Takenaka, and T. Hashimoto, "Effects of shear flow on a semidilute polymer solution under phase-separating condition," *Polymer*, vol. 47, no. 20, pp. 7271–7281, 2006.

[52] E. Moses, T. Kume, and T. Hashimoto, "Shear microscopy of the "butterfly pattern" in polymer mixtures," *Physical Review Letters*, vol. 72, no. 13, p. 2037, 1994.

[53] V. R. Mhetar and L. A. Archer, "Slip in Entangled Polymer Solutions," *Macromolecules*, vol. 31, no. 19, pp. 8617–8622, 1998.

[54] Y. T. Hu and A. Lips, "Kinetics and mechanism of shear banding in an entangled micellar solution," *Journal of Rheology*, vol. 49, no. 5, pp. 1001–1027, 2005.

[55] J. Crocker and D. Grier, "Methods of Digital Video Microscopy for Colloidal Studies," *Journal of Colloid and Interface Science*, vol. 179, no. 1, pp. 298–310, 1996.

[56] R. G. Larson, E. S. Shaqfeh, and S. J. Muller, "A purely elastic instability in Taylor-Couette flow," *Journal of Fluid Mechanics*, vol. 218, pp. 573–600, 1990.

[57] T. Inoue, Y. Yamashita, H. Watanabe, M. K. Endoh, and T. Hashimoto, "Stress Overshoot of Entangled Polymers in Θ Solvent," *Macromolecules*, vol. 37, no. 11, pp. 4317–4320, 2004.

[58] S. Mani, M. F. Malone, and H. H. Winter, "Shear-induced demixing in a polystyrene/poly (vinyl methyl ether) blend: In-situ fluorescence and rheometry," *Macromolecules*, vol. 25, no. 21, pp. 5671–5676, 1992.

[59] R. G. Larson, "Flow-induced mixing, demixing, and phase transitions in polymeric fluids," *Rheologica Acta*, vol. 31, no. 6, pp. 497–520, 1992.

[60] J. Magda, C. Lee, S. J. Muller, and R. Larson, "Rheology, flow instabilities, and shear-induced diffusion in polystyrene solutions," *Macromolecules*, vol. 26, no. 7, pp. 1696–1706, 1993.

[61] J. F. Le Meins and J. F. Tassin, "Shear-induced phase separation in an associating polymer solution," *Macromolecules*, vol. 34, no. 8, pp. 2641–2647, 2001.

[62] P. Boltenhagen, Y. Hu, E. F. Matthys, and D. J. Pine, "Observation of bulk phase separation and coexistence in a sheared micellar solution," *Physical Review Letters*, vol. 79, no. 12, pp. 2359–2362, 1997.

[63] B. A. Schubert, N. J. Wagner, E. W. Kaler, and S. R. Raghavan, "Shear-induced phase separation in solutions of wormlike micelles," *Langmuir*, vol. 20, no. 9, pp. 3564–3573, 2004.

[64] P. Thareja, I. H. Hoffmann, M. W. Liberatore, M. E. Helgeson, Y. T. Hu, M. Gradzielski, and N. J. Wagner, "Shear-induced phase separation (SIPS) with shear banding in solutions of cationic surfactant and salt," *Journal of Rheology*, vol. 55, no. 2011, p. 1375, 2011.

[65] B. Belzung, F. Lequeux, J. Vermant, and J. Mewis, "Flow-induced anisotropy in mixtures of associative polymers and latex particles," *Journal of Colloid and Interface Science*, vol. 224, no. 1, pp. 179–187, 2000.

[66] M. W. Liberatore, N. B. Wyatt, M. Henry, P. L. Dubin, and E. Foun, "Shear-induced phase separation in polyelectrolyte/mixed micelle coacervates," *Langmuir*, vol. 25, no. 23, pp. 13376–13383, 2009.

Chapter 5

Non-local flow-concentration coupling in entangled polybutadiene solutions[1]

5.1 Abstract

Recent models have predicted entangled polymer solutions could shear band due to unstable flow-induced demixing. This work provides the first experimental probe of the *in situ* concentration profile of entangled polymer solutions under shear. At shear rates above a critical value, we show that the concentration and velocity profiles can develop bands, in quantitative agreement with steady-state model predictions. These findings highlight the critical importance of flow-concentration coupling in entangled polymer solutions.

[1]The contents of this Chapter are reprinted with permission from Burroughs, Zhang, Shetty, Bates, Leal, and Helgeson *Physical Review Letters*, **126**, 207901, 2021. Copyright 2021 by the American Physical Society.

5.2 Introduction

Traditionally, it is assumed that the flow of entangled polymeric fluids in shear-based rheometric devices is homogeneous across the polymeric fluid [1, 2]; however, important departures from homogeneous flow can sometimes occur [3]. For example, the flow can become shear banded with two or more regions of locally distinct shear rates under an applied shear flow [4, 5]. Such nonhomogeneous flows have been observed in numerous complex fluids including wormlike micelles [6–11], telechelic polymers [12], and soft colloidal glasses [13, 14], but the existence of shear banded flows in entangled polymer solutions has remained elusive [15–20] and has sparked immense controversy in recent years [21–24]. If entangled polymeric liquids do indeed shear band, then prior interpretations of the nonlinear flow behavior, and models for entangled polymer rheology more generally, will need to be reconsidered to account for the large spatial inhomogeneities present in the flow.

Commonly, shear banding has been explained as the result of a constitutive instability [5, 25], where an underlying nonmonotonic dependence of shear stress on the shear rate leads to a range of applied shear rates where uniform shear flow is unstable. With reference to entangled polymers, decades of experimental measurements [26–28] and resulting modifications to constitutive models [29–33] have led most to believe that the constitutive relationship is monotonic, seeming to preclude the possibility of shear banding for compositionally homogeneous polymeric liquids. Despite this perceived consensus, evidence of shear banded velocity profiles in entangled polymer solutions has been reported [15–18, 26, 34, 35]. Recently, conflicting conclusions regarding the existence of shear banding in entangled polymers were reported [15, 23], as determined from particle tracking velocimetry (PTV) measurements, even though the levels of entanglement per

molecule (Z) and dimensionless applied shear rates

$$Wi_{app} = \tau_d \, \dot{\gamma}, \tag{5.1}$$

were held fixed. Here, τ_d represents the longest relaxation time and $\dot{\gamma}$ is the nominal shear rate. A notable distinction in these two studies is the different polymer-solvent system used; however, the possible role of solution thermodynamics on the resulting flow was not addressed. Instead, inconsistencies in the measured flow profiles were argued to arise from several artifacts including edge fracture [21, 36], secondary flows [21] , unsteady flow [16], and even issues with how data were analyzed [24]. Clearly, the existence of shear banding in entangled polymer solutions remains an unresolved issue, and to reach consensus there is a strong need to support any experimental results with a fundamental theoretical description of the underlying physics.

Constitutive instability is not the only possible explanation for why steady shear banded flows might develop. Models that incorporate an explicit coupling between the polymer concentration and the stress, so called two-fluid models, predict regions of parameter space where a homogeneous, linear shear flow is unstable to infinitesimal perturbations in polymer concentration [37–43]. This instability is predicted to result in a shear-induced demixing of polymer and solvent to form gradients in polymer concentration on macroscopic length scales[2], which coincide with banded velocity profiles, even with monotonic constitutive behavior [37–39]. The propensity for shear-induced demixing in entangled polymer solutions is shown by the theory to depend on the flow-concentration coupling parameter, E,

$$E = \frac{G(\phi)}{\chi^{-1} \, \phi^2} \tag{5.2}$$

[2]By "macroscopic length scales" we refer to length scales comparable to the flow domain (*i.e.*, in shear flow, comparable to the gap width between the bounding surfaces).

with $G(\phi)$ being the concentration-dependent shear modulus, χ^{-1} the osmotic susceptibility, and ϕ the polymer concentration [37–39]. Thus, the polymer-solvent system specific value of E provides one possible explanation for why banding is observed in some solutions but not others (despite Z and Wi_{app}).

In the two-fluid model, polymer migration arises naturally *via* an imbalance between the elastic, osmotic, and drag forces acting on the polymers. This migration can amplify thermal fluctuations in concentration, known as shear-enhanced concentration fluctuations (SECF), and also lead to macroscopically inhomogeneous flow starting from a shear-induced demixing instability at higher shear rates. The microscale nonuniformities in polymer concentration due to SECF [44, 45] have been confirmed by indirect measurements, such as *in situ* small angle scattering, in entangled polymer solutions under shear [44, 46–49]. However, no prior experiments have demonstrated that gradients in concentration indeed form on macroscopic length scales in entangled polymer solutions.

In this Chapter, we report measurements of both the velocity and concentration profiles in entangled polybutadiene (PBD) in dioctyl phthalate (DOP) solutions under a range of applied shear rates. The data demonstrate that the predicted shear-induced demixing instability does occur in entangled polymer solutions, and results in gradients of both concentration and shear rate on macroscopic length scales. The concentration measurements rely on a novel rheofluorescence methodology to visualize and estimate macroscopic changes in polymer concentration (Figure 5.1).

5.3 Materials and Methods

Entangled polymer solutions with $Z = 38$ (10 wt%) were prepared by dissolving low-dispersity 1,4-polybutadiene (PBD(1M), $M_w = 9.6 \times 10^5$ g/mol, $Đ = 1.08$, Polymer Standards Services) in dioctyl phthalate (DOP, Sigma-Aldrich). All measurements were

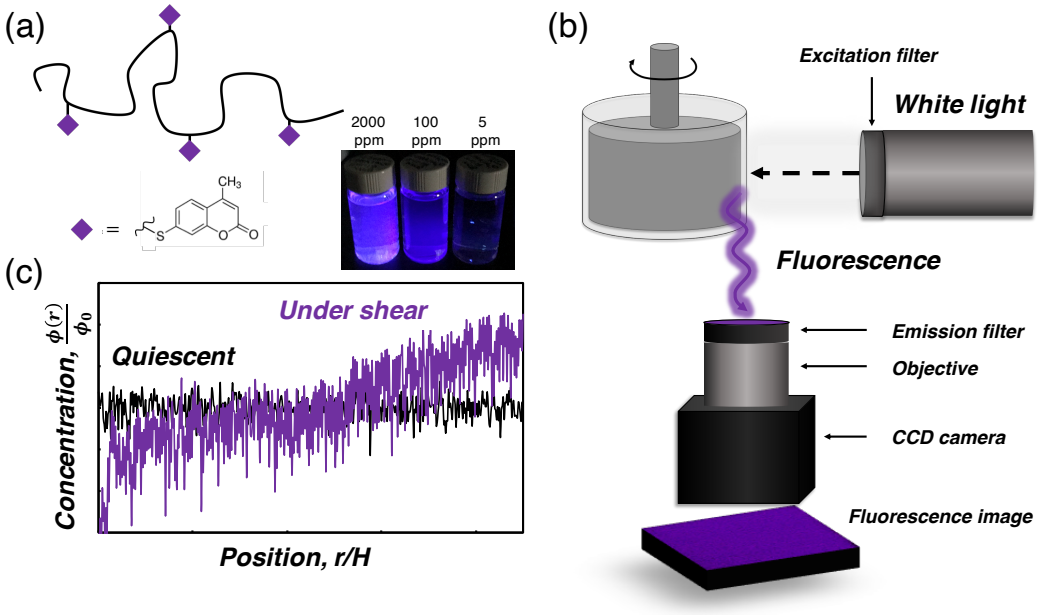

Figure 5.1: (a) Cartoon of PBD tagged with coumarin fluorophore (PBDC) and the resulting fluorescence across a concentration series of PBDC (vials), (b) rheofluorescence setup with 350 nm incident light and emission wavelengths filtered to 415 nm, (c) representative data for quiescent fluorescence versus fluorescence measured under shear.

performed at $T = 50$ ℃. For this temperature, we approximate the PBD-DOP solution to exhibit behavior intermediate to theta and good solvent conditions. Approximately 10 μm glass tracer particles (TSI, Inc.) were suspended in the entangled solution (300 ppm) for rheo-PTV measurements. 2000 ppm of fluorescently-tagged PBD (PBDC) was added to the solution for rheofluorescence measurements.

Velocity profiles were measured by rheo-PTV using a custom optical setup fitted to a Paar Physica MCR 300 rheometer [50–52]. One important feature for this study is the startup mode, which goes from rest to steady rotation in 0.05 s. The diameter of the inner cylinder is 34 mm and the curvature ratio is 0.029. The aspect ratio is 2.125. Steady-state velocity profiles were determined by averaging the velocity profiles determined from individual image pairs over time after the measured shear stress reached a steady value.

Concentration profiles were determined using a new combined rheometry and *in situ* fluorescence imaging technique ("rheofluorescence") using an Anton Paar MCR 702 rheometer. The transparent Taylor-Couette cup and anodized aluminum bob were identical to those used in rheo-PTV measurements [50–52], however, the Anton Paar MCR 702 shear startup process takes 1 s. The fluorescence intensity of the PBD-DOP solution with trace PBDC was monitored during shear flow at different Wi_{app} ($\tau_d = 1.9$ s). A Xenon light source (ASB-XE-175, 250 W, Spectral Products) was filtered to the excitation wavelength of the fluorophore (350 nm) to irradiate the entangled polymer solution with trace PBDC. The fluorescence emission signal passes through a 415 nm bandpass filter before reaching the CCD detector. Relative changes in the local polymer concentration from the initial uniform state were determined by monitoring changes in the intensity of the fluorescence image relative to the background and normalized by the quiescent image given by

$$\frac{\phi(r,t,\dot{\gamma})}{\phi_0} \approx \frac{I(r,t,\dot{\gamma}) - I_{bg}}{I_0 - I_{bg}}. \tag{5.3}$$

Here $\phi(r)/\phi_0$ is the normalized polymer concentration, $I(r,t,\dot{\gamma})$ is the transient fluorescence intensity at a particular applied shear rate, I_{bg} is the background intensity without illumination, and I_o is the fluorescence intensity at rest.

5.4 Results and Discussion

An example of the measured steady state velocity profiles of the entangled PBD(1M)-DOP solution is shown in Figure 5.2, together with two-fluid (Rolie-Poly, R-P) model [38] predictions for several values of E. The velocity profiles were collected after shearing for at least $50\tau_d$ and averaged over time using greater than 2000 data points. The small associated standard errors suggest that these data reflect the steady-state flow profiles. Although this timescale to steady state is significantly shorter than one might expect from either the stability analysis or previous numerical simulations fo the two-fluid model in a linear shear flow [38], this is not surprising. First, while the previous analyses began from the homogeneous solution with uniform concentration, the experiments are implemented via an abrupt startup from rest as noted above. Second, the intrinsic curvature of the Couette device will also shorten the timescale [39]. Last, the magnitude of perturbations in concentration for experiments are likely larger than what was previously investigated theoretically.

The profile in Figure 5.2 exhibits variations in the local shear rate that are much greater than would occur in a homogeneous fluid due to the combination of shear thinning and the intrinsic curvature of the Taylor-Couette flow cell. Furthermore, as shown in Figure 5.2, the homogeneous R-P model predictions ($E = 0$) also underpredict the measured variations in the local shear rate despite again accounting for the curvature of the Taylor-Couette flow cell and the shear thinning of the fluid.

In contrast, the two-fluid R-P model [39] provides an excellent fit of the data for

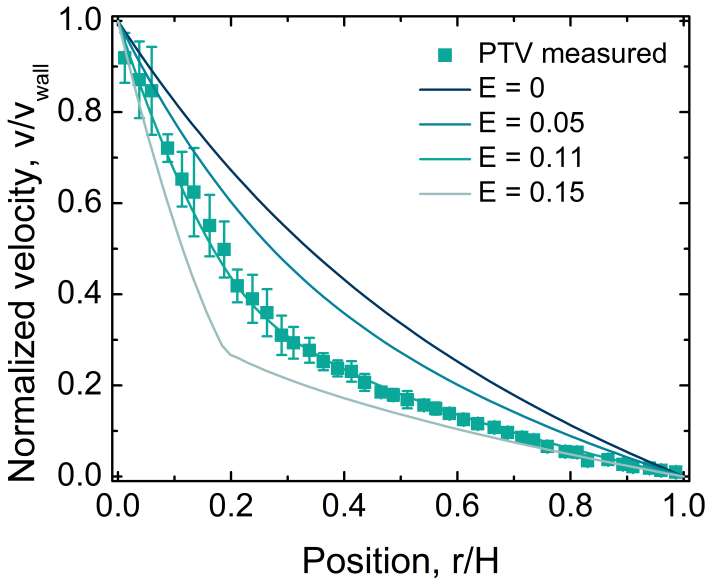

Figure 5.2: Steady state velocity profile of 10 wt% PBd(1M)-DOP with $Z = 38$ at $Wi_{app} = 5$ with model fits for varying E. The position (r/H) is determined by normalizing the radial distance from the moving wall (r) by the fluid thickness (H).

$E = 0.11$ (Figure 5.2). $E = 0.11$ is a reasonable value for theta solutions where E is estimated to be $O(0.1)$ [53]. Although the velocity profile does not appear sharply banded, it is in fact a shear banded profile as shall be discussed shortly. We note that the theory predicts more sharply banded profiles than exhibited in Figure 5.2 for entangled polymer systems with higher Z and larger values of E [37–39].

The value of E is intrinsic to the polymer-solvent system, since $G(\phi)$ depends on the number of Kuhn monomers in an entanglement strand (N_e) and χ^{-1} is sensitive to the solvent quality. Thus, the value of $E = 0.11$, obtained by fitting data for one value of Wi_{app}, yields remarkable agreement between model predictions of the flow profiles and the measured velocimetry data across a wide range of Wi_{app} (Figure 5.3).

In spite of the fact that the velocity profiles show much more curvature than would be the case from the combination of the flow geometry-imposed curvature and shear

thinning in a homogeneous fluid, one may still question whether the velocity profiles in Figure 5.3 are truly "banded." To address this point, a previously proposed model-free experimental procedure for calculating the interface width between "bands" [51] of the velocity profiles is employed. It was shown in [51] that the width of the interface remains invariant to changes in the applied shear rate, for shear banded velocity profiles. This property is confirmed in Figure 5.3(c), providing strong evidence that the flow profiles are indeed shear banded. A more detailed investigation of this and related findings is left to ongoing investigations, including the sensitivity of the apparent interface width to changes in fluid properties (such as E and Z).

Turning now to the rheofluorescence measurements during shear, we show transient concentration profiles in Figure 5.4 for $Wi_{app} = 2.7$ and 5. For $Wi_{app} = 5$, significant nonuniformities develop over time, consistent with flow-concentration coupling. After shearing for $t/\tau_d = 95.2$, the concentration is depleted near the moving wall ($r/H = 0.0$) and enriched near the stationary wall ($r/H = 1.0$). The direction of this change in concentration across the fluid qualitatively agrees with the expectation that polymer migration occurs across curved streamlines in which the polymer moves to regions of lower shear stress [39, 54, 55]. A similar evolution of the concentration profiles occurs for all other cases considered $Wi_{app} = 3.25, 6$, and 8, with the exception of $Wi_{app} = 2.7$. For this case, the measured concentration profiles in Figure 5.4(a) do not show appreciable change over the duration of steady shearing, with the normalized concentration remaining around 1.00.

The resulting measured estimates of the longtime concentration profiles from rheofluorescence were found to agree quantitatively with the two-fluid model predictions for $E = 0.11$ without any adjustable parameters (Figure 5.5). As described earlier, this value of E was determined from best fits of the model predictions to the measured flow profiles using rheo-PTV, a totally independent measurement from rheofluorescence. An

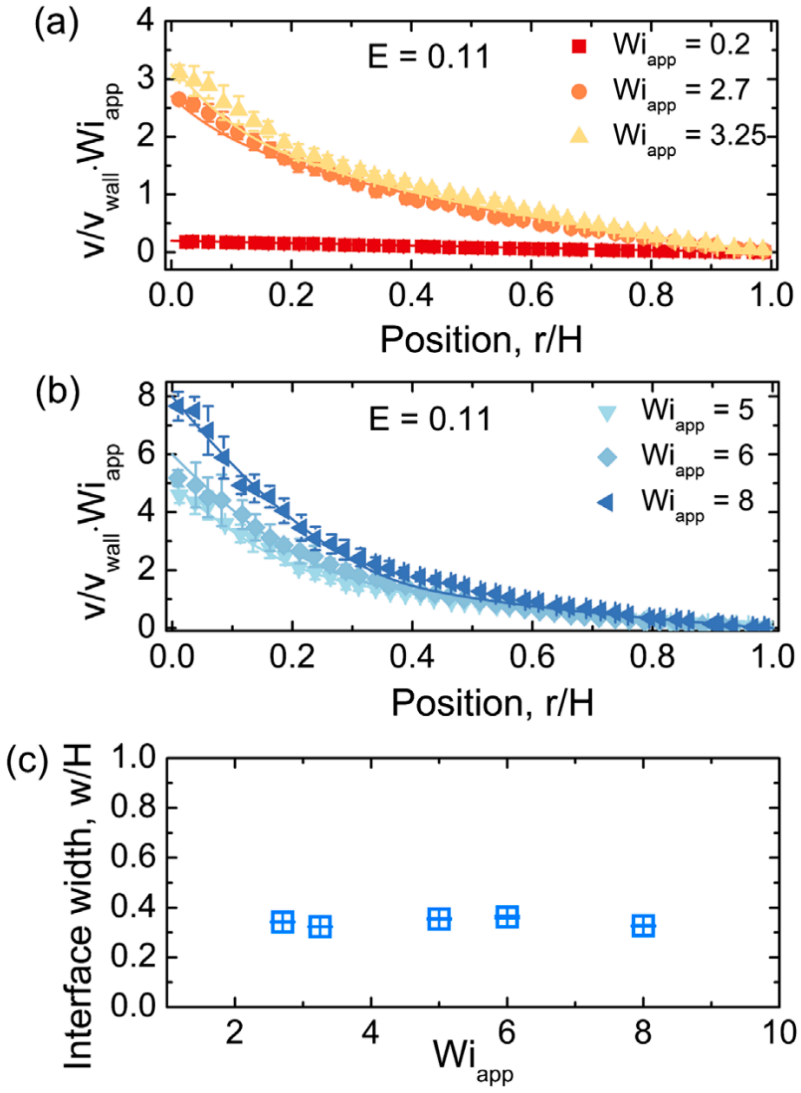

Figure 5.3: (a,b) Steady state velocity profiles for varying Wi_{app} at $T = 50$ °C. Symbols correspond to experimentally measured values from rheo-PTV and solid lines are two-fluid model predictions for $E = 0.11$. (c) Interface widths of the flow profiles calculated using the method detailed in Cheng et al. [51].

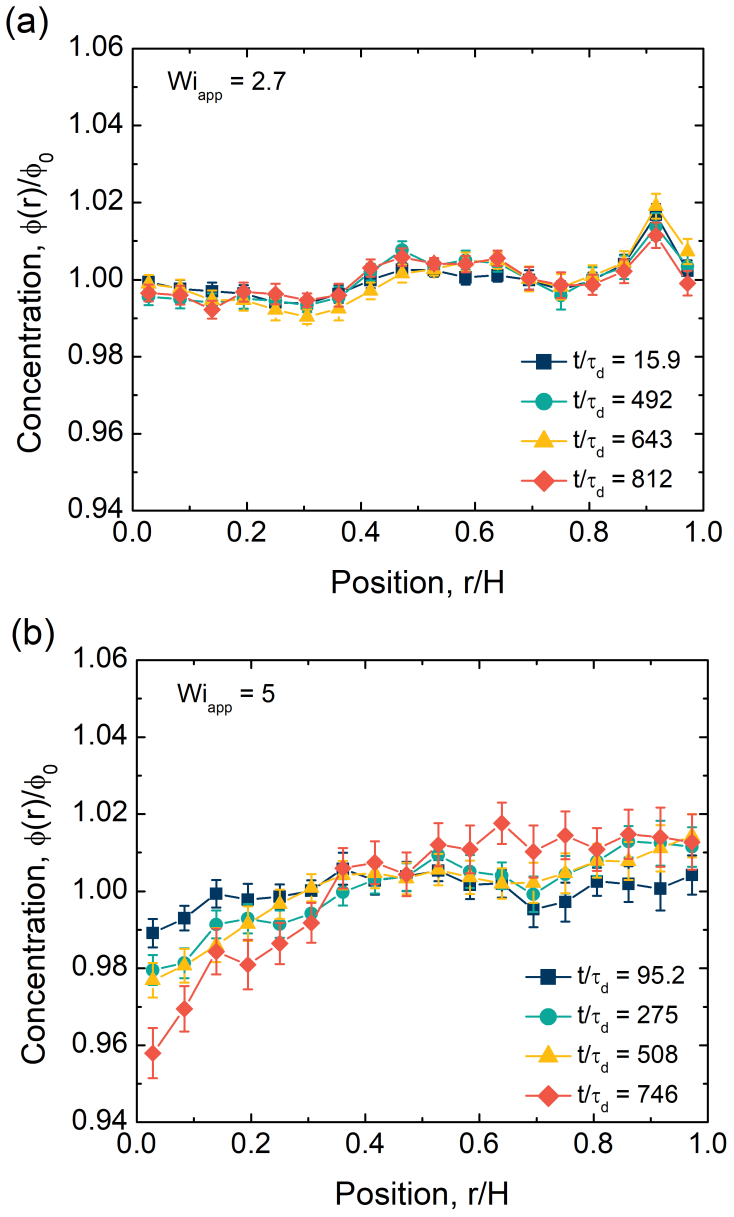

Figure 5.4: Transient evolution of the concentration profile as measured from rheo-fluorescence under an applied shear flow of (a) $Wi_{app} = 2.7$ and (b) $Wi_{app} = 5$. Error bars represent the standard error associated with the fluorescence pixel intensities within each bin.

upper bound on the timescale for changes in concentration across the fluid is therefore estimated to be 1250 s based on the Einstein-Smoluchowski relation $D = \frac{H^2}{2t}$ where H is the fluid thickness (500 μm). Based on the scaling relation $D \sim M^{-2}$, where M is the polymer molecular weight, the polymer diffusivity is estimated to be $O(10^{-10}\,\mathrm{m}^2/\mathrm{s})$. Thus, it is believed the fluorescence profiles reported in Figure 5.5, which were taken at least 1400 s after the start of shear flow, represent the longtime concentration dynamics. These changes in the measured concentration profile are found to occur over longer time scales than what is required for the velocity profile to reach an apparent steady state. We believe the velocity profile banding initiates on short time scales following shear startup in the absence of changes to the concentration profile as discussed in detail by Adams *et al.* [56, 57]. The two-fluid theory shows that the velocity profile evolves as a consequence of the changes in the concentration profile when the flow and fluid are initially homogeneous, but it is not clear in the current experiments whether the concentration nonuniformity drives the changes in the velocity profile or vice versa. Regardless of the transient evolution, with the exception of the case $Wi_{app} = 2.7$, both the magnitude of concentration change across the fluid and the interface location at steady state agree with the model predictions.

The measured concentration profile at $Wi_{app} = 2.7$ suggests that the fluid concentration profile remains uniform under shear, though both the theory and the measured velocity profile predict it should change. This apparent discrepancy likely results from the proximity of $Wi_{app} = 2.7$ to the stability boundary, where the two-fluid model predicts coexistence of both a banded and a nonbanded solution depending on the startup protocol [38]. The velocity and concentration profiles were obtained in two separate experiments with significantly different startup protocols as noted in the description of the flow devices. We speculate that the milder startup protocol in the concentration measurements compared to the velocity measurements bypasses instability [38]. The difference in

startup protocol is not expected to change the final steady state profiles for Wi_{app} values away from the stability boundary, consistent with our results at higher Wi_{app}.

Nevertheless, at higher Wi_{app}, the agreement in experimental flow and concentration measurements with the two-fluid prections is strong support for steady profiles involving a shear-induced demixing of polymer and solvent. The only other noticeable difference between the model and the measured concentration is the two data points nearest the inner wall for $Wi_{app} = 8$. We are uncertain why this discrepancy arises, but suspect that it could arise from uncertainty in the measurement near the boundary due to the continuously moving inner wall during the time period in which fluorescence is measured; however, we do not believe that it significantly alters the basic conclusion that quantitative agreement between experiment and model predictions is remarkable considering that the particular value of E used was determined completely independently from the rheofluorescence measurements.

5.5 Conclusions

This study reveals new physics regarding a mechanism for the development of shear banded velocity profiles in entangled polymers. The rheofluorescence measurements confirm that nonhomogeneous velocity profiles appear concomitant with nonlocal flow-concentration coupling, a notion that, until now, was based on purely theoretical grounds. Additionally, these results present the first experimental evidence for banding in entangled polymer solutions that is corroborated by spatially resolved theoretical predictions. Transient emergence of macroscopic concentration nonuniformity is found to occur at high Wi_{app} and leads to banded concentration profiles that coincide with banded velocity profiles. Strong agreement between the measured velocimetry and concentration profile data with two-fluid model predictions for nonzero values of E suggests an importance of the

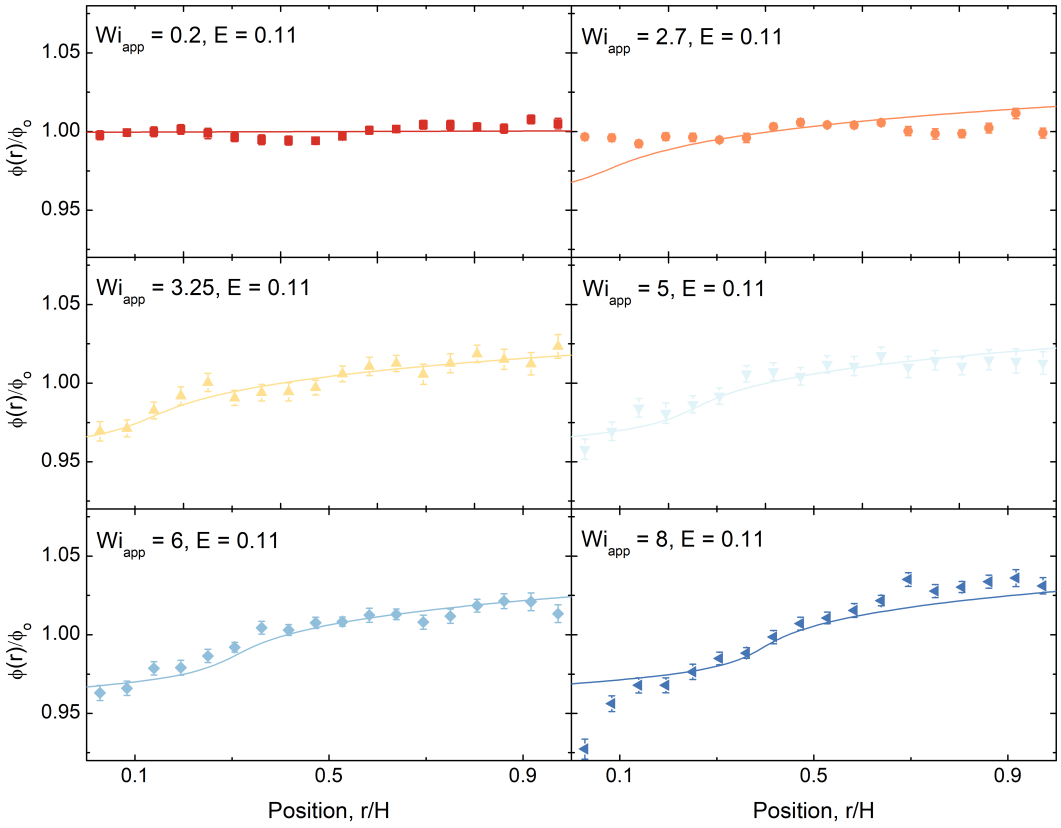

Figure 5.5: Steady state concentration profiles at varying Wi_{app}. Symbols reflect experimentally measured concentration estimates from rheo-fluorescence and solid lines correspond to model predictions for $E = 0.11$. Error bars represent the standard error associated with the fluorescence pixel intensities within each bin.

constituent polymer chemistry on the observed flow behavior, beyond what is intrinsic to the rheological parameters. To investigate this hypothesis, a systematic study of varying polymer chemistry and/or solvent quality to understand the impact of these variables on the resulting value of E is needed. Differences in E between different polymer systems could explain the longstanding disagreement in the measured flow behavior of entangled polymer-solvent systems that differ in underlying chemical composition.

We suspect that the observations made here will catalyze a number of new investigations into the coupling of changes in concentration to the microstructure and bulk flow behavior of entangled polymer systems. The physics of shear-induced demixing in polymer solutions is also relevant to entangled polymer blends, where essentially the same theory predicts that a force imbalance due to chains of different molecular weights leads to spatial nonuniformities in the molecular weight distribution, which could have similar consequences on the flow [58]. We further anticipate that this evidence for flow-concentration coupling will inspire *in situ* concentration measurements to become more commonplace in the complex fluids community, where modifications to this rheofluorescence technique can be made to isolate the dynamics of the different components within the fluid. Finally, and perhaps the most important outcome of this study, is that it suggests that theoretical studies of the non-Newtonian flow behavior of polymer solutions must account for the possibility of changes in the flow due to coupling between the polymer concentration and the stress.

Bibliography

[1] M. Doi and S. F. Edwards, "Dynamics of Concentrated Polymer Systems: Part III - The Constitutive Equation," *Journal of the Chemical Society, Faraday Transactions 2: Molecular and Chemical Physics*, vol. 74, pp. 1818–1832, 1978.

[2] M. Doi and S. F. Edwards, "Dynamics of Concentrated Polymer Systems: Part II - Molecular Motion under Flow," *Journal of the Chemical Society, Faraday Transactions 2: Molecular and Chemical Physics*, vol. 74, pp. 1802–1817, 1978.

[3] G. Marrucci and N. Grizzuti, "The Free Energy Function of the Doi-Edwards Theory : Analysis of the Instabilities in Stress Relaxation," *Journal of Rheology*, vol. 27, no. 1983, p. 433, 1983.

[4] P. D. Olmsted, "Perspectives on shear banding in complex fluids," *Rheologica Acta*, vol. 47, no. 3, pp. 283–300, 2008.

[5] T. Divoux, M. A. Fardin, S. Manneville, and S. Lerouge, "Shear Banding of Complex Fluids," *Annual Review of Fluid Mechanics*, vol. 48, no. 1, pp. 81–103, 2016.

[6] J.-B. Salmon, A. Colin, S. Manneville, and F. Molino, "Velocity profiles in shear-banding wormlike micelles.," *Physical review letters*, vol. 90, no. June, p. 228303, 2003.

[7] M. R. López-González, W. M. Holmes, P. T. Callaghan, and P. J. Photinos, "Shear banding fluctuations and nematic order in wormlike micelles," *Physical Review Letters*, vol. 93, no. 26, p. 268302, 2004.

[8] M. W. Liberatore, F. Nettesheim, N. J. Wagner, and L. Porcar, "Spatially resolved small-angle neutron scattering in the 1-2 plane: A study of shear-induced phase-separating wormlike micelles," *Physical Review E - Statistical, Nonlinear, and Soft Matter Physics*, vol. 73, no. 2, p. 020504, 2006.

[9] M. R. Lopez-Gonzalez, W. M. Holmes, and P. T. Callaghan, "Rheo-NMR phenomena of wormlike micelles," *Soft Matter*, vol. 2, no. 10, pp. 855–869, 2006.

[10] M. E. Helgeson, P. A. Vasquez, E. W. Kaler, and N. J. Wagner, "Rheology and spatially resolved structure of cetyltrimethylammonium bromide wormlike micelles

through the shear banding transition," *Journal of Rheology*, vol. 53, no. 2009, p. 727, 2009.

[11] K. W. Feindel and P. T. Callaghan, "Anomalous shear banding: Multidimensional dynamics under fluctuating slip conditions," *Rheologica Acta*, vol. 49, no. 10, pp. 1003–1013, 2010.

[12] J. F. Berret and Y. Séréro, "Evidence of shear-induced fluid fracture in telechelic polymer networks," *Physical Review Letters*, vol. 87, no. 4, p. 048303, 2001.

[13] S. A. Rogers, D. Vlassopoulos, and P. T. Callaghan, "Aging, yielding, and shear banding in soft colloidal glasses," *Physical Review Letters*, vol. 100, no. 12, p. 128304, 2008.

[14] R. Besseling, L. Isa, P. Ballesta, G. Petekidis, M. E. Cates, and W. C. Poon, "Shear banding and flow-concentration coupling in colloidal glasses," *Physical Review Letters*, vol. 105, no. 26, p. 268301, 2010.

[15] S. Ravindranath, S.-Q. Wang, M. Olechnowicz, and R. P. Quirk, "Banding in simple steady shear of entangled polymer solutions," *Macromolecules*, vol. 41, no. 7, pp. 2663–2670, 2008.

[16] Y. T. Hu, "Steady-state shear banding in entangled polymers?," *Journal of Rheology*, vol. 54, no. 6, pp. 1307–1323, 2010.

[17] P. E. Boukany, S.-Q. Wang, S. Ravindranath, and L. J. Lee, "Shear banding in entangled polymers in the micron scale gap: a confocal-rheoscopic study," *Soft Matter*, vol. 11, pp. 8058–8068, 2015.

[18] S. Jaradat, M. Harvey, and T. A. Waigh, "Shear-banding in polyacrylamide solutions revealed via optical coherence tomography velocimetry," *Soft Matter*, vol. 8, no. 46, pp. 11677–11686, 2012.

[19] K. A. Hayes, M. R. Buckley, I. Cohen, and L. A. Archer, "High resolution shear profile measurements in entangled polymers," *Physical Review Letters*, vol. 101, no. 21, p. 218301, 2008.

[20] K. A. Hayes, M. R. Buckley, H. Qi, I. Cohen, and L. A. Archer, "Constitutive curve and velocity profile in entangled polymers during start-up of steady shear flow," *Macromolecules*, vol. 43, no. 9, pp. 4412–4417, 2010.

[21] Y. Li, M. Hu, G. B. McKenna, C. J. Dimitriou, G. H. McKinley, R. M. Mick, D. C. Venerus, and L. A. Archer, "Flow field visualization of entangled polybutadiene solutions under nonlinear viscoelastic flow conditions," *Journal of Rheology*, vol. 57, no. 5, pp. 1411–1428, 2013.

[22] S.-Q. Wang, G. Liu, S. Cheng, P. E. Boukany, Y. Wang, X. Li, Y. Li, M. Hu, G. B. McKenna, C. J. Dimitriou, G. H. McKinley, R. M. Mick, D. C. Venerus, and L. a. Archer, "Letter to the Editor: Sufficiently entangled polymers do show shear strain localization at high enough Weissenberg numbers"," *Journal of Rheology*, vol. 58, no. 4, pp. 1059–1069, 2014.

[23] Y. Li and G. B. McKenna, "Startup shear of a highly entangled polystyrene solution deep into the nonlinear viscoelastic regime," *Rheologica Acta*, vol. 54, no. 9-10, pp. 771–777, 2015.

[24] Y. Li, M. Hu, G. B. McKenna, C. J. Dimitriou, G. H. McKinley, R. M. Mick, D. C. Venerus, and L. A. Archer, "Response to: Sufficiently entangled polymers do show shear strain localization at high enough Weissenberg numbers"," *Journal of Rheology*, vol. 58, no. 4, pp. 1071–1082, 2014.

[25] S. Lerouge and P. D. Olmsted, "Non-local Effects in Shear Banding of Polymeric Flows," *Frontiers in Physics*, vol. 7, no. January, pp. 1–11, 2020.

[26] Y. T. Hu, L. Wilen, A. Philips, and A. Lips, "Is the constitutive relation for entangled polymers monotonic?," *Journal of Rheology*, vol. 51, no. 2, pp. 275–295, 2007.

[27] W. W. Graessley, "The entanglement concept in polymer rheology. In: The Entanglement Concept in Polymer Rheology," *Advances in Polymer Science*, vol. 16, pp. 1–179, 1974.

[28] E. Menezes and W. W. Graessley, "Nonlinear Rheological Behavior of Polymer Systems for Several Shear-Flow Histories," *Journal of Polymer Science, Part B: Polymer Physics*, vol. 20, pp. 1817–1833, 1982.

[29] D. W. Mead, R. G. Larson, and M. Doi, "A Molecular Theory for Fast Flows of Entangled Polymers," *Macromolecules*, vol. 31, no. 22, pp. 7895–7914, 1998.

[30] S. T. Milner, T. C. B. McLeish, and A. E. Likhtman, "Microscopic theory of convective constraint release," *Journal of Rheology*, vol. 45, no. 2, pp. 539–563, 2001.

[31] A. E. Likhtman and T. C. B. McLeish, "Quantitative theory for linear dynamics of linear entangled polymers," *Macromolecules*, vol. 35, no. 16, pp. 6332–6343, 2002.

[32] R. S. Graham, A. E. Likhtman, T. C. B. McLeish, and S. T. Milner, "Microscopic theory of linear, entangled polymer chains under rapid deformation including chain stretch and convective constraint release," *Journal of Rheology*, vol. 47, no. 5, p. 1171, 2003.

[33] A. E. Likhtman and R. S. Graham, "Simple constitutive equation for linear polymer melts derived from molecular theory: Rolie-Poly equation," *Journal of Non-Newtonian Fluid Mechanics*, vol. 114, no. 1, pp. 1–12, 2003.

[34] S.-Q. Wang, S. Ravindranath, and P. E. Boukany, "Homogeneous shear, wall slip, and shear banding of entangled polymeric liquids in simple-shear rheometry: A roadmap of nonlinear rheology," *Macromolecules*, vol. 44, no. 2, pp. 183–190, 2011.

[35] S. Shin, K. D. Dorfman, and X. Cheng, "Shear-banding and superdiffusivity in entangled polymer solutions," *Physical Review E*, vol. 96, no. 6, pp. 1–9, 2017.

[36] E. J. Hemingway and S. M. Fielding, "Edge-Induced Shear Banding in Entangled Polymeric Fluids," *Physical Review Letters*, vol. 120, no. 13, p. 138002, 2018.

[37] M. Cromer, M. C. Villet, G. H. Fredrickson, and L. G. Leal, "Shear banding in polymer solutions," *Physics of Fluids*, vol. 25, no. 5, p. 051703, 2013.

[38] M. Cromer, G. H. Fredrickson, and L. G. Leal, "A study of shear banding in polymer solutions," *Physics of Fluids*, vol. 26, no. 6, p. 063101, 2014.

[39] J. D. Peterson, M. Cromer, G. H. Fredrickson, and L. G. Leal, "Shear banding predictions for the two-fluid Rolie-Poly model," *Journal of Rheology*, vol. 60, no. 5, pp. 927–951, 2016.

[40] X. F. Yuan and L. Jupp, "Interplay of flow-induced phase separations and rheological behavior of complex fluids in shearbanding flow," *Europhysics Letters*, vol. 60, no. 5, pp. 691–697, 2002.

[41] S. M. Fielding and P. D. Olmsted, "Flow phase diagrams for concentration-coupled shear banding," *European Physical Journal E*, vol. 11, no. 1, pp. 65–83, 2003.

[42] S. M. Fielding and P. D. Olmsted, "Kinetics of the shear banding instability in startup flows.," *Physical Review E*, vol. 68, no. 3, p. 036313, 2003.

[43] S. M. Fielding and P. D. Olmsted, "Early stage kinetics in a unified model of shear-induced demixing and mechanical shear banding instabilities.," *Physical review letters*, vol. 90, no. 22, p. 224501, 2003.

[44] X. L. Wu, D. J. Pine, and P. K. Dixon, "Enhanced concentration fluctuations in polymer solutions under shear flow," *Physical Review Letters*, vol. 66, no. 18, pp. 2408–2411, 1991.

[45] E. Helfand and G. H. Fredrickson, "Large Fluctuations in Polymer Solution under Shear," *Physical Review Letters*, vol. 62, no. 21, pp. 2468–2471, 1989.

[46] P. K. Dixon, D. J. Pine, and X. L. Wu, "Mode selection in the dynamics of sheared polymer solutions," *Physical Review Letters*, vol. 68, no. 14, pp. 2239–2242, 1992.

[47] K. Migler, C. H. Liu, and D. J. Pine, "Structure evolution of a polymer solution at high shear rates," *Macromolecules*, vol. 29, no. 5, pp. 1422–1432, 1996.

[48] J. W. van Egmond, D. E. Werner, and G. G. Fuller, "Time-dependent small-angle light scattering of shear-induced concentration fluctuations in polymer solutions," *The Journal of Chemical Physics*, vol. 96, no. 10, p. 7742, 1992.

[49] T. Kume, T. Hashimoto, T. Takahashi, and G. G. Fuller, "Rheo-optical studies of shear-induced structures in semidilute polystyrene solutions," *Macromolecules*, vol. 30, no. 23, pp. 7232–7236, 1997.

[50] Y. T. Hu and A. Lips, "Kinetics and mechanism of shear banding in an entangled micellar solution," *Journal of Rheology*, vol. 49, no. 5, pp. 1001–1027, 2005.

[51] P. Cheng, M. C. Burroughs, L. G. Leal, and M. E. Helgeson, "Distinguishing shear banding from shear thinning in flows with a shear stress gradient," *Rheologica Acta*, vol. 56, no. 12, pp. 1007–1032, 2017.

[52] M. C. Burroughs, A. M. Shetty, L. G. Leal, and M. E. Helgeson, "Coupled nonhomogeneous flows and flow-enhanced concentration fluctuations during startup shear of entangled polymer solutions," *Physical Review Fluids*, vol. 5, no. 4, p. 043301, 2020.

[53] E. Raspaud, D. Lairez, and M. Adam, "On the Number of Blobs per Entanglement in Semidilute and Good Solvent Solution: Melt Influence," *Macromolecules*, vol. 28, no. 4, pp. 927–933, 1995.

[54] M. J. MacDonald and S. J. Muller, "Experimental study of shear-induced migration of polymers in dilute solutions," *Journal of Rheology*, vol. 40, no. 2, p. 259, 1996.

[55] K. A. Dill and B. H. Zimm, "A rhelogical separator for very large DNA molecules," *Nucleic Acids Research*, vol. 7, no. 3, pp. 735–749, 1979.

[56] J. M. Adams and P. D. Olmsted, "Nonmonotonic Models are Not Necessary to Obtain Shear Banding Phenomena in Entangled Polymer Solutions," *Physical Review Letters*, vol. 102, no. 6, p. 067801, 2009.

[57] J. M. Adams, S. M. Fielding, and P. D. Olmsted, "Transient shear banding in entangled polymers: A study using the Rolie-Poly model," *Journal of Rheology*, vol. 55, no. 5, p. 1007, 2011.

[58] J. D. Peterson, G. H. Fredrickson, and L. G. Leal, "Shear Induced Demixing in Bidisperse and Polydisperse Polymer Blends: Predictions From a Multi-Fluid Model," *Journal of Rheology*, vol. 64, no. 6, p. 1391, 2020.

Chapter 6

Sensitivity of flow-concentration coupling to fluid properties[1]

6.1 Abstract

Shear banding in entangled polymer solutions is an elusive phenomenon in polymer rheology. One theoretically proposed explanation for the existence of banded velocity profiles in entangled polymer solutions stems from a coupling of the flow to concentration. Recent work [Burroughs *et al. Phys. Rev. Lett.* (2021) [1]] provided experimental evidence for the development of large gradients in concentration across the fluid. Here, a systematic investigation is reported of the transient and steady state banded velocity profiles and the corresponding concentration profiles of entangled polybutadiene (PBD) in dioctyl phthalate (DOP) solutions as a function of temperature, number of entanglements (Z), and applied shear rate (Wi_{app}). The degree of flow-concentration coupling (E) in these entangled PBD-DOP solutions is determined from fitting two-fluid model

[1]The contents of this Chapter are in preparation to be submitted for publication in the form of a journal article.

predictions of the flow to the measured velocimetry data. The differences in bands of dissimilar shear rate and concentration, resulting from flow-concentration coupling, are sensitive to both the temperature and number of entanglements in solution. Strong agreement is found between the two-fluid model predictions and measured concentration profiles for varying temperature, Z, and Wi_{app}. The interface locations and widths of the time-averaged, steady state velocity profiles are quantified from high-order numerical derivatives of the data computed using a statistical algorithm. At high levels of entanglement and large Wi_{app}, significant wall slip is observed at both the inner and outer surfaces of the flow geometry but is not a necessary criterion for nonhomogeneous flow. Finally, the transient evolution of the flow profiles for large Z indicate transitions from curved to "stair-stepped" and finally a banded steady state. These observed transitions are qualitatively consistent with model predictions of shear-induced demixing.

6.2 Introduction

Rheological models can inform optimal processing conditions and identify the onset of flow instabilities in non-Newtonian fluids. Unstable flows are detrimental to the processing of uniform polymeric materials. Numerous complications are well-documented in flows of entangled polymers above a critical flow rate such as elastic turbulence, die-swell, and the so-called “sharkskin” instability [2]. Even flows in devices that produce a shear flow can be complicated. Some complex fluids, such as wormlike micelles, exhibit a shear banding instability, where the fluid separates into two, or more, regions of different shear rates under an applied shear flow [3]. Shear banding is often explained to result from a nonmonotonic relationship between the shear stress and shear rate [4]. The general belief is that entangled polymers exhibit monotonic constitutive behavior [5–11], and, as a result, the possibility of shear banding in entangled polymer solutions is hotly debated.

A nearly universal assumption in all experimental studies of flowing polymer solutions, in a wide spectrum of different flows, is that the polymer concentration remains homogeneous. However, it is well-known that shear flow can enhance local fluctuations in polymer concentration [12, 13]; recent work has suggested these fluctuations could lead to drastic modifications of the transient flow profile in startup of Taylor-Couette flow [14]. Further, two-fluid models with a monotonic constitutive equation for entangled polymers predict linearly unstable fluctuations in concentration that result in shear-induced demixing [15–17]. This instability leads to steady state, banded concentration profiles where each region of distinct concentration coincides with a locally distinct shear rate in the corresponding shear banded flow profile.

Over the last decade, conflicting results concerning shear banding in entangled polymer solutions have been reported [18–21]. Numerous studies have testified that shear banding occurs for highly entangled polybutadiene liquids, with the "degree of banding" being sensitive to the polymer molecular weight [22] and viscosity of the solvent [23, 24]. The shear banded velocity profiles were observed to occur in the presence of significant wall slip. A "phase diagram" was reported to describe the observed empirical interplay between wall slip and shear banding, and a mechanism for shear banding that originates from wall slip was discussed [25]. These results seemed to suggest that wall slip is a necessary condition for shear banding to occur in entangled polymer solutions. Conversely, several studies have refuted the interpretations of these findings, as they measured no significant departure from homogeneous flows for fluids with similar numbers of entanglements per chain and applied dimensionless shear rates in the absence of wall slip [21, 26]. As a result, it was concluded that the observations of shear banded velocity profiles in entangled polymers are likely a consequence of experimental complications such as boundary effects [18, 20, 21, 26, 27].

In most cases, the conclusions were limited by poor spatiotemporal resolution of the

data, affording great difficulty in distinguishing banded velocity profiles from curved velocity profiles that result from geometry-induced curvature. To address this ambiguity, a model-free statistical method was developed to distinguish between shear thinning and shear banding flow profiles by calculating numerical derivatives of dense, time-averaged velocimetry data [28]. Importantly, it was shown that the interface width of the flow profile in a shear banding fluid is independent of Wi_{app},

$$Wi_{app} = \tau_d \, \dot{\gamma} \tag{6.1}$$

where τ_d is the reptation time of the fluid and $\dot{\gamma}$ is the applied shear rate assuming homogeneous flow. In contrast, the interface width of a shear thinning fluid increases with Wi_{app}. Until recently [1], however, no attempt has been made to rationalize the experimental findings in support and/or against banding with direct comparison to model predictions.

Two-fluid model predictions of coupled, non-local concentration variations and shear banded velocity profiles [15–17, 29–31] offer a potential explanation for the disagreement between these conflicting reports [21, 32] of the flow profiles of entangled polymer solutions. The theory provides one possible mechanism for shear banding in entangled polymer solutions. However, macroscopic variations in concentration do not imply the existence of shear banded flow profiles. Shear-induced migration of high molecular weight polymers in dilute solutions occurs across curved streamlines, and leads to an approximately linear macroscopic concentration gradient across the fluid [33], which would suggest minimal changes to the resulting shear rate profile. Thus, in the context of shear banding in entangled polymer solutions, it is crucial to complement concentration profile measurements with corresponding velocimetry data.

According to the two-fluid model, the magnitude of concentration variation is depen-

dent upon, amongst several other parameters, the ratio of the elastic stresses to osmotic stresses, E, where

$$E = \frac{G(\phi)}{\chi^{-1}\,\phi^2} \tag{6.2}$$

with $G(\phi)$ being the shear modulus, χ^{-1} the osmotic susceptibility, and ϕ the polymer concentration [15–17]. This ratio, and the physics it represents, has been overlooked in considering the apparent inconsistencies of the results in the experiments in support and denial of shear banding in entangled polymers. Differences in E are expected for polymeric liquids of differing chemical composition, since χ^{-1} is a chemistry dependent parameter, and thus, could be an explanation for why banding is observed in some solutions and not others despite subjecting fluids of similar levels of entanglement to the same range of dimensionless shear rates [21, 32].

Until very recently, the suggestion that flow-induced concentration nonuniformities might be a possible source of shear banded velocity profiles was just a theoretical prediction. A first step toward experimental verification was reported in a recent paper [1]. Specifically, using a new fluorescence imaging technique, the first experimental evidence was reported for steady state, macroscopic concentration nonuniformities in a narrow gap Taylor-Couette flow cell for a 10 wt% solution of 1,4-polybutadiene ($M_w = 9.6 \times 10^5$ g/mol, $Đ$= 1.08) in dioctyl phthalate (corresponding to $Z = 38$ entanglements per chain). These nonuniformities were far larger than what could be caused by the combination of shear thinning and the intrinsic curvature of the Taylor-Couette flow velocity profile, thus confirming the existence of a demixing instability, and directly challenging the long-held notion that polymer concentration remains macroscopically uniform in flow [1]. The nonuniformities of the steady state concentration profiles were accompanied by corresponding changes in the steady state velocity profiles. Furthermore, after obtaining a value of E by fitting the predicted velocity profiles of the two-fluid model to the mea-

sured data, the measured concentration profiles were in good agreement with the resulting predictions of the two-fluid model [1, 15–17].

Under the limited conditions of these initial experiments, however, the velocity profiles were not obviously banded by visual inspection; the profiles were proven to be shear banded by application of the previously developed statistical method [28], which showed that the width of the interface between the banded velocity profiles was independent of the applied shear rate. Given the single value of T and Z studied, it is unclear whether the flow profiles of entangled polymer solutions are sensitive to changes in these molecular properties, as predicted by the theory. Another outstanding question concerns the transient development of the measured flow profiles, which appeared to reach a steady state long before the measured concentration profiles. Lastly, no wall slip was observed at steady state under the previous set of experimental conditions, despite significant nonuniformity in the flow; thus, a more detailed investigation is necessary to elucidate the interplay between flow nonuniformity and wall slip.

The present paper expands considerably on the results from this initial publication [1]. In particular, the initial work [1] only explored flow-concentration coupling for a single set of experimental conditions; thus, a detailed study of flow-concentration coupling that examines variations in molecular properties (*i.e.*, solvent quality and number of entanglements) of the solutions is needed to ascertain whether such details influence the extracted value of E, the "degree of banding", and changes in fluid composition. An observed sensitivity of these molecular properties to the resulting flows could, for example, resolve discrepancies in the flows observed in polymer solutions of different constituent chemistry [1, 14, 21, 32].

In this work, we again use entangled polybutadiene (PBD) in dioctyl phthalate (DOP) solutions as a model system, and we utilize the same experimental procedures that were described in the previous paper [1]. The propensity for entangled polymer solutions to ex-

hibit nonhomogeneous flows is explored through systematic variations of E (by changing temperature (T)), the number of entanglements per chain (Z), and the applied dimensionless shear rate (Wi_{app}). The results confirm that the magnitude of nonuniformity in flow is sensitive to the solvent quality of the PBD-DOP solutions as well as the number of entanglements. A higher Z results in greater nonuniformity of the steady state flow, consistent with two-fluid model predictions. Temperature (and the corresponding change to solvent quality) is also found to influence flow nonuniformity, albeit in a nonmonotonic way. Steady state concentration profile data are compared to the concentration predictions of the two-fluid model. Additionally, we investigate the influence of wall slip on the resulting flows to understand whether wall slip is necessary for nonhomogeneous flow. The magnitude of wall slip at the inner and outer walls is compared between the fluids with different Z for varying Wi_{app}, and it is found that wall slip, while significant under some flow conditions, is not necessary for the existence of nonhomogeneous, shear banded flows. To address past ambiguity in analysis of shear banded profiles with sparse spatiotemporal data, numerical derivatives of the measured flow profiles are quantified using a previously reported statistical method [28] and are used to identify the interface locations and widths of each velocity profile. The numerical derivatives suggest that there is a critical value of E above which shear banded flows develop, in agreement with the previous linear stability of the two-fluid model. Finally, transient changes to the velocity profiles of PBD-DOP solutions in shear flow provide details about the development of steady state nonhomogeneous flows and the role of wall slip in governing the bulk flow. The evolution of velocity profiles from shear startup to steady state flow are consistent with the two-fluid model predictions. Namely, initial deviations from uniform flow are due to the viscoelasticity of the fluid upon startup shear, followed by the onset of concentration heterogeneity which leads to a "stair-stepped" velocity profile, and finally a coarsening to a steady state banded velocity profile.

6.3 Materials and methods

6.3.1 Materials

1,4-trans-polybutadiene with $M_w = 9.82 \times 10^5$ g/mol (PBD(1M), $Đ$= 1.08) was purchased from Polymer Standards Service. 1,4-trans-polybutadiene with $M_w = 4.0 \times 10^6$ g/mol (PBD(4M), $Đ$ = unknown) was generously donated by Prof. Shi-Qing Wang (University of Akron). Dioctyl phthalate (DOP, CAS:117-81-7, $\geq$ 99.5% purity), anhydrous tetrahydrofuran (THF, CAS: 109-99-9, $\geq$ 99.9 %), 7-methyl-3-mercapto-coumarin (CAS: 137215-27-1, $\geq$ 97.0 % purity), and 2,2-dimethoxy-2-phenylacetophenone (DMPA, CAS: 24650-42-8, 99 % purity) were purchased from Sigma-Aldrich and used without further purification. Glass tracer particles ($\approx 10\mu$m in diameter) were donated by TSI, Inc.

6.3.2 Synthesis of fluorescently-labeled PBD

Synthesis details for the fluorescent-tagging reaction of PBD-coumarin (PBDC) were described in detail elsewhere [1]. Briefly, 7-methyl-3-mercapto-coumarin was reacted with PBD in anhydrous THF under 365 nm UV light with DMPA functioning as the reaction initiator. Success of the reaction was confirmed with wavelength specific GPC data included in Chapter 2.

6.3.3 Sample preparation

Entangled PBD-DOP solutions were prepared by adding DOP to PBD solids to prepare a $\approx$ 10 g sample. The number of entanglements (Z) in each solution was estimated by the relation

$$Z = \frac{M_w}{M_e}\phi^{1.2} \tag{6.3}$$

where M_w is the weight-averaged molecular weight of the polymer, M_e is the entanglement molecular weight (1650 g/mol for PBD), and ϕ is the concentration of polymer in solution. In all samples, 0.2 wt % butylated hydroxytoluene (BHT) was added as an antioxidant. For rheo-PTV experiments, 300-500 ppm of glass tracer particles were added to the PBD and DOP. For rheo-fluorescence experiments, 0.2 wt % of PBDC, synthesized using the same molecular weight of PBD as the rest of the sample, was added to the PBD and DOP. PBD-DOP mixtures were diluted with $\sim$ 30 mL of toluene to serve as a cosolvent. Samples were placed in an oil bath at $T = 50$ ℃ and gently stirred for several days until they were visually homogeneous. Next, samples were uncapped and left in an oil bath under gentle stirring in the hood to evaporate off the toluene. Once the samples became too viscous for a magnetic stir bar, the samples were placed in a vacuum oven to remove the residual toluene. To prepare the PBD-DOP solution with $Z = 38$, the required amount of DOP was added to PBD(1M) to yield a 10 wt % PBD(1M) in DOP sample. Likewise, to prepare the PBD-DOP solution with $Z = 66$, DOP was added to PBD(4M) to achieve a 5 wt % PBD(4M) in DOP sample.

6.3.4 Rheo-particle tracking velocimetry

All rheo-PTV measurements were performed on a Paar Physica MCR 300 rheometer. Specifics of this custom setup are described in detail elsewhere [14, 28, 34]. All measurements were performed using a Taylor-Couette flow cell with a gap of 500 μm, a rotating inner cylinder of radius 17 mm, and a stationary outer cylinder of radius 17.5 mm. The small gap reduces the stress gradient imposed by the geometry, which decreases the curvature of the velocity profile for fluids with shear thinning rheology. A transparent outer cup and anodized aluminum bob permitted flow visualization measurements to be conducted simultaneously with steady shearing. Glass tracer particles were added to the

entangled PBD-DOP solutions and the particle trajectories were tracked between image pairs using a widely-known image analysis algorithm [35].

6.3.5 Rheo-fluorescence

All rheo-fluorescence measurements were performed on an Anton Paar MCR 702 rheometer. The PBD-DOP solutions with small amounts of PBDC were illuminated with 350 nm UV light under shear to excite the fluorophore, and changes in the fluorescence intensity were recorded with a CCD camera. Spatiotemporal changes in the fluorescence intensity were related to the local effective concentration of the solution by

$$\frac{\phi(r,\dot{\gamma},t)}{\phi_0(r)} \approx \frac{I(r,\dot{\gamma},t) - I_{bg}}{I_0(r) - I_{bg}} \tag{6.4}$$

where $I(r,\dot{\gamma},t)$ is the transient measured fluorescence intensity at a particular shear rate and location, $I_0(r)$ is the measured fluorescence intensity before shearing, and I_bg is the quiescent image intensity without illumination. Additional details of the rheo-fluorescence custom setup are described in further detail in a previous publication [1]. All rheo-fluorescence measurements were performed using a Taylor-Couette flow cell identical to the one used for rheo-PTV measurements.

6.4 Results and discussion

6.4.1 Linear viscoelasticity of *Z=38* and *66* PBD-DOP solutions

Small amplitude oscillatory shear frequency sweeps were performed in the linear viscoelastic regime to quantity the relaxation times of two entangled PBD-DOP solutions with different numbers of entanglements at varying temperatures (Figure 6.1). As ex-

pected, the longest relaxation time (τ_d) is found to decrease with increasing temperature (Figure 6.1 insets). Further, the plateau modulus is higher in the PBD-DOP solution with $Z = 38$ (Figure 6.1(a)) than the solution with $Z = 66$ (Figure 6.1(b)) due to the higher polymer concentration in solution necessary to achieve the targeted number of entanglements for a lower molecular weight of PBD. This behavior is expected since the plateau modulus (G_N^0) depends on the number density of entanglement strands as

$$G_N^0 = \nu k_B T \tag{6.5}$$

where ν is the number density of entanglement strands, k_B is the Boltzmann constant, and T is the temperature. The PBD-DOP solutions exhibit the expected rheological behavior for entangled polymer solutions for both $Z = 38$ and 66 as well at all temperatures investigated. Importantly, the fluids show no apparent anomalous rheological behavior as the temperature is decreased towards the phase boundary for PBD-DOP ($T_{UCST} \approx 13$ ℃) [36]. Thus, the PBD-DOP solutions serve as an ideal model fluid to explore the effects of flow-concentration coupling on the resulting measured flows. Specifically, we postulate that changes in temperature of the fluid will result in changes of the solvent quality (as accounted for in χ^{-1}), and therefore impact the strength of flow-concentration coupling (E).

6.4.2 Steady state velocity profiles for varying T (Z=38)

Time-averaged, steady state velocity profiles were measured to investigate the effect of changes in Wi_{app} and temperature on the observed flow profiles. Previously, shear banded velocity profiles were observed in a PBD-DOP solution with $Z = 38$ for the particular case of $T = 50$ ℃ [1], but the temperature sensitivity of the bulk flow behavior was not investigated. According to the two-fluid model predictions, the bulk flow behavior

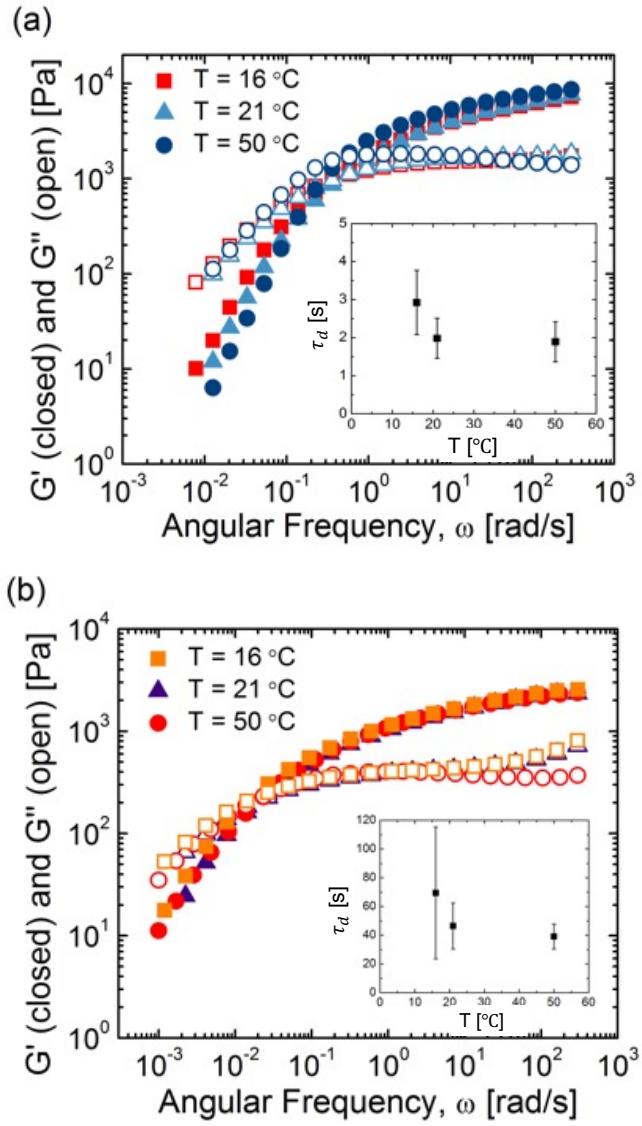

Figure 6.1: Small amplitude oscillatory shear frequency sweeps showing the linear viscoelasticity of the entangled PBD-DOP solutions for (a) $Z = 38$ and (b) $Z = 66$ at varying temperatures. Inset plots show the estimated longest relaxation time at each temperature as determined from the crossover frequency of G' and G''.

(and propensity for shear banding) should be dependent on the solution temperature, as implicitly included in E. The resulting flows for the PBD-DOP solution with $Z = 38$ at $T = 16$ ℃ are shown in Figure 6.2. As can be seen in Figure 6.2(a) and (b), curvature in the steady state velocity profiles becomes increasingly pronounced with increasing Wi_{app}. For $Wi_{app} \geq 3.2$, the profiles exhibit two distinct regions of different shear rates. At $T = 21$ ℃ (Figure 6.2(c) and (d)), the steady state velocity profiles exhibit qualitatively similar behavior with increasing Wi_{app}; however, the distinction between regions of different shear rate at high Wi_{app} (Figure 5(d)) is significantly less pronounced. The qualitative differences in the curvature between the high Wi_{app} profiles of Figure 6.2(b) and (d) indicate a dependence of the flow kinematics on temperature aside from just a change of relaxation time (as accounted for in Wi_{app}).

Further increasing the temperature to $T = 50$ ℃ yields similarly shaped velocity profiles, with enhanced curvature for $Wi_{app} > 1$. Interestingly, the curvature of the velocity profiles at $T = 50$ ℃ appears more pronounced than $T = 21$ ℃, suggesting that temperature has a nonlinear influence on flow profile curvature.

6.4.3 Steady state velocity profiles for varying T (Z=66)

Steady state velocity profiles with significant curvature are also observed in the more entangled PBD-DOP solution with $Z = 66$ (Figure 6.3). For $T = 16$ ℃ (Figure 6.3(a) and (b)), the measured flow profiles undergo several transformations with increasing Wi_{app}. At $Wi_{app} = 4.8$, the flow profile is curved with a high shear rate region near the inner wall ($r/H = 0.0$) and low shear rate region adjacent to the outer wall ($r/H = 1.0$). The curvature is less apparent as Wi_{app} is increased to 7.1, with slip occurring at the outer wall. As Wi_{app} is further increased to 9.8, the flow profile appears to develop three regions of distinct shear rates. A high shear rate region exists between $r/H = 0.1$ and

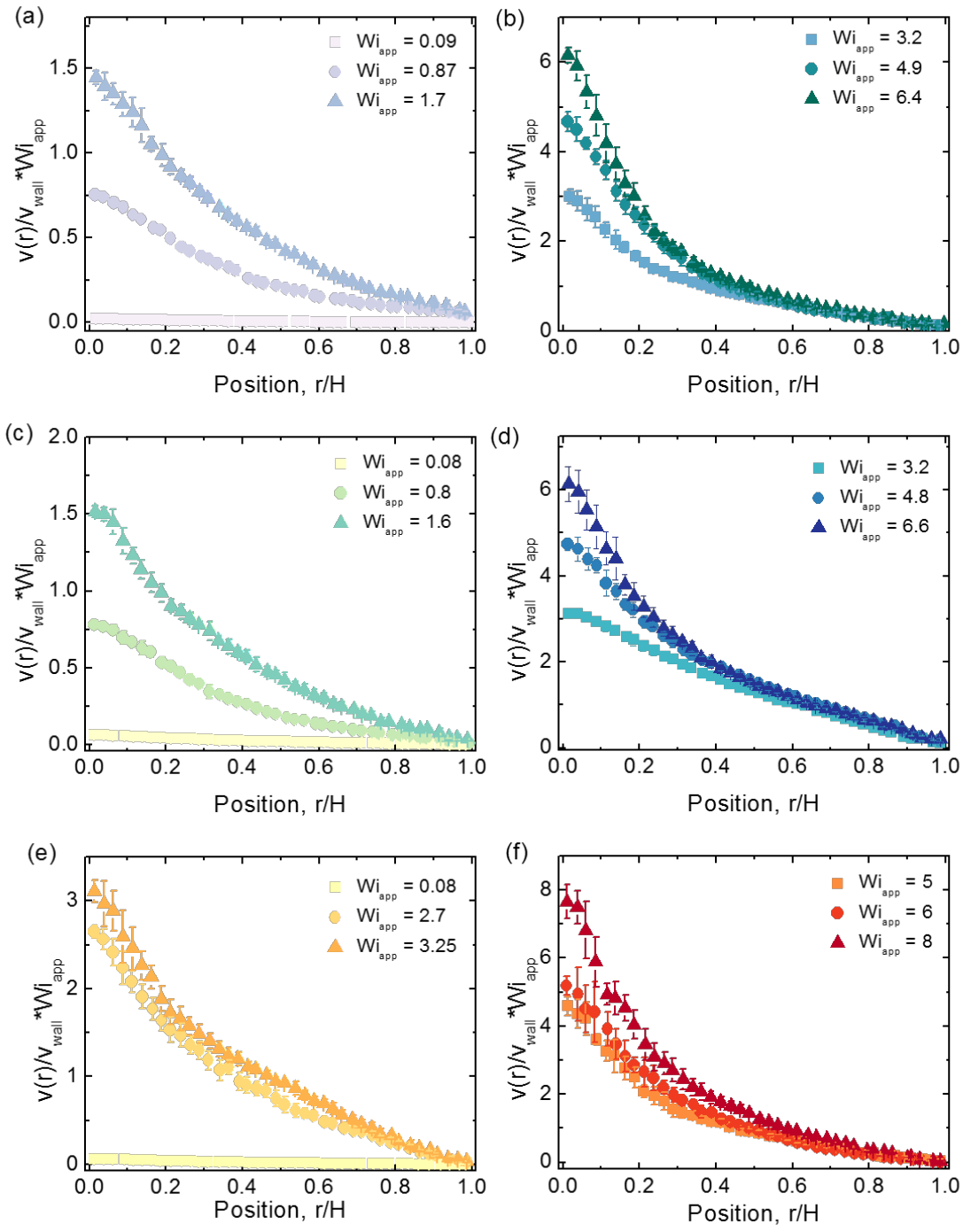

Figure 6.2: Time-averaged steady state velocity profiles for PBD-DOP solution with $Z = 38$. (a,b) $T = 16$ ℃ (c,d) $T = 21$ ℃ (e,f) $T = 50$ ℃.

0.3 and a low shear rate region manifests from $r/H = 0.3$ to 1.0. It seems that a second low shear rate region occurs adjacent to the inner wall ($r/H = 0.0$ to 0.1). At this time, the cause of this "three-banded" profile is still unclear. The flow behavior adjacent to the boundary surface could be governed by wall slip, but it is generally assumed that wall slip is an interfacial phenomenon, confined to a distance on the order of the radius of gyration of the polymer [37, 38]. The low shear rate region adjacent to the inner wall in $Wi_{app} = 9.8$ is 50˘100 μm thick and is thus orders of magnitude greater than the anticipated length scale of slip. Further, three-banded profiles due to flow-concentration coupling are predicted in the low curvature limit for TC flow [16]. With increasing Wi_{app}, the velocity profile remains banded, and the interface separating the bands of different shear rates moves towards the outer wall (Figure 6.3(b)). As seen for $Wi_{app} = 39$, the velocity profile has a high shear rate band spanning $r/H = 0.0$ to 0.8 and a low shear rate band from $r/H = 0.8$ to 1.0. At $Wi_{app} = 47$, the velocity profile remains curved, but distinct bands are not apparent.

Similar trends with increasing Wi_{app} are observed for $T = 21$ ℃ (Figure 6.3(c) and (d)). Significant curvature in the velocity profiles is observed for $Wi_{app} \geq 4.4$. The interface separating the regions of different shear-rates is found to move towards the outer wall with increasing Wi_{app}. Again, as was observed for $Z = 38$, the velocity profiles do not appear as sharply banded for $T = 21$ ℃ compared to $T = 16$ ℃.

For $T = 50$ ℃, the velocity profiles of the PBD-DOP solution with $Z = 66$ develop shear bands for $Wi_{app} > 1$ (Figure 6.3(e) and (f)). At $Wi_{app} = 9.4$ the high shear rate band has a lower slope than $Wi_{app} = 12$ and the location of the interface separating the two bands appears to be further from the inner wall ($r/H = 0.0$). At $Wi_{app} = 35$, the velocity profile is the most significantly banded with a high shear rate region that spans $r/H = 0.0$ to 0.2, and a low shear rate region with a slope that is commensurate with the lower Wi_{app} profiles. It is important to note that wall slip at both the inner and outer

surfaces are present, most notably in the $Z = 66$ PBD-DOP solution. Although wall slip is believed to be a purely interfacial phenomena, there is a possibility that it could be influencing (either initiating or amplifying) the velocimetry results shown here.

The steady state velocity profiles measured for varying Z and T indicate the importance of the number of entanglements and solvent quality on the bulk flow of entangled polymer solutions (Figure 6.2 and 6.3). From visual inspection, the measured velocity profiles have the greatest spatial variation of local shear rate at the lowest T studied. This temperature sensitivity is consistent with the speculation that flow-concentration coupling is strongest close to the T_{UCST}.

6.4.4 Determining strength of flow-concentration coupling through comparison of measured velocity profiles to two-fluid R-P model predictions

The time-averaged steady state velocity profiles at varying Wi_{app}, Z, and T were compared with the two-fluid R-P model predictions. The pronounced curvature of the measured velocity profiles is greater than one would expect for the degree of shear thinning of these entangled polymer solutions and in the low-curvature TC flow cell employed in this study [1]. Figure 7(a) and (b) directly compare the measured velocity profiles at particular Wi_{app}, Z, and T to the corresponding two-fluid R-P model predictions for varying values of E. E represents the balance of elastic stresses, which store stress under flow, to osmotic stresses, which act to homogenize gradients in fluid composition. Therefore, $E = 0$ corresponds to the case where the polymer concentration remains homogeneous across the fluid due to the absence of flow-concentration coupling. As seen in both Figure 6.4(a) and (b), the $E = 0$ prediction poorly captures the local shear rate variation across the PBD-DOP solution that is measured experimentally. With increasing magnitude of

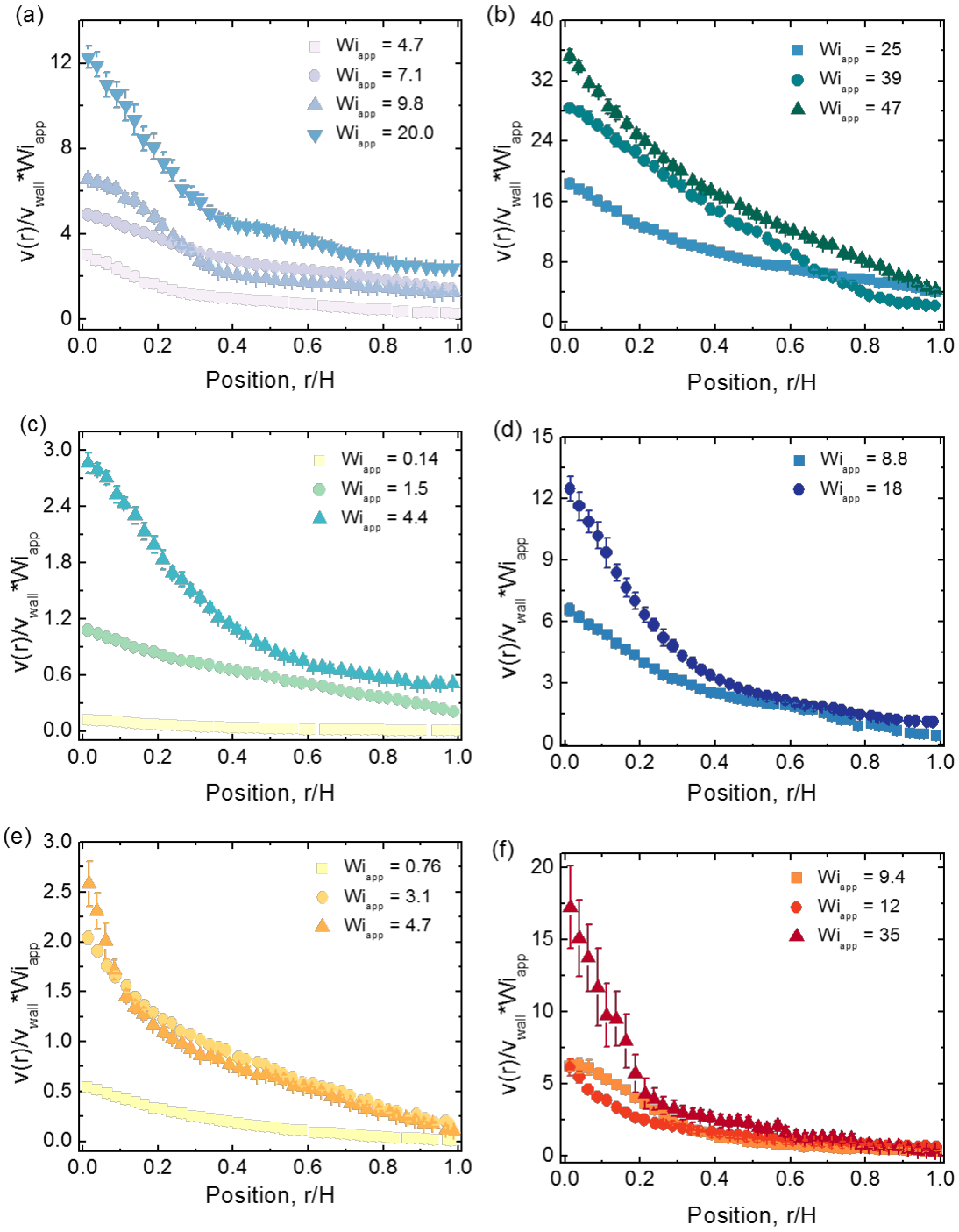

Figure 6.3: Time-averaged steady state velocity profiles for PBD-DOP solution with $Z = 66$. (a,b) $T = 16$ ℃ (c,d) $T = 21$ ℃ (e,f) $T = 50$ ℃.

E, agreement is improved between the curvature of the measured velocity profiles and the two-fluid R-P model predictions.

There is excellent agreement between the measured velocity profile and two-fluid R-P model prediction with $E = 0.14$ for the fluid with $Z = 38$ (Figure 6.4(a)). For $Z = 66$ (Figure 6.4(b)), there is disagreement between the model predictions and the measured velocity profile from $r/H = 0.0$ to 0.2 for all E. Notably, there is significant slip occurring at the inner wall ($r/H = 0.0$). In the region adjacent to the inner wall ($r/H < 0.1$), the measured velocity is less than what is predicted by the two-fluid R-P model. Additionally, between $r/H = 0.15$ and 0.25, the measured velocity exceeds the model predictions, and appears to broaden the "sharpness" of the interface that is predicted by the model. For $r/H > 0.25$, the model predictions agree very strongly with the measured values.

To evaluate the strength of the model fit to the experimental data, the following objective function was minimized

$$\min\left(\frac{SSE}{v_i^2}\right) = \min\left(\sum_i \frac{[v_m(r) - v_i(r)]^2}{v_i(r)^2}\right) \tag{6.6}$$

where $v_m(r)$ is the model predicted velocity and $v_i(r)$ is the experimentally measured velocity. The results of this optimization are included in Figure 6.4(c). The best fits of the model predictions to experimentally measured profiles are found for $E = 0.14$ and $E = 0.18$ for $Z = 38$ and $Z = 66$, respectively.

6.4.5 Strength of flow-concentration coupling is dependent on temperature

The values of E determined from the optimization are found to agree across the range of Wi_{app} examined at each Z and T (Figure 6.5(a)). At $Wi_{app} = 4.7$ and 9.8,

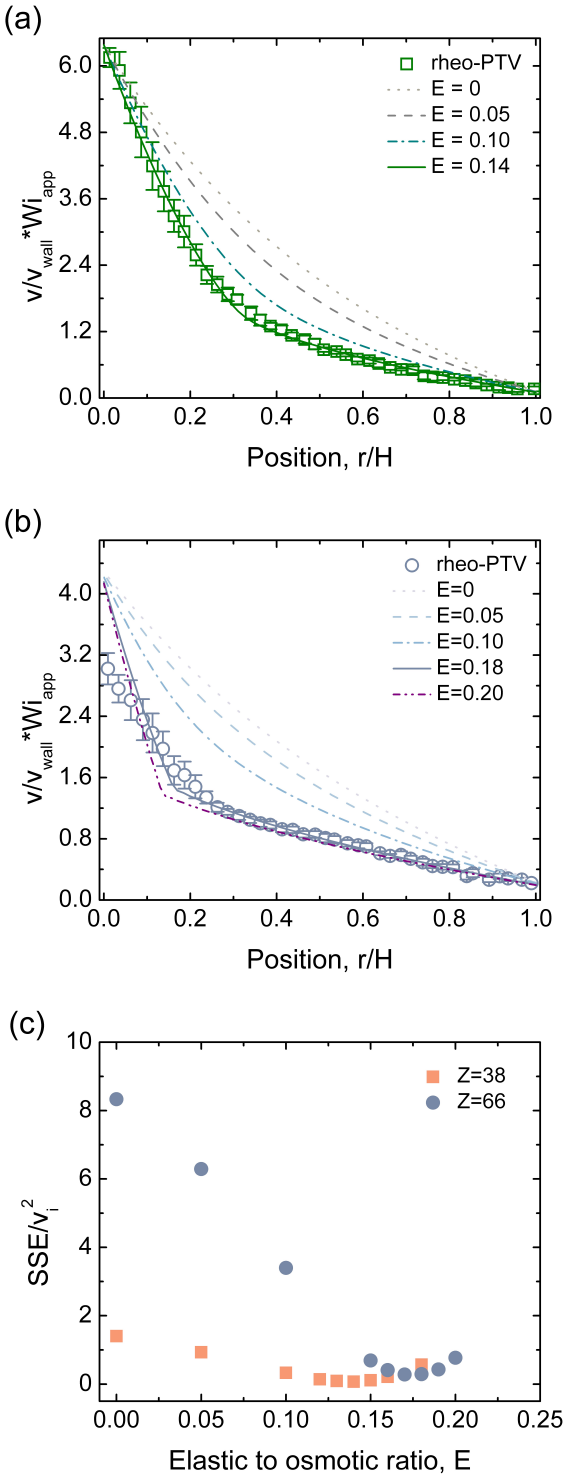

Figure 6.4: Two-fluid R-P model fits to experimentally measured velocity profiles (a) $Z = 38$, $Wi_{app} = 6.4$ (b) $Z = 66$, $Wi_{app} = 4.7$ (c) evaluation of model fit to experimental data depending on the value of E used in the model calculation.

the disagreement between the measured velocities and model predictions persist in the region adjacent to the inner wall. At $Wi_{app} = 39$, there is excellent agreement between the model predictions and measured values across the entire flow domain. The E values determined from optimization at each Z and T are shown in Figure 6.5(b). E is higher for the $Z = 66$ PBD-DOP solution than the $Z = 38$ solution at all T. The highest E value is found at $T = 16$ ℃ for both Z. This intuitively makes sense as PBD-DOP is known to exhibit temperature-dependent phase behavior, with an upper critical solution temperature $T_{UCST} \approx 13$ ℃ [36]. As a phase boundary is approached, the solution osmotic susceptibility is expected to tend toward zero, meaning that E would approach infinity. Interestingly, the change in E with increasing T is nonmonotonic for both Z values. The nonmonotonicity could stem from the different T-dependencies of the elastic modulus and the osmotic susceptibility. The elastic modulus is expected to scale linearly with T, but the osmotic susceptibility could contain a more complicated T-dependence, particularly in the vicinity of the phase boundary. The agreement between the model predictions and measured velocity profiles for non-zero values of E is suggestive of flow-concentration coupling but is not a direct measurement of the existence of concentration variations.

6.4.6 Estimates of the steady state concentration profiles from rheo-fluorescence

Variations in the polymer concentration for a particular Wi_{app} at different temperatures are shown in Figure 9. The most significant changes in concentration are measured for $T = 16$ ℃, which corresponds to the lowest temperature and highest degree of flow-concentration coupling as determined from E-fits to the measured velocity profiles (Figure 6.6(a)). The variations in concentration predicted by the two-fluid R-P model

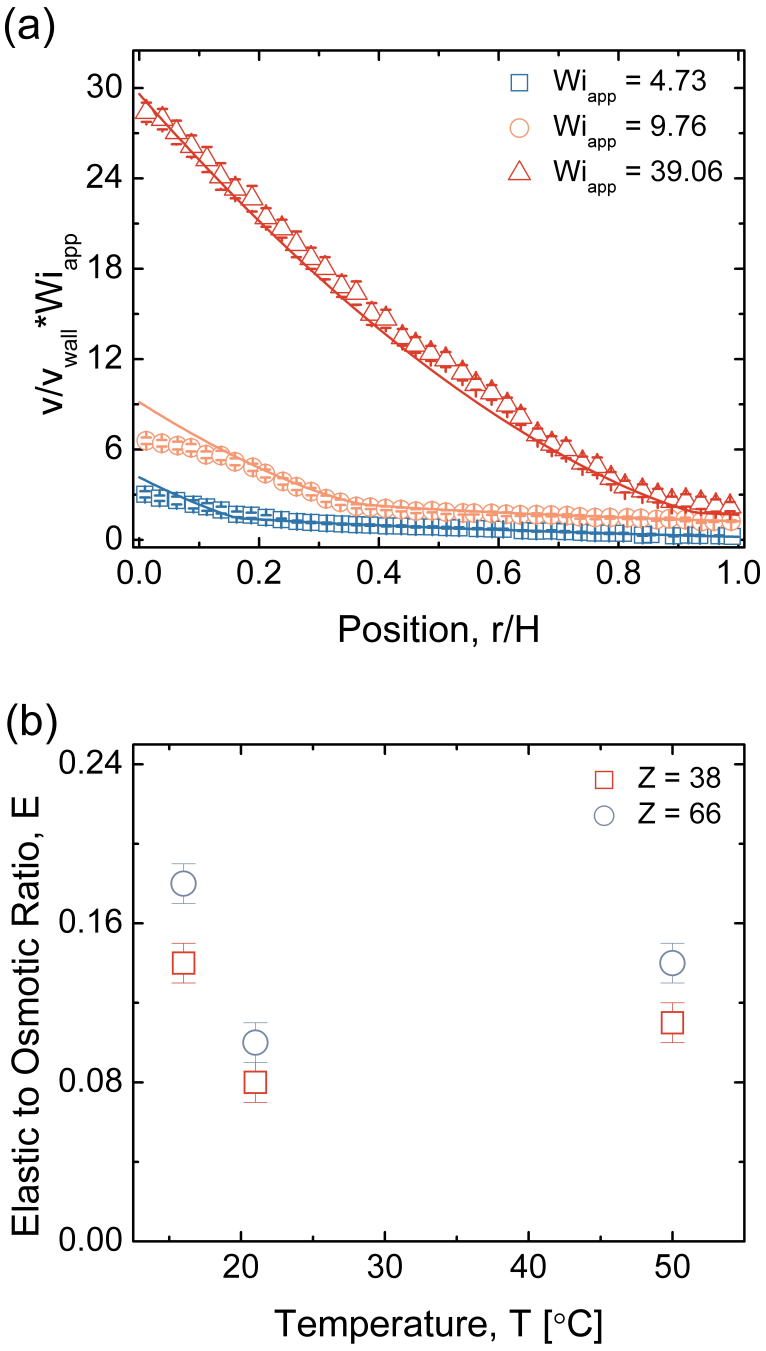

Figure 6.5: (a) Two-fluid R-P model fits to experimentally measured velocity profiles at varying Wi_{app} using a single value of E ($E = 0.18$) and (b) value of E that yields the best fit to measured velocity profiles across range of Wi_{app} at each T.

underestimate the magnitude of concentration changes measured by rheo-fluorescence. The smallest variation of concentration is observed for $T = 21$ ℃ (Figure 6.6(b)), consistent with the estimates of E with temperature (Figure 6.5(b)). At $T = 50$ ℃ (Figure 6.6(c)), measured concentration changes are larger than $T = 21$ ℃, but less than $T = 16$ ℃. The agreement between the experiment and model predicted concentration profiles are quite strong at $T = 50$ ℃ where both the magnitude of concentration variation and interface location are captured by the model. The measured T-dependence of the concentration variations in Figure 6.6 gives further support to the nonmonotonicity of flow-concentration coupling (E) as quantified in Figure 6.5(b). As mentioned previously, this nonmonotonicity likely results from a complex T-dependence of χ^{-1} [36].

Slight discrepancies are observed when comparing the rheo-fluorescence determined concentration profiles to the model predictions of the $Z = 66$ PBD-DOP solution (Figure 6.7). Although the magnitude of concentration variation measured via rheo-fluorescence and predicted from the two-fluid R-P model are in agreement, the spatial variation disagrees in some regions. Perhaps most striking, is the disagreement in the high shear-rate region (predicted low concentration) from $r/H = 0.00$ to about 0.15 in Figure 6.7(a). The measured concentration is much higher in this region compared to the two-fluid R-P model prediction. As discussed previously, there is also a disparity in the measured and model predicted velocimetry data in this region. A higher concentration, as measured by rheo-fluorescence in Figure 6.7(a), would give rise to a lower shear-rate as measured in Figure 6.4(b) and Figure 6.5(a) due to an increase in fluid viscosity. Additionally, the measured concentration is less than the model predictions for $r/H = 0.2$ to 0.4. This discrepancy could potentially explain the "broadening" of the interface observed in Figure 6.4(b), where the measured velocity gradient is lower than model predictions for $r/H = 0.00$ to 0.15 and higher than model predictions for $r/H = 0.20$ to 0.40. Stronger agreement is found between the rheo-fluorescence measurements and model

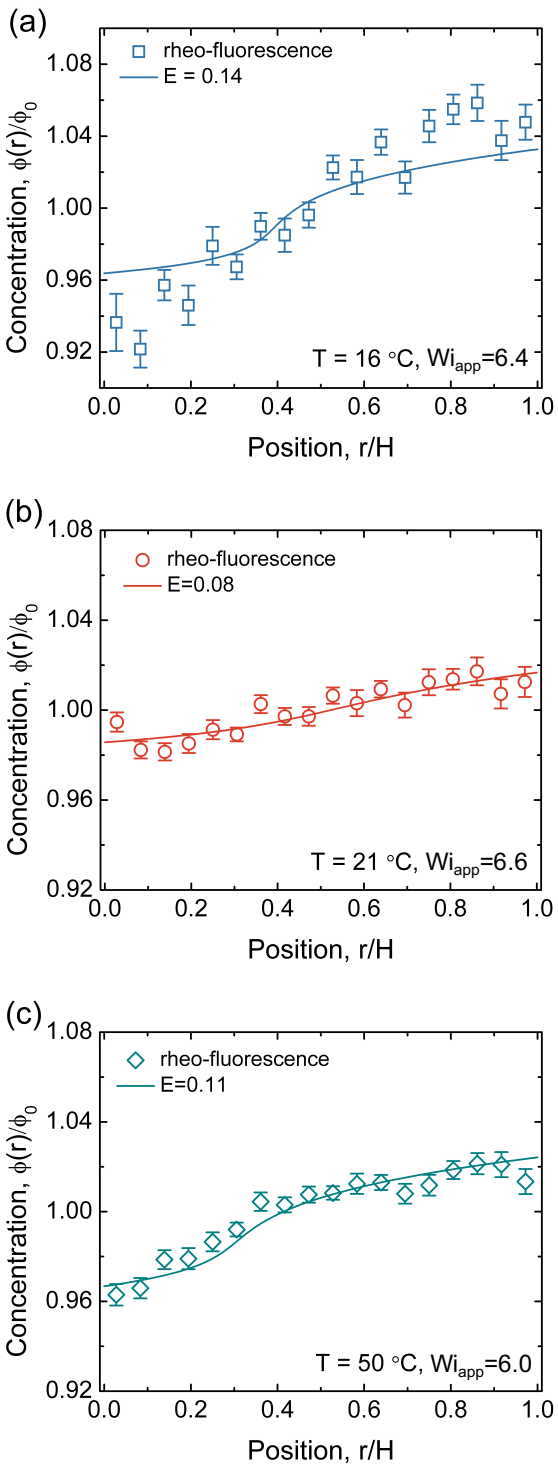

Figure 6.6: Concentration profiles determined from rheo-fluorescence in PBD-DOP solution with $Z = 38$. Solid lines represent the resulting model fits determined from fitting to the measured velocity profiles with no further adjustable parameters.

predictions for $T = 50$ ℃ (Figure 6.7(b)). The only discrepancies between the measured and predicted concentration values exist near the boundaries ($r/H = 0.00$ and 1.00). At $Wi_{app} = 39$, the interface location has moved to $r/H = 0.90$ as reflected in both the measured and model predicted concentration profiles (Figure 6.7(c)).

6.4.7 Quantifying the presence of wall slip at the inner and outer boundaries

Wall slip is known to occur in entangled polymer solutions, and the magnitude of slip depends on many variables, including: the polymer chemistry, solvent, surface chemistry, concentration, and number of entanglements [39]. Thus, it is important to quantify the magnitude of slip present in flows of entangled polymer solutions to understand whether the presence of slip impacts the measured nonuniform flows. Slip at solid boundaries could influence compositional heterogeneity in the bulk fluid, and potentially give rise to the "three-banded" flow profiles observed for PBD-DOP solutions with $Z = 66$.

Slip velocities at the boundaries for the $Z = 38$ PBD-DOP solution at varying Wi_{app} are shown for the inner and outer surfaces in Figure 6.8(a) and Figure 6.8(b), respectively. The slip velocities at the inner ($v_{i,slip}$) and outer ($v_{o,slip}$) walls were determined according to

$$v_{i,slip} = v_{wall} - v(r/H = 0) \tag{6.7}$$

$$v_{o,slip} = v(r/H = 1). \tag{6.8}$$

For all temperatures investigated, the resulting slip velocities at the inner surface remain effectively negligible (Figure 6.8(a)). Likewise, in Figure 6.8(b), the outer slip velocities are effectively zero across the range of Wi_{app} investigated. Thus, it can be

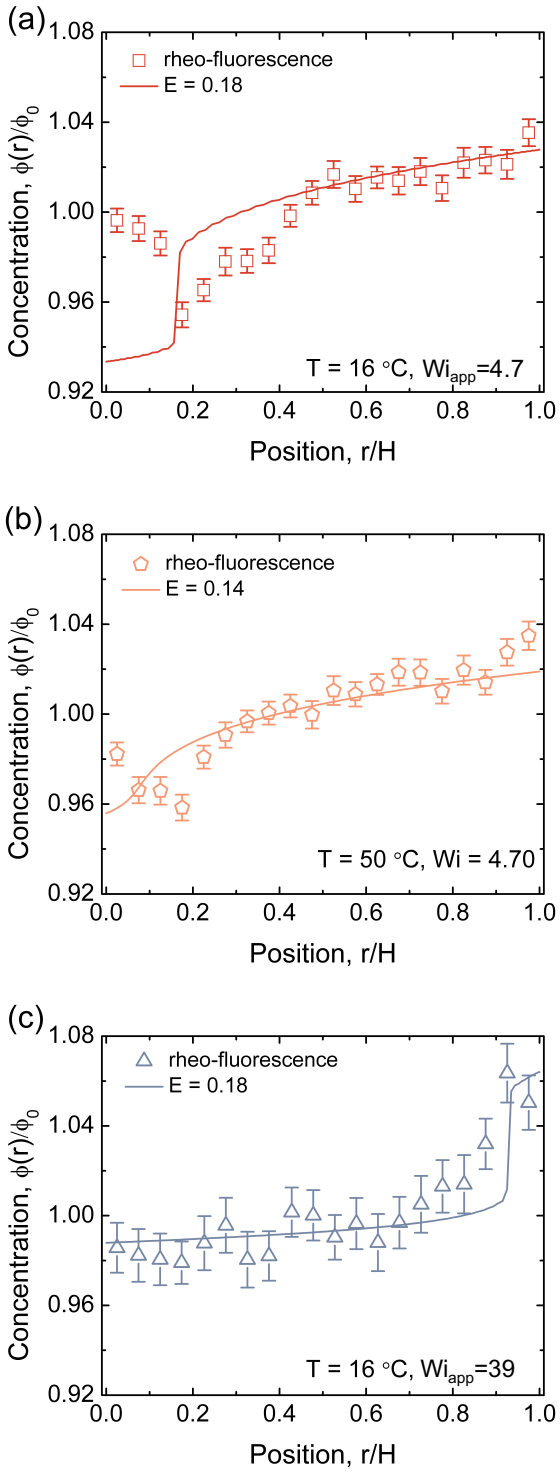

Figure 6.7: Concentration profiles determined from rheo-fluorescence for PBD-DOP solution with $Z = 66$. Solid lines represent the resulting model fits determined from fitting to the measured velocity profiles with no further adjustable parameters.

concluded that the curvature of the steady state velocity profiles in Figure 6.2 results from the bulk behavior of the fluid and is not significantly influenced by the presence of wall slip.

Unlike the $Z = 38$ fluid, appreciable wall slip is observed at both bounding surfaces for the $Z = 66$ PBD-DOP solution (Figure 6.9). This finding is consistent with other reports of an increase in slip as the polymer molecular weight increases and concentration decreases [39, 40]. Although higher Wi_{app} were explored for the PBD-DOP fluid with $Z = 66$ compared to $Z = 38$, it is clear that wall slip at the inner (Figure 6.9(a)) and outer (Figure 6.9(b)) surfaces increases with Wi_{app}. Additionally, higher temperatures are found to result in more prominent slip at both the inner and outer walls. This temperature dependence of wall slip can be rationalized in the context of a Navier-Slip condition, where the magnitude of slip is proportional to the shear stress, as higher stresses are measured in the $Z = 66$ fluid at higher temperatures for similar Wi_{app}. Reliable measurements of the $Z = 38$ solution for $Wi_{app} > 10$ were infeasible because of rod climbing and edge fracture complications due to the higher plateau modulus of the $Z = 38$ fluid (Figure 6.1(a)).

6.4.8 Distinguishing between shear thinning and shear banding by quantifying the interface location and width

The nonuniform, steady state velocity profiles (Figure 6.2 and Figure 6.3) have been shown to coincide with spatial changes in concentration (Figure 6.6 and Figure 6.7) as predicted by a two-fluid model for entangled polymer solutions [17]. However, it is unclear whether these flows are shear banded or merely curved due to the combination of shear thinning rheological behavior and the shear stress gradient of a small curvature Taylor-Couette flow cell. To distinguish between these two possible flow behaviors, a

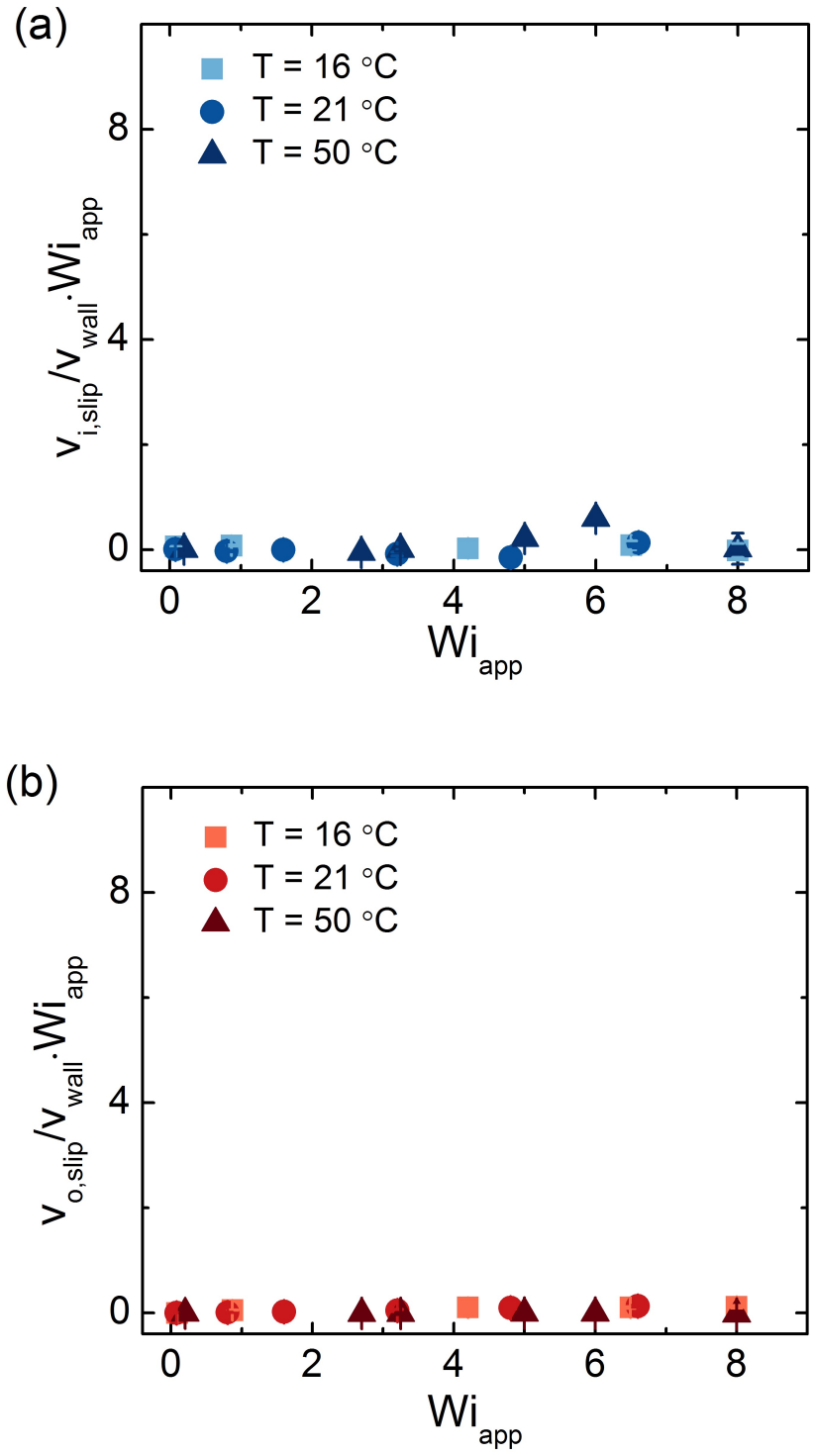

Figure 6.8: Wall slip in the $Z = 38$ PBD-DOP solution for varying Wi_{app} at the (a) inner wall and (b) outer wall.

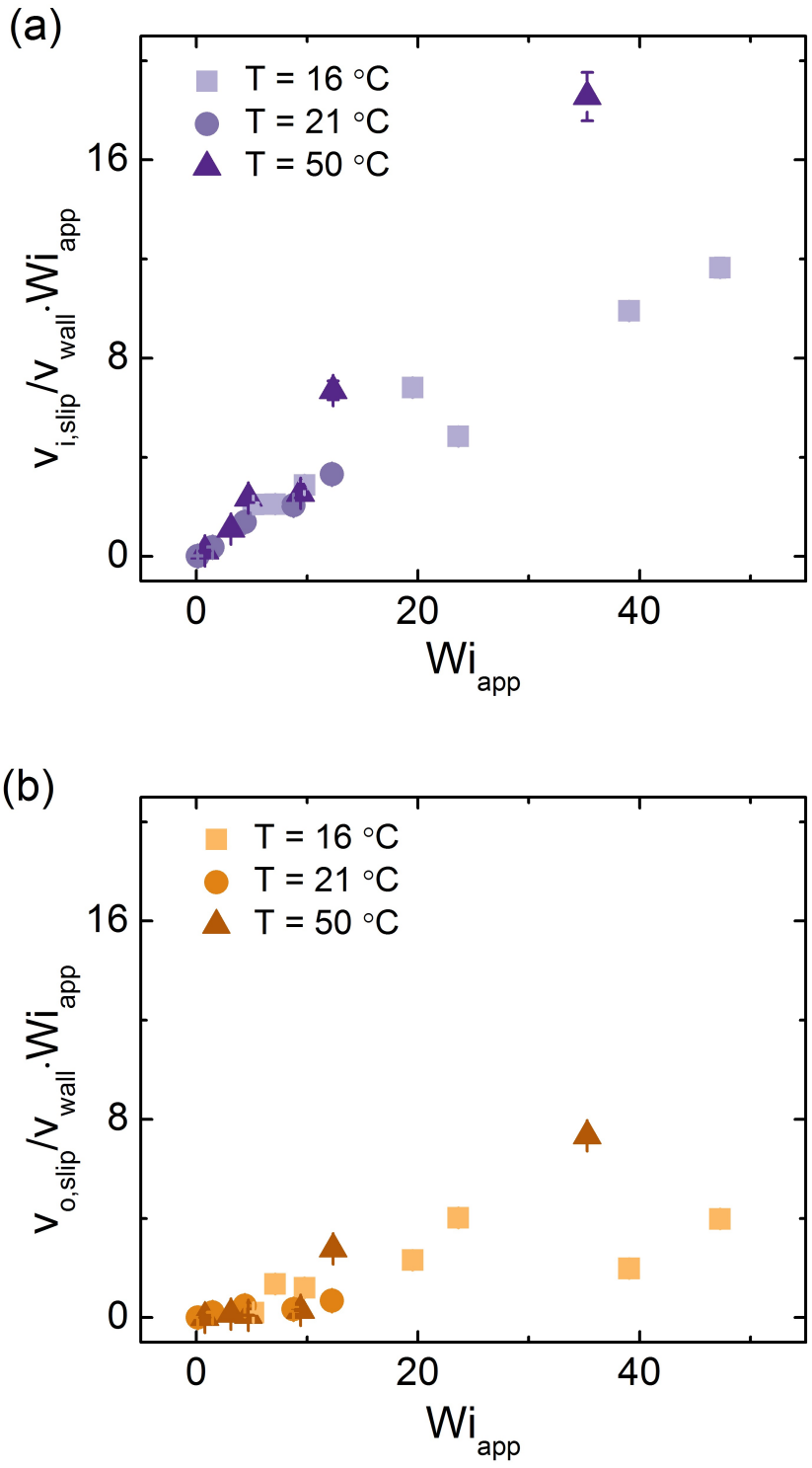

Figure 6.9: Wall slip in the $Z = 66$ PBD-DOP solution for varying Wi_{app} at the (a) inner wall and (b) outer wall.

statistical method was employed to calculate numerical derivatives of the high spatial density velocity profiles [28]. Third derivatives of the velocimetry data were used to determine both the interface locations and widths across a range of Wi_{app} for the $Z = 38$ (Figure 6.10) and $Z = 66$ (Figure 6.11) PBD-DOP solutions.

The location of the interface in the flow profiles is found to move from the inner wall ($r/H = 0.0$) to the outer wall ($r/H = 1.0$) as Wi_{app} is increased above $Wi_{app} \approx 2$ (Figure 6.10(a)), in qualitative agreement with the two-fluid model predictions (Chapter 3). The determined interface width for the $Z = 38$ PBD-DOP solution is nearly constant at $w/H = 0.40$ across the examined Wi_{app} range for $T = 16$ and 50 ℃ but increases with Wi_{app} for $T = 21$ ℃ (Figure 6.10(b)). This interface width is similar to other shear banding fluids [34, 41–45] and is consistent with the value determined for a shear banding wormlike micellar solution determined from the rLOESS method [28]. Conversely, the interface width is found to increase with Wi_{app} when $T = 21$ ℃. Thus, it is concluded that whether shear banding occurs in entangled polymer solutions depends on the value of E. Specifically, $E = 0.08$ is an insufficient degree of flow-concentration coupling to induce shear banded flows despite a measured macroscopic variation in concentration across the fluid (Figure 6.6(b)).

In the $Z = 66$ fluid, the calculated interface location moves into the bulk of the fluid with different sensitivity to Wi_{app} depending on the temperature (Figure 6.11(a)). At $T = 16$ ℃, the interface location moves from $r^*/H = 0.20$ at the lowest Wi_{app} to $r^*/H = 0.80$ at the highest Wi_{app}. At higher temperatures, the interface location is found to not move as far into the bulk of the fluid with increasing Wi_{app}. At $T = 21$ ℃, the interface location resides at $r^*/H = 0.25$ at low Wi_{app} and approaches $r^*/H = 0.4$ with increasing Wi_{app}. At $T = 50$ ℃, the interface location is observed to move nonmonotonically from $r^*/H = 0.10$ to 0.35 in over a decade of Wi_{app}. The computed interface widths for the $Z = 66$ fluid are fairly constant across the range of Wi_{app} (Figure

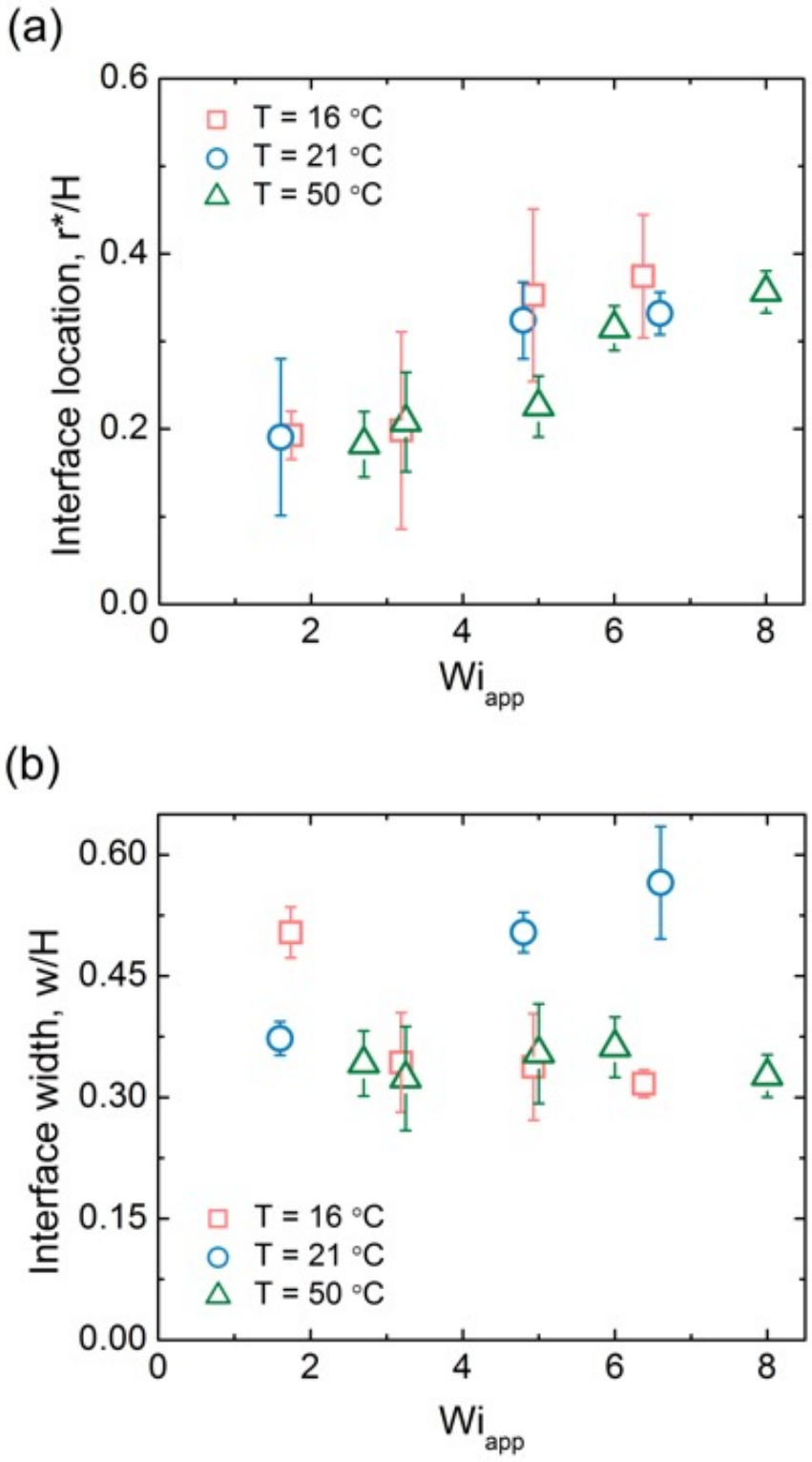

Figure 6.10: rLOESS determined (a) interface location and (b) interface width for varying Wi_{app} and T in the $Z = 38$ PBD-DOP solution.

6.11(b)). The w/H values for the $Z = 66$ fluid at $T = 16$ ℃ are the lowest of any temperature examined, ranging from $w/H = 0.20$ to 0.35. These values of w/H are similar to the interface widths determined using this same statistical method for a shear banding wormlike micellar solution [28]. The calculated interface widths for $T = 21$ ℃ and $T = 50$ ℃ range from $w/H = 0.40$ to 0.50 and $w/H = 0.30$ to 0.40, respectively.

6.4.9 Does wall slip initiate nonhomogeneous flow?

Previous explanations for the occurrence of shear banded flows in entangled polymer solutions have asserted that nonhomogeneous flow arises from disentanglements of the entangled polymer chains that initiate at the solid boundary in the form of wall slip and propagate into the bulk of the fluid [32, 46]. In the following, it is shown that wall slip is not necessary to observe nonhomogeneous flow.

Wall slip can occur transiently during startup shear of entangled polymer solutions without resulting in nonhomogeneous flow. The transient shear stress measured for shearing the $Z = 38$ PBD-DOP solution follows the expected behavior for nonlinear shear of an entangled polymer solution as evidenced by a large shear stress overshoot at early times, followed by a plateau to steady state at long times (Figure 6.12(a)). As shown in Figure 6.12(b), wall slip occurs at the moving boundary ($r/H = 0.0$) shortly after the startup of shear flow but subsides in the steady state (Figure 6.12(c)). At steady state, the velocity profile is nearly linear, which shows that the wall slip observed at early times (Figure 6.12(b)) does not result in nonhomogeneous flow.

By contrast, at $Wi_{app} = 3.2$, the $Z = 38$ PBD-DOP fluid exhibits simultaneous wall slip and development of nonhomogeneous flow (Figure 6.13). Similar to the flow in Figure 6.12, wall slip at the moving boundary is observed at early times (Figure 6.13(b)), but not at longer times (Figure 6.13(c)). However, unlike the flow measured in Figure 6.12,

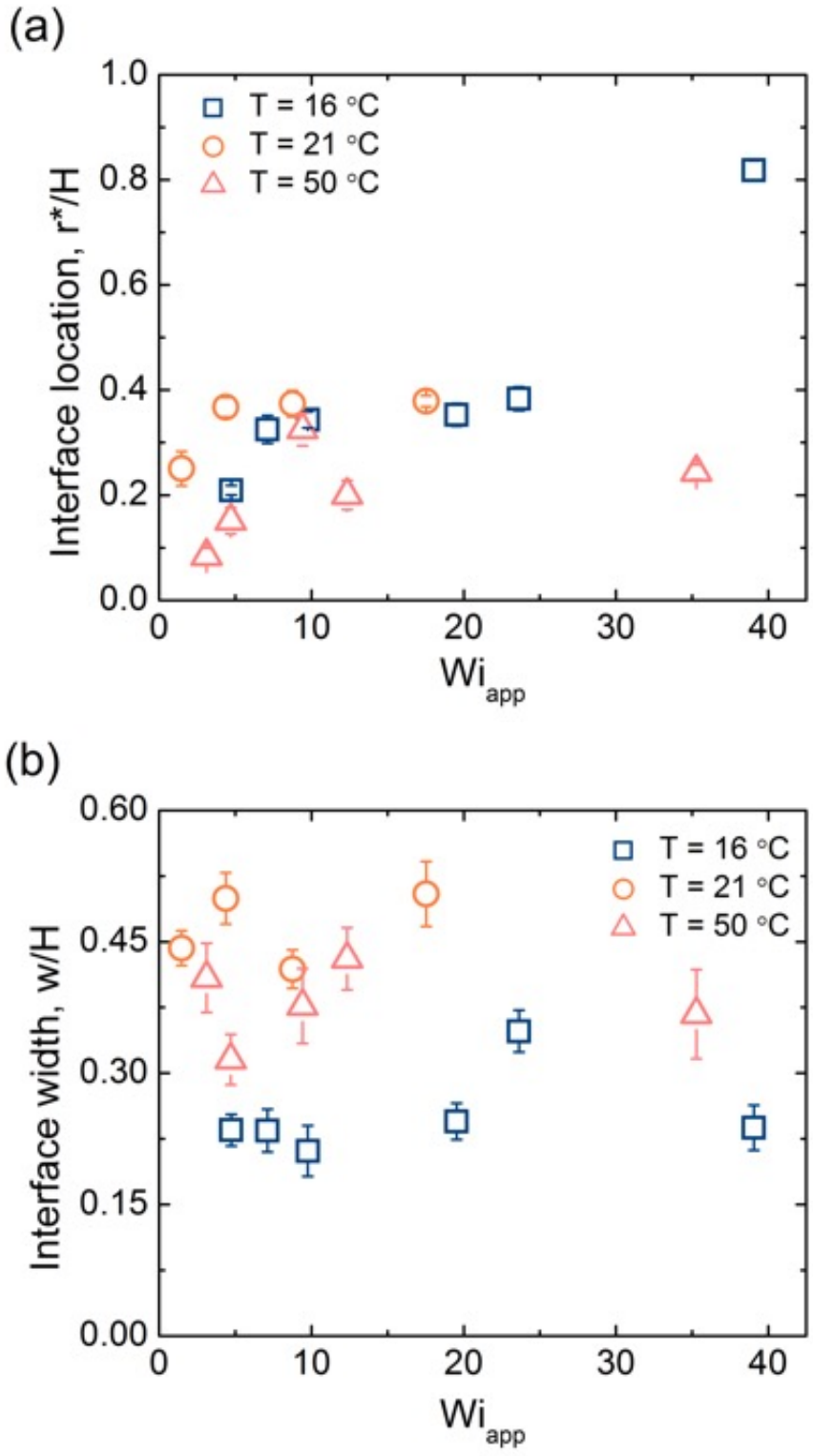

Figure 6.11: rLOESS determined (a) interface location and (b) interface width for varying Wi_{app} and T in the $Z = 66$ PBD-DOP solution.

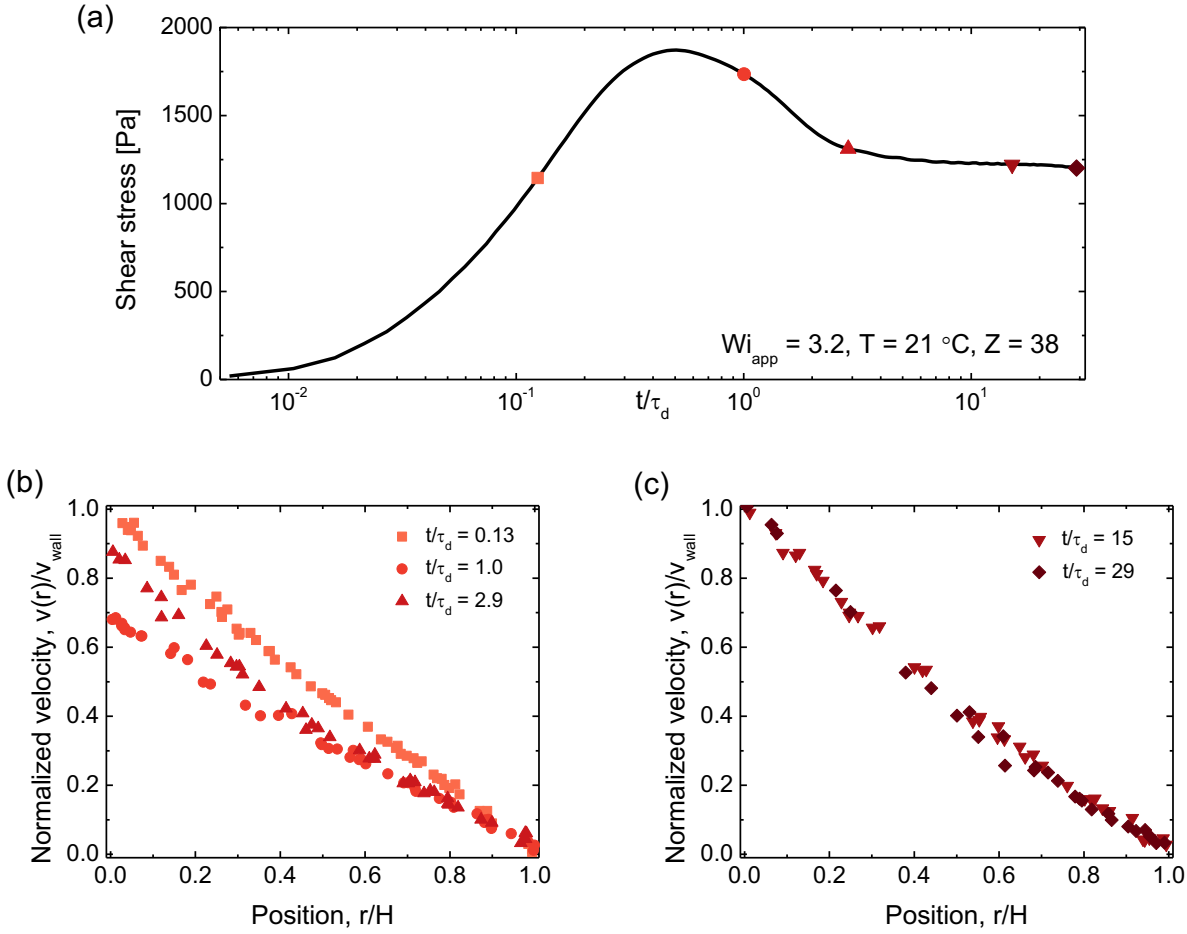

Figure 6.12: (a) Transient shear stress development under shear of $Wi_{app} = 3.2$ at $T = 21$ ℃ for the $Z = 38$ PBD-DOP solution. The black line corresponds to measured shear stress whereas symbols correspond to the times at which the velocity profiles were measured in (b) and (c).

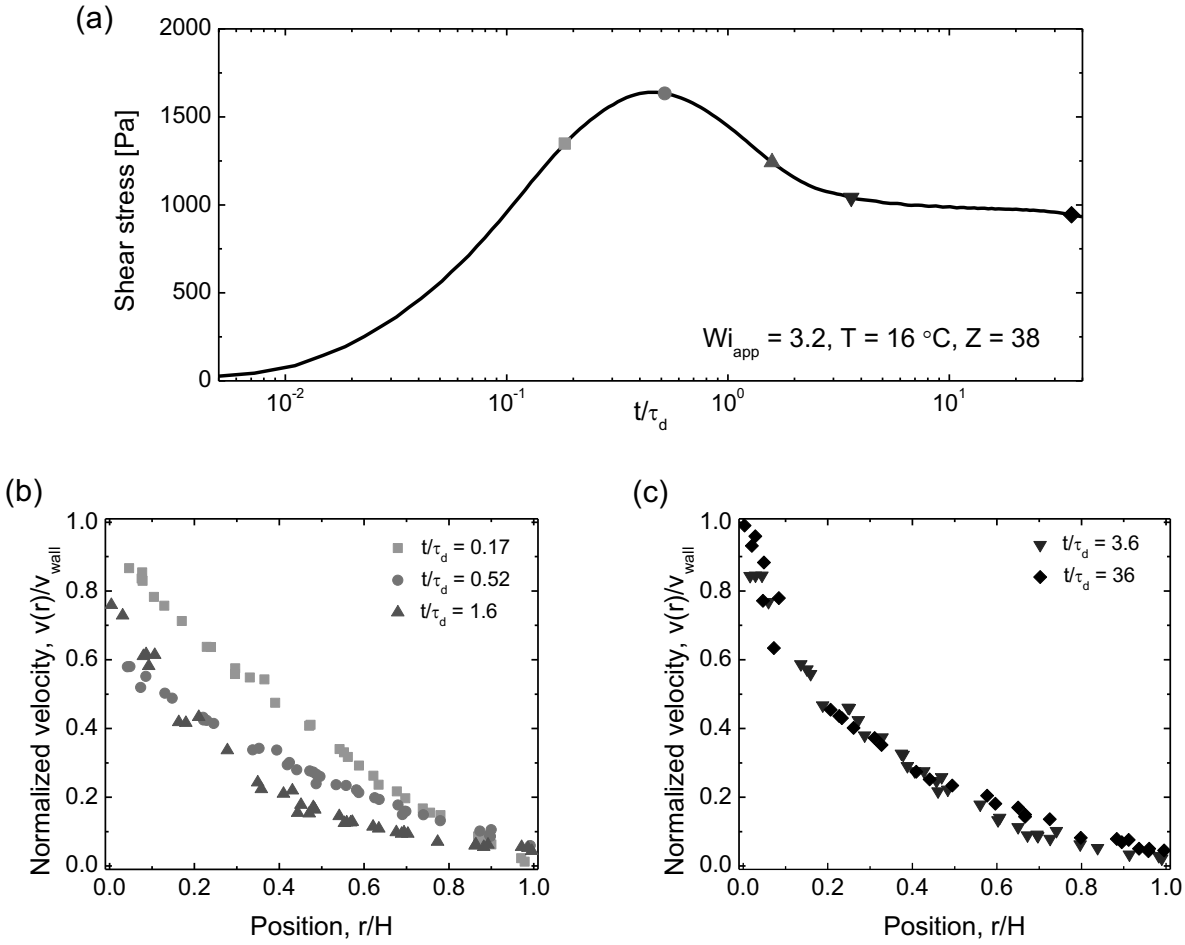

Figure 6.13: (a) Transient shear stress for $Wi_{app} = 3.2$ at $T = 16$ ℃ in the $Z = 38$ PBD-DOP solution. The black line corresponds to the measured shear stress and the symbols correspond to the times at which the velocity profiles in (b) and (c) were measured.

the flow appears nonhomogeneous after wall slip occurs (Figure 6.13). Following the shear stress overshoot, the flow profiles appear to have two regions of different shear rate beginning at $t/\tau_d = 1.55$ (Figure 6.13(b)). At steady state (Figure 6.13(c)), the fluid experiences a high shear rate region between $r/H = 0.0$ and 0.2, and a low shear rate region from $r/H = 0.2$ to 1.0.

The occurrence of wall slip is unnecessary for the development of nonhomogeneous flows. The measured shear stress at $Wi_{app} = 5$ and $T = 50$ ℃ (Figure 6.14a) exhibits a

smaller overshoot relative to the lower temperatures (Figure 6.12(a) and Figure 6.13(a)). Interestingly, the velocity profiles in Figure 6.14(b) and (c) show no evidence of wall slip at the moving boundary at all times. Despite the lack of wall slip, nonhomogeneous flows with pronounced curvature develop shortly after the start of shear flow (Figure 6.14(b)). This curvature persists even at long times, where the low shear band (from $r/H = 0.4$ to 1.0) remains constant whereas the high shear band exhibits some scatter before reaching a steady shape by $t/\tau_d = 21.3$. Ultimately, the flow profiles for the $Z = 38$ PBD-DOP solution show a relatively quick development of nonhomogeneous flow, without clear changes such as "stair-stepped" velocity profiles resulting from a coarsening of the concentration heterogeneities as shown in Chapter 3. As discussed in Burroughs *et al.* (2021) [1], the nonhomogeneous flows observed at short times relative to the formation of concentration heterogeneity could result from "transient" shear banding in the startup of shear.

In summary, we find that although wall slip can accompany nonhomogeneous flow, the experimental results clearly show that wall slip – either during transient startup or at steady shear – is neither a necessary nor sufficient condition for the presence of apparent steady state shear banding.

6.4.10 Transient development of nonhomogeneous velocity profiles for PBD-DOP solution with *Z=66*

To quantify the flow kinematics of entangled PBD-DOP solutions from shear startup to steady state, rheo-PTV measurements were performed to allow for simultaneous determination of the rheology and velocity profiles. Figures 6.15-6.17 show the evolution of the shear stress and measured velocity profiles under shearing at different temperatures and Wi_{app} for the PBD-DOP solution with $Z = 66$.

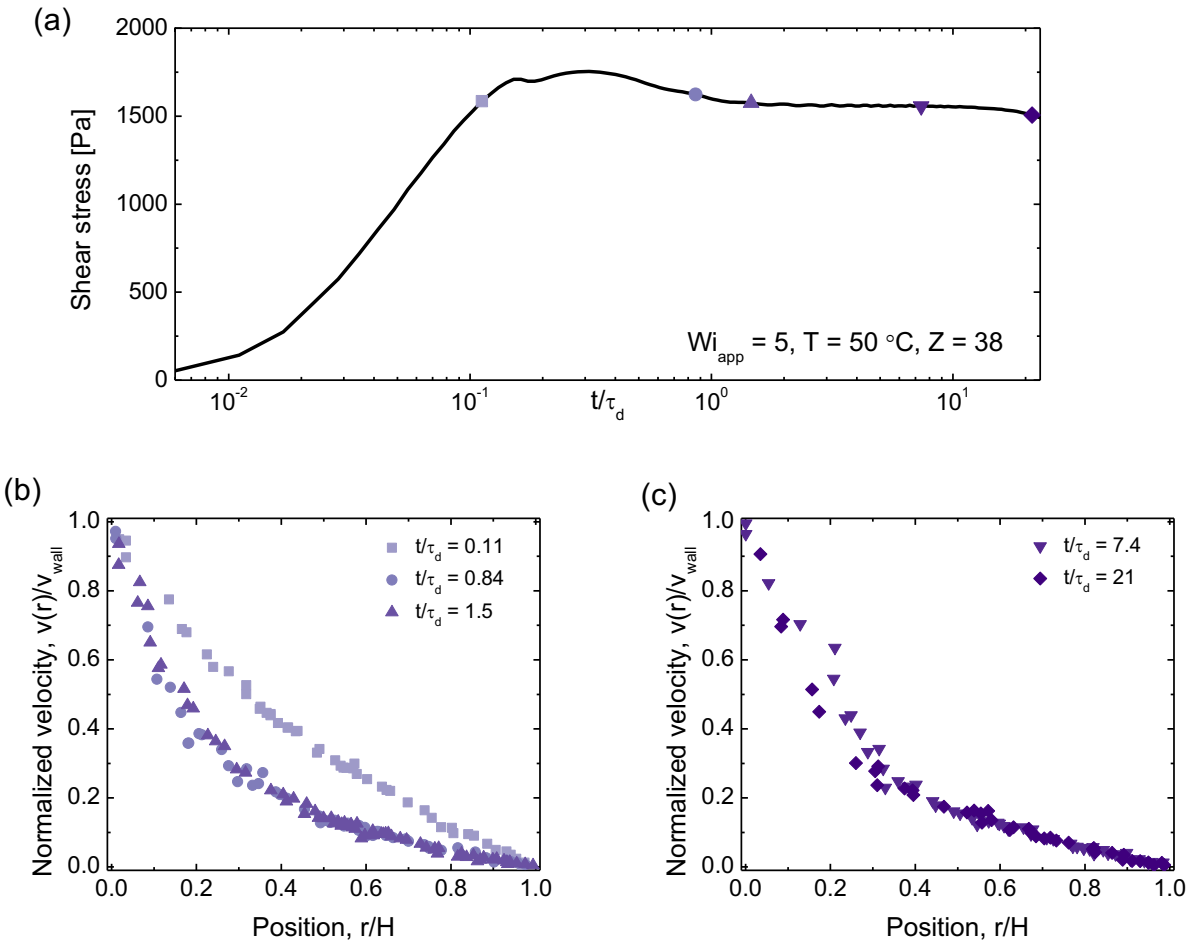

Figure 6.14: (a) Transient shear stress for $Wi_{app} = 5$ at $T = 50$ °C for the $Z = 38$ PBD-DOP solution. The black line corresponds to the measured shear stress whereas the symbols represent the times at which the velocity profiles in (b) and (c) were measured.

Upon the startup of steady shear flow, the shear stress initially increases in time up to a maximum $\approx 0.3\tau_d$ (6.15(a)), during which the velocity profile (Figure 6.15(b)) is linear (uniform shear rate) with some wall slip at the inner wall ($r/H = 0.0$). Following a maximum at early times, the shear stress first decreases rapidly before decreasing at a slower rate beginning around $2\tau_d$. At the start of this more gradual decrease in shear stress, the velocity profile remains linear with additional slip at the outer wall ($r/H = 1.0$). At later times, the velocity profile begins to show a departure from a uniform shear rate. As shown in the velocity profiles at $6.8\tau_d$ and $13\tau_d$, curvature in the velocity profile becomes significant, presumably due to the onset of shear thinning following the initial elastic response of the fluid to shear startup. The curvature of the velocity profile reduces slightly from 13 to $50.0\tau_d$, as expected from model predictions. As the shear stress approaches steady state, a high shear rate region develops adjacent to the inner wall ($57\tau_d$) and propagates into the bulk of the fluid ($86\tau_d$) (Figure 6.15(c)). This progression of nonhomogeneous flow is consistent with the two-fluid model predicted formation of concentration heterogeneities at long time scales (Chapter 3). At steady state, the measured velocity profile appears banded with a high shear rate region adjacent to the inner wall and a low shear rate region adjacent to the outer wall. This banded profile is notably distinct from the curved profiles measured at earlier times ($12.54\tau_d$ and $50.0\tau_d$) as evidenced by a sharp transition between the bands of different shear rates at $r/H \approx 0.4$ (Figure 6.15(c)).

The measured rheology and flow profiles are found to exhibit qualitative differences at a higher temperature, as shown in Figure 6.16. First, the ratio of the maximum in shear stress relative to the steady state shear stress is clearly lower in Figure 6.16(a) than Figure 6.15(a). In addition, while the initial evolution of the shear stress is similar to Figure 6.15(a), with an overshoot at early times, there is a slight increase in the shear stress after $50\tau_d$ (Figure 6.16(a)). This increase in the shear stress at long times coincides

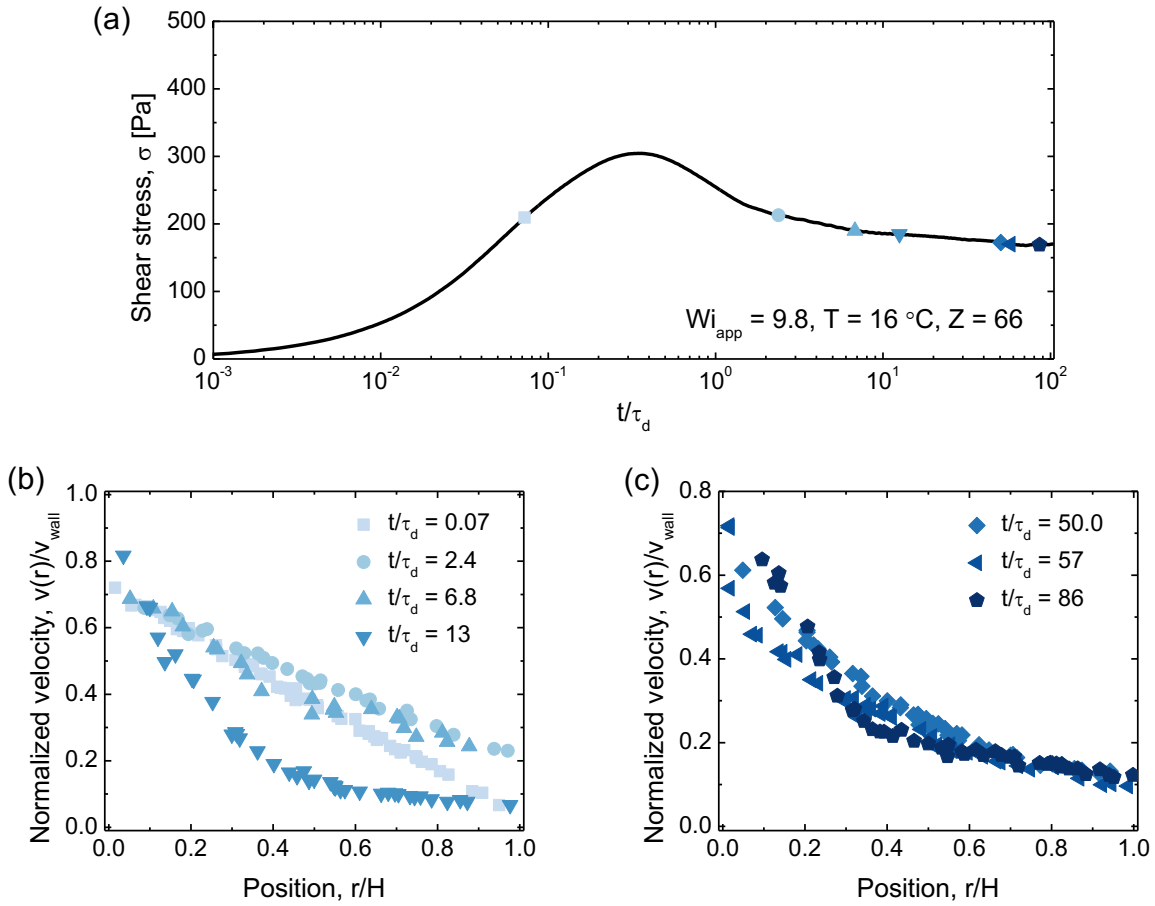

Figure 6.15: Transient response of PBD-DOP solution with $Z = 66$ at $T = 16$ °C and $Wi_{app} = 9.8$. (a) the evolution of the measured shear stress following the startup of shear. The symbols correspond to the times at which each velocity profile was measured in (b) and (c). (b) The transient velocity profiles measured from $t/\tau_d = 0.07$ to 13 and (c) from $t/\tau_d = 50.0$ to 86.

with detectable changes to the velocity profile. As shown in Figure 6.16(b), the velocity profile develops increasing curvature and slip at the inner wall during shear startup as the stress increases and goes through an overshoot. At $1.1\tau_d$, the curvature of the velocity profile is most significant following the decrease in shear stress after the overshoot. At $15\tau_d$, the velocity profile becomes "stair-stepped", where multiple regions of different shear rates are observed (Figure 6.16(b)). An attempt to quantify the shear rate within each region is not made due to the low spatial resolution at a single time point. From $23\tau_d$ to $90\tau_d$ (Figure 6.16(c)) the regions of differing shear rates appear to merge together, forming two distinct regions of different shear rates at steady state ($90\tau_d$).

A combination of wall slip at both surfaces and a "stair-stepped" transient velocity profile is also observed at $Wi_{app} = 12$ Figure 6.17. Slip becomes increasingly prominent at the inner wall during the shear stress increase to a maximum (Figure 6.17(b)) as with Figure 6.16. Following the overshoot in shear stress, wall slip at the inner wall is reduced and the velocity profile exhibits pronounced curvature for a long time ($28\tau_d$, Figure 6.17(c)). At longer times, the magnitude of the shear rate within the high shear band is reduced temporarily ($69\tau_d$, Figure 6.17(c)). A "stair-stepped" profile then develops ($82\tau_d$) and coarsens into a two-banded profile at steady state ($180\tau_d$).

In summary, for the more entangled PBD-DOP solution with $Z = 66$, we observed significant wall slip at the inner wall that develops shortly after the startup of shear. The magnitude of wall slip varies transiently following the startup of shear but reaches a steady value after shearing for long times.

6.5 Conclusions

The interplay of flow-concentration coupling in entangled polymer solutions was investigated through simultaneous measurements of the velocity and concentration profiles of

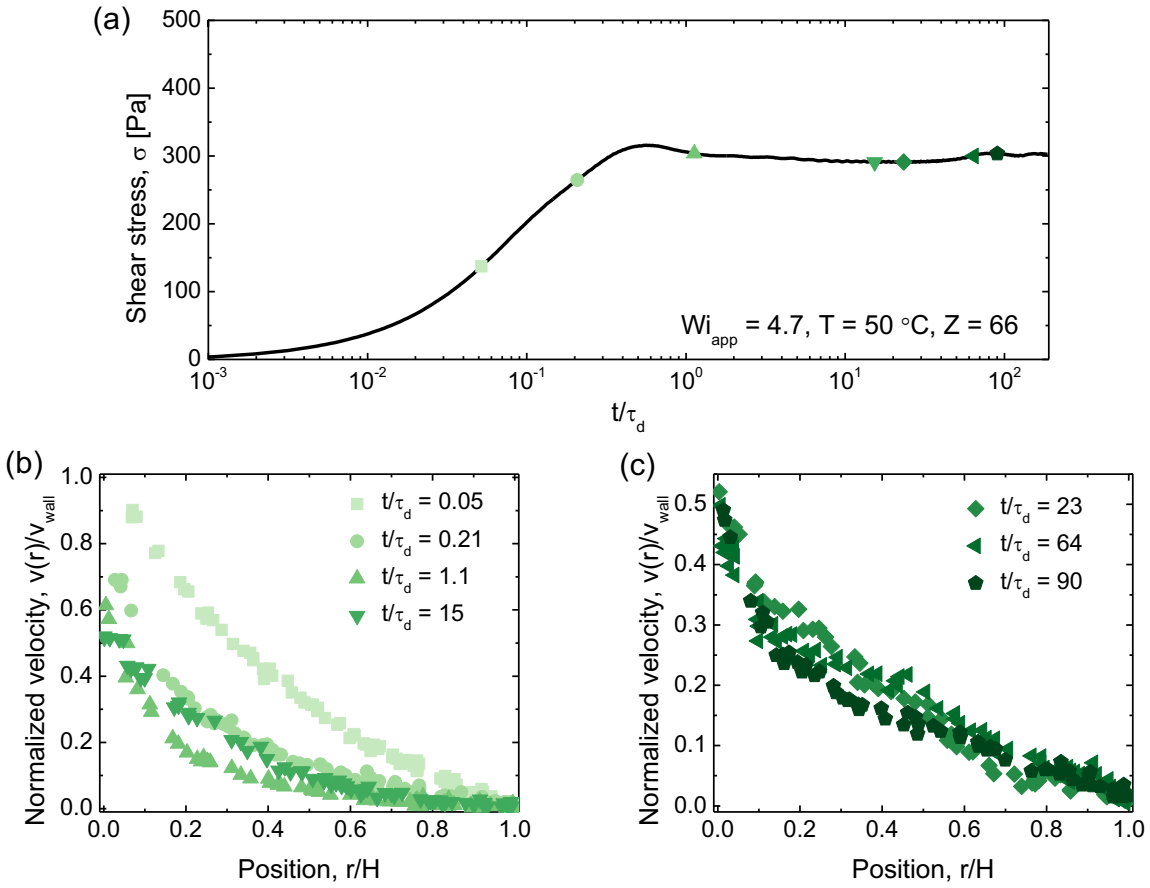

Figure 6.16: Transient response of PBD-DOP solution with $Z = 66$ at $T = 50$ ℃ and $Wi_{app} = 4.7$. (a) the evolution of the measured shear stress following the startup of shear. The symbols correspond to the times at which each velocity profile was measured in (b) and (c). (b) The transient velocity profiles measured from $t/\tau_d = 0.05$ to 15 and (c) from $t/\tau_d = 23$ to 90.1.

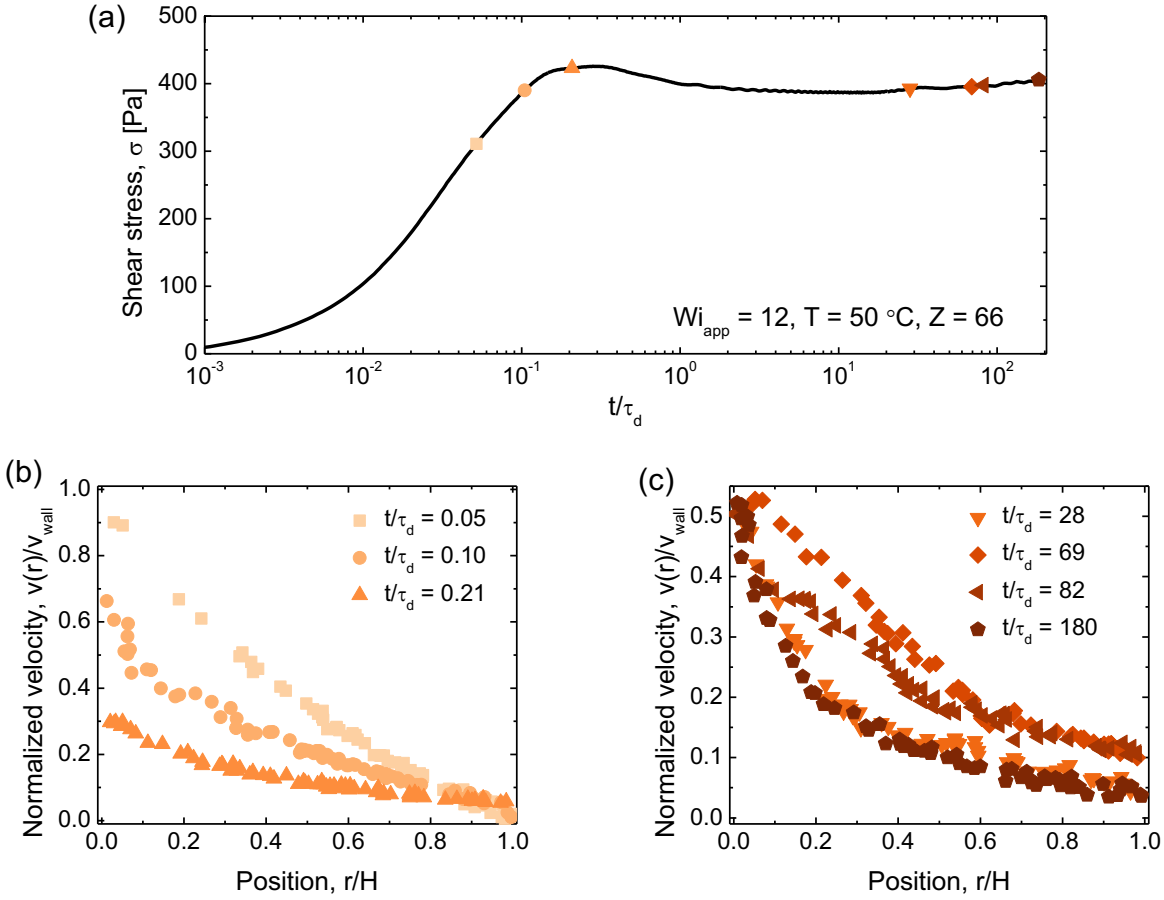

Figure 6.17: Transient response of PBD-DOP solution with $Z = 66$ at $T = 50$ °C and $Wi_{app} = 12$. (a) the evolution of the measured shear stress following the startup of shear. The symbols correspond to the times at which each velocity profile was measured in (b) and (c). (b) The transient velocity profiles measured from $t/\tau_d = 0.05$ to 0.21 and (c) from $t/\tau_d = 28$ to 180.

entangled PBD-DOP solutions and comparison to predictions of a two-fluid Rolie-Poly model. The results revealed that either significantly curved or shear banded velocity profiles develop in Taylor-Couette flow depending on the applied Weissenberg number, number of entanglements, and temperature of the entangled polymer solutions. Measured steady state velocity profiles are analyzed using a statistical method for calculating numerical derivatives of data to determine whether the profiles are shear banded by quantifying the width and location of the interface separating the two bands of different shear rate. Model predicted flow profiles were fit to the experimental measurements using a single adjustable parameter (E) that represents the extent of coupling for flow to the polymer concentration, and specific values of E were found to yield agreement in the flow profiles across a range of applied Weissenberg numbers in solutions at particular levels of entanglement and temperatures. Rheo-fluorescence measurements provide estimates of the steady state concentration profiles that develop under shear and show agreement with the predictions of the two-fluid model. The magnitude of estimated concentration heterogeneity is sensitive to the determined value of E. When the extracted value of E is low, the measured macroscopic concentration variation does not show clear evidence of "bands", as expected from the two-fluid R-P model, which predicts a linear variation in concentration below a threshold value for a flow-induced demixing instability. This linear variation in concentration can be attributed to concentration variation arising from polymer migration across curved streamlines, as reported in dilute solutions [33], rather than a flow-induced demixing instability [15–17]. Although steady state banding is often accompanied by measurable wall slip, wall slip is observed to be neither necessary nor sufficient for the presence of shear banding. These findings provide strong evidence that shear banding can result from flow-concentration coupling in entangled PBD-DOP solutions.

Bibliography

[1] M. C. Burroughs, Y. Zhang, A. M. Shetty, C. M. Bates, L. G. Leal, and M. E. Helgeson, "Flow-Induced Concentration Nonuniformity and Shear Banding in Entangled Polymer Solutions," *Physical Review Letters*, vol. 126, no. 20, p. 207801, 2021.

[2] M. M. Denn, "Extrusion Instabilities and Wall Slip," *Annual Review of Fluid Mechanics*, vol. 33, pp. 265–287, 2001.

[3] T. Divoux, M. A. Fardin, S. Manneville, and S. Lerouge, "Shear Banding of Complex Fluids," *Annual Review of Fluid Mechanics*, vol. 48, no. 1, pp. 81–103, 2016.

[4] P. D. Olmsted, "Perspectives on shear banding in complex fluids," *Rheologica Acta*, vol. 47, no. 3, pp. 283–300, 2008.

[5] N. Germann, "Shear banding in semidilute entangled polymer solutions," *Current Opinion in Colloid & Interface Science*, vol. 39, pp. 1–10, 2019.

[6] E. Menezes and W. W. Graessley, "Nonlinear Rheological Behavior of Polymer Systems for Several Shear-Flow Histories," *Journal of Polymer Science, Part B: Polymer Physics*, vol. 20, pp. 1817–1833, 1982.

[7] Y. T. Hu, L. Wilen, A. Philips, and A. Lips, "Is the constitutive relation for entangled polymers monotonic?," *Journal of Rheology*, vol. 51, no. 2, pp. 275–295, 2007.

[8] G. Marrucci, "Dynamics of entanglements : A nonlinear model consistent with the Cox-Merz rule I," *Journal of Non-Newtonian Fluid Mechanics*, vol. 62, pp. 279–289, 1996.

[9] D. W. Mead, R. G. Larson, and M. Doi, "A Molecular Theory for Fast Flows of Entangled Polymers," *Macromolecules*, vol. 31, no. 22, pp. 7895–7914, 1998.

[10] S. T. Milner, T. C. B. McLeish, and A. E. Likhtman, "Microscopic theory of convective constraint release," *Journal of Rheology*, vol. 45, no. 2, p. 539, 2001.

[11] R. S. Graham, A. E. Likhtman, T. C. B. McLeish, and S. T. Milner, "Microscopic theory of linear, entangled polymer chains under rapid deformation including chain stretch and convective constraint release," *Journal of Rheology*, vol. 47, no. 5, p. 1171, 2003.

[12] C. Rangel-Nafaile, A. B. Metzner, and K. F. Wissbrun, "Analysis of Stress-Induced Phase Separations in Polymer Solutions," *Macromolecules*, vol. 17, pp. 1187–1195, 1984.

[13] X. L. Wu, D. J. Pine, and P. K. Dixon, "Enhanced concentration fluctuations in polymer solutions under shear flow," *Physical Review Letters*, vol. 66, no. 18, pp. 2408–2411, 1991.

[14] M. C. Burroughs, A. M. Shetty, L. G. Leal, and M. E. Helgeson, "Coupled nonhomogeneous flows and flow-enhanced concentration fluctuations during startup shear of entangled polymer solutions," *Physical Review Fluids*, vol. 5, no. 4, p. 043301, 2020.

[15] M. Cromer, M. C. Villet, G. H. Fredrickson, and L. G. Leal, "Shear banding in polymer solutions," *Physics of Fluids*, vol. 25, no. 5, p. 051703, 2013.

[16] M. Cromer, G. H. Fredrickson, and L. G. Leal, "A study of shear banding in polymer solutions," *Physics of Fluids*, vol. 26, no. 6, p. 063101, 2014.

[17] J. D. Peterson, M. Cromer, G. H. Fredrickson, and L. G. Leal, "Shear banding predictions for the two-fluid Rolie-Poly model," *Journal of Rheology*, vol. 60, no. 5, pp. 927–951, 2016.

[18] Y. Li, M. Hu, G. B. McKenna, C. J. Dimitriou, G. H. McKinley, R. M. Mick, D. C. Venerus, and L. A. Archer, "Flow field visualization of entangled polybutadiene solutions under nonlinear viscoelastic flow conditions," *Journal of Rheology*, vol. 57, no. 5, pp. 1411–1428, 2013.

[19] S.-Q. Wang, G. Liu, S. Cheng, P. E. Boukany, Y. Wang, X. Li, Y. Li, M. Hu, G. B. McKenna, C. J. Dimitriou, G. H. McKinley, R. M. Mick, D. C. Venerus, and L. a. Archer, "Letter to the Editor: Sufficiently entangled polymers do show shear strain localization at high enough Weissenberg numbers"," *Journal of Rheology*, vol. 58, no. 4, pp. 1059–1069, 2014.

[20] Y. Li, M. Hu, G. B. McKenna, C. J. Dimitriou, G. H. McKinley, R. M. Mick, D. C. Venerus, and L. A. Archer, "Response to: Sufficiently entangled polymers do show shear strain localization at high enough Weissenberg numbers"," *Journal of Rheology*, vol. 58, no. 4, pp. 1071–1082, 2014.

[21] Y. Li and G. B. McKenna, "Startup shear of a highly entangled polystyrene solution deep into the nonlinear viscoelastic regime," *Rheologica Acta*, vol. 54, no. 9-10, pp. 771–777, 2015.

[22] P. E. Boukany and S.-Q. Wang, "A correlation between velocity profile and molecular weight distribution in sheared entangled polymer solutions," *Journal of Rheology*, vol. 51, no. 2, pp. 217–233, 2007.

[23] P. E. Boukany and S.-Q. Wang, "Exploring the transition from wall slip to bulk shearing banding in well-entangled DNA solutions," *Soft Matter*, vol. 5, pp. 780–789, 2009.

[24] P. E. Boukany, S.-Q. Wang, S. Ravindranath, and L. J. Lee, "Shear banding in entangled polymers in the micron scale gap: a confocal-rheoscopic study," *Soft Matter*, vol. 11, pp. 8058–8068, 2015.

[25] S.-Q. Wang, S. Ravindranath, and P. E. Boukany, "Homogeneous shear, wall slip, and shear banding of entangled polymeric liquids in simple-shear rheometry: A roadmap of nonlinear rheology," *Macromolecules*, vol. 44, no. 2, pp. 183–190, 2011.

[26] K. A. Hayes, M. R. Buckley, H. Qi, I. Cohen, and L. A. Archer, "Constitutive curve and velocity profile in entangled polymers during start-up of steady shear flow," *Macromolecules*, vol. 43, no. 9, pp. 4412–4417, 2010.

[27] K. A. Hayes, M. R. Buckley, I. Cohen, and L. A. Archer, "High resolution shear profile measurements in entangled polymers," *Physical Review Letters*, vol. 101, no. 21, p. 218301, 2008.

[28] P. Cheng, M. C. Burroughs, L. G. Leal, and M. E. Helgeson, "Distinguishing shear banding from shear thinning in flows with a shear stress gradient," *Rheologica Acta*, vol. 56, no. 12, pp. 1007–1032, 2017.

[29] S. M. Fielding and P. D. Olmsted, "Early stage kinetics in a unified model of shear-induced demixing and mechanical shear banding instabilities.," *Physical review letters*, vol. 90, no. 22, p. 224501, 2003.

[30] S. M. Fielding and P. D. Olmsted, "Kinetics of the shear banding instability in startup flows.," *Physical Review E*, vol. 68, no. 3, p. 036313, 2003.

[31] S. M. Fielding and P. D. Olmsted, "Flow phase diagrams for concentration-coupled shear banding," *European Physical Journal E*, vol. 11, no. 1, pp. 65–83, 2003.

[32] S. Ravindranath, S.-Q. Wang, M. Olechnowicz, and R. P. Quirk, "Banding in simple steady shear of entangled polymer solutions," *Macromolecules*, vol. 41, no. 7, pp. 2663–2670, 2008.

[33] M. J. MacDonald and S. J. Muller, "Experimental study of shear-induced migration of polymers in dilute solutions," *Journal of Rheology*, vol. 40, no. 2, p. 259, 1996.

[34] Y. T. Hu and A. Lips, "Kinetics and mechanism of shear banding in an entangled micellar solution," *Journal of Rheology*, vol. 49, no. 5, pp. 1001–1027, 2005.

[35] J. Crocker and D. Grier, "Methods of Digital Video Microscopy for Colloidal Studies," *Journal of Colloid and Interface Science*, vol. 179, no. 1, pp. 298–310, 1996.

[36] R. H. Colby, L. J. Fetters, W. G. Funk, and W. W. Graessley, "Effects of Concentration and Thermodynamic Interaction on the Viscoelastic Properties of Polymer Solutions," *Macromolecules*, vol. 24, pp. 3873–3882, 1991.

[37] K. B. Migler, H. Hervet, and L. Leger, "Slip transition of a polymer melt under shear stress," *Physical Review Letters*, vol. 70, no. 3, pp. 287–290, 1993.

[38] L. A. Archer, R. G. Larson, and Y. L. Chen, "Direct Measurements of Slip in Sheared Polymer Solutions," *Journal of Fluid Mechanics*, vol. 301, pp. 133–151, 1995.

[39] V. R. Mhetar and L. A. Archer, "Slip in Entangled Polymer Solutions," *Macromolecules*, vol. 31, no. 19, pp. 8617–8622, 1998.

[40] V. Mhetar and L. A. Archer, "Slip in Entangled Polymer Melts . 1 . General Features," *Macromolecules*, vol. 31, no. 24, pp. 8607–8616, 1998.

[41] Y. T. Hu, C. Palla, and A. Lips, "Comparison between shear banding and shear thinning in entangled micellar solutions," *Journal of Rheology*, vol. 52, no. 2, pp. 379–400, 2008.

[42] K. W. Feindel and P. T. Callaghan, "Anomalous shear banding: Multidimensional dynamics under fluctuating slip conditions," *Rheologica Acta*, vol. 49, no. 10, pp. 1003–1013, 2010.

[43] H. Tang, T. Kochetkova, H. Kriegs, J. K. G. Dhont, and M. P. Lettinga, "Shear-banding in entangled xanthan solutions: tunable transition from sharp to broad shear-band interfaces," *Soft Matter*, vol. 14, pp. 826–836, 2018.

[44] H. Mohammadigoushki and S. J. Muller, "A flow visualization and superposition rheology study of shear-banding wormlike micelle solutions," *Soft Matter*, vol. 12, pp. 8–11, 2015.

[45] P. E. Boukany, Y. T. Hu, and S.-Q. Wang, "Observations of wall slip and shear banding in an entangled DNA solution," *Macromolecules*, vol. 41, no. 7, pp. 2644–2650, 2008.

[46] S. Ravindranath and S.-Q. Wang, "Steady state measurements in stress plateau region of entangled polymer solutions: Controlled-rate and controlled-stress modes," *Journal of Rheology*, vol. 52, no. 2008, p. 957, 2008.

Chapter 7

A two-fluid model for entangled bidisperse polymer blends[1]

7.1 Introduction

The purpose of this Chapter is to introduce a theoretical description of bidisperse entangled polymer blends and recent advances in the modeling of such polymer melts. The vast majority of industrially relevant polymers are polydisperse with a smoothly varying molecular weight distribution; however, the rheological behaviors of these systems are notoriously difficult to predict given the many different types of chain entanglements present. To this end, bidisperse blends are an important class of polymer melts as they offer a systematic method to understand effects of dispersity on the fluid rheology. This Chapter describes the different dynamics of bidisperse blends depending on composition of long and short polymer chains. Constitutive models for entangled polymer melts typically assume that the fluid is monodisperse, and historically, polydispersity effects

[1]This Chapter is largely based off of the recent publications by Boudara *et al.* (2019) [1] and Peterson *et al.* (2020) [2].

have been accounted for by a simple linear superposition of monodisperse constitutive equations, weighted by the volume fraction of blend components. This Chapter begins with an introduction to the two-fluid formalism, first discussed in Chapter 3, extended to describe polymer blends (*i.e.*, both components of the fluid are polymeric). Theory predicts shear-induced demixing effects, like in entangled polymer solutions, that depend on the blend composition. Predicted compositional changes are significantly higher in bidisperse blends than solutions, with the local composition of long chain polymers predicted to vary by as much as $\approx 60\%$!

7.2 Categorizing the rheology of bidisperse blends

Bidisperse polymer blends contain polymer species of two different molecular weights. This dispersity of polymer molecular weight complicates the description of entanglement dynamics compared to monodisperse solutions and melts. In a monodisperse polymer melt, reptation is the main mechanism for stress relaxation, because all the chains are the same size; thus, neighboring chains release their constraints on the same time scale as reptation. In a bidisperse blend, long chains are confined by both long and short chains for a finite time, and in some cases, the short chain constraints are released on a timescale much shorter than long chain reptation. Thus, different rheology and polymer chain dynamics are expected depending on the volume fraction and molecular weight of each polymer species. Early experiments by Struglinski and Graessley found that the measured small amplitude oscillatory shear rheology of bidisperse blends displayed qualitatively different behaviors as the long chain volume fraction was increased, depending on the ratio of long and short chain molecular weights [3]. This ratio was defined by what later

became known as the Graessley number (Gr)

$$Gr = \frac{M_L M_e^2}{M_S^3} \tag{7.1}$$

where M_L is the molecular weight of the long chains, M_e is the entanglement molecular weight, and M_S is the molecular weight of the short chains. Specifically, for $Gr \ll 1$, the molecular weights are comparable in size and the frequency at which G'' is maximum ($\omega_{m,L}$) due to the long chains depends on the long chain volume fraction (ϕ_L) according to $\omega_{m,L} = \omega^0_{m,L}\phi_L$, where $\omega^0_{m,L}$ is the frequency at which G'' is maximum for a monodisperse melt of the long chain polymer. This is equivalent to assuming that only entanglements between long chains and other long chains contribute to the viscoelastic relaxation. For $Gr \gg 1$, the frequency at which G'' is a maximum is insensitive to ϕ_L, such that $\omega_{m,L} = \omega^0_{m,L}$ [3]. This is equivalent to assuming that all entanglements of the long chains contribute equally to the viscoelastic relaxation, regardless of whether they are with long or short chains.

The conceptual idea used to reconcile the behavior in between these two limits was that of a long chain confined within two tubes [4, 5]. A "fat" tube, to characterize the entanglements between long chains, and a "thin" tube, to characterize the combined short and long chain entanglements. In addition to describing the relative size of the polymer chains, Gr also represents the ratio of time scales for reptation of the long chain ($\tau_{d,L}$) and Rouse constraint release (τ_{RCR}), where τ_{RCR} represents relaxation of the thin tube by constraint release of the short chains. Previously, τ_{RCR} has also been referred to as "tube reorganization" [4, 6].

Reconciliation of how to properly describe the tube dynamics once constraint release of the short chains occurs is still ongoing. One idea is that the long chain reptates along the fat tube once constraint release by the short chains has occurred, with a diffusion

coefficient solely dependent on chain friction [5]. Alternatively, others believe that the motion of the long chain through the fat tube is dependent upon friction related to the constraint release of short chains [4]. The former school of thought appears consistent with experimental observations of the acceleration of long chain reptation as long chains are diluted by shorter chains [7, 8]. These initial theoretical descriptions for bidisperse blends neglected contributions to stress relaxation dynamics resulting from contour length fluctuations (CLFs) [9]. Recently, the role of CLFs was included in tube-based models for bidisperse polymer blends [10, 11]. In doing so, it was shown that the acceleration of long chain reptation by dilution with short chains can be accounted for with CLFs.

These different tube dynamics for bidisperse polymer blends were assumed to occupy different regions in a Viovy diagram [4], which as originally constructed, contained four different regions depending on Gr and the number of effective long chain entanglements ($\tilde{Z}_L = \phi_L Z_L$) (Figure 7.1). In Region I of the Viovy diagram, neither the long nor short chains are entangled. In Region II, the short chains are entangled, but the long chain is dilute and unentangled with other long chains. The long chain confining tube is therefore "thin" since the entanglements that comprise the tube come from entanglements with short chains. In Region III, both the long and short chains are entangled. In Region IV, the long chains are entangled with other, the short chains may also be entangled at low Gr. In the limit of high Gr, a Region IV blend behaves as an entangled polymer solution.

7.3 The two-fluid formalism for bidisperse blends

Given a suitable constitutive description, the two-component bidisperse polymer blend can also be described according to a two-fluid model, similar to entangled polymer solutions. A notable distinction for bidisperse blends is that both components are vis-

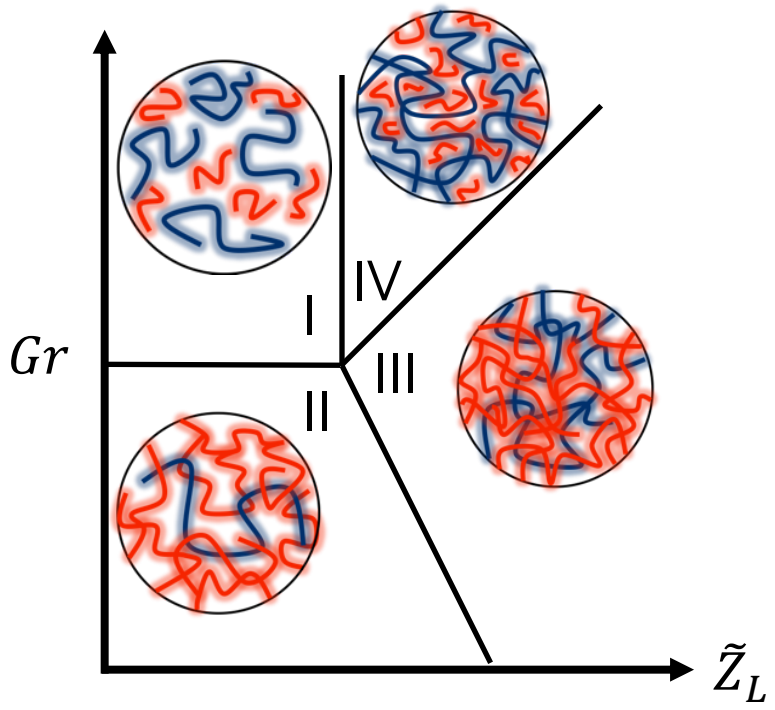

Figure 7.1: Cartoon illustration of the Viovy diagram which characterizes regions of different rheological behavior depending on Gr and Z_L.

coelastic and exhibit non-Newtonian rheology. An added complexity is the issue of how to account for entanglements of different types (*i.e.*, entanglement points made up of long-long, long-short, short-long, and short-short chains). Nevertheless, short and long chain force balances are written as follows

$$\zeta_S(\boldsymbol{u}_S - \boldsymbol{u}_T) = \nabla\frac{\delta F}{\delta\phi_S} + \nabla P - \frac{\zeta_S}{\bar{\zeta}}\boldsymbol{\mathcal{F}} - \eta_D\nabla^2\langle\boldsymbol{u}\rangle \tag{7.2}$$

$$\zeta_L(\boldsymbol{u}_L - \boldsymbol{u}_T) = \nabla\frac{\delta F}{\delta\phi_L} + \nabla P - \frac{\zeta_L}{\bar{\zeta}}\boldsymbol{\mathcal{F}} - \eta_D\nabla^2\langle\boldsymbol{u}\rangle \tag{7.3}$$

with ζ_S and ζ_L representing the drag coefficient of short and long chains, respectively, $\boldsymbol{u}_T$ is the "tube velocity", F is the free energy of the system (includes both elastic and mixing forces), P is the total pressure, $\boldsymbol{\mathcal{F}}$ is a description of elastic body forces that

promote migration due to an imbalance of stress across components in the system, η_D represents a small Newtonian viscosity contribution to the stress that may arise from the volume-averaged velocity ($\langle \boldsymbol{u} \rangle$). Specific expressions for F and $\boldsymbol{\mathcal{F}}$ can be found in Peterson *et al.* (2020) [12]. The mean velocity ($\langle \boldsymbol{u} \rangle$) is defined as the volume fraction weighted sum of species velocities

$$\langle \boldsymbol{u} \rangle = \phi_L \boldsymbol{u}_L + \phi_S \boldsymbol{u}_S. \tag{7.4}$$

For blends, it makes more sense conceptually to describe the relative motion of short and long chains from a "tube velocity" which is defined as

$$\boldsymbol{u}_T = \frac{1}{\bar{\zeta}}(\zeta_L \phi_L \boldsymbol{u}_L + \zeta_S \phi_S \boldsymbol{u}_S) \tag{7.5}$$

and is a measure of the collective motion of neighboring constraints. The mean drag coefficient ($\bar{\zeta}$) is defined as the volume fraction weighted sum of the short (ζ_S) and long (ζ_L) chain drag coefficients

$$\bar{\zeta} = \zeta_L \phi_L + \zeta_S \phi_S. \tag{7.6}$$

7.4 Describing bidisperse polymer blends in terms of the Rolie-Double-Poly model

Stresses are calculated by a sum of individual short and long chain configuration tensors, each weighted by their respective volume fractions

$$\boldsymbol{\sigma}(t) = G_N^0(\phi_S \boldsymbol{Q}_S(t) + \phi_L \boldsymbol{Q}_L(t)) \tag{7.7}$$

where G_N^0 is the plateau modulus and $\boldsymbol{Q}_i$ is the configuration tensor of either long or short chains. To account for chain entanglements comprised of polymers of different molecular weight, each configuration tensor ($\boldsymbol{Q}_i$) is defined as

$$\boldsymbol{Q}_S = \phi_S \boldsymbol{Q}_{SS} + \phi_L \boldsymbol{Q}_{SL} \tag{7.8}$$

and

$$\boldsymbol{Q}_L = \phi_L \boldsymbol{Q}_{LL} + \phi_S \boldsymbol{Q}_{LS}. \tag{7.9}$$

7.4.1 Rolie-Double-Poly (RDP) constitutive equation for bidisperse polymer melts

In its original form, the Rolie-Poly model was derived as a single-mode approximation of the GLaMM model for monodisperse polymer melts. Recent work [1], inspired by the double reptation idea [13, 14], and derived from a more detailed extension of the GLaMM model for bidisperse blends [10], extended the monodisperse Rolie-Poly model to account for polydispersity. The Rolie-Double-Poly model for polydisperse polymers is defined as

$$\begin{aligned}\frac{\partial \boldsymbol{Q}_{ij}}{\partial t} + \boldsymbol{u}_T \cdot \nabla \boldsymbol{Q}_{ij} - (\nabla \boldsymbol{u}_T)^T \cdot \boldsymbol{Q}_{ij} - \boldsymbol{Q}_{ij} \cdot \nabla \boldsymbol{u}_T = \\ - \frac{1}{2}[\frac{1}{\tau_{d,i}} + \frac{1}{\tau_{d,j}}](\boldsymbol{Q}_{ij} - \boldsymbol{I}) - \frac{1}{2}[f_{ret,i} + f_{ret,j}]\boldsymbol{Q}_{ij} - \frac{1}{2}[\frac{f_{ret,i}}{\lambda_i} + \frac{f_{ret,j}}{\lambda_j}](\boldsymbol{Q}_{ij} - \boldsymbol{I})\end{aligned} \tag{7.10}$$

where the subscripts i and j are denoted either s or l for short or long chains, respectively. The left-hand side of the equation is the upper-convected time derivative. The first term of the right-hand side describes stress relaxation by reptation (τ_d is the reptation time), where the blend rate of reptation is the average reptation rate of short and long chains. The second term of the right-hand side of the equation describes the removal of entanglements by retraction of neighboring chains (convective constraint release, CCR).

The f_{ret} term quantifies the rate of chain retraction according to

$$f_{ret,i} = \frac{2}{\tau_{R,i}}(1 - \frac{1}{\lambda_i}) \tag{7.11}$$

where τ_R is the Rouse time and λ_i quantifies the degree of chain stretch, defined as

$$\lambda_i = \sqrt{\frac{Tr\,\boldsymbol{Q}_i}{3}} \tag{7.12}$$

The last term of the right-hand side represents the relaxation from chain stretch when the deformation rate exceeds the Rouse time. Importantly, this Rolie-Double-Poly constitutive equation reduces to the monodisperse Rolie-Poly equation when the short and long chains are the same size (*i.e.*, no chain dispersity). Finally, compositional changes evolve according to the species continuity equations, describing polymer migration across curved streamlines

$$\frac{\partial \phi_L}{\partial t} = -\nabla \cdot (\phi_L \boldsymbol{u}_L) \tag{7.13}$$

and

$$\frac{\partial \phi_S}{\partial t} = -\nabla \cdot (\phi_S \boldsymbol{u}_S). \tag{7.14}$$

7.4.2 Symmetric Rolie-Double-Poly (SRDP)

To simplify the model equations, and therefore reduce the computational expense, the Symmetric Rolie-Double-Poly (SRDP) formulation assumes that the entanglements formed between different species are equivalent such that

$$\boldsymbol{Q}_{SL} = \boldsymbol{Q}_{LS}. \tag{7.15}$$

This approximation has previously been shown to retain sufficient accuracy of the RDP model for most cases [1].

7.5 Stability predictions

A linear stability analysis of the model equations for bidisperse polymer blends predicts regions of instability depending on the chain dispersity ($I_P = \bar{Z} \sum_i^N \frac{\phi_i}{z_i}$) and applied Wi (Figure 7.2). The unstable region extends to lower Wi and a greater region of dispersity as the number of long chain entanglements increases. Interestingly, the predicted unstable region extends to $Wi < 1$, suggesting that nonuniform flows develop prior to the nonlinear flow regime.

7.6 Transient flow calculations using the two-fluid RDP model

As shown by the linear stability analysis, bidisperse blends are predicted to undergo a shear-induced demixing instability, similar to what was predicted [2, 15, 16] and observed [17] in entangled polymer solutions, which leads to spatial heterogeneities in the molecular weight distribution [12]. Figure 7.3 illustrates the transient evolution of this shear-induced demixing behavior in a bidisperse polymer blend. At short times following the growth of concentration heterogeneities, the nonuniform concentration profile adopts a preferred wavelength for shear-induced demixing (Figure 7.3(a)). At moderate times, significant shear-induced demixing has occurred, resulting in spatial variations of $\approx 60\%$ in ϕ_L, with sharp interfaces separating regions of differing blend composition Figure 7.3(b). Finally, at steady-state the concentration profile contains significant compositional nonuniformity (Figure 7.3(c)), that coincides with a shear banded velocity

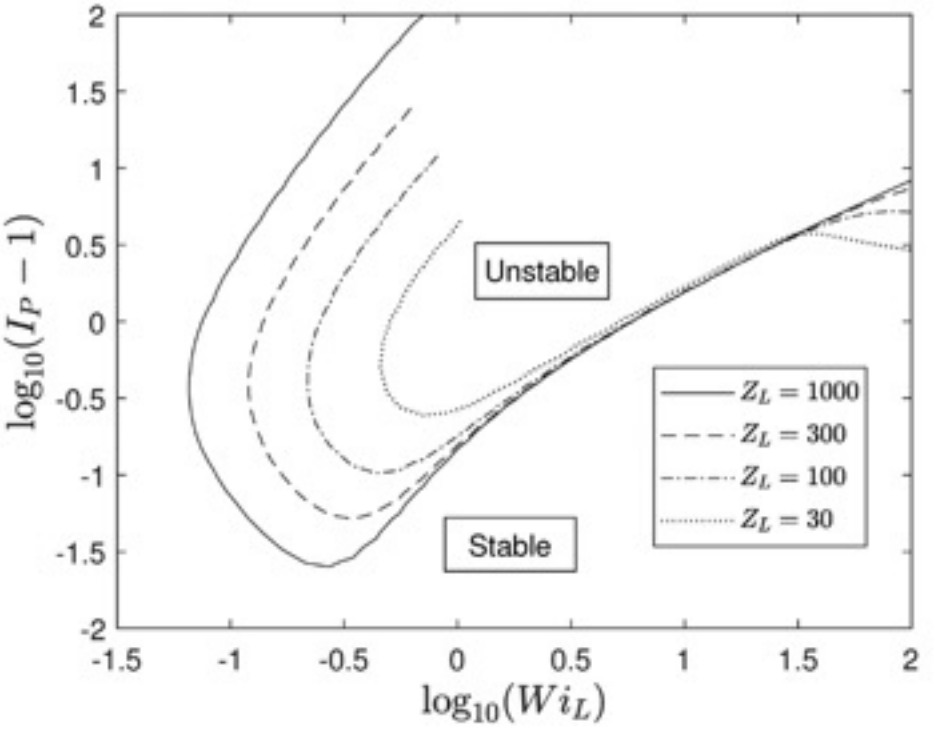

Figure 7.2: Predicted stability depending on the dispersity ($I_P = \bar{Z}(\frac{\phi_L}{Z_L} + \frac{\phi_S}{Z_S})$) of the blend and applied Wi for a bidisperse blend with $\phi_L = 0.5$. The unstable region extends to lower Wi and a larger dispersity range as Z_L increases. Reprinted with permission from Peterson, Fredrickson, and Leal, *Journal of Rheology*, **64**, 1391, (2020). Copyright 2020, The Society of Rheology.

profile [12].

7.7 Summary

This chapter summarizes the key ideas pertinent to a two-fluid theory for bidisperse polymer blends. The chapter begins with a historical summary of conceptual advances in describing bidisperse polymer blends, particularly the role of constraint release. Recent advances in the constitutive modeling for polydisperse polymer melts are then discussed with respect to the special case of bidispersity. This two-fluid theory is shown to predict large changes in fluid composition for chemically identical polymer blends, suggesting that significant nonuniform flows develop in these systems.

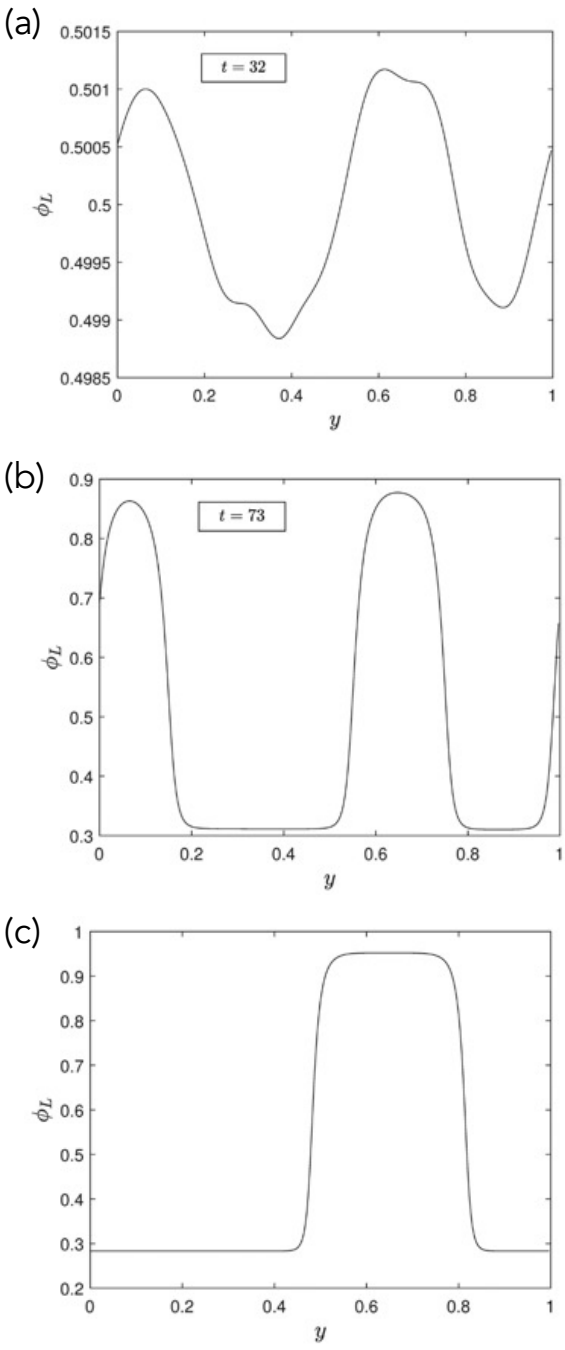

Figure 7.3: Transient evolution of shear-induced demixing of a Region III bidisperse blend with $Z_L = 100$ and $Z_S = 30$ deformed under a constant shear stress ($\sigma_{xy} = 0.16$) at (a) short times following the onset of concentration heterogeneity growth, (b) moderate times, and (c) steady state. Reprinted with permission from Peterson, Fredrickson, and Leal, *Journal of Rheology*, **64**, 1391, (2020). Copyright 2020, The Society of Rheology.

Bibliography

[1] V. A. H. Boudara, J. D. Peterson, L. G. Leal, and D. J. Read, "Nonlinear rheology of polydisperse blends of entangled linear polymers: Rolie-Double-Poly models," *Journal of Rheology*, vol. 63, no. 1, pp. 71–91, 2019.

[2] J. D. Peterson, M. Cromer, G. H. Fredrickson, and L. G. Leal, "Shear banding predictions for the two-fluid Rolie-Poly model," *Journal of Rheology*, vol. 60, no. 5, pp. 927–951, 2016.

[3] M. J. Struglinski and W. W. Graessley, "Effects of Polydispersity on the Linear Viscoelastic Properties of Entangled Polymers. 1. Experimental Observations for Binary Mixtures of Linear Polybutadiene," *Macromolecules*, vol. 18, no. 12, pp. 2630–2643, 1985.

[4] J. L. Viovy, M. Rubinstein, and R. H. Colby, "Constraint Release in Polymer Melts: Tube Reorganization versus Tube Dilation," *Macromolecules*, vol. 24, no. 12, pp. 3587–3596, 1991.

[5] M. Doi, W. W. Graessley, E. Helfand, and D. S. Pearson, "Dynamics of Polymers in Polydisperse Melts," *Macromolecules*, vol. 20, no. 8, pp. 1900–1906, 1987.

[6] P. G. De Gennes, "Dynamics of Entangled Polymer Solutions. I. The Rouse Model," *Macromolecules*, vol. 9, no. 4, pp. 587–593, 1976.

[7] H. Watanabe, S. Ishida, Y. Matsumiya, and T. Inoue, "Test of full and partial tube dilation pictures in entangled blends of linear polyisoprenes," *Macromolecules*, vol. 37, no. 17, pp. 6619–6631, 2004.

[8] H. Watanabe, S. Ishida, Y. Matsumiya, and T. Inoue, "Viscoelastic and Dielectric Behavior of Entangled Blends of Linear Polyisoprenes Having Widely Separated Molecular Weights: Test of Tube Dilation Picture," *Macromolecules*, vol. 37, no. 5, pp. 1937–1951, 2004.

[9] M. Doi, "Explanation for the 3.4 power law of viscosity of polymeric liquids on the basis of the tube model," *Journal of Polymer Science: Polymer Letters Edition*, vol. 19, no. 5, pp. 265–273, 1981.

[10] D. J. Read, K. Jagannathan, S. K. Sukumaran, and D. Auhl, "A full-chain constitutive model for bidisperse blends of linear polymers," *Journal of Rheology*, vol. 56, no. 4, pp. 823–873, 2012.

[11] D. J. Read, M. E. Shivokhin, and A. E. Likhtman, "Contour length fluctuations and constraint release in entangled polymers: Slip-spring simulations and their implications for binary blend rheology," *Journal of Rheology*, vol. 62, no. 4, pp. 1017–1036, 2018.

[12] J. D. Peterson, G. H. Fredrickson, and L. G. Leal, "Shear Induced Demixing in Bidisperse and Polydisperse Polymer Blends: Predictions From a Multi-Fluid Model," *Journal of Rheology*, vol. 64, no. 6, p. 1391, 2020.

[13] J. Des Cloizeaux, "Double Reptation vs. Simple Reptation in Polymer Melts," *Europhysics Letters*, vol. 5, no. 5, pp. 437–442, 1988.

[14] M. Rubinstein and R. H. Colby, "Self-consistent theory of polydisperse entangled polymers: Linear viscoelasticity of binary blends," *The Journal of Chemical Physics*, vol. 89, no. 8, pp. 5291–5306, 1988.

[15] M. Cromer, M. C. Villet, G. H. Fredrickson, and L. G. Leal, "Shear banding in polymer solutions," *Physics of Fluids*, vol. 25, no. 5, p. 051703, 2013.

[16] M. Cromer, G. H. Fredrickson, and L. G. Leal, "A study of shear banding in polymer solutions," *Physics of Fluids*, vol. 26, no. 6, p. 063101, 2014.

[17] M. C. Burroughs, A. M. Shetty, L. G. Leal, and M. E. Helgeson, "Coupled nonhomogeneous flows and flow-enhanced concentration fluctuations during startup shear of entangled polymer solutions," *Physical Review Fluids*, vol. 5, no. 4, p. 043301, 2020.

Chapter 8

A study of the flow kinematics and composition of entangled bidisperse polymer blends[1]

8.1 Abstract

Polymer processing often involves mixtures of polymers with disparate molecular weights. Recently, two- and multi-fluid models have incorporated molecularly informed constitutive models of linear, entangled polymers to account for chain dispersity in the molecular weight distribution. Interestingly, the two-fluid model for bidisperse blends was found to predict shear-induced demixing, similar to what has been reported in entangled polymer solutions, due to asymmetry between long and short polymer chains. This work investigates the extent to which nonuniform flows develop during shearing of entangled bidisperse blends. Three blend formulations are studied including two blends which

[1]The contents of this Chapter are in preparation to be submitted for publication in the form of a journal article.

correspond to Region III and Region IV in the original Viovy diagram and a third blend, which is a bidisperse mixture of entangled long and short chains diluted in an oligomer solvent. All three blend formulations are predicted to undergo shear-induced demixing for certain applied shear rates according to a recent two-fluid theory. A combination of particle tracking velocimetry and fluorescence measurements are performed to quantify the flow and concentration profiles, respectively. Results suggest that while nonuniform flows are observed in both Region III and Region IV blends, it is inconclusive whether these nonuniformities arise from heterogeneities in composition.

8.2 Introduction

Industrial processing of polymeric materials often involves complex mixtures of polymer melts that exhibit immiscibility, differing chain architecture, and/or a distribution of molecular weights. Blending polymers of disparate chemistry, architecture, and molecular weight allow for optimization of material properties towards the intended application. As such, molecularly informed models for polymeric materials are imperative for the design and implementation of materials processing strategies [1, 2]. Despite the utility and ubiquity of polymer blends, molecularly based constitutive models are typically developed for the simple case of single component, monodisperse polymer melts [1].

In a bidisperse polymer melt, two polymers of differing molecular weight, but identical constituent chemistry, are blended together. Different rheology is observed depending on the size disparity between polymer chains and the long chain volume fraction [3]. The dynamics of bidisperse blends are categorized within the so-called "Viovy Diagram" [4] (Figure 8.1) according to the long chain volume fraction (ϕ_L) and the Graessley number (Gr)

$$Gr = \frac{M_L M_e^2}{M_S^3} = \frac{Z_L}{Z_S^3} \tag{8.1}$$

where Z_L is the number of long chain entanglements in a melt of pure long chains and Z_S is the number of short chain entanglements in a melt of pure short chains. The Viovy Diagram categorizes the dynamics of bidisperse polymer blends into four regions [4]. In Region I, both the long and short chains are unentangled with themselves and with one another. In Region II, Gr is small indicating a small size discrepancy between the short and long chains, and the long chains are dilute relative to other long chains. Thus, Region II blends can be viewed as dilute long chains within a matrix of entangled short chains. In Region III, both the long and short chains are entangled with one another, and the relaxation time of short chains is comparable to that of long chains. In Region IV, the long chains are entangled with one another and relax on timescales much longer than the short chains. In the limit of high Gr, a Region IV blend can be viewed as an entangled polymer solution that is chemically homologous.

Until recently, the rheology of bidisperse polymer blends has been described using the "double reptation" approximation [5, 6] with simplistic constitutive models that account for few mechanisms for stress relaxation in each of the components. Recently, modeling of bidisperse entangled polymer blends (and, by extension, polydisperse mixtures generally) has been improved by applying the double reptation approximation to more accurate constitutive models for entangled polymers, namely the Rolie-Poly model [7] in a suitably named Rolie-Double-Poly (RDP) model [8]. The computational cost of this model is reduced by assuming long-short and short-long chain entanglement points are identical, yielding a Symmetric Rolie-Double-Poly (SRDP) model that agrees well with experimental data [8].

Importantly, the development of the SRDP model enables self-consistent flow calculations of bidisperse entangled polymer blends, but it also allows for the exploration of flow-induced changes to fluid composition [9], as has been explored previously in polymer solutions [10–12]. The SRDP model predicts shear-induced demixing of long and

short polymer chains to arise due to size contrast between polymer chains, leading to large disparities in local molecular weight distributions in the flow. These predictions are potentially consistent with a number of reported flow complications in the industrial processing of polymer materials, such as melt fracture and die drool [13]. Surprisingly, these flow-induced compositional changes are found to occur even below $Wi = 1$, suggesting that nonlinear flows are not necessary for these effects to manifest. Additionally, the predictions for shear-induced demixing assume that the bidisperse polymer blend is chemically homologous, signifying that differences in polymer chemistry are unnecessary for shear-induced compositional changes. This finding is in contrast to previous studies of shear-induced mixing and demixing of polymer blends which have exclusively investigated bidisperse blends of chemically different polymers [14–28]. To date, there are a large amount of data that quantify the rheology of chemically homologous bidisperse polymer blends from small amplitude oscillatory shear [3, 29–35]. Comparatively few studies have explored linear and nonlinear steady shear flows of these bidisperse blends and the resulting flow profiles.

In this work, the kinematics and composition of three different classes of bidisperse entangled polymer blends are studied using rheo-particle tracking velocimetry (rheo-PTV) and rheo-fluorescence microscopy. Region III and IV blends are compared with a Region III blend "in solution" which is a 3-component blend where the long and short chain polymers are diluted with an oligomeric solvent. The number of entanglements in each blend is held fixed ($Z \approx 40$) to enable comparison with past work on entangled polymer solutions. Departures from uniform flow are observed that coincide with theoretically predicted regions for shear-induced demixing according to the SRDP model. In general, it is unclear whether the observed flow nonuniformity results from measurable macroscopic variations to the polymer composition in contrast with recent work on entangled polybutadiene solutions [36].

8.3 Materials and experimental methods

8.3.1 Materials

1,4-polybutadiene (PBD, $M_w = 8.17 \times 10^5$, 4.30×10^5, 1.69×10^5, and 1.84×10^4 g/mol with $Đ = 1.05$, 1.03, 1.07, and 1.02) was purchased from Polymer Standards Services GmbH. Low molecular weight polybutadiene (o-PBD, $M_w \approx 1.5 \times 10^3$), anhydrous tetrahydrofuran (THF, CAS: 109-99-9, ≥ 99.9 %), 7-methyl-3-mercapto-coumarin (CAS: 137215-27-1, ≥ 97.0 % purity), and 2,2-dimethoxy-2-phenylacetophenone (DMPA, CAS: 24650-42-8, 99 % purity) were purchased from Sigma-Aldrich and used without further purification. Glass tracer particles ($\approx 10\,\mu$m in diameter) were donated by TSI, Inc.

8.3.2 Sample preparation

Entangled polymer blends were prepared by adding desired pure melts of particular molecular weights together with ≈ 30 mL toluene to aid in dissolution. The samples were mixed with a magnetic stir bar at $T = 50$ °C with a stir rate of $50 - 100$ rpm. Once the samples became homogeneous, the vials were uncapped under constant stirring to enable toluene cosolvent evaporation. After several days, the samples became too viscous to mix with a stir bar, so the vials were transferred to a vacuum oven to remove the residual toluene prior to conducting experiments.

The total number of entanglements in each blend ($\bar{Z}$) was determined from the volume-weighted sum of pure components

$$\bar{Z} = \phi_L Z_L + \phi_S Z_S \tag{8.2}$$

where ϕ_L and ϕ_S are the long and short volume fractions, respectively. Z_L and Z_S are the number of long and short chain entanglements, respectively, determined from $Z = \frac{M_w}{M_e}$

where M_e is the entanglement molecular weight.

For rheo-particle tracking velocimetry measurements, $300 - 500$ ppm of glass tracer particles were added to samples during sample preparation to enable flow visualization. For rheo-fluorescence measurements, 2000 ppm of PBDC was added to solution during sample preparation.

8.3.3 Rheo-particle tracking velocimetry (rheo-PTV)

In situ velocimetry measurements were performed during rheological measurements using a custom optical setup fitted to a Paar Physica MCR 300 rheometer. Specifics of the device are described in detail elsewhere [37–39].

8.3.4 Rheo-fluorescence microscopy

In situ fluorescence measurements were performed by adding trace amounts of fluorescently tagged polybutadiene to the entangled bidisperse blends and illuminated using bandpass filters described in detail elsewhere [36]. The recorded fluorescence intensity was related to the composition of the long chain polymer species by

$$\frac{\phi(r,t,\dot{\gamma})}{\phi_0} \approx \frac{I(r,t,\dot{\gamma}) - I_{bg}}{I_0 - I_{bg}} \tag{8.3}$$

where $I(r,t,\dot{\gamma})$ is the fluorescence intensity under flow, I_{bg} is the background image intensity and I_o is the quiescent fluorescence intensity.

8.3.5 Fluorescent-tagging reaction

Polybutadienes of varying molecular weight were fluorescently tagged with the fluorophore 7-mercapto-4-methylcoumarin according to the following procedure. PBD was

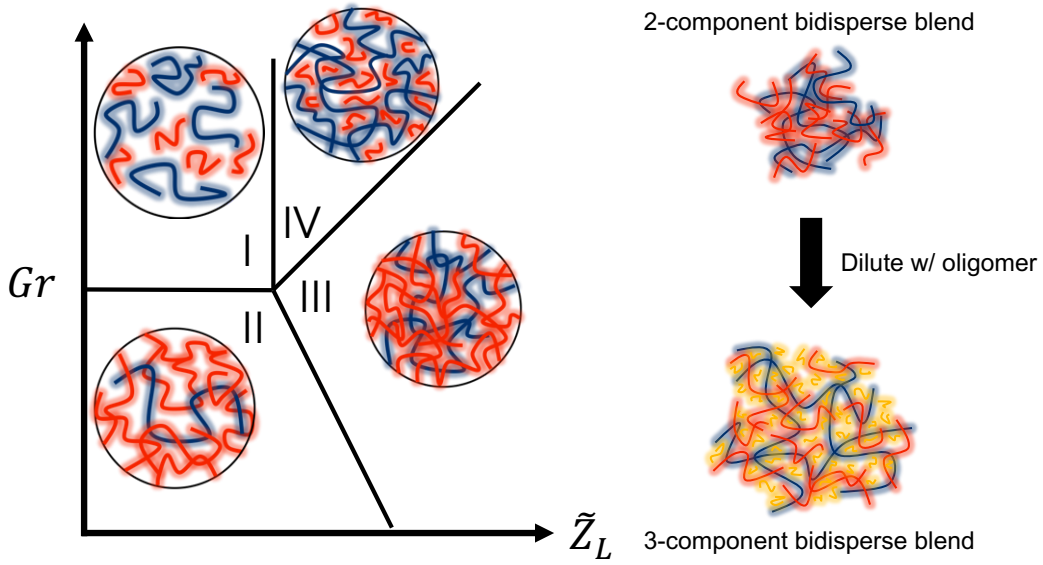

Figure 8.1: (a) Classic Viovy diagram for characterizing bidisperse blends according to the Graessley number and effective long chain entanglements (cartoon illustration of Region III blend and Region III blend "in solution".

dissolved in anhydrous THF at a concentration of 15 mM in a round bottom flask. Once the PBD was fully dissolved, the fluorophore and reaction initiator were added to the flask under constant stirring. The flask was purged with nitrogen for at least 30 minutes prior to reaction. The reaction was initiated by exposing the sample to 365 nm UV light for 5 to 15 minutes depending on the molecular weight of PBD. The reaction was quenched by uncapping the round bottom flask, exposing the system to atmospheric oxygen. Following reaction, the sample was rotovapped and precipitated in acetone 3 times. Success of the reaction was determined from wavelength specific GPC traces which confirmed the covalently attached small molecule fluorophore eluted the column at the same time as PBD without fluorophores.

Table 8.1: Compositional, rheological, and molecular details of each entangled polymer blend in this study.

Sample	ϕ_L	ϕ_S	ϕ_3	$M_{w,L}$ (g/mol)	$M_{w,S}$ (g/mol)	$M_{w,3}$ (g/mol)	Z_L	Z_S	$\bar{Z}$	$\tau_{d,L}$ (s)	Gr
0.11PBD(430k)/ 0.89PBD(18.4k)	0.11	0.89	N/A	4.30×10^5	1.84×10^4	N/A	29	10	39	0.86	4.0×10^{-2}
0.08PBD(817k)/ 0.92DBd(1.5k)	0.08	0.92	N/A	8.17×10^5	$\approx 1.5\times10^3$	N/A	40	1	41	2.0	6.6×10^2
0.4PBD(817k)/ 0.6PBD(169k) in o-PBD(1.5k)	0.40	0.60	0.85	8.17×10^5	1.69×10^5	$\approx 1.5\times10^3$	30	9	39	2.2	4.6×10^{-4}

8.4 Results and discussion

8.4.1 Small amplituded oscillatory shear rheology of entangled bidisperse polymer blends in the melt and in solution

Small amplitude oscillatory shear (SAOS) rheology reveals different dynamics of entangled bidisperse polymer blends depending on the location within the Viovy Diagram (Figure 8.2) and whether the blend is comprised of two or three components. Bidisperse blends of Region III and Region IV exhibit qualitatively similar SAOS rheology, with terminal relaxation observed at frequencies below the G',G'' crossover point. Above the crossover point, both the Region III and IV blends exhibit a plateau in G' for multiple decades in frequency. One distinction between the two blends is that the Region III blend exhibits an increase in G'' at high frequencies. This increase results from the higher $M_{w,S}$ in the Region III blend compared to the weakly entangled short chain species in the Region IV blend.

Further, there is a notable qualitative distinction between the dynamics of truly bidisperse blends in the melt (Figure 8.2(a)) and the bidisperse blend in solution (Figure 8.2(b)). The bidisperse blend in solution, which is characterized as a Region III blend based on the short and long chain components but is diluted with a third component butadiene oligomer, has a much lower plateau modulus compared to the bidisperse blends in the melt. This reduction of plateau modulus results from the dilution of the entangle-

ment network despite retaining the same number of entanglements as the two component blends. Additionally, the bidisperse blend in solution exhibits an onset of terminal relaxation approximately two decades in frequency below the measured G',G'' crossover. This rheological behavior is attributed to the low Gr of the Region III blend in solution due to a small separation of $M_{w,L}$ and $M_{w,S}$. Qualitatively similar SAOS rheology has been observed for bidisperse blends of polymers with higher M_e than PBD [40, 41]. Despite a large body of experimental data of the linear rheology for different bidisperse polymer blends, there exist comparatively few studies exploring the nonlinear rheology and steady shear behavior of these materials [42].

Measurements of the nonlinear rheology of polymer blends pose experimental challenges due to the large normal stress differences that typically occur in flows of entangled polymer melts, and, as an alternative, some bidisperse blends have been diluted in a third component solvent. These particular systems result in flows with sufficiently lower normal stresses, permitting standard rheological measurements using conventional rotational rheometers, but as will be shown, alter the predicted and measured flow behavior. In most studies of bidisperse blends the flow is assumed to be uniform, but there is evidence to suggest flows become nonuniform for certain blend compositions [9, 43, 44]. One possible explanation for why the flow would become nonuniform is shear-induced demixing.

8.4.2 Linear stability predictions of a two-fluid theory for bidisperse entangled polymer blends

The two-fluid model stability predictions for the three different classes of bidisperse blends are shown in Figure 8.3. The growth rate for instability is dependent on several quantities including the blend dispersity, number of entanglements, long chain volume

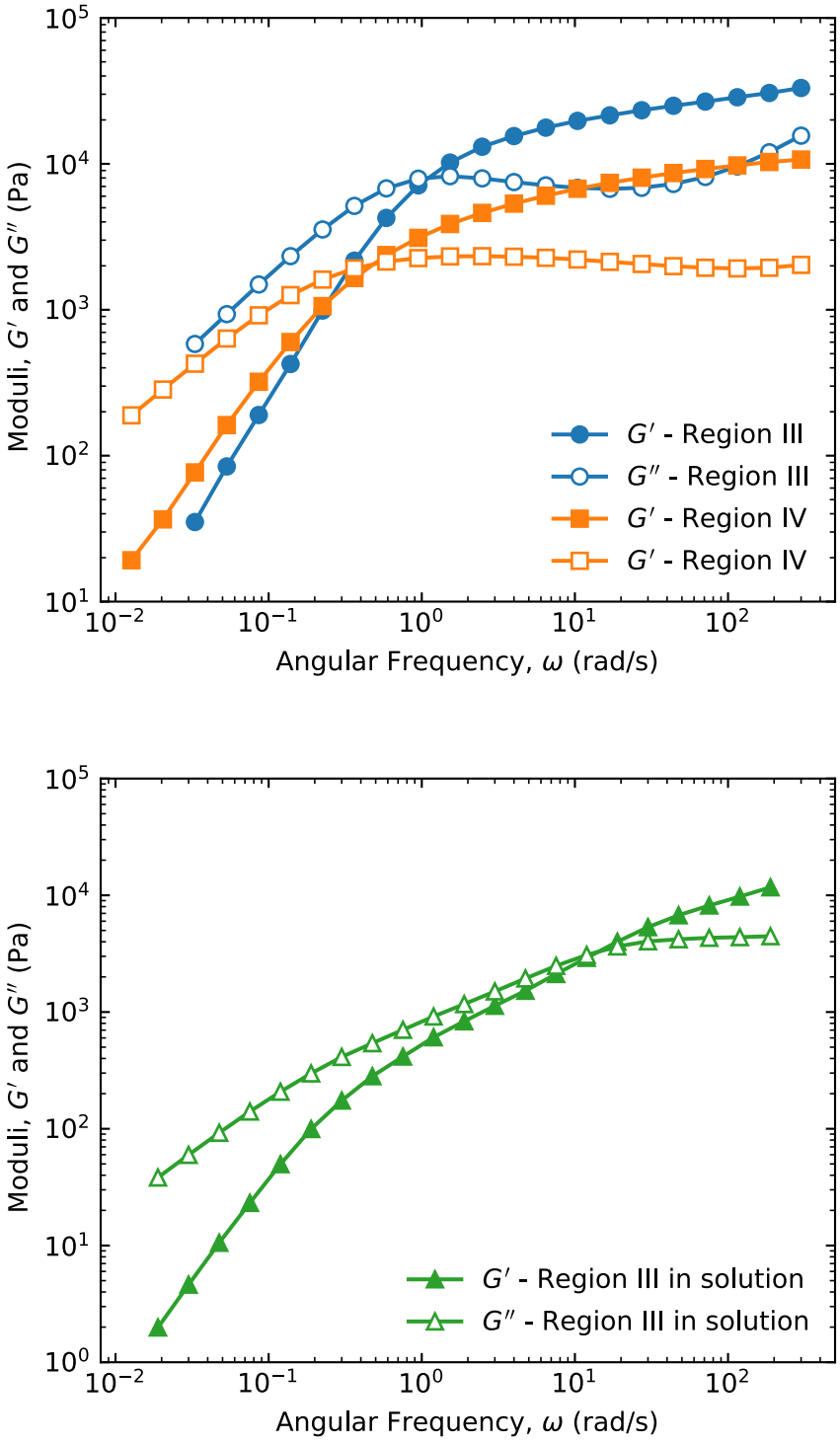

Figure 8.2: Small amplitude oscillatory shear rheology of (a) Region III and Region IV bidisperse blends and (b) Region III blend in solution. The strain amplitude was set to 1% for all measurements.

fraction, and applied Weissenberg number. A detailed discussion of how this expression was determined was reported in Peterson *et al.* (2020) [9]. Positive values of the eigenvalue σ represent unstable growth of infinitesimal perturbations. Negative values of σ correspond to infinitesimal perturbations that decay in time. The Region IV blend is the most unstable of the three blends, with a predicted instability window for $Wi > 0.7$ and a maximum unstable growth rate occurring around $Wi \approx 6$. The theory also predicts an unstable window for the Region III blend from $Wi = 0.4$ to 10. The predicted maximum unstable growth rate for the Region III blend is significantly lower than the Region IV blend. This discrepancy is believed to result from the size disparity of the long chains relative to the short chains in each blend. Finally, weak instability is predicted for the bidisperse blend in solution relative to the Region III and IV bidisperse blend melts. The unstable window for the Region III blend in solution is also appreciably smaller than the two bidisperse blend melts, which results from the ϕ_L and ϕ_S dependencies of σ. For $Wi > 70$ the bidisperse blend in solution exhibits a second window of instability, presumably from polymer-solvent demixing as predicted by the similar two-fluid theory for entangled polymer solutions. From the results in Figure 8.2 and Figure 8.3, the dilution of a bidisperse blend with a third component solvent is shown to significantly alter both the rheology and the propensity for shear-induced demixing of long and short chains as predicted by the two-fluid model for entangled polymer blends.

8.4.3 *In situ* velocimetry and concentration measurements of bidisperse entangled polymer blends

Region III bidisperse blend in solution

Figure 8.4 shows the flow profiles of the entangled bidisperse blend in solution under a range of Wi_{app}. All flow profiles exhibit uniform flow, as evidenced by the constant shear

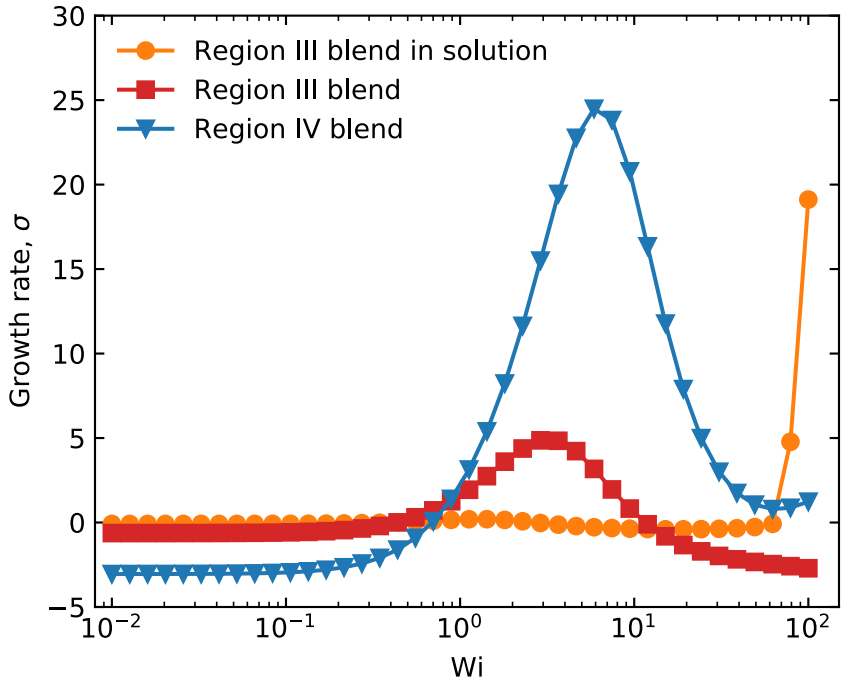

Figure 8.3: Predictions of the Wi sensitivity of eigenvalues according to a linear stability analysis using a two-fluid model for bidisperse blends.

rate that was observed to persist indefinitely at each Wi_{app}. This measured flow behavior across a range of Wi_{app} contrasts with studies of entangled polybutadiene solutions that are comprised of monodisperse high molecular weight polymer dissolved in small molecule solvents that were found to exhibit shear banded flow profiles [36, 43, 45, 46]. These results, taken together with previous investigations, suggest an importance of the types of entanglements (*i.e.*, long-long, long-short, and short-short) on the resultant flow behavior.

The steady state, uniform flow profiles suggest that the composition of the bidisperse blend in solution remains homogeneous across the fluid during shear. This is confirmed by rheo-fluorescence measurements(Figure 8.5), in which the concentration is found to remain effectively constant across the fluid at each Wi_{app}. We hypothesize that although theory predicts a weak instability for the blend in solution, the unstable growth rate is sufficiently low such that the timescale for the development of heterogeneity in the fluid composition is longer than observable in experiment. In fact, rheo-PTV measurements performed on the blend in solution for $t/\tau_d > 10^5$ indicated no nonuniformity of the flow. In addition to the weak growth rate of instability, it is possible that the predicted compositional changes for the blend in solution are immeasurable from rheo-fluorescence, which would also be consistent with the very small amplitude of the predicted growth rate of the instability for the bidisperse blend in solution.

Region III bidisperse blend

The flow profiles exhibit slight nonuniformity for the Region III blend (Figure 8.6). The flow profile remains uniform at the lowest Wi_{app} measured but develop nonuniformity with increasing Wi_{app} in the vicinity of the theory predicted stability boundary (Figure 8.3). As shown in Figure 8.6, there appears to be nonuniformity in the measured flow profiles above $Wi_{app} = 0.24$. For greater Wi_{app}, the dimensionless shear rate seemingly remains constant at ≈ 0.24 from $r/H = 0.8$ to 1.0, while a higher shear rate is observed

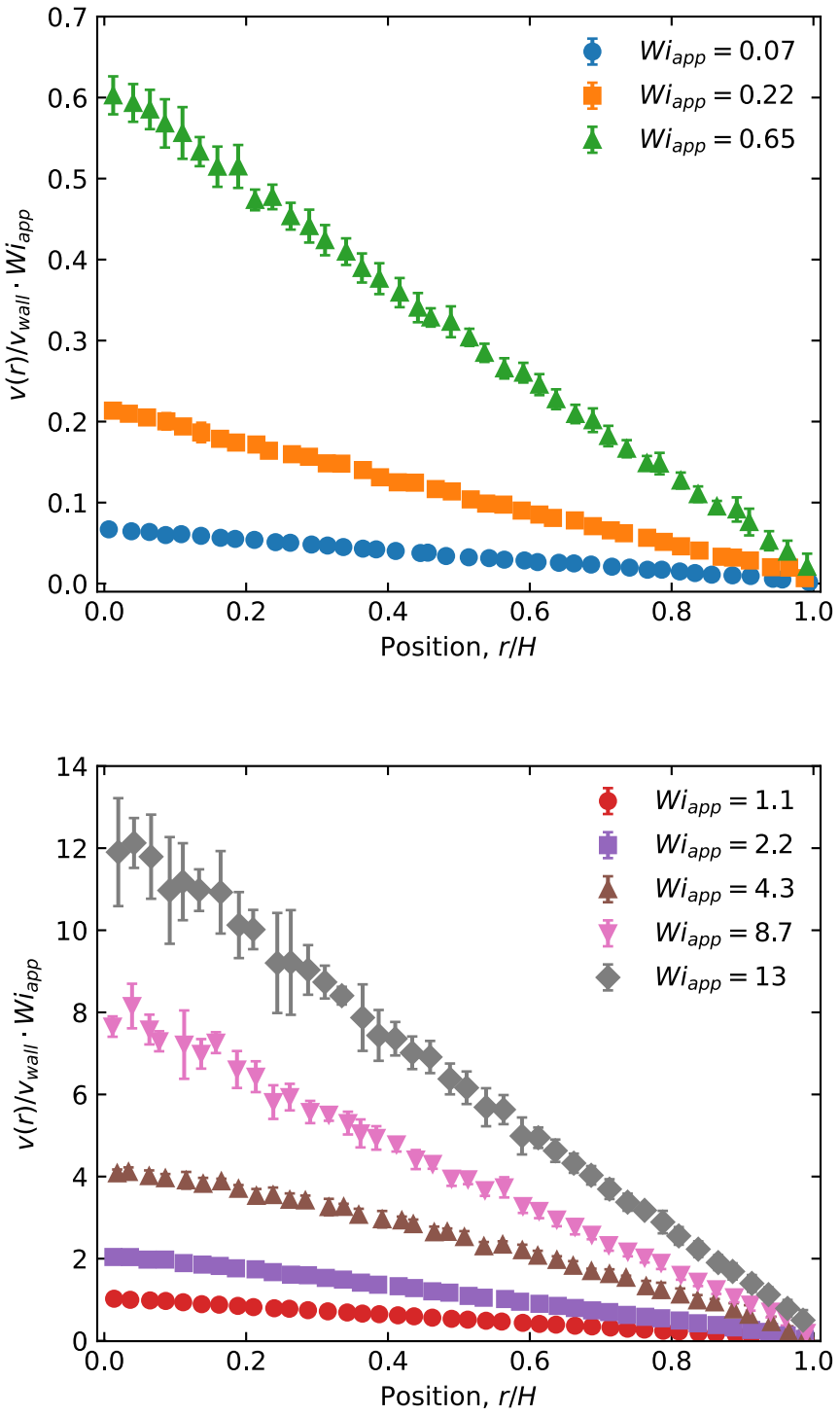

Figure 8.4: Flow kinematics of the Region III blend in solution at varying Wi_{app}.

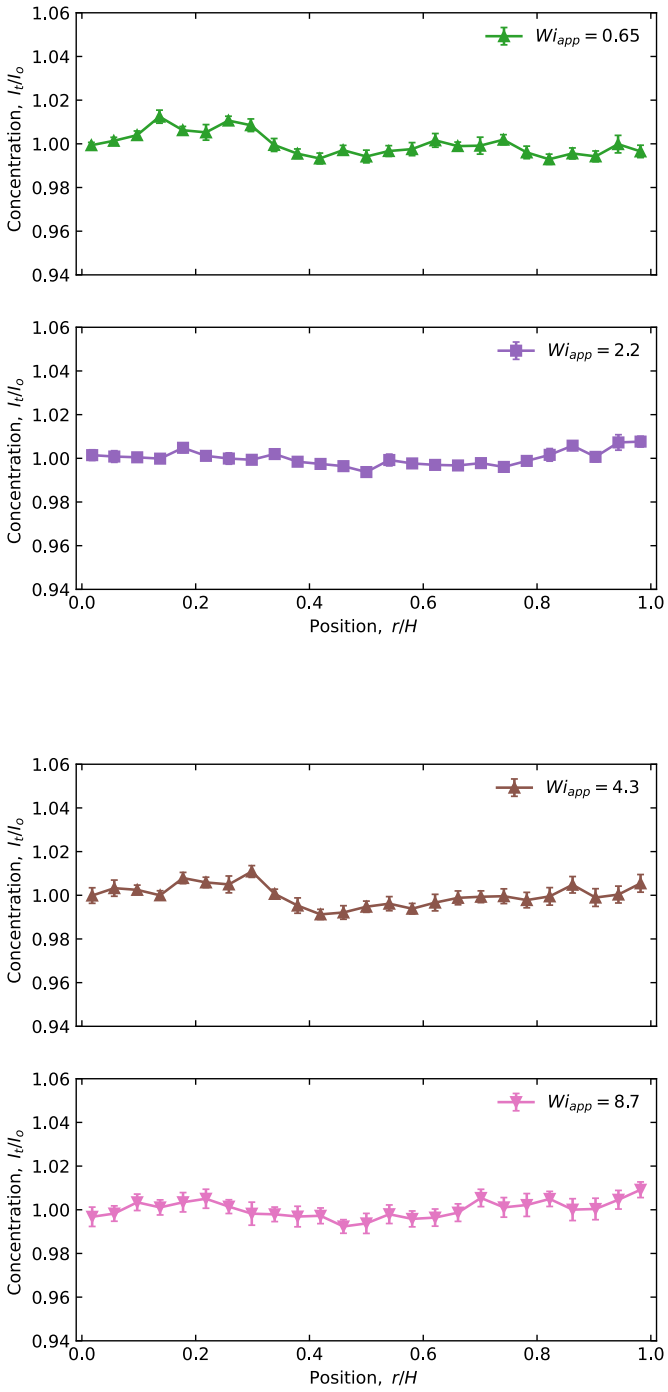

Figure 8.5: Concentration profiles of the Region III blend in solution measured by rheo-fluorescence under shear at specified Wi_{app}.

in the other portion of the fluid. Measurements at higher Wi_{app} were infeasible due to the torque limit of the rheometer.

The corresponding concentration profiles are shown in Figure 8.7. Minimal changes to the concentration profile of the Region III bidisperse blend are observed via rheo-fluorescence (Figure 8.7). At $Wi_{app} = 0.12$, there is slight enrichment of polymer concentration near the stationary wall. This compositional change could explain the slight curvature measured in the flow profile for $Wi_{app} = 0.12$, despite the Wi_{app} being much lower than expected for shear thinning. The remaining concentration profiles in Figure 8.7 are essentially uniform for higher Wi_{app}. For $Wi_{app} = 0.73$, the concentration profile is slightly enriched in polymer adjacent to the two boundaries, which is consistent with the low shear rate regions measured in the corresponding flow profile (Figure 8.6), but these changes of $\approx 1\%$ are likely within the measurement uncertainty of the fluorescence signal.

Region IV bidisperse blend

Inversely banded flow profiles are observed in the predicted unstable region for the Region IV blend (Figure 8.8). The prominence of the inversely banded profiles appears to be correlated with the predicted growth rate of instability as discussed in Figure 8.3. Namely, the linear stability analysis predicts a maximum growth rate of instability at approximately $Wi_{app} \approx 6$. This maximum is consistent with the magnitude of inverse bowing apparent in the flow profile for $Wi_{app} = 4.8$. Similar flow behavior has been reported, albeit transiently, for entangled polystyrene solutions and was attributed to the coupling of flow to shear-enhanced concentration fluctuations [39]. Here, we suspect microscale compositional heterogeneity, as predicted by theory [9], results in the observed inversely banded flow behavior. Wall slip at the stationary wall ($r/H = 1.0$) is observed at $Wi_{app} = 0.80$ and 1.6, but subsides at higher Wi_{app}.

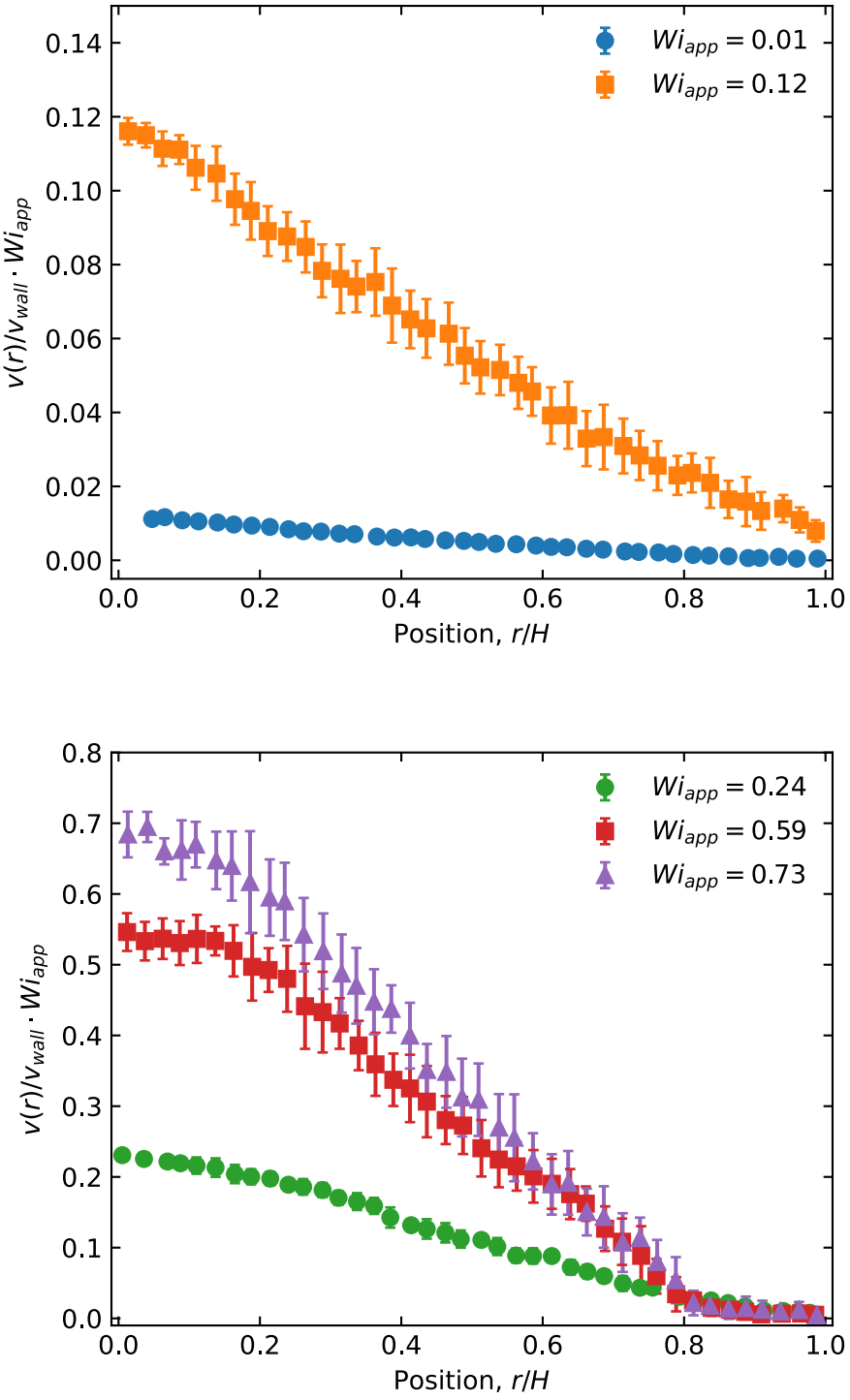

Figure 8.6: Flow kinematics of the Region III blend at varying Wi_{app}.

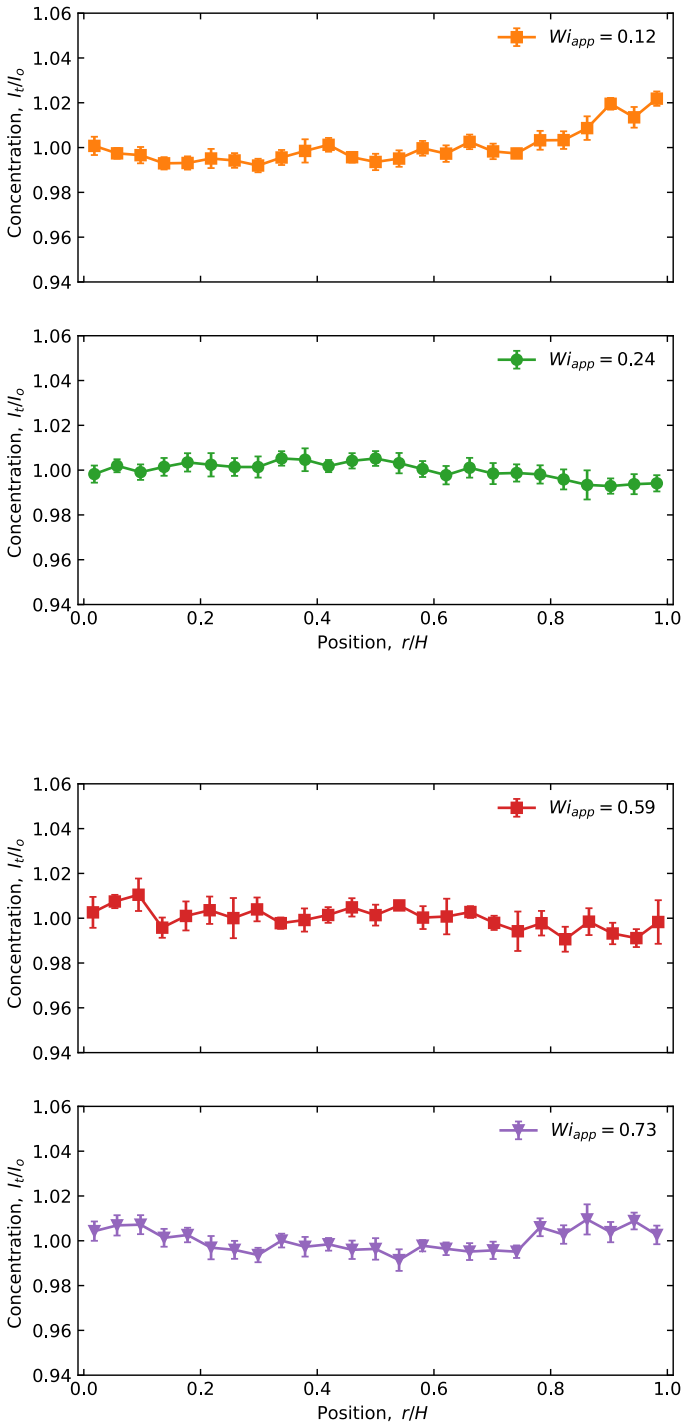

Figure 8.7: Concentration profiles of the Region III blend measured by rheo-fluorescence under shear at specified Wi_{app}.

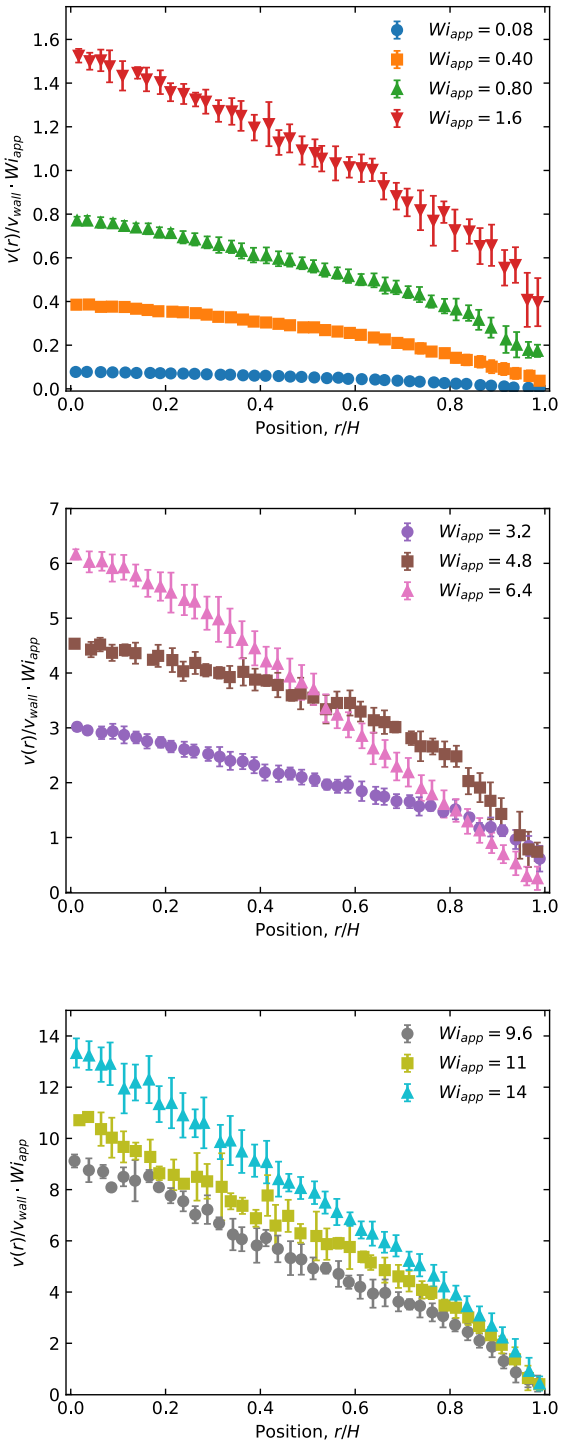

Figure 8.8: Flow kinematics of the Region IV blend at varying Wi_{app}.

Rheo-fluorescence measurements were performed at specific Wi_{app} to understand the interplay between fluid composition and flow. The composition of the Region IV blend remains nearly uniform for $Wi_{app} = 1.6$ and 4.8 (Figure 8.9). Compared to the Region III blend and blend in solution, the error bars of the measured fluorescence intensities are greater for the Region IV blend. This increase in measurement uncertainty could be the result of microscale heterogeneities or time fluctuations in composition below the spatial detection limit of the rheo-fluorescence apparatus. At $Wi_{app} = 8.0$, there is an increase in polymer concentration near the moving boundary ($r/H = 0.0$), consistent with the small low shear rate region measured in the flow profile (Figure 8.8). At a higher shear rate ($Wi_{app} = 14$), the concentration profile is approximately uniform (Figure 8.9), as expected from velocimetry (Figure 8.8).

8.5 Conclusions

A combination of two-fluid model stability predictions, small amplitude oscillatory shear measurements, rheo-PTV, and rheo-fluorescence measurements reveal complex rheological differences between bidisperse blends belonging to different regions of the Viovy diagram. Further, diluting a bidisperse blend with a third component oligomer is found to qualitatively change the measured small amplitude oscillatory shear rheology relative to a truly bidisperse two component blend, despite having similar numbers of entanglements. Uniform flows are observed at all Wi_{app} for the Region III blend in solution, but nonuniform flows are observed in the truly bidisperse Region III and IV blends. These observations, in combination with stability predictions and measured compositional changes, indicate that the type of chain entanglement is important to the rheological behavior of bidisperse blends. Additionally, these results suggest that diluting a bidisperse polymer blend in a third component solvent is not a suitable proxy for studying the dynamics

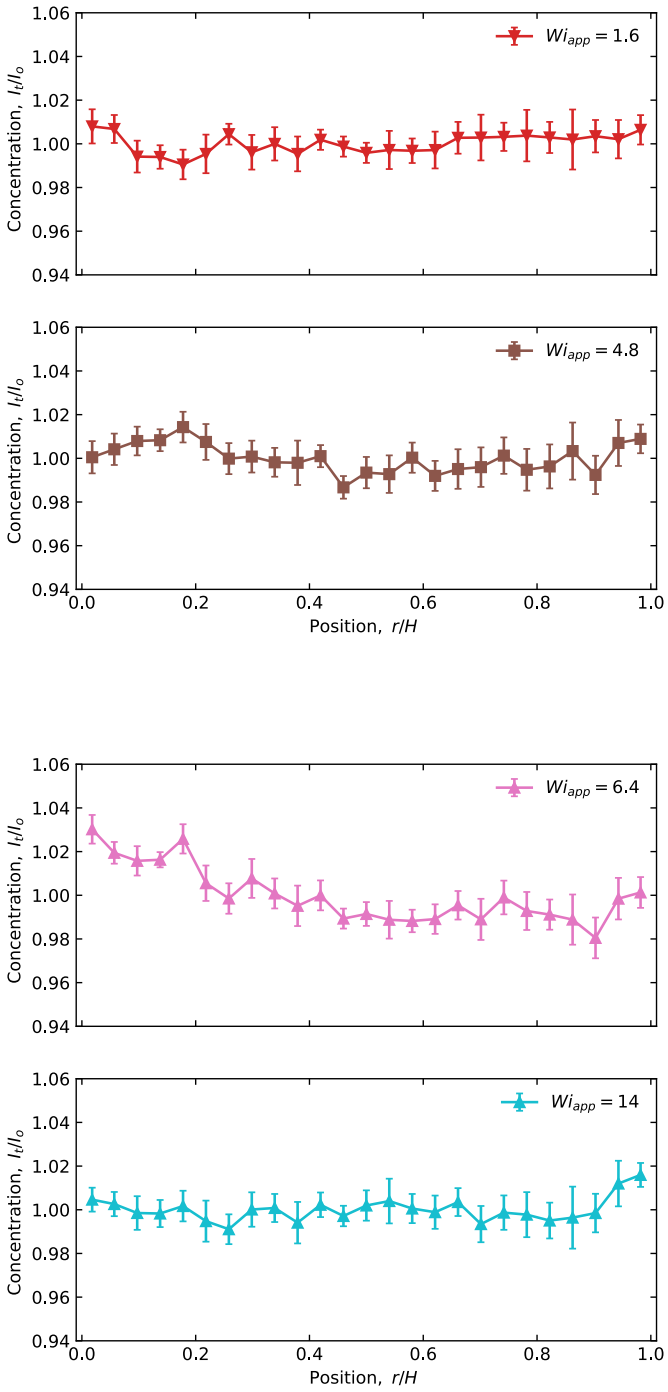

Figure 8.9: Concentration profiles of the Region IV blend measured by rheo-fluorescence under shear at specified Wi_{app}.

of entangled bidisperse polymer blends. Future efforts should be focused on modifying measurement capabilities to enable the investigation of blends that develop high stresses under flow. Rheo-fluorescence measurements are largely inconclusive regarding the relationship between compositional changes in the fluid to nonuniformity of the measured flows by rheo-PTV. This work should catalyze new experimental and theoretical investigations into the coupling of flow to spatial molecular weight distributions in entangled polymer blends.

Bibliography

[1] R. S. Graham, A. E. Likhtman, T. C. B. McLeish, and S. T. Milner, "Microscopic theory of linear, entangled polymer chains under rapid deformation including chain stretch and convective constraint release," *Journal of Rheology*, vol. 47, no. 5, p. 1171, 2003.

[2] T. C. B. McLeish and R. G. Larson, "Molecular constitutive equations for a class of branched polymers: The pom-pom polymer," *Journal of Rheology*, vol. 42, no. 1, pp. 81–110, 1998.

[3] M. J. Struglinski and W. W. Graessley, "Effects of Polydispersity on the Linear Viscoelastic Properties of Entangled Polymers. 1. Experimental Observations for Binary Mixtures of Linear Polybutadiene," *Macromolecules*, vol. 18, no. 12, pp. 2630–2643, 1985.

[4] J. L. Viovy, M. Rubinstein, and R. H. Colby, "Constraint Release in Polymer Melts: Tube Reorganization versus Tube Dilation," *Macromolecules*, vol. 24, no. 12, pp. 3587–3596, 1991.

[5] J. Des Cloizeaux, "Double Reptation vs. Simple Reptation in Polymer Melts," *Europhysics Letters*, vol. 5, no. 5, pp. 437–442, 1988.

[6] M. Rubinstein and R. H. Colby, "Self-consistent theory of polydisperse entangled polymers: Linear viscoelasticity of binary blends," *The Journal of Chemical Physics*, vol. 89, no. 8, pp. 5291–5306, 1988.

[7] A. E. Likhtman and R. S. Graham, "Simple constitutive equation for linear polymer melts derived from molecular theory: Rolie-Poly equation," *Journal of Non-Newtonian Fluid Mechanics*, vol. 114, no. 1, pp. 1–12, 2003.

[8] V. A. H. Boudara, J. D. Peterson, L. G. Leal, and D. J. Read, "Nonlinear rheology of polydisperse blends of entangled linear polymers: Rolie-Double-Poly models," *Journal of Rheology*, vol. 63, no. 1, pp. 71–91, 2019.

[9] J. D. Peterson, G. H. Fredrickson, and L. G. Leal, "Shear Induced Demixing in Bidisperse and Polydisperse Polymer Blends: Predictions From a Multi-Fluid Model," *Journal of Rheology*, vol. 64, no. 6, p. 1391, 2020.

[10] M. Cromer, M. C. Villet, G. H. Fredrickson, and L. G. Leal, "Shear banding in polymer solutions," *Physics of Fluids*, vol. 25, no. 5, p. 051703, 2013.

[11] M. Cromer, G. H. Fredrickson, and L. G. Leal, "A study of shear banding in polymer solutions," *Physics of Fluids*, vol. 26, no. 6, p. 063101, 2014.

[12] J. D. Peterson, M. Cromer, G. H. Fredrickson, and L. G. Leal, "Shear banding predictions for the two-fluid Rolie-Poly model," *Journal of Rheology*, vol. 60, no. 5, pp. 927–951, 2016.

[13] C. J. Petrie and M. M. Denn, "Instabilities in polymer processing," *AIChE Journal*, vol. 22, no. 2, pp. 209–236, 1976.

[14] N. Clarke and T. C. McLeish, "Shear flow effects on phase separation of entangled polymer blends," *Physical Review E - Statistical Physics, Plasmas, Fluids, and Related Interdisciplinary Topics*, vol. 57, no. 4, pp. R3731–R3734, 1998.

[15] C. Krause, R. Horst, and B. A. Wolf, "Shear effects on the phase diagrams of solutions of highly incompatible polymers in a common solvent. 2. Experiment and theory," *Macromolecules*, vol. 30, no. 4, pp. 890–895, 1997.

[16] S. Madbouly, M. Ohmomo, T. Ougizawa, and T. Inoue, "Effect of the shear flow on the phase behaviour of polystyrene/poly(vinyl methyl ether) blend," *Polymer*, vol. 40, no. 6, pp. 1465–1472, 1999.

[17] H. Gerard and J. S. Higgins, "The effect of shear flow on the mesoscopic structure of partially miscible polymer blends," *Physical Chemistry Chemical Physics*, vol. 1, no. 13, pp. 3059–3064, 1999.

[18] L. An, A. Hinrichs, R. Horst, C. Krause, and B. A. Wolf, "Shear Induced Mixing/Demixing: Blends of Homopolymers, of Homopolymers plus Copolymers, and Blends in Solution," *Macromolecular Symposia*, vol. 149, pp. 75–79, 2000.

[19] M. L. Fernandez, J. S. Higgins, and S. M. Richardson, "Flow instabilities in polymer blends under shear," *Polymer*, vol. 36, no. 5, pp. 931–939, 1995.

[20] D. Vlassopoulos, T. Terakawa, and G. G. Fuller, "Microstructural changes of a binary polymer blend in simple shear flow across the phase boundary," *Journal of Rheology*, vol. 47, no. 1, pp. 143–161, 2003.

[21] C. Lei, G. Li, Q. Yang, D. Chen, and S. Jiang, "Effect of Shear Flow on the Phase-Separation Behavior in a Blend of Polystyrene and Polyvinyl Methyl Ether.pdf," *Journal of Polymer Science Part B: Polymer Physics*, vol. 41, pp. 661–669, 2003.

[22] L. Jupp, T. Kawakatsu, and X. F. Yuan, "Modeling shear-induced phase transitions of binary polymer mixtures," *Journal of Chemical Physics*, vol. 119, no. 12, pp. 6361–6372, 2003.

[23] L. Jupp and X.-F. Yuan, "Dynamic phase separation of a binary polymer liquid with asymmetric composition under rheometric flow," *Journal of Non-Newtonian Fluid Mechanics*, vol. 124, pp. 93–101, 2004.

[24] R. Zhang, H. Cheng, C. Zhang, T. Sun, X. Dong, and C. C. Han, "Phase separation mechanism of polybutadiene/polyisoprene blends under oscillatory shear flow," *Macromolecules*, vol. 41, no. 18, pp. 6818–6829, 2008.

[25] X. F. Yuan and L. Jupp, "Interplay of flow-induced phase separations and rheological behavior of complex fluids in shearbanding flow," *Europhysics Letters*, vol. 60, no. 5, pp. 691–697, 2002.

[26] M. Criado-Sancho, D. Jou, J. Casas-Vázquez, and L. F. del Castillo, "Shear-induced shift of spinodal line in entangled polymer blends," *Physical Review E - Statistical Physics, Plasmas, Fluids, and Related Interdisciplinary Topics*, vol. 66, no. 6, p. 6, 2002.

[27] I. A. Hindawi, J. S. Higgins, and R. A. Weiss, "Flow-induced mixing and demixing in polymer blends," *Polymer*, vol. 33, no. 12, pp. 2522–2529, 1992.

[28] C. C. Han, Y. Yao, R. Zhang, and E. K. Hobbie, "Effect of shear flow on multicomponent polymer mixtures," *Polymer*, vol. 47, pp. 3271–3286, 2006.

[29] H. Watanabe, S. Ishida, Y. Matsumiya, and T. Inoue, "Test of full and partial tube dilation pictures in entangled blends of linear polyisoprenes," *Macromolecules*, vol. 37, no. 17, pp. 6619–6631, 2004.

[30] H. Watanabe, S. Ishida, Y. Matsumiya, and T. Inoue, "Viscoelastic and Dielectric Behavior of Entangled Blends of Linear Polyisoprenes Having Widely Separated Molecular Weights: Test of Tube Dilation Picture," *Macromolecules*, vol. 37, no. 5, pp. 1937–1951, 2004.

[31] Juliani and L. A. Archer, "Linear and nonlinear rheology of bidisperse polymer blends," *Journal of Rheology*, vol. 45, no. 3, pp. 691–708, 2001.

[32] J. K. Jackson and H. H. Winter, "Entanglement and Flow Behavior of Bidisperse Blends of Polystyrene and Polybutadiene," *Macromolecules*, vol. 28, no. 9, pp. 3146–3155, 1995.

[33] S. J. Park and R. G. Larson, "Tube dilation and reptation in binary blends of monodisperse linear polymers," *Macromolecules*, vol. 37, no. 2, pp. 597–604, 2004.

[34] S. J. Park and R. G. Larson, "Long-chain dynamics in binary blends of monodisperse linear polymers," *Journal of Rheology*, vol. 50, no. 1, pp. 21–39, 2006.

[35] M. Doi, W. W. Graessley, E. Helfand, and D. S. Pearson, "Dynamics of Polymers in Polydisperse Melts," *Macromolecules*, vol. 20, no. 8, pp. 1900–1906, 1987.

[36] M. C. Burroughs, Y. Zhang, A. M. Shetty, C. M. Bates, L. G. Leal, and M. E. Helgeson, "Flow-Induced Concentration Nonuniformity and Shear Banding in Entangled Polymer Solutions," *Physical Review Letters*, vol. 126, no. 20, p. 207801, 2021.

[37] Y. T. Hu and A. Lips, "Kinetics and mechanism of shear banding in an entangled micellar solution," *Journal of Rheology*, vol. 49, no. 5, pp. 1001–1027, 2005.

[38] P. Cheng, M. C. Burroughs, L. G. Leal, and M. E. Helgeson, "Distinguishing shear banding from shear thinning in flows with a shear stress gradient," *Rheologica Acta*, vol. 56, no. 12, pp. 1007–1032, 2017.

[39] M. C. Burroughs, A. M. Shetty, L. G. Leal, and M. E. Helgeson, "Coupled nonhomogeneous flows and flow-enhanced concentration fluctuations during startup shear of entangled polymer solutions," *Physical Review Fluids*, vol. 5, no. 4, p. 043301, 2020.

[40] J. K. Nielsen, H. K. Rasmussen, O. Hassager, and G. H. McKinley, "Elongational viscosity of monodisperse and bidisperse polystyrene melts," *Journal of Rheology*, vol. 50, no. 4, pp. 453–476, 2006.

[41] D. J. Read, K. Jagannathan, S. K. Sukumaran, and D. Auhl, "A full-chain constitutive model for bidisperse blends of linear polymers," *Journal of Rheology*, vol. 56, no. 4, pp. 823–873, 2012.

[42] C. Pattamaprom and R. G. Larson, "Constraint release effects in monodisperse and bidisperse polystyrenes in fast transient shearing flows," *Macromolecules*, vol. 34, no. 15, pp. 5229–5237, 2001.

[43] S. Ravindranath, S.-Q. Wang, M. Olechnowicz, and R. P. Quirk, "Banding in simple steady shear of entangled polymer solutions," *Macromolecules*, vol. 41, no. 7, pp. 2663–2670, 2008.

[44] M. Boudaghi-Khajehnobar, B. J. Edwards, and B. Khomami, "Effects of chain length and polydispersity on shear banding in simple shear flow of polymeric melts," *Soft Matter*, vol. 16, no. 28, pp. 6468–6483, 2020.

[45] Y. T. Hu, L. Wilen, A. Philips, and A. Lips, "Is the constitutive relation for entangled polymers monotonic?," *Journal of Rheology*, vol. 51, no. 2, pp. 275–295, 2007.

[46] Y. T. Hu, "Steady-state shear banding in entangled polymers?," *Journal of Rheology*, vol. 54, no. 6, pp. 1307–1323, 2010.

Chapter 9

A numerical study of the two-fluid Rolie-Poly model in Large Amplitude Oscillatory Shear[1]

9.1 Abstract

Recent advances in the interpretation of large amplitude oscillatory shear (LAOS) data have rendered the flow protocol useful as a rheological measurement to understand the nonlinear dynamics of different complex fluids. Central to these analysis techniques is the assumption that the flow is described by a spatially uniform shear rate. A number of complex fluids, however, undergo a shear banding flow instability for certain applied shear rates that results in a spatially nonuniform flow. Here, a two-fluid Rolie-Poly model for entangled polymer solutions is used to investigate nonuniform flows in LAOS. In this model, shear banded flows arise from a shear-induced demixing instability that

[1]The contents of this Chapter are in preparation to be submitted for publication in the form of a journal article.

leads to spatial heterogeneities in polymer concentration. The heterogeneities that arise from shear-induced demixing, along with the resulting flow profiles, are found to vary throughout the intracycle shear. Additionally, the magnitude and number of predicted shear bands is found to depend upon the strength of flow-concentration coupling, as specified by the elastic to osmotic stress ratio (E). Local strains and shear rates are computed for spatially resolved fluid elements to afford accurate depiction of material behavior when represented in elastic and viscous Lissajous-Bowditch curves. These results suggest that all LAOS rheological measurements, for fluids that are expected to produce flow nonuniformities, should be accompanied by a spatially resolved analysis of the fluid kinematics.

9.2 Introduction

Complex fluids are subjected to myriad time-varying deformations and shear rates during their processing and intended application. By contrast, the traditional rheological methods for analyzing material behavior include steady shear flow sweeps and small amplitude oscillatory shear (SAOS) [1, 2]. In a steady shear measurement, a fixed shear rate is imposed on the fluid and stresses are recorded until a steady state is reached. Nonlinear flow behavior is observed when steady shear measurements are performed at shear rates that exceed the characteristic relaxation time (*e.g.*, the reptation time in entangled polymers) of the fluid. This measurement protocol, however, only reflects the response of a fluid at fixed shear rates and is therefore not reflective of more general processing conditions that a material may experience, which are often both nonlinear and transient. In a small amplitude oscillatory shear measurement, an oscillatory shear flow of sufficiently low amplitude is applied to a fluid to ensure that the flow remains in the linear viscoelastic regime (LVE). At larger amplitudes, however, the flow becomes

nonlinear, and the stress is no longer a simple sinusoidal phase shift of the imposed strain and shear rate.

When the strain amplitude is sufficiently high, such that the fluid response is outside of the LVE, the amplitude is defined as "large". Large amplitude oscillatory shear (LAOS) is a nonlinear flow protocol that imposes a time-varying strain, and as a consequence, a time-varying shear rate, on a fluid; however, unlike SAOS, the shear stress is no longer a simple sinusoidal phase shift between the imposed strain and shear rate. Data analysis of LAOS measurements has proven to be a difficult endeavor, because unlike SAOS, the measured stresses in LAOS are not simple sinusoidal phase shifts from the imposed shear. Instead, the measured stress is often a complex, time-varying function of the imposed strain and shear rate.

Significant advances have been made over the last two decades to facilitate the interpretation of these highly nonlinear data [3]. Early work found that the time dependent nonlinear shear response to oscillatory shear flows ($\sigma(t)$) could be Fourier transformed to identify relative intensities of higher-order harmonics [4]. In particular, the relative intensity of the third harmonic frequency relative to the fundamental was shown to be a sensitive indicator of nonlinearities in material deformation [4], and even capable of distinguishing between different polymer topologies [5]. Despite the mathematical robustness of Fourier Transform Rheology, little rheologically specific information can be inferred about higher-order nonlinearities without restricting interpretation to the predictions of a specific constitutive model. Additionally, 1^{st}-order harmonic moduli were found to poorly or incorrectly represent nonlinearities during LAOS [6]. Instead, representation of nonlinear data by way of elastic (shear stress vs. strain) and viscous (shear stress vs. shear rate) projections, as Lissajous-Bowditch curves, reflect intracycle material evolution during LAOS more faithfully (see representative Lissajous-Bowditch curves in Figure 9.1. Subsequent efforts by Ewoldt *et al.* [6] found that physical information about elastic

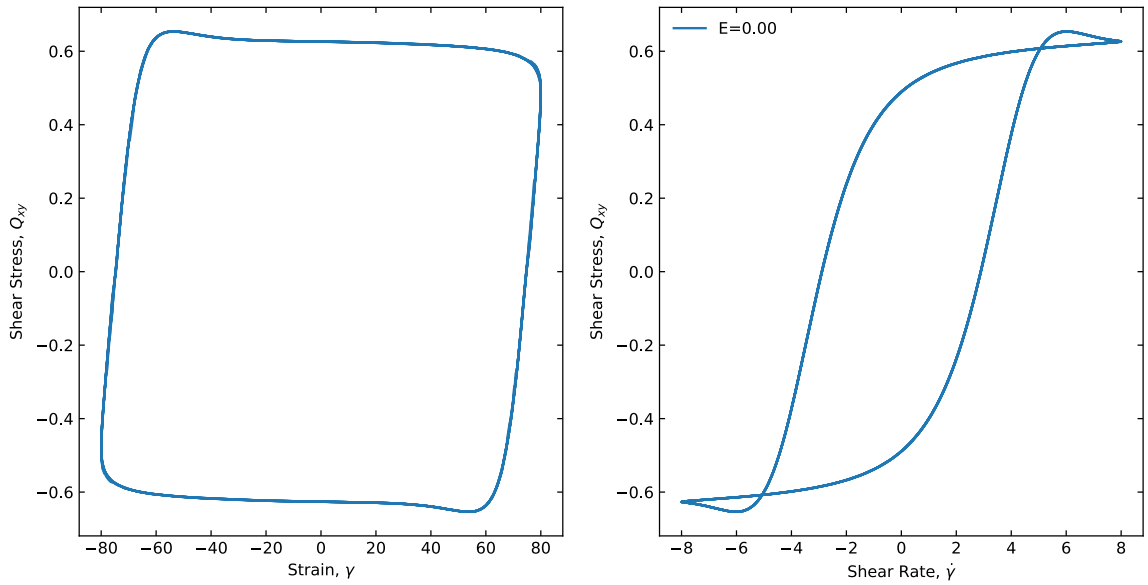

Figure 9.1: Representative elastic (left) and viscous (right) Lissajous-Bowditch curves, illustrating how the measured shear stress can be plotted parametrically against either the imposed strain (left) or shear rate (right).

and viscous nonlinearities could be inferred from the signs of third harmonic Chebyshev coefficients. Specifically, positive values for the third harmonic elastic/viscous Chebyshev coefficients indicate strain stiffening/shear thickening behavior and negative values reflect strain softening/shear thinning. Third harmonic Chebyshev coefficients equal to zero imply linear behavior. More recently, new methodology for analyzing LAOS by Rogers *et al.* [7–10] that interprets the 3D space curve (shear stress vs. strain vs. shear rate) in terms of a *Sequence of Physical Processes* eliminated the need to fit Lissajous-Bowditch curves *via* spectral decomposition and rather computes physically meaningful quantities at each point along the 3D space curve trajectory by computing the tangent, normal, and binormal vectors. These vectors were shown to relate to meaningful transient descriptors of the elastic and viscous moduli as well as the rates at which material properties change during a LAOS oscillation [10].

A central assumption to all of the aforementioned methods of analysis and interpretation for LAOS is that the applied deformation across the fluid and the resulting velocity profile remains uniform throughout the entire oscillation period. However, numerous complex fluids exhibit shear banded or otherwise nonuniform flows under certain flow conditions, which would seemingly compromise analyses that assume the fluid is subjected to a spatially uniform shear rate. Recently, entangled polymer solutions were observed to undergo shear banded flows and, in some cases, the banded flows were coupled to a shear-induced demixing instability. In the case of shear banding by the shear-induced demixing mechanism, both the flow and concentration profile develop heterogeneity under shear [11–14]. Preliminary analysis has revealed that this same shear-induced demixing of entangled polymer solutions in steady shear flow can also be present in LAOS flow [15].

In this work, we explore LAOS flow dynamics using a two-fluid model based upon the Rolie-Poly constitutive theory that predicts a shear-induced demixing instability of entangled polymer solutions in steady shear flows. Stability boundaries for shear-induced demixing are shifted for LAOS flows compared to steady shear, this change in stability is attributed to the finite intracycle strain accumulation inherent to oscillatory flows. Shear banded flows are found to arise from a shear-induced demixing instability, and the degree of flow-concentration coupling (E) influences the nonuniformity of flow and magnitude of concentration heterogeneity across the fluid. The predicted nonuniformity of flows arising from the shear-induced demixing instability depend significantly on the oscillation frequency of the imposed flow, suggesting a complex dependence of the instability on the timescale(s) of LAOS and more genereal time-varying flows. Importantly, it is found that traditional methods of reporting LAOS data are insufficient when shear banding and shear-induced demixing occur. To improve upon this shortcoming, a "local" approach is discussed for reporting LAOS data in nonuniform flows.

9.3 Methods

9.3.1 Dimensionless timescales

Two dimensionless timescales characterize the imposed flow in large amplitude oscillatory shear; namely, the frequency of oscillation (ω) as represented by the Deborah number (De), where

$$De = \omega\tau_d \tag{9.1}$$

and the maximum rate of deformation as represented by the Weissenberg number (Wi)

$$Wi = \gamma_0\omega\tau_d, \tag{9.2}$$

where τ_d is the characteristic timescale for stress relaxation by reptation (for entangled polymer solutions) and γ_0 is the imposed strain amplitude.

9.3.2 Two-fluid model

A two-fluid model for entangled polymer solutions [11–13] was utilized for LAOS flow calculations. The important equations of this model are the momentum balance that couples relative motion of polymer and solvent

$$0 = -\nabla p + \varpi\nabla^2\boldsymbol{u}_S + \nabla\cdot\boldsymbol{\Pi} \tag{9.3}$$

where p is the isotropic pressure, ϖ is the ratio of solvent to polymer viscosity, $\boldsymbol{u}_S$ is the solvent velocity vector, and $\boldsymbol{\Pi}$ is the total stress tensor. The total stress tensor is comprised of viscoelastic polymer stresses ($\boldsymbol{Q}-\boldsymbol{I}$), isotropic elastic stresses (π^{el}), and

osmotic stresses ($\boldsymbol{\pi}$) according to

$$\boldsymbol{\Pi} = (\boldsymbol{Q} - \boldsymbol{I}) - \boldsymbol{I}\pi^{el} - \boldsymbol{\pi}. \tag{9.4}$$

Here $\boldsymbol{Q}$ is the polymer conformation tensor, $\boldsymbol{Q} = \langle \boldsymbol{RR} \rangle / R_0^2$, and $\boldsymbol{I}$ is the identity matrix. Details of π^{el} and $\boldsymbol{\pi}$ can be found elsewhere [13]. The polymer conformation was calculated using the monotonic Rolie-Poly constitutive model

$$\frac{\partial \boldsymbol{Q}}{\partial t} + \boldsymbol{u}_P \cdot \nabla \boldsymbol{Q} - (\nabla \boldsymbol{u}_P)^T \cdot \boldsymbol{Q} - \boldsymbol{Q} \cdot \nabla \boldsymbol{u}_P = -\phi^{-3/2}(\boldsymbol{Q} - \boldsymbol{I}) + 2\frac{\tau_d}{\tau_R}(1 - \lambda^{-1})(\boldsymbol{Q} + \lambda^{-1}(\boldsymbol{Q} - \boldsymbol{I}) \tag{9.5}$$

where τ_d and τ_R are the reptation and Rouse timescales, respectively, and λ is a measure of the amount of chain stretch ($\lambda = \sqrt{Tr(\boldsymbol{Q})/3}$). Differences in the polymer and solvent velocities are driven by a divergence in stress

$$\boldsymbol{u}_P - \boldsymbol{u}_S = \bar{\phi}^{-3/2} \frac{E}{\bar{H}^2} \nabla \cdot \boldsymbol{\Pi}. \tag{9.6}$$

Clearly, a necessary condition for differences in the relative velocities of polymer and solvent is a non-zero value of the flow-concentration coupling parameter (E), which is defined as

$$E = \frac{G(\phi)}{\chi^{-1}\phi^2}, \tag{9.7}$$

where $G(\phi)$ is the shear modulus and χ^{-1} is the osmotic susceptibility. E can be thought of as a measure of elastic stresses (promoting demixing) relative to osmotic stresses (acting to homogenize the fluid composition). Thus, compositionally uniform flows are predicted when $E = 0$, and heterogeneity develops for sufficiently large values of E. Experiments have confirmed that E is sensitive to the chemistry of polymer and solvent as well as the solution temperature [16, 17]. Finally, the polymer concentration changes according to

the continuity equation

$$\frac{\partial \bar{\phi}}{\partial t} = -\nabla \cdot (\boldsymbol{u}_P \bar{\phi}) \tag{9.8}$$

where $\bar{\phi}$ is the polymer concentration normalized by the mean polymer concentration.

To simulate LAOS flow conditions, the boundary condition of the moving wall was set to $u_P(x/H = 1) = u_S(x/H = 1) = \gamma_0 De \cos(De\, t)$. Additional boundary conditions include the no-slip boundary condition at the stationary wall ($u_P(x/H = 0) = u_S(x/H = 0) = 0$) and the no-flux boundary condition ($\frac{\partial \bar{\phi}}{\partial x} = \frac{\partial^3 \bar{\phi}}{\partial x^3} = 0$ at $x/H = 1$ and 1).

9.3.3 Numerical simulation details

Model equations were solved numerically for cartesian coordinates using the ode15s solver in MATLAB. LAOS flow simulations were conducted for at least 20 oscillation cycles after reaching a steady oscillatory shear stress to ensure steady LAOS flow.

9.4 Results and discussion

9.4.1 Characterizing homogeneous LAOS flow of entangled polymer solutions according to the Rolie-Poly model

Rolie-Poly model predictions of the elastic and viscous Lissajous-Bowditch curves for large amplitude oscillatory shear (LAOS) at particular imposed oscillation frequencies (De) and shear rate amplitudes (Wi) are grouped into elastic and viscous Pipkin diagrams of Figure 9.2. It is important to note that these predictions are for homogeneous flow and concentration profiles (*i.e.*, no flow-concentration coupling or shear banded flow profiles ($E = 0$)). In the limit of low De, the elastic projection of the Lissajous-Bowditch curve is rectangular in shape for all Wi (Figure 9.2(a)). This predicted rheological behavior is in

agreement with previous numerical studies of the Rolie-Poly model in LAOS, albeit with parameters selected to yield a nonmonotonic constitutive relationship [18]. There is a small overshoot in the shear stress at the strain maximum that becomes more apparent as Wi is increased (Figure 9.2(a)). Following the stress overshoot, the shear stress continues to rise as the imposed strain is reduced. This local maximum of the shear stress is the result of the nonlinear flow and the time-dependent viscoelasticity of the fluid as is similarly observed in the transient startup of steady shear. At intermediate De, shear stress overshoots are observed in the elastic Lissajous-Bowditch curves (Figure 9.2(a)) and secondary loops are observed in the viscous Lissajous-Bowditch curves (Figure 9.2(b)). Secondary loops have been reported previously and are indicative of strong nonlinearities in the conjugate stress projection (*i.e.*, shear stress overshoots in the elastic Lissajous-Bowditch curve) [19, 20]. Unlike at low De, the shear stress overshoots are global maxima in the elastic projections at intermediate De, again similar to what is observed in the transient startup of steady shear. In the limit of high De, the elastic Lissajous-Bowditch projection is nearly a straight line oriented 45° to the abscissa, and the viscous Lissajous-Bowditch projection is an ellipse. This shape is indicative of an elastic solid-like response, as expected for the short timescale limit of a viscoelastic material.

9.4.2 Propensity for shear-induced demixing in LAOS

As mentioned, the curves of Figure 9.2 describe uniform fluid flow and composition; however, there is growing evidence that suggests flow nonuniformity develops for some entangled polymer solutions [14, 21–25]. The majority of prior investigations into nonuniform flows of entangled polymer solutions have used steady shear flow, but other flow protocols, such as LAOS, could also lead to shear-induced demixing and nonuniform flows. Here, we use simulations of the two-fluid Rolie-Poly model with non-vanishing

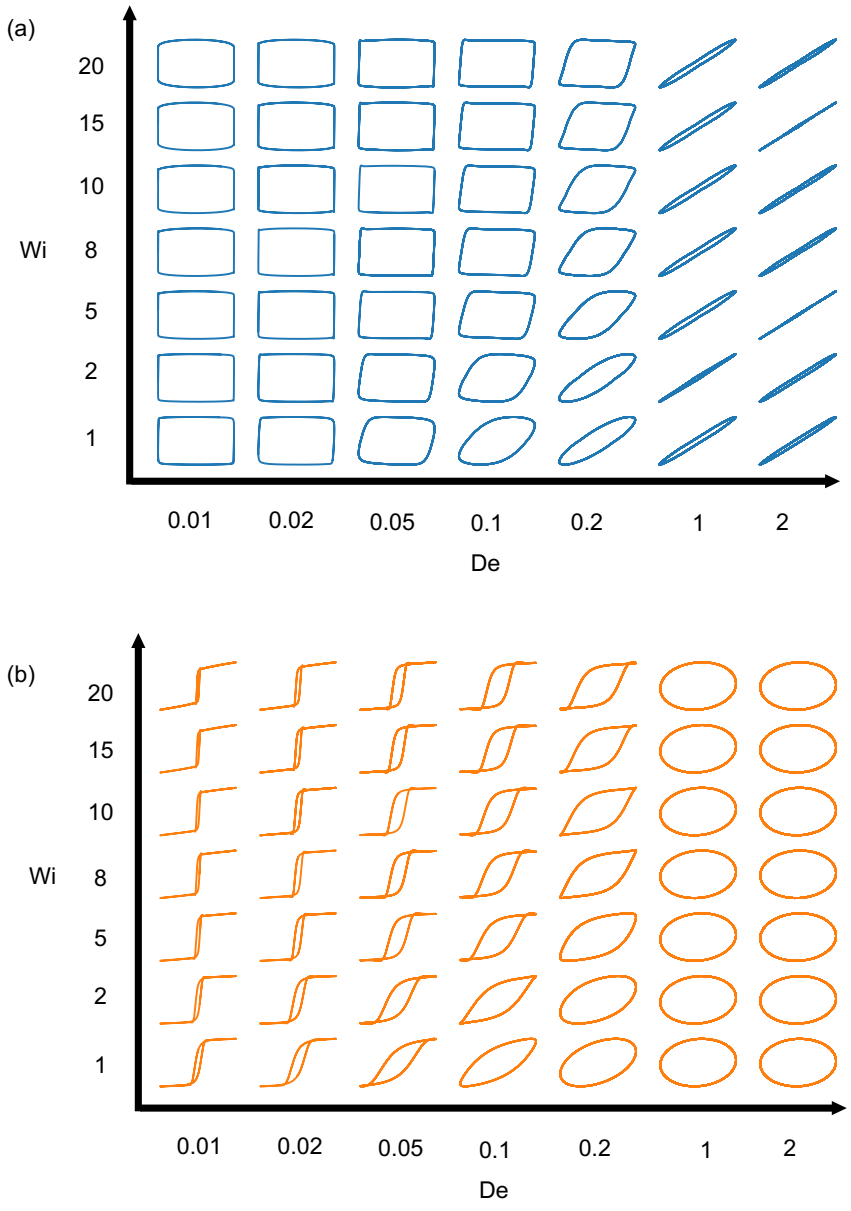

Figure 9.2: Pipkin diagram of (a) elastic and (b) viscous Lissajous-Bowditch curves at particular Wi and De. All data were computed using the two-fluid Rolie-Poly model with $Z = 40$ and $E = 0$ (the flow and concentration remain uniform).

flow-concentration coupling (non-zero values of E) to understand the influence of the transient nature of LAOS flow to enhance or suppress shear-induced demixing.

To understand the criteria for shear-induced demixing in LAOS flows of entangled polymer solutions, numerical simulations were used to identify the critical Wi for which fluctuations in concentration are unstable and grow in time. As shown in Figure 9.3, there is a sensitivity of the stability boundaries to the particular De of the LAOS flow, which results in changes to the stability boundaries relative to those determined for simple steady shear. The results are somewhat surprising given the expectation that the stability boundaries should converge towards the simple steady shear stability curve in the limit of low De, when the time between the flow reversal is very long. However, at low De the unstable window encompasses a much smaller Wi range for varying E compared to steady shear. Similar stabilizing effects at low De were previously observed in LAOS flows using a homogeneous Rolie-Poly model [18] and the two-fluid Rolie-Poly model [15] for similar parameters as used here. At $De = 0.1$, the unstable region shifts to higher Wi and spans a greater Wi range compared to steady shear. Here, we hypothesize that the oscillatory nature of the flow stabilizes against shear-induced demixing at low Wi due to the low intracycle strain accumulation. This shift is attributed to the large strains necessary to initiate shear-induced demixing.

9.4.3 Intracycle velocity and concentration profiles following shear-induced demixing

The composition of the fluid and relative nonuniformity of the velocity profiles vary throughout an oscillation cycle (Figure 9.4). The distinction between bands of different shear rate is most apparent when the instantaneous imposed shear rate is at a maximum ($\gamma = 0$). Interestingly, the intracycle velocity profiles depend on the direction of strain

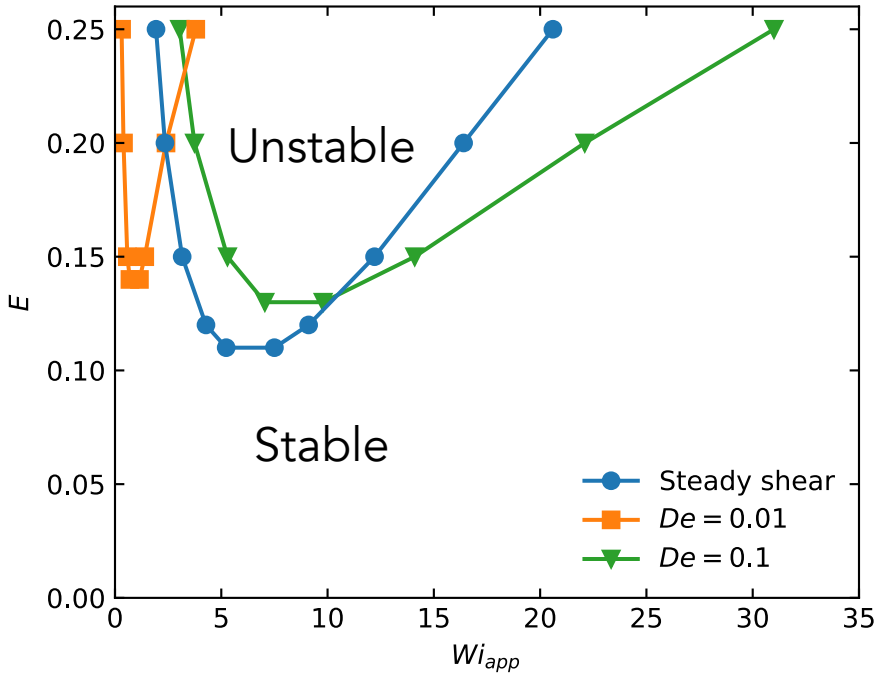

Figure 9.3: Stability boundaries for the two-fluid Rolie-Poly model with $Z = 40$ in steady shear and LAOS flows as determined from numerical simulation. The demixing instability was initiated by ($\partial\bar{\phi}_0 = 1 \times 10^{-5}$) perturbations to the initial concentration profile.

(*i.e.*, whether the imposed strain is increasing or decreasing). The qualitative intracycle changes to the flow are attributed to the relaxation in stress that occurs as the shear rate is reduced to zero. At intermediate times within a cycle, when the instantaneous shear rate is relatively low but non-zero ($\gamma = -\frac{1}{2}\gamma_0$), the velocity profile appears uniform unlike other time points within the strain cycle that are clearly shear banded. The concentration profile of the fluid is found to remain constant for the final quarter of a period during the strain increase. While the composition of the fluid varies throughout a single oscillation cycle in LAOS flow, it never completely relaxes to a homogeneous state at any point within the strain cycle once shear-induced demixing has occurred. The fluid composition is least heterogeneous during the reduction of an imposed strain, but not at the point of zero strain. Here, the partial intracycle re-homogenization of the nonuniform fluid composition results from the LAOS flow protocol, and specifically, the effect of flow reversal.

9.4.4 Sensitivity of the velocity and concentration profiles to E

The predicted velocity and concentration profiles are sensitive to the degree of flow-concentration coupling (Figure 9.5). When $E = 0.13$ and $Z = 40$, the fluid is weakly unstable as indicated by the small undulations to fluid composition that result in minimal changes to the velocity profile. As E is increased, the variations in composition become more pronounced. Additionally, the heterogeneities in concentration appear to coarsen as E is increased, resulting in fewer shear bands. Thus, the two-fluid R-P theory predicts shear banded velocity profiles in LAOS, and the number of bands depends on the degree of flow-concentration coupling.

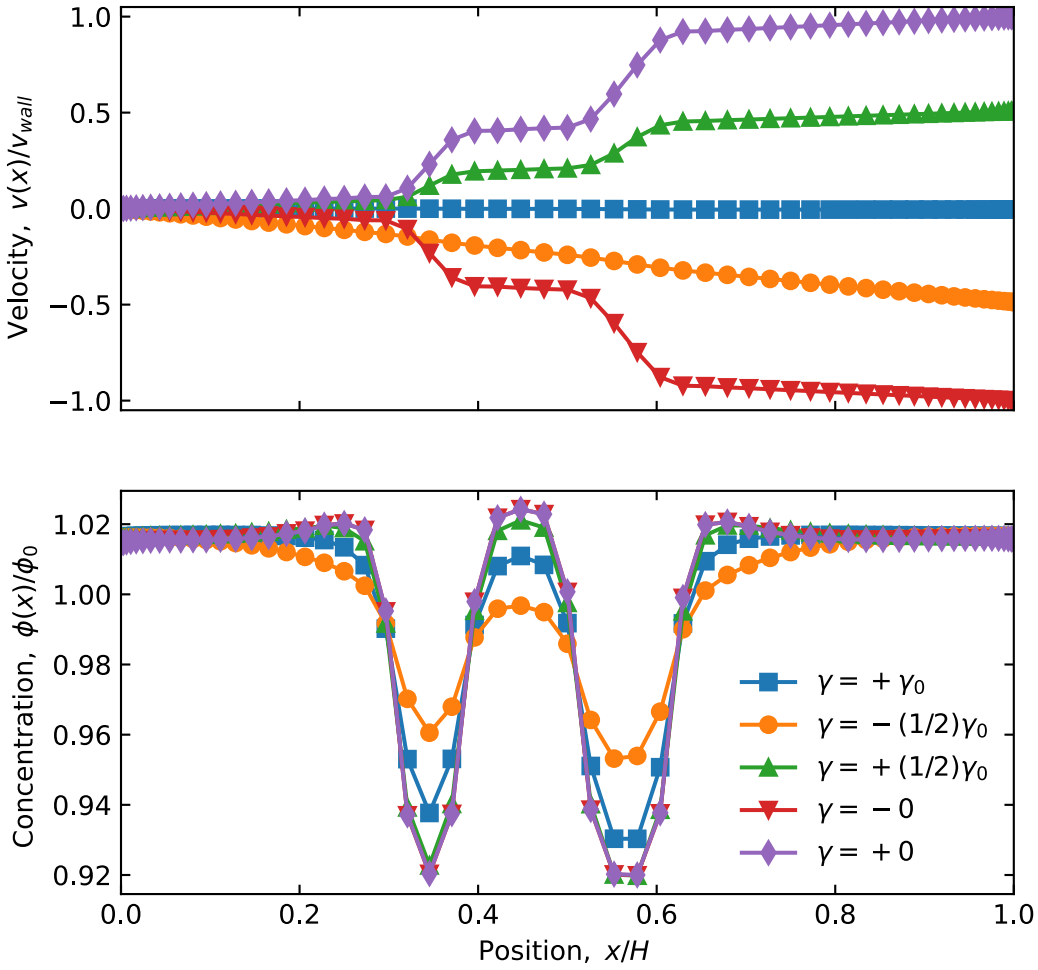

Figure 9.4: Steady time-varying velocity profiles (top) and corresponding concentration profiles (bottom). $Wi = 8$, $De = 0.1$, $Z = 40$, and $E = 0.20$.

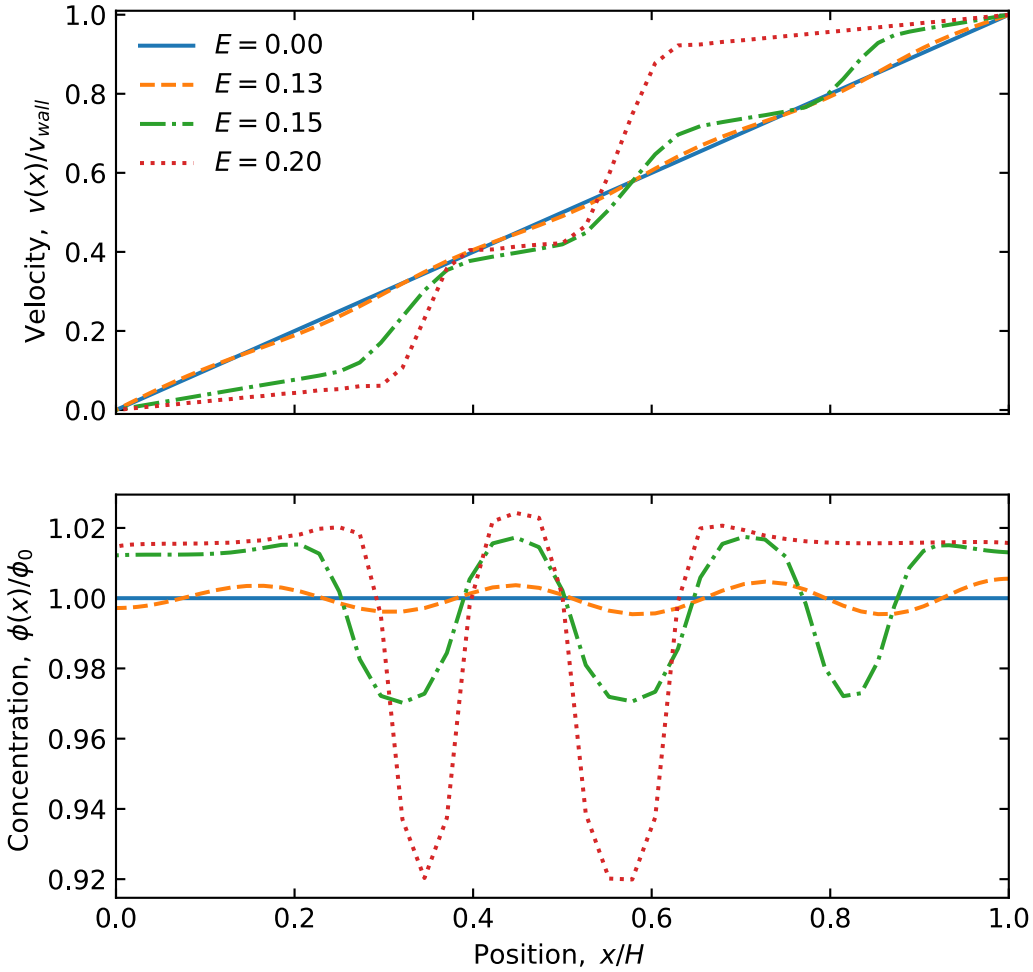

Figure 9.5: Velocity (top) and concentration (bottom) profiles when the wall imposed shear rate is at a maximum for varying degrees of flow-concentration coupling. $Wi = 8$, $De = 0.1$, and $Z = 40$.

9.4.5 Changes to Lissajous-Bowditch plots resulting from shear-induced demixing and shear banding

As shown in the last section, flow-concentration coupling of entangled polymer solutions in LAOS is predicted to have significant implications for the flow and concentration profiles of the fluid even in planar shear. To this end, it is of interest to determine whether and how the wall shear stress (*i.e.*, the value that is measured in most rheological experiments) and the resulting Lissajous-Bowditch curves are affected by the changes to the fluid velocity and concentration profiles. As shown in Figure 9.6, the intracycle shear stress decreases following the overshoot as E is increased. For $E = 0.13$, the elastic and viscous Lissajous-Bowditch curves are nearly indistinguishable from the uniform flow and concentration ($E = 0$) case. This minimal change is attributed to the weak undulations of polymer composition at low degrees of flow-concentration coupling prior to the strong demixing at high E that results in coarsened flow and concentration profiles with sharp interfaces separating the different shear and concentration bands. Additionally, the shear stress decreases from the overshoot to the plateau occurs over a smaller range of strain (Figure 9.6(left)). Presumably this is the result of shear-induced demixing to form shear banded flows, where the shear rate is low in regions high in polymer concentration and the shear rate is high in regions low in polymer concentration (Figure 9.5). However, these Lissajous-Bowditch plots for varying E fail to accurately describe the material evolution under LAOS flow, because while the average shear rate and strain of shear banded and uniform flows are equivalent, no material element is deformed according to the time-varying average shear rate and strain once shear-induced demixing occurs. As a result, the presence of flow nonuniformity invalidates the conventional interpretation and analysis of "global" Lissajous-Bowditch curves in terms of stress decomposition or local curvature, because the nominal imposed (wall) shear rate no longer reflects the kinematics

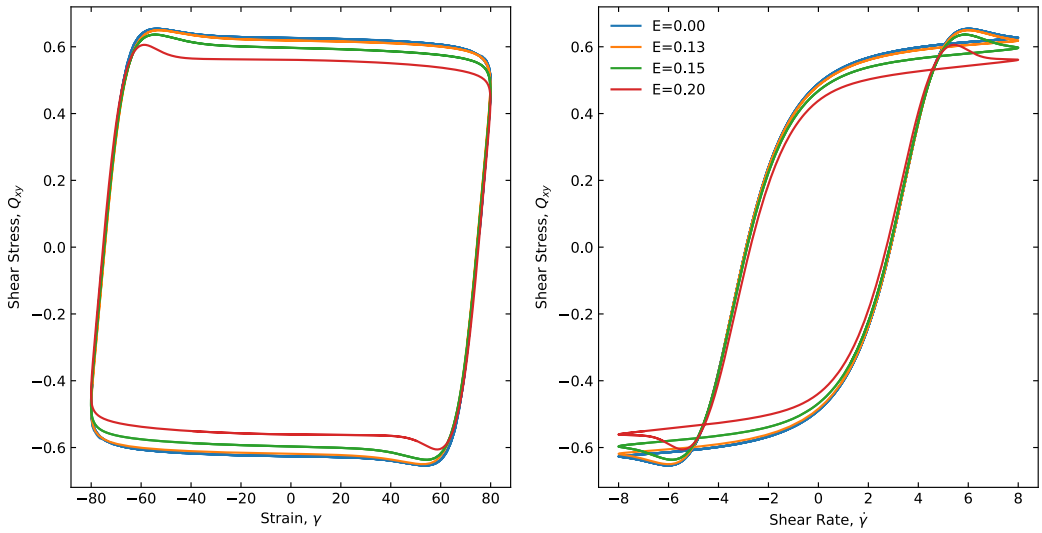

Figure 9.6: Sensitivity of elastic (left) and viscous (right) Lissajous-Bowditch plots to the degree of flow-concentration coupling (E). $Wi = 8, De = 0.05, Z = 40$.

of the imposed flow, and therefore the deformation that the material is undergoing.

9.4.6 Spatially resolved Lissajous-Bowditch plots for "local" material trajectories

Given that inhomogeneous flow renders meaningless the nominal imposed shear rate, and therefore any analysis of the LAOS response based on it, we examine whether meaningful interpretation can be regained if one instead analyzes the intracycle response at the local scale, *i.e.*, through examination of a "local" Lissajous-Bowditch plot determined by the locally observed shear stress, strain, and shear rate. Spatially resolved quantities for the local strain and shear rate were computed by integrating the velocity profile with respect to time and differentiating the velocity profile with respect to position, respectively (*i.e.*, $\gamma(x,t) = 1/De \int_{t_i}^{t_{i+1}} u(x,t)\,\mathrm{d}t$ and $\dot{\gamma} = \frac{\mathrm{d}}{\mathrm{d}x}u(x,t)$, where t_i and t_{i+1} are the times of subsequent velocity profiles set by the adaptive time discretization of the ode15s

solver in MATLAB). These local measures of strain and shear rate more accurately reflect the fluid response under LAOS when the flow becomes nonuniform, and more faithfully resemble the responses observed when examining the "global" LAOS response for polymeric materials undergoing homogeneous flow. As evident from Figure 9.7, the spatially resolved Lissajous-Bowditch curves reveal how drastic an under- or overprediction can be when it is assumed that the velocity profile is linear and the composition is uniform. In addition to obvious changes in both the strain and shear rate amplitudes for “local” fluid elements relative to the wall-imposed uniform strain and shear rate, there are also qualitative changes to the shapes of the Lissajous-Bowditch curves in the high and low shear rate regions. This distinction is most apparent in comparing the viscous Lissajous-Bowditch curve of a fluid element in the low shear band compared to an assumed uniform flow (Figure 9.7 (top right)). In particular, there is a “kink” in the viscous Lissajous-Bowditch plot that signifies a reduction of the local shear rate as the wall-imposed shear rate increases (Figure 9.7 (top right)). The maximum shear rate experienced by a fluid element within the low shear band is less than half of the maximum wall-imposed shear rate (Figure 9.7 (top right)). Further, the viscous Lissajous-Bowditch curves for the low shear band and uniform flow converge as the wall-imposed shear rate is reduced to zero. This convergence of the local and uniform curves reiterates the apparent return to uniform flow for portions of the oscillation cycle, as observed in Figure 9.4. In comparing the local viscous Lissajous-Bowditch for a fluid element in the high shear band to the uniform viscous Lissajous-Bowditch curve (Figure 9.7 (bottom right)), a greater than 5-fold increase in the shear rate amplitude is observed. Again, there is a qualitative change to the local viscous Lissajous-Bowditch curve in the high shear band compared to that of the wall-imposed shear rate. Unlike the reduction of shear rate in the low shear band as the wall-imposed shear rate is increased, the local shear rate in the high shear band continuously increases with the wall-imposed shear rate.

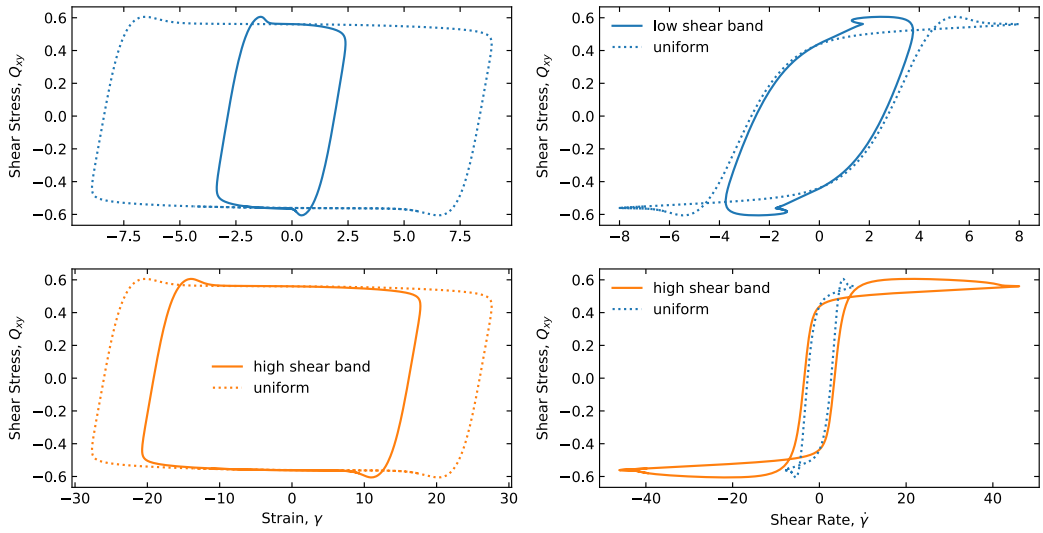

Figure 9.7: Spatially resolved Lissajous-Bowditch curves illustrating the difference in local material strain and strain rates. $Wi = 8$, $De = 0.1$, $Z = 40$, and $E = 0.20$. Legend is the same for top two plots.

9.5 Conclusions

We investigated the propensity for entangled polymer solutions to undergo shear-induced demixing in LAOS flow using a two-fluid Rolie-Poly model. Compared to simple shear, the stability boundaries for shear-induced demixing are notably different in LAOS. Importantly, there is a sensitivity of the stability boundaries to the imposed De that is explained by an accumulated strain threshold necessary to induce shear-induced demixing of polymer and solvent. When shear-induced demixing occurs, there are significant changes to the fluid concentration and resulting flow profiles. As such, typical approaches to reporting and analyzing LAOS data are complicated by the presence of these nonuniform flows. Local measures of the strain and shear rate are computed to illustrate the discrepancies between the actual material response of a fluid element in LAOS and what is inferred by assuming that the flow remains uniform. Collectively, these results high-

light the importance and necessity of complementing standard rheological measurements with independent measurements of the flow kinematics to ensure that nonuniformities of flow are properly described.

Bibliography

[1] C. W. Macosko, *Rheology: Principles, Measurements, and Applications*. Wiley-VCH, 1st ed., 1994.

[2] R. G. Larson, *The Structure and Rheology of Complex Fluids*. New York: Oxford University Press, Inc., 1st ed., 1999.

[3] K. Hyun, M. Wilhelm, C. O. Klein, K. S. Cho, J. G. Nam, K. H. Ahn, S. J. Lee, R. H. Ewoldt, and G. H. McKinley, "A review of nonlinear oscillatory shear tests: Analysis and application of large amplitude oscillatory shear (LAOS)," *Progress in Polymer Science (Oxford)*, vol. 36, no. 12, pp. 1697–1753, 2011.

[4] M. Wilhelm, "Fourier-Transform Rheology," *Macromolecular Materials and Engineering*, vol. 287, no. 2, pp. 83–105, 2002.

[5] T. Neidhöfer, S. Sioula, N. Hadjichristidis, and M. Wilhelm, "Distinguishing linear from star-branched polystyrene solutions with Fourier-transform rheology," *Macromolecular Rapid Communications*, vol. 25, no. 22, pp. 1921–1926, 2004.

[6] R. H. Ewoldt, A. E. Hosoi, and G. H. McKinley, "New measures for characterizing nonlinear viscoelasticity in large amplitude oscillatory shear," *Journal of Rheology*, vol. 52, no. 6, pp. 1427–1458, 2008.

[7] S. A. Rogers, B. M. Erwin, D. Vlassopoulos, and M. Cloitre, "A sequence of physical processes determined and quantified in LAOS : Application to a yield stress fluid," *Journal of Rheology*, vol. 55, no. 2, pp. 435–458, 2011.

[8] S. A. Rogers and M. P. Lettinga, "A sequence of physical processes determined and quantified in large-amplitude oscillatory shear (LAOS): Application to theoretical nonlinear models," *Journal of Rheology*, vol. 56, no. 1, pp. 1–25, 2012.

[9] S. A. Rogers, "A sequence of physical processes determined and quantified in LAOS: An instantaneous local 2D/3D approach," *Journal of Rheology*, vol. 56, no. 5, pp. 1129–1151, 2012.

[10] S. A. Rogers, "In search of physical meaning: defining transient parameters for nonlinear viscoelasticity," *Rheologica Acta*, vol. 56, no. 5, pp. 501–525, 2017.

[11] M. Cromer, M. C. Villet, G. H. Fredrickson, and L. G. Leal, "Shear banding in polymer solutions," *Physics of Fluids*, vol. 25, no. 5, p. 051703, 2013.

[12] M. Cromer, G. H. Fredrickson, and L. G. Leal, "A study of shear banding in polymer solutions," *Physics of Fluids*, vol. 26, no. 6, p. 063101, 2014.

[13] J. D. Peterson, M. Cromer, G. H. Fredrickson, and L. G. Leal, "Shear banding predictions for the two-fluid Rolie-Poly model," *Journal of Rheology*, vol. 60, no. 5, pp. 927–951, 2016.

[14] M. C. Burroughs, Y. Zhang, A. M. Shetty, C. M. Bates, L. G. Leal, and M. E. Helgeson, "Flow-Induced Concentration Nonuniformity and Shear Banding in Entangled Polymer Solutions," *Physical Review Letters*, vol. 126, no. 20, p. 207801, 2021.

[15] J. D. Peterson, G. H. Fredrickson, and L. G. Leal, "Does shear induced demixing resemble a thermodynamically driven instability ?," *Journal of Rheology*, vol. 63, no. 2, pp. 335–359, 2019.

[16] E. Raspaud, D. Lairez, and M. Adam, "On the Number of Blobs per Entanglement in Semidilute and Good Solvent Solution: Melt Influence," *Macromolecules*, vol. 28, no. 4, pp. 927–933, 1995.

[17] M. K. Endoh, S. Saito, and T. Hashimoto, "Shear-induced structures in semidilute polystyrene solution: Effect of solvent quality," *Macromolecules*, vol. 35, no. 20, pp. 7692–7699, 2002.

[18] K. A. Carter, J. M. Girkin, and S. M. Fielding, "Shear banding in large amplitude oscillatory shear (LAOStrain and LAOStress) of polymers and wormlike micelles," *Journal of Rheology*, vol. 60, no. 5, pp. 883–904, 2016.

[19] R. S. Jeyaseelan and A. J. Giacomin, "Network theory for polymer solutions in large amplitude oscillatory shear," *Journal of Non-Newtonian Fluid Mechanics*, vol. 148, no. 1-3, pp. 24–32, 2008.

[20] R. H. Ewoldt and G. H. McKinley, "On secondary loops in LAOS via self-intersection of Lissajous-Bowditch curves," *Rheologica Acta*, vol. 49, no. 2, pp. 213–219, 2010.

[21] M. C. Burroughs, A. M. Shetty, L. G. Leal, and M. E. Helgeson, "Coupled nonhomogeneous flows and flow-enhanced concentration fluctuations during startup shear of entangled polymer solutions," *Physical Review Fluids*, vol. 5, no. 4, p. 043301, 2020.

[22] S. Ravindranath, S.-Q. Wang, M. Olechnowicz, and R. P. Quirk, "Banding in simple steady shear of entangled polymer solutions," *Macromolecules*, vol. 41, no. 7, pp. 2663–2670, 2008.

[23] P. E. Boukany, S.-Q. Wang, S. Ravindranath, and L. J. Lee, "Shear banding in entangled polymers in the micron scale gap: a confocal-rheoscopic study," *Soft Matter*, vol. 11, pp. 8058–8068, 2015.

[24] P. Tapadia, S. Ravindranath, and S.-Q. Wang, "Banding in entangled polymer fluids under oscillatory shearing," *Physical Review Letters*, vol. 96, no. 19, p. 196001, 2006.

[25] S. Ravindranath and S.-Q. Wang, "Large amplitude oscillatory shear behavior of entangled polymer solutions: Particle tracking velocimetric investigation," *Journal of Rheology*, vol. 52, no. 2, pp. 341–358, 2008.

Chapter 10

Conclusions

10.1 Summary

In this dissertation research, we investigated the effect of coupling flow to concentration in entangled polymeric liquids. Nearly all rheological studies of entangled polymer liquids to date have assumed that the fluid composition remains uniform, but the potential presence of compositional heterogeneities uncovered in this work has profound implications for both materials processing and interpretation of measured data. Recent advances in the theoretical modeling of entangled polymer solutions and blends have found that a shear-induced demixing instability results in large compositional changes to the fluid under flow, accompanied by substantial changes to the flow field, and in some cases, shear banded flows. In this work, the first direct comparison is made for model predictions of shear-induced demixing to experimental measurements. Advances in experimental techniques enable both the fluid's velocity field and composition to be measured. For entangled polybutadiene solutions, measured steady state velocity and concentration profiles are found to yield strong agreement with two-fluid model predictions and show a sensitivity to molecular details of the entangled polymer solution (*i.e.*, number of en-

tanglements and solvent quality). Preliminary results for bidisperse entangled polymer blends, with similar numbers of entanglements to the solutions, suggest that nonuniform flow develops for certain blend compositions, but corresponding measurements of shear-induced compositional changes in bidisperse entangled polymer blends are inconclusive. It is hypothesized that the nonuniform flow could arise from microscopic compositional changes below experimental detection limits. Finally, two-fluid modeling of entangled polymer solutions is extended beyond steady shear flow to include large amplitude oscillatory shear (LAOS). Commonly, LAOS data are interpreted assuming that the flow field remains uniform, but two-fluid modeling of entangled polymer solutions suggests strong nonuniformities in the flow can arise from the same shear-induced demixing instability as observed for steady shear flow. These modeling results give further credence to the importance of complementing standard rheological measurements with some form of flow visualization technique (*e.g.*, particle tracking velocimetry).

10.2 Conclusions

In Chapter 4, a study of the startup flow of entangled polystyrene (PS) in dioctyl phthalate (DOP) solutions was discussed. Entangled PS-DOP solutions were previously established as the ideal model system for studying shear-enhanced concentration fluctuations due to the large refractive index difference between polymer and solvent. Interestingly, inversely banded flow profiles were found to develop transiently following shear startup. These banded profiles were "opposite" of what the two-fluid model predicts for an entangled polymer solution, where low shear rate regions were measured in the region adjacent to the moving wall (high shear stress) and high shear rate regions were measured adjacent to the stationary wall (low shear stress). Rheo-microscopy measurements revealed a correlation between the low shear rate regions of the flow field and optical

heterogeneity arising from shear-enhanced concentration fluctuations. Thus, it was hypothesized that shear-enhanced concentration fluctuations resulted in a local effective viscosity increase in the fluid.

Chapter 5 presented a novel way to measure the composition of entangled polymer solutions using fluorescence microscopy. Thiol-ene chemistry facilitated the fluorescent-tagging of high molecular weight polybutadiene chains to enable the polymer concentration to be estimated from spatial variations in fluorescence intensity under shear flow. This was the first study to measure both fluid flow and concentration in an entangled polymer solution. The measured flow profiles were subjected to a recently developed method [1] to distinguish between shear banded flow profiles and curvature resulting from the shear thinning constitutive behavior. Using this method, the determined interface widths of the flow profiles were insensitive to the applied shear rate, indicative of banded flow profiles. Interestingly, remarkable agreement was found between the measured flow and concentration profiles compared to the corresponding two-fluid model predictions, which suggests that shear banded flow profiles can arise from shear-induced demixing of polymer and solvent.

Building upon the study of Chapter 5, Chapter 6 examined the sensitivity of the flow profiles and magnitude of compositional variations depending on molecular details of the fluid, such as the number of entanglements and the solvent quality. The measured flow and concentration profiles were found to become more nonhomogeneous as the number of entanglements was increased. The distinction between bands in the flow profile and the corresponding variation in concentration were also found to increase as the solvent quality of the fluid decreased. PBD-DOP solutions have an upper critical solution temperature around $T = 13\,^{\circ}\mathrm{C}$, so the solvent quality was altered by modulating the fluid temperature during experiments. Additionally, longstanding questions in the field pertaining to the influence of wall slip on the flow profiles were examined. Significant wall slip was observed

under some flow conditions, but it was found to be unnecessary for the development of shear banded flows.

Chapter 8 complements the prior work on entangled polymer solutions by examining flow-concentration coupling in bidisperse entangled polymer blends. Experiments were performed on three different bidisperse blends according to the Viovy diagram for characterizing blend dynamics. The Region IV blend is observed to adopt inversely banded flow profiles in the predicted region of instability. It is hypothesized that the inversely banded profiles, similar to what was observed in entangled PS-DOP solutions, result from local heterogeneities in fluid composition. Different flow kinematics are observed for blends with similar numbers of entanglements as the polymer solutions. This finding further underscores the apparent importance of constituent chemistry of the fluid on the flow behavior.

Finally, in Chapter 9 two-fluid modeling of entangled polymer solutions is utilized to explore shear-induced demixing in large amplitude oscillatory shear flow (LAOS). The stability boundaries for shear-induced demixing are found to be sensitive to the frequency of shear oscillation. Once shear-induced demixing has occurred, the fluid composition varies both spatially and throughout the shear cycle, but never completely re-homogenizes. The heterogeneities in fluid composition result in a banded flow profile similar to steady shear. Further, the presence of banded flow profiles is shown to complicate the standard analyses of LAOS data, which assume the fluid concentration, strain, and shear rate profiles are all uniform. Moving forward, it is imperative that rheological analyses are supplemented with corresponding measurements of the fluid flow field. Results of this chapter detail how drastically different evolution of material points in the fluid evolve in a single shear cycle.

10.3 Future directions

Several important future investigations have been identified through this work, including efforts from both modeling and experimental standpoints. In the following, numerous potential directions for research efforts are discussed.

First, this research only investigated polymer blends of chemically identical polymer melts. While this class of polymer blend is important, as nearly all melts have an inherent dispersity of molecular weight, many commercial blend formulations also incorporate disparate polymer chemistries. Numerous investigations have studied shear-induced demixing and mixing of polymer blends of differing chemistry using simplified constitutive models. The two-fluid model for polymer blends summarized in Chapter 7 suggests that chemical incompatibility is not necessary for shear-induced demixing/mixing effects. Future work should focus on connecting the early work of shear-induced demixing of partially miscible blends with blends that have polydisperse molecular weight distributions but homologous chemistry to better understand the role of entanglements on nonuniform flow.

Second, is the need to conduct *in situ*, spatially resolved microstructural measurements of entangled polymer blends under shear to identify nanometer to micrometer heterogeneity in blend composition and/or microstructure and potentially identify an explanation for the observed nonuniform flow present in some blend formulations. Common techniques for such measurements, such as rheo-small angle scattering (x-ray or neutron) are infeasible to this end due to either a lack of electron contrast (x-rays) or phase separation resulting from isotopic substitution (neutrons). Additionally, while the research presented on polymer blends only included the case of bidisperse blends, future efforts should extend these investigations to examine shear-induced demixing in more complex and industrially relevant molecular weight distributions such as a log-normal

distribution.

Furthermore, this dissertation research has solely focused on entangled linear polymers. Polymer solutions and melts with more complex chain architectures, such as branched polymers and rings, are finding commercial relevance as packaging materials and drug delivery vehicles. Thus, it is crucial to develop constitutive models for these varying polymer architectures to enable predictive flow calculations for their processing. Using properly formulated constitutive models, it would then be of interest to investigate whether two-fluid models using constitutive models for architecturally complex polymers predict shear-induced demixing as for linear chains. This comparison of flow behavior for polymers with varying architectural complexity could enable molecular-level design rules for engineering flow stability in entangled polymer solutions and blends.

Experimental studies of entangled polymer solutions in LAOS would be beneficial to confirm two-fluid model predictions of shear-induced demixing and shear banded flows. As revealed by the two-fluid model LAOS predictions, spatially resolved flow fields are imperative for accurate interpretation of rheological data (which often assumes uniform flow). The modeling results in this dissertation were performed for planar shear flow, but subsequent efforts should modify the code to permit LAOS flow calculations for flows with a stress gradient (*i.e.*, Taylor-Couette flows). A similar, spatially resolved analysis of model predictions for flows with a stress gradient will enable modeling comparison to experimental measurements in rotational rheometers.

Lastly, a limitation of the model predictions included in this dissertation is that they are all 1D simulations. Advances in computation and theory should make full 3D simulations possible. 3D simulations will enable flow predictions of entangled polymer liquids that are better suited for comparison to experiments. One aspect of this thesis research that would immediately benefit from such 3D simulations is the effective viscosity increase arising from local heterogeneities in fluid composition due to SECF, as hypothesized in

Chapter 4.

While this thesis specifically investigated different entangled polymer liquids, the concept of flow-concentration coupling is likely important in complex fluids more generally. Future rheological measurements and models should account for and examine these effects as the modeling and experiments in this dissertation suggest many flow complexities arise in shear flow.

Bibliography

[1] P. Cheng, M. C. Burroughs, L. G. Leal, and M. E. Helgeson, "Distinguishing shear banding from shear thinning in flows with a shear stress gradient," *Rheologica Acta*, vol. 56, no. 12, pp. 1007–1032, 2017.